DESIGN OF PLATE PANELS UNDER BIAXIAL COMPRESSION, SHEAR AND LATERAL PRESSURE

A Thesis submitted for the degree of Doctor of Philosophy in the Faculty of Engineering of the University of London

by Paul Cameron Davidson,
BSc(Eng), MSc, DIC

Imperial College of Science,
Technology and Medicine

October 1989

Frontispiece : HMS Manchester
(Courtesy of RN Recruiting)

For Linda,

and

Sarah & Deborah

ABSTRACT

Current design methods for panels in stiffened plate structures, under combinations of in-plane forces and lateral pressure are limited in scope and accuracy. In addition, there are many aspects of plate behaviour, especially in the elasto-plastic range, which are not well understood. The purpose of this thesis is to further behavioural understanding and to formulate rational models which enable the results of numerical analysis to be generalized for purposes of design of plate panels.

The structural and design implications of the basic assumptions of previous numerical analyses are examined (with particular attention paid to their boundary conditions), and where necessary improvements are made to the assumptions, this being assisted by the latest non-linear elasto-plastic analysis tools. New analyses are carried out which replace some previous analyses, and augment others, in order to clarify certain aspects of behaviour. Some new conceptual thinking is used, not only to specify the details of the numerical modelling, but also to define how the analyses should be interpreted and generalized, introducing the concept of limiting strain, as well as maximum resistance, as an appropriate design ultimate limit state. The maximum resistance of the panel may be attained at a strain at which the resistance of the remainder of the structure has already diminished, and this is avoided when a limiting strain criterion is used. The limiting strain criterion also provides a consistent basis for the interaction between thrust and lateral pressure. A new elastic analysis is derived, for panels subjected to biaxial compression and lateral pressure, and this is used as a basis for generalizing the numerical studies.

Examination of the structural behaviour revealed by the analyses is used to construct conceptual models of the behaviour of the panel. These are then used to provide rational design models for panel shear and compressive strength, and also for the interaction between biaxial compressions, with or without coexistent shear or lateral pressure. These models give a much better representation of behaviour than do existing design methods for combined loading.

The proposed design models are summarized for ease of reference and application.

ACKNOWLEDGEMENTS

The author would like to express his gratitude to the following:

My supervisors, Dr J.C. Chapman and Prof P.J. Dowling, for their generous and helpful guidance during the period of this project, and for the many fruitful and stimulating discussions on plating behaviour and design which have been one of the pleasures of carrying out this work.

Dr C.S. Smith of the Admiralty Research Establishment, Dunfermline, for his most useful input in helping to determine the direction which the project should take, and his comments on its progress throughout.

Dr R.S. Dow, and his colleagues at the Admiralty Research Establishment, Dunfermline, for the assistance they provided over the use of ASASNL, at Dunfermline.

The ARE, in general, for agreeing to co-sponsor my CASE studentship.

Dr A.F. Dier, currently of The Steel Construction Institute, for providing the original numerical data from his own research project, and for explaining the use of the Dynamic Relaxation program he had developed.

My erstwhile room-mates, at Imperial College, Drs D.N. Bates, and A.K. Chelghoum, for the generous part they played in helping me to overcome the idiosyncracies of FINAS.

CONTENTS

NOTATION

a	panel dimension in the long direction
a_0	coefficient in equation 6.1
a_{mn}	fourier coefficient
$\bar{a}$	coefficient in equation 6.19
b	panel dimension in short direction
b_0	coefficient in equation 6.1
$\bar{b}$	coefficient in equation 6.19
c_0	coefficient in equation 6.1
c_1-c_6	coefficients in shear strength model
$\bar{c}$	coefficient in equation 6.19
k	ratio of buckling displacement to initial imperfection, $=w/w_0$
k_x,k_y,k_τ	critical buckling coefficients for σ_x, σ_y, and τ, respectively in the presence of other stress components - see σ_{cr}, τ_{cr} and K_x, etc.
m	number of half-waves in long direction
n	number of half-waves in short direction
t	plate thickness
u	displacement in x direction
v	displacement in y direction
w	displacement in z direction (out-of-plane deflection)
w_0	out-of-plane initial imperfection
w_0'	notional out-of-plane imperfection prior to welding
w_{01},w_{03}	magnitude of initial imperfection modes with 1 halfwave and 3 halfwaves in longitudinal direction
w_1,w_3	magnitude of out-of-plane displacement mode components with 1 and 3 halfwaves in longitudinal direction
w_{tot}	total out-of-plane displacement, including initial displacement, ie = w_0 + w
x	coordinate axis in long direction of the panel
y	coordinate axis in short direction of the panel
z	coordinate axis out of the plane of the panel
C	denotes a constrained boundary - see U
E	Young's Modulus, taken to be 205,000 N/mm^2
G	Shear Modulus, = $E/2(1+\nu)$
K	coefficient in equations 6.15 and 6.17
K_x,K_y,K_τ	critical buckling coefficients for single stress load cases, ie for σ_x, σ_y, and τ alone, respectively - see σ_{cr} and τ_{cr}

Q	magnitude of uniform lateral pressure, in N/mm^2. Occasionally in the text lateral pressure will be referred to in units of metres head of water, where 1 metres head = $.00981 N/mm^2$
Q_{xu}	pressure end point of linear interactions between uniaxial σ_x and lateral presusre
Q_{yu}	pressure end point of linear interactions between uniaxial σ_y and lateral pressure
Q_{YL}	yield line pressure
S	denotes a constrained boundary with an incompressible stiffener attached to it (ie zero tangential strain)
U	denotes an unconstrained boundary - see C
α	aspect ratio of panel, = a/b
α_b	aspect ratio of single halfwave of buckle, = λ_b/b
α_p	aspect ratio of both the doubly curved end regions of a single halfwave of buckle
β	plate slenderness, $=b/t\sqrt{(\sigma_0/E)}$
β_{cr}	value of β for which the critical buckling stress is equal to the yield stress
γ	shear strain
γ_0	shear yield strain, = τ_0/G
γ'	normalized shear strain, = γ/γ_0
ϵ	direct strain
ϵ_x, ϵ_y	longitudinal and transverse direct strain
ϵ_0	direct yield strain, = σ_0/E
ϵ'	normalized direct strain, = ϵ/ϵ_0. $\epsilon_x'=\epsilon_x/\epsilon_0$, and $\epsilon_y'=\epsilon_y/\epsilon_0$
η	cross-product coefficient in biaxial compression interactions
η_q	cross-product coefficient in biaxial compression interactions, in the presence of lateral pressure
ζ	factor for the reduction in biaxial compressive strength due to coexistent shear
λ	ratio of panel slenderness to critical slenderness, = β/β_{cr}
λ_b	half-wavelength of buckling mode in longitudinal direction
ν	Poisson's ratio, =0.3
σ	direct stress
σ_r	residual compressive stress, due to welding
σ_{rmax}	maximum residual compressive stress consistent with a specified level of w_0
σ_x	direct stress in the longitudinal direction (usually the average direct stress)
σ_y	direct stress in the transverse direction (usually the average direct stress)
σ'	non-dimensionalized stress, = σ/σ_0

$\bar{\sigma}_x, \bar{\sigma}_y$	average direct stresses in x and y directions, only where it is needed to distinguish them from local direct stresses
σ_0	yield stress, assumed to be = 245 N/mm^2
σ_u	uniaxial compressive stress end points of a square plate biaxial compression interaction
σ_b	biaxial compressive stress where the line $\sigma_x=\sigma_y$ meets the biaxial interaction for square plates
σ_c	compressive capacity of the strut assumed to exist in the central prismatically deformed region of transversely (and biaxially) compressed rectangular plates
σ_{cp}	design resistance of a strut whose slenderness is given by $\alpha_p\beta$, used in equation 4.7
σ_{cr}	uniaxial compression critical buckling stress
σ_{crb}	biaxial compression critical buckling stress (for $\sigma_x = \sigma_y$)
σ_{xe}, σ_{ye}	edge stresses predicted by elastic model
σ_{xu}	uniaxial longitudinal compression design resistance, in the absence of other load effects
σ_{yu}	uniaxial transverse compression design resistance, in the absence of other load effects
σ_{y1}	local transverse compression applied to doubly-curved end regions of a single halfwave of buckling mode
σ_{xu1}	design resistance for the longitudinal compression which can be applied to a rectangular plate deforming in a buckling mode of aspect ratio α_b
σ_{xup}	longitudinal compression design resistance of a square plate whose slenderness is given by $\alpha_p\beta$, used in equation 4.7
σ_{yu1}	design resistance for the local transverse compression which can be applied to the doubly curved end regions of a single halfwave of buckling mode
σ_{xq}, σ_{yq}	reduced uniaxial compression design resistances, due to coexistent pressure
σ_{bq}	reduced biaxial compression design resistance, due to coexistent pressure
τ	shear stress
τ_0	shear yield stress, = $\sigma_0/\sqrt{3}$
τ'	non-dimensionalized shear stress, = τ/τ_0
τ_{cr}	critical buckling shear stress
τ_{cc}	design shear resistance of CCCC panels
τ_{cu}	design shear resistance of CUCC or CUCU panels
τ_{uu}	design shear resistance of UUCC, UUCU or UUUU panels
τ_u	design shear resistance

CHAPTER 1 INTRODUCTION

1.1 Background

There has been a great deal of research, over recent years, into the design of stiffened plate structures, from which a number of trends have become apparent. It will be useful briefly to describe these trends, and to make some comment on the direction in which they seem to be leading, in order to put this thesis into a proper context.

The first trend is the application of reliability methods to the design of ship and offshore structures. Although the application of reliability methods to plate structures (as opposed to tubular structures) is in its relative infancy, some potentially useful statistical models of the resistance of plate panels to single stress component loads have been developed. These take as their starting point statistical models of material and geometric variability (see references (1) to (6)) and apply them to strength functions of, for instance, longitudinal compressive strength (7) and shear strength (8), which include some of these parameters as input variables. Reference (7), in particular, contains a good presentation of the technique. Useful recent overviews of the application of reliability methods to plated structures are to be found in (9) and (10).

The second trend which is being developed mainly for ship and offshore structures, has come to be known either as the Idealized Structural Unit Method or the Super Element Method. This involves discretizing a large three dimensional plated structure, such as a ship's hull, into "idealized structural units", which may be plate panels between the orthogonal stiffening, or even groups of panels with their associated stiffeners. The load-displacement characteristics (in particular the compressive stress-strain curves) of each of these structural units is previously defined by a much finer discretization of the structural unit in non-linear elasto-plastic finite element analyses. The non-linearities in load response that are revealed by these detailed analyses are then incorporated in the load-displacement curve of a single structural unit in a global grillage or girder type of analysis (11)-(14), with considerable economy of analysis. This has been shown to provide a powerful technique for predicting hull-girder bending strengths, and has been useful in identifying contributory factors to a number of ship failures (15). A general review of the literature on this technique is given in (16).

The third note-worthy trend is the use of formal optimization techniques in structural

design. These techniques, which are briefly reported in (17), take into account the consequences of design decisions on the production costs (labour, overheads, etc.,) and material costs of the fabricated structure. In one study referred to in (17), an elastic stress analysis of a stiffened grillage was linked to optimization algorithms, using data of shipyard fabrication practice. Even with only six design variables (such as stiffener spacing, stiffener geometry, and so on), this produced an extremely complex calculation, but when the optimization was applied to an ultimate strength calculation the method became much less cumbersome. A development which is reported in (17) which may result in a greater application of these techniques is the linking of reliability modelling with the optimization process.

It is clear that there are a number of strands of research that are, more or less, evolving separately, whose synthesis (along the lines of that mentioned at the end of the previous paragraph) will have a significant impact on design practice, leading to consistent structural safety on the one hand, and structural and design economy on the other.

One thing which is common to all of these, however, is their partial reliance on (deterministic) ultimate strength (and stiffness) models. A lot of work has been carried out over the past two decades, and more, into developing and improving such models, for the wide range of load conditions that panels may be subject to. The discussion in this section will be limited to the subject of panels under shear, biaxial compression and lateral pressure.

Considering the shear strength of slender web panels, civil engineering design practice until the nineteen-sixties was largely based on the theoretical critical buckling capacity of the panel (as current ship and offshore design practice still is), even though, in the aeronautics field, the post-critical buckling reserve of shear panels had long been explicitly recognized (18), by utilizing an inclined tension throughout the plate to define the web shear capacity. This concept was introduced into the civil engineering field by Basler (19), who developed a tension field model appropriate to transversely stiffened steel plate girder webs. Basler's model envisaged a state of uniform shear stress in the web up to a value of shear stress equal to the critical buckling stress. Thereafter a Pratt-truss mode of behaviour developed in the plate where an inclined "tension field" developed (at an angle equal to half the angle of the diagonal), which was reacted by compressions in the flanges and stiffeners. This inclined tension system was superimposed on the underlying uniform critical shear stress, and the magnitude of the tension was such that yield occured within the diagonal band. It is interesting to note that this maximum strength model predates by many years the adoption of ultimate limit state concepts in civil engineering structures.

This very neat analysis has since stimulated a wide variety of enhancements and variations to the basic theme. The first that should be mentioned is given in (20), where an error in the original formulation of (19) is corrected, and the suggestion is made that the critical buckling stress should be that for a panel with clamped boundaries, rather than rotationally free boundaries. This was shown to reduce a conservatism (relative to test data) in the corrected Basler model which was not present in the original incorrect version.

A significant conceptual addition was due to (21) and later (22), where the influence of the bending rigidity of the flanges is explicitly allowed for, by permitting the tension field to react against the horizontal boundaries of the web panel. This results in a steepening of the tension field (and hence a greater vertical component), and the mobilization of a plastic frame mechanism in the Vierendeel panel formed by the stiffeners and flanges, acting with an effective portion of web. The observation was made in (21) that the tension field observed in tests lies much closer to the diagonal than to the half the angle of the diagonal predicted by Basler. The model of (22), has been shown (for instance in (23)) to give good agreement with large scale plate girder tests, and with some small refinements, has been incorporated in many recent design codes (24),(25) and (26).

When no account is taken of flexural rigidity of the flanges, the model of (22) basically yields the Basler model (there is a small refinement where the Von Mises (27) yield criterion is adopted in (22) rather than Tresca (28), as in (19)). There are, however, quite a variety of Tension Field models, and a detailed summary of these is to be found in (29). Only one of the alternative models will be mentioned here, and that is due to Dubas (30). This model also assumes that a uniform shear stress equal to the buckling shear stress exists in the plate, on which a tension field is superimposed, but the inclination and width of the tension field is obtained by assuming that a gusset of yielding plate exists in the corner of the panel. The size of the yielding gusset is obtained by assuming that it has an aspect ratio equal to that of the overall web panel, and that it is of such an extent that its critical buckling stress (assuming the same simply supported boundary conditions as the overall panel) is equal to the yield stress. This produces a much simpler analysis than that due to (22), although it does not distinguish between the shear strength of long and tall panels, and in this respect is not so representative of the actual behaviour of transversely stiffened shear webs. A development of this method has, however, been offered in the latest draft of Eurocode 3 (26), where it is described as the "simple post-critical method" to distinguish it from the "tension field method" from (22) which is also offered in that document.

Another interesting shear strength conceptual model is presented in (31) & (32). In this model a series of struts running at 45 degrees to the panel boundaries are envisaged which are reacted by orthogonal tensions of the same magnitude as the strut capacities, and which therefore do not impose normal forces on the panel boundaries. Since the length of these struts reduces, as they move nearer to the corners at either end of the tension diagonal, then their strut capacity increases, with a commensurate increase in the magnitude of the orthogonal tensions. In this manner, an alternative conceptual approach can be used to describe the mechanism whereby diagonal tension fields develop, although the tension field is not uniform and distinct from the remainder of the plate, as in the previously mentioned models. The basic concept of orthogonal struts and ties at 45 degrees to the panel boundaries is the same as that described at the end of Basler's original paper (19).

The model presented in (22) was also intended for use in longitudinally stiffened webs, which it did by considering them as webs with transverse stiffeners only, but whose critical stress is given by the least critical buckling stress of the various sub-panels bounded by the longitudinal stiffeners. This approach is based on the observation of tests on longitudinally stiffened plate girders, where, in the ultimate condition, a single tension field extending over all the sub-panels is reported. This approach is different from an earlier model described in (33), where tension field modelling is applied to each of the sub-panels in turn, and where internal boundaries are idealized as a flange stiff enough to force the frame mechanism hinge onto the mid-point of the internal boundary.

The only approach to longitudinally stiffened webs which has been utilized in recent UK codes is based on elasto-plastic analyses, and is described in (34). These analyses, which are described in detail in (35) and (36), involved carrying out a large parametric study of webs subjected to shear with direct and bending stresses, using a non-linear elasto-plastic finite difference analysis. This analysis was especially powerful in that through-thickness yielding was correctly modelled by a multi-layer Von Mises approach, rather than the Ilyushin (37) single layer yield criterion used in previous work. The adoption of the multi-layer approach was rendered feasible as a result of utilizing the Dynamic Relaxation (DR) method (38), which is very economic in terms of computer storage. The boundary conditions employed in the analyses were used to represent internal and external panels in longitudinally stiffened webs.

Many large scale tests on plate and box girder webs have also been carried out, and these have been used to verify the transversely and longitudinally stiffened models of (22) and are reported in, for instance, (39) and (40). A summary of all the

available plate girder tests is included in (41). Most of the plate girder tests were for cases with little coexistent bending moment, as pointed out in (42). Reference (42) presents the few available test results for webs subjected to significant amounts of bending and shear. These tests suggest that the numerically derived rules in (24) for shear and bending in longitudinally stiffened webs are too conservative, and a less conservative model is suggested.

A different aspect of shear web design is the question of fatigue cracking due to web "breathing". A slender shear web will experience significant buckling displacements at loads below its ultimate capacity. If repeated cycles of loading occur , sufficient to cause these buckling displacements, then this may give rise to a repeated flexural yielding at the ends of the tension diagonal (or at the foot of a truncated transverse stiffener), which can precipitate a fatigue crack. A theoretical analysis is presented in (43) which establishes the relationship between these flexural stresses and the applied loads. The method is based on an elastic solution of the Marguerre equations (44) for imperfect rectangular plates subject to shear. The problem of fatigue cracking due to web breathing is of particular concern in the slender aluminium webs found in aircraft structures, and (45) reports a recent experimental study of this problem.

Regarding plates subject to combined loads, the numerical study of plates under shear, compression and bending in (35) and (36), and the plate girder tests under bending and shear (42) have already been mentioned.

An interaction model suitable for use in design, for biaxial compression in square and rectangular plates was presented in (46), which was validated by some finite element analyses. This was shown in (47)–(49), however, to give a variable degree of correspondence with a much wider range of elasto-plastic analyses. These analyses formed a detailed investigation into the behaviour of square and rectangular plates under biaxial compression and lateral pressure, carried out on behalf of the British Ship Research Association and the Admiralty Marine Technology Establishment (Dunfermline) – now Admiralty Research Establishment (ARE). The Dynamic Relaxation method was used for this investigation, again using a multi-layer Von Mises model of through-thickness yielding, and the results obtained still represent the most thorough and relevant data available on the problem of biaxial compression and lateral pressure. Although only three slendernesses and two aspect ratios were considered in (47) and (48), the analyses were later extended to derive biaxial compression interactions in the absence of lateral pressure, over a wider range of slendernesses, and this was reported in (49). Reference (47) also contains a comprehensive review of the literature in the field of combined loading, up to 1981,

to which the interested reader is referred.

Contemporary with the studies presented in (47) - (49), another investigation into biaxial compression and lateral pressure was carried out in Norway (50),(51), using an elasto-plastic Rayleigh-Ritz analysis. Panels with various imperfection and residual stress magnitudes are analysed, and the influence of pressure and imperfections on the biaxial compression behaviour of plates is demonstrated. This rather elegant analysis produces similar results to those of (47) - (49).

Much of the work that has been published in the period since then has relied on elastic critical buckling theory, or elastic post-buckling theory. For instance, in (52) an elastic analysis is derived for the post-buckling of simply supported imperfect plates under biaxial compression, with edges constrained to remain straight but free to draw in, and for pressure loaded plates with edges simply supported but restrained against drawing in. The stress systems from each analysis are then combined and incorporated into a strength criterion based on Von Mises yield.

In (53) and (54) elastic post-buckling solutions are derived for long rectangular isotropic and orthotropic plates under biaxial compression, longitudinal compression with coexistent shear, and transverse compression with shear. The same author produced the earliest general solutions for the elastic critical buckling of rectangular plates under uniaxial longitudinal or transverse compression with coexistent shear, in (55) and (56).

Elastic critical buckling interactions were also derived in (57) and (58) for plates under biaxial compression, biaxial bending and shear. Due to mode changes many of the theoretical critical buckling interactions were formed from the intersection of interactions for different mode types, so single interaction curves were approximately fitted to the inner envelope of the intersecting critical interactions, by defining an interaction equation which incorporates exponent terms which were defined as functions of aspect ratio. These were then used as components in ultimate strength interactions together with Von Mises criteria applied at various points in the plate, using simple models of local stress variations. In (59), these interactions were then scaled to end at interaction end-points which were obtained as the mean of experimental results for single stress component load cases. The ultimate strength interaction between shear and compression was taken to be the parabola found in (56) for longitudinal compression and shear, and which is also used in (24).

In (60)-(62) a quite different approach to defining ultimate strength interaction curves for biaxial compression and shear is presented. This uses as its basis the Von Mises

yield surface for biaxial compression and shear, with correction factors applied to it which vary, not only with slenderness and aspect ratio, but also with stress ratio, which gives rise to an interaction shape different from Von Mises. Finite element analyses are employed in order to define these correction factors. A feature of the interactions which are produced is that their non-dimensionalised form is always symmetric (as is Von Mises), unlike the interactions in (24),(47) and (53)-(59).

1.2 Aims and Scope of this Thesis

The existing studies of the behaviour of shear panels all have the common feature of relying on the stiffeners (and flanges) which surround the panel being able to supply tangential forces and restraint to the panel boundaries. This applies to the numerical study of (34) to (36), to the various conceptual design models, and to some extent, to the large scale experimental investigations.

For the panel shear resistances which are indicated by these studies to be safely used in design, the stiffeners and flanges must have reserve axial stiffness and strength, additional to that required by their resistance to global force effects. This is also additional to the provision of out-of-plane restraint to the panel boundaries (by virtue of the flexural stiffness and strength of the stiffener) which is one of the primary purposes of these elements.

Transverse stiffeners in a plate girder very often have no other function than to provide the necessary restraints, and although design codes vary in the details of the method they use to ensure that the transverse stiffener can provide this restraint, there is, in principle, a consistency between design practice as it is applied to transverse web stiffeners, and to the shear capacity of the web panels themselves.

Flanges in a plate or box girder, however, may be fully mobilized in their primary purpose of resisting global bending moments so that the compression flange may not be able to supply the additional compression needed to react the horizontal component of the inclined tension field. This is particularly the case since the need to design the flanges to withstand the tension field forces (as distinct from frame actions) is not stated in design codes.

In ship and offshore structures, the stiffeners are more likely to be expected to resist global forces, either contributing to the flange of a hull girder, or by resisting lateral loads through grillage action. As a consequence, a design shear capacity which relied on the presence of additional stiffener forces will severely complicate the design of

these stiffeners.

On the other hand, the limitation of panel shear capacities to the critical buckling stress in (63), or the restrictions on panel slenderness in (64) and (65) which ensure that shear buckling will not take place, are likely to be overly conservative.

One aim of this thesis, therefore, is to investigate the panel shear resistance which can be mobilized in the absence of tangential restraint, and to produce a design model for panel shear resistance which should reasonably allow the axial forces in the stiffeners (and flanges) due to tension field effects to be ignored.

Considering biaxial compression, the recent studies, and in particular the elasto-plastic numerical investigations, have clearly identified the main features of the interaction between biaxial compressions in square and rectangular plates. Codes of practice, however, for the design of bridges, or of offshore structures, use interaction models which have the great merit of simplicity, but which offer, at best, only passing resemblance to the behaviour demonstrated by the various studies. Part of the difficulty in incorporating the result of the biaxial compression investigations into design codes is that these investigations have either produced wide ranging parametric studies, without providing generalized models, or have produced a wide range of empirical curve fit models which, lacking a rational conceptual basis, can only be said to be truly valid for the particular slendernesses and aspect ratios for which they have been validated.

As a result, a second aim of this thesis is to use the investigation of (47) - (49) as the basis for developing and validating a rational interaction model which will offer the prospect of a wider validity than the particular spot-checks which may be available. As part of this task, and in order to be able to present meaningful comparisons between the proposed model and the numerical data, it will be necessary to provide a design model for longitudinal and transverse uniaxial compression which will be consistent with the end-points of the biaxial interactions of (47) - (49).

It is also the purpose of the thesis to define a design model which will estimate the biaxial compression resistance when the maximum average direct strain in the panel is equal to the yield strain. This will have beneficial implications for compactness limits for the stiffeners which will not then be required to maintain their flexural stiffness in the presence of plastic axial strains which may be to two or three times yield strain. It will also allow the simple evaluation of a stiffened flange compression capacity, by means of adding the design resistances of the individual panels in the flange, since all the resistances will be defined as occuring at the same applied

compressive strain. The yield strain criterion will also provide a consistent basis for interacting pressure with thrust.

A further aim of the thesis is to produce a model of the interaction between shear and biaxial compression, and of the influence of coexistent lateral pressure on the biaxial compression behaviour of the panel. The case of biaxial compression with lateral pressure, in particular, has been shown in previous studies to contain some quite complicated trends of behaviour, and in (66) it was shown that the design rules of (63) for this load condition bore very little resemblance to the behaviour revealed in (47) and (48). Part of the task of this thesis is, therefore, to carry out further analyses (and these will be both theoretical and numerical) in order to further understanding of the phenomena, and to permit a rational, conceptually-based, model for the interaction between lateral pressure and biaxial compression to be developed.

The development of the design methods begins in the next chapter with the treatment of the shear resistance of plate panels.

CHAPTER 2 SHEAR

2.1 Choice of Boundary Conditions

When defining the strength of plate panels in isolation from the rest of the structure, it is necessary to take into account the restraint afforded to the panel boundaries by the surrounding structure. This is especially important for shear strength which, it will be seen, is sensitive to the restraint conditions at the boundaries. Therefore, before a shear strength design model can be developed it is necessary to select the boundary conditions to be assumed in the model. These boundary conditions are made up of both in-plane and out-of-plane restraints on the edges of the panel.

Considering the out-of-plane restraint first, the primary purpose of the stiffeners is to prevent out-of-plane displacements of the boundaries of the panel (which they do by having sufficient flexural stiffness and strength). They will also provide a degree of rotational restraint. The non-uniform torsions that will be imposed on the stiffeners will be transmitted as end-moments to the orthogonal stiffeners (or flanges) at the panel corners. There will also be either positive or negative rotational restraint on the panel boundaries from adjacent panels which may be in a more or less stable condition.

A design method which sought to invoke this rotational restraint in evaluating the shear strength of the panel would not only be complicated in itself, but would also require the consequential torsions and end moments to be included in the stiffener design. As a result, it is appropriate to assume that the panel boundaries are simply supported, and this assumption will be made in the present work.

Where the buckling displacements of the panel are expected to be significant it will be necessary to take into account the in-plane, or 'membrane', boundary conditions. The boundaries of a shear panel devoid of any in-plane restraint will deform in the doubly curved manner shown in figure 2.1. This figure is at maximum resistance for a square mild steel panel (σ_0=245 N/mm^2), with b/t=180 and an imperfection given by a single half sine-wave in both directions of amplitude w_0=b/200. No residual stresses were included in the analysis. The shear is applied as a uniform shear stress on the panel edges.

Membrane boundary conditions consist of in-plane restraints both normal and tangential to the panel boundaries. The presence of an adjacent panel at the

boundaries will serve to reduce the normal displacements at the boundary, and it has been assumed in previous analyses (34) - (36) that such a boundary remains straight, implying a non-uniform system of normal restraint forces. The boundary stiffeners (and flanges) will also offer normal restraint, as they bend in the plane of the plate, provided they are not fully mobilized in their primary purpose of preventing out-of-plane displacements of the panel boundaries and, in the case of flanges, resisting primary bending forces in the structure as a whole. The effective section of the stiffener (or flange) bending in the plane of the plate will include an amount of plate panel, to form an effective cruciform or tee section (if flat bar stiffeners are being used). Although the restraint offered by the adjacent panels will not, in general, maintain the edges completely straight, it seems reasonable to assume that it does if the rotational restraint introduced by the adjacent panels is being ignored at the same time. Some evidence to support this will be offered later.

There is also some tangential restraint offered by the adjacent panels, but it is the boundary stiffeners and flanges which can be expected to supply the greater tangential restraint, albeit with the same proviso as above, that they are not fully mobilized in their primary purpose.

Shear panels may be found in a wide range of situations, from an internal panel in an orthogonally stiffened assemblage, such as a ship's side in torsion, to a totally 'external' panel (in the sense that there are no adjacent panels), such as an unstiffened diaphragm in a box beam or column also subject to torsion. There can be, as a result, a variety of restraints that can be afforded to the panel boundaries.

This would not be so significant for design were it not for the considerable sensitivity of the calculated shear strength to the membrane boundary conditions. Figure 2.2 shows stress-strain curves for the same panel as in figure 2.1, but with a range of different membrane boundary conditions, giving rise to a variation in shear strength from 55% to 100% of shear yield. The greatest shear strength results from boundaries which are totally rigid, and which merely rotate and translate in a 'lozenging' mode, whereas the lowest shear strength results from boundaries devoid of any membrane restraint, as in figure 2.1. The strain which is plotted is the average shear strain in the plate measured from the relative displacements of the four corners of the panel.

Stress-strain curves I and III of figure 2.2 are from the investigation into the interaction between shear and direct stresses in (35), but the remainder of the stress-strain curves have been produced as part of the present work. All of the stress-strain curves are from non-linear elasto-plastic analyses with multi-layer Von

Mises representations of plasticity. The two curves from (35) were based on a finite difference representation of the plate, solved by the Dynamic Relaxation method, whereas the remainder are from finite element analyses using the packages ASASNL (67) (at ARE, Dunfermline) and the Imperial College program, FINAS (68). An important difference between the finite difference and finite element analyses was the means by which load was applied. In (35) the loading was applied to the panels as increasing magnitudes of horizontal and vertical boundary displacements, such that the applied shear and direct strains were kept in a fixed ratio to one another. This proportional straining gave rise to a varying proportion of average shear and direct stresses in the panel as the strains are increased. The loading in the finite element cases was applied as proportional stresses.

In (35), panels with two different combinations of membrane boundary conditions were considered for shear loading, these panels being described as "restrained" and "unrestrained". In both cases the vertical edges of the panels were required to remain straight, and were prevented from shortening, although they could be translated by amounts specified in the loading condition. In the case of restrained panels the horizontal edges also remain straight, while rotating in the plane of the panel in accordance with the shear deformations specified in the loading condition. The horizontal edges were also required to shorten by an amount specified in the loading condition, the horizontal strain being constant along the edge. This condition that $\partial u/\partial x$ is constant along the horizontal edges was also deemed to exist in the unrestrained panels, but in this case the horizontal edges were devoid of any normal restraint. It should be emphasized that the description of restrained or unrestrained in (35) is applied to the panel as a whole, even though the distinction between restrained and unrestrained panels is only in the normal restraint condition on the horizontal edges. It should also be emphasized that the horizontal edges in 'unrestrained' panels are not wholly devoid of in-plane restraint since the tangential strains are required to be uniform. Nevertheless, in the discussion of the results of (35) and (36) the same terminology will be adopted.

Curves I and III of figure 2.2 are particular cases of the restrained and unrestrained plate analyses, for which there was no direct strain applied to the plate, that is the vertical edges were kept the same distance apart while the shear strain was applied. Curves Ia and IIIa were produced using ASASNL, for the same boundary conditions as curves I and III and give quite good agreement.

The purpose of the restrained boundary condition was to model the case of internal panels in a transversely and longitudinally stiffened box-girder web, whereas the purpose of the unrestrained condition was to model the edge panel in such a web (or

the case of a web without longitudinal stiffeners). The data formed the basis of the current UK design rules for longitudinally stiffened webs in (24), as described in (34).

Proportional straining was used in the Dynamic Relaxation analyses because it turns out to be more convenient from a computing point of view, than the more representative case where the applied stresses are kept in a fixed proportion to one another. Such a proportional stress loading would have substantially increased the computer processing time taken in the analysis. (Proportional straining was also a feature of the DR analyses in (47)–(49), although a modification to the method was made in (49) to allow proportional stress loading for the special case of uniaxially compressed plates.)

If, however, it is assumed that the order of loading does not greatly influence the stresses at any value and proportion of applied strain, whatever the strain (and stress) history to that value, then with sufficient, and sufficiently close, proportional strain load cases it becomes possible to use the resulting stress–strain curves to obtain a stress–strain curve consistent with the loading being applied as proportional stresses. This is done by interpolating between the stress ratios which exist at a given level of strain in each of the proportional strain stress–strain curves, to obtain the magnitudes of the stresses which would exist if they were in some specified ratio. This 'cross–plotting' procedure, being repeated at sufficiently close increments of strain, will enable shear and direct stress stress–strain curves to be inferred for the case where the stresses are applied proportionally.

This procedure has been applied to the original data for the b/t=180 plate with unrestrained edges from (35), for a variety of ratios of direct to shear stress, in figure 2.3. Also shown are the original proportional straining stress–strain curves.

A special case of the cross–plotted stress–strain curves, and the one of interest in the present context, is the case with zero net direct stress. The stress–strain curves for this case have been cross–plotted for both restrained and unrestrained boundaries and are shown as curves II and IV, respectively, on figure 2.2.

For the case of biaxial compression, it was shown in (47), that order of loading did not significantly affect the ultimate biaxial strength of plates. To verify that this is the case for plates in shear, and also that the stress can be interpolated at different strain levels, a proportionally stressed analysis has been carried out with boundary and load conditions equivalent to the cross–plotted unrestrained curve, curve VI of figure 2.2. This analysis (giving curve VI a on figure 2.2) was carried out using ASASNL, and very good agreement was found with the cross–plotted curve. The very close

agreement may be to some extent fortuitous since the numerical meshes were different in the 2 analyses. The interlaced mesh used in (35) had an 8x8 Nxy mesh, whereas the 6x6 element mesh used in the ASASNL analyses had a 12x12 array of stress integration points. However, it is not possible to make direct comparisons between the results obtained by FE and FD meshes, because the errors associated with the two techniques arise from different causes. Other checks on the cross-plotting procedure will be presented in Chapter 4.

The restrained case with no direct strain included in the applied loading implies no deformation of any of the four boundaries, merely rigid body in-plane translations and rotations. As a result, when the shear buckle develops and it tries to draw the edges together, the fact that they are prevented from doing so means that a net biaxial tension is applied to the plate. This will tend to suppress the buckling displacements, and a higher strength can be expected to result, compared to the case where at least one pair of edges is allowed to draw together. To some extent this can be seen by comparing curves I and II of figure 2.2, but the effect is not significant in this case, since even the stress-strain curve for no net horizontal force reaches 98% of shear yield.

If, on the other hand, the panel is unrestrained (ie no normal stress on the horizontal edges), a more significant reduction in strength results from allowing the horizontal edges to shorten. The case with no applied direct strain (III) has a maximum stress of 88% of yield but this is reduced to about 71% of yield when the horizontal edges are allowed to shorten sufficiently for there to be no net direct stress, in curve IV.

The actual shortening of the edges will in fact depend on the stiffness of the flanges which must exist on these horizontal edges, and the extent to which they have reserve capacity beyond their resistance to overall bending and axial forces, but must fall somewhere between these two extremes of zero or full tangential restraint.

It should be noted that the tension field model due to Basler (19), and its subsequent derivatives, including the model of (22), do not apply a net shear alone to the panel. Due to the horizontal component of the diagonal tension, a net horizontal tension is also being applied to the panel, in addition to the shear force. This horizontal tension is not symmetrically disposed about the vertical edges and is thus reacted by unequal axial compressions in the top and bottom flanges. The original formulation of (19) was incorrect in disregarding the flange forces, as pointed out in (20), and, as a result, used an erroneous formulation of horizontal equilibrium. As also pointed out in (20), this neglect of the additional flange compressions over and above any

primary bending forces is non-conservative as far as the compression flange is concerned, and may even give rise to a net compression in the flange which carries the tension due to overall bending. Although the effect of these flange compressions on the plastic hinge moment in the flange was taken into account in (22), the design rules of (24)-(26) which are based on (22) do not take this effect into account, and neither do they require the flanges to be designed to resist the flange compressions due to the tension field. That they need to do so has recently been pointed out in (69) and (70).

By considering horizontal equilibrium of the vertical edge in the numerical analyses of (35), it is possible to deduce the flange axial forces which have to be supplied at the ends of the stiffeners to react the net forces. These forces will vary along the length of the flange due to the shear flows which exist on the horizontal edge of the panel. The end-forces imposed on the flange by various ratios of applied strains can be compared with the flange forces implicit in the tension field model. Although tension field models say nothing about the shear and direct strains in the plate, they do require a net tension force to be applied to the plate. It is, therefore, of interest to compare the flange forces in the tension field model with those deduced from the $\epsilon_x'=0$ case ($\epsilon_x'=\epsilon_x/\epsilon_0$), since this also imposes a net tension on the panel.

Figure 2.4 shows the distribution of horizontal stress on the vertical edge of the square b/t=180 plate at a shear strain of 2.5 times the shear yield strain. At this strain, the average shear stress in the panel is 88% of shear yield, and the average direct stress is a tension of 36% of tensile yield. By equilibrium, the flange end compressions are found to be 13.0 and 14.9 kN, whereas the flange forces implied by the Basler model are 7.2 and 17.3 kN, respectively. The net tensions applied to the plate are therefore 27.9 kN from the analysis, and 24.5 kN from the tension field model. These forces are calculated on the basis of the plate dimensions, used in (35), of 240m x 240mm x 1.333mm. As explained above, the inequality of flange forces is a result of normal forces which are not distributed symmetrically along the vertical edges. The greater inequality in the Basler model is a result of the normal forces being concentrated largely in only one half of the vertical edge.

If the vertical edges are allowed to draw together such that there is no net normal stress on them, then the diagonal tension field will be equilibrated by edge compressions within the plate itself. Figure 2.5 is a similar plot to figure 2.4, of the horizontal stress on the vertical edges when $\gamma'=2.5$, but in this case with a coexistent direct compressive strain of 1.25 times the direct yield strain. This proportional strain case is the nearest to the cross-plotted case for no net direct stress. The average shear stress has been reduced from 88% to 72% of shear yield, but the

tensile direct stress has reduced from 36% of yield to a compression of 8% of yield. The flange axial forces calculated from horizontal equilibrium in figure 2.5 are now 0.9 kN compression, and 7 kN tension. It can be seen that a net tension needs to be supplied by the flanges in order to react the net compression experienced by the panel.

Principal stress distributions throughout the plate for both the cases represented by figures 2.4 and 2.5, but with a uniform critical shear stress subtracted from the actual shear stress throughout the plate are presented in figure 2.6. By subtracting the critical shear stresses, the equivalent of the post-buckling stress distribution assumed in tension field models can be examined. A number of interesting features are apparent in the second case. Clearly visible is the presence of a diagonal tension field, of off-diagonal regions with very little post-critical stress, and of the edge compressions along the horizontal boundaries. These effects tend to be obscured by the overall net tension in the $\epsilon_x'=0$ case, even though this net tension is comparable to that in the tension field model.

It is worth mentioning that although the inference of a zero net direct stress solution from the DR analyses corresponds to the shear end-points of a shear-compression or shear-bending interaction, the zero net direct stress condition is, none the less, a little anomalous for the boundary conditions used in (35). Horizontal stiffeners or flanges which have no reserve axial stiffness to enable them to react a net tension on the panel would not be in a position to impose the uniform straining on the horizontal boundaries that is assumed in the analyses.

The boundary condition assumed on the vertical edges of both restrained and unrestrained plates, required not only that the edges remained straight, but also that they did not shorten. This implies the presence of incompressible stiffeners at the panel vertical boundaries, and gives rise to a system of non-uniform shear stresses on the vertical edge. Figure 2.7 shows the development of these non-uniform shears at various levels of applied shear strain for the unrestrained square plate with b/t=180, with a coexistent compressive strain of $\epsilon_x'=0.5\gamma'$ (where $\gamma'=\gamma/\gamma_0$). If an identical panel exists on the other side of the vertical boundary, then an identical, but inverted, system of shear stresses will exist in the adjacent panel at the boundary. Since the shear flows are not symmetrical about the mid-height (due to the concentration of diagonal tensions at one end of the vertical edge) they will not be balanced by the shear flows in the adjacent panel. Consideration of shear equilibrium on the vertical edge will supply the tractions which exist along the length of the stiffener, and hence the stiffener axial force, in a similar manner to the stiffener forces calculated from tension field models.

Figure 2.8 shows the distribution of axial force in the stiffener, inferred from the shear flows of figure 2.7, at γ'=2.5, with the equivalent stiffener force distribution due to Basler's tension field model. The maximum stiffener force deduced from the analysis is 10.2kN whereas the tension field model gives a stiffener force of 7.2kN.

Close correspondence between the stiffener force deduced from the analysis and the stiffener force implied by the tension field model, is not to be expected, since the choice of applied strain ratio from the analyses is somewhat arbitrary. The tension field model does, however, predict a stiffener force of the same order as that in the numerical analysis. Furthermore, tension field predictions of stiffener force were shown in (23) and (40) to give good correspondence with the stiffener forces measured in large-scale laboratory tests on plate girders.

Figure 2.9 plots the variation in maximum stiffener force with applied shear strain from the shear flows of figure 2.7. The stiffener force has been non-dimensionalised by dividing it by the plastic shear capacity V_o of the plate. Also shown are the variations in stiffener force from the ϵ_x'=0 solutions for b/t=120, 180 and 240. At ϵ_x'=0 and γ'=2.5 the b/t=180 plate has a stiffener force of 3.11kN compared to 10.19kN for the same plate with ϵ_x'=0.5 γ'. It is also evident that all the ϵ_x'=0 results show a peak in the stiffener force at around the yield strain, whereas the ϵ_x'=0.5 γ' case has a stiffener force that is still increasing at γ'=2.5. The fact that the ϵ_x'=0 solution for b/t=180 has less stiffener force than the ϵ_x'=0.5γ' solution is a reflection of the shallower angle of the diagonal tension field, and its less localized extent, when net tension is applied, as seen in figure 2.6.

Figure 2.10 presents the stiffener forces calculated from the unrestrained numerical analyses, at ϵ_x'=0 and γ'=2.5, for aspect ratios from 0.5 to 3, for plates with b/t=120 and 180 (a/t=120 and 180, if a/b=.5). In addition, where there were sufficient data, the stiffener forces have been interpolated at γ'=2.5 for the case with no net direct stress. The stiffener forces are presented as fractions of the ultimate shear strengths of the panels, and the same calculation has been carried out using the design rules of (24), and the tension field models of (30) and (19) (as corrected in (20)). The plot shows occasional agreement between either the ϵ_x'=0 or the $\Sigma\sigma_x$=0 case, and the various design methods. According to the analyses, the stiffener force is smaller relative to the panel shear capacity for square plates than it is for long or tall plates, and, in general, this is also evident from all the design methods.

It has been of some interest to see how the boundary condition assumptions of (35) can be made to produce information about stiffener forces. However, these forces

are a function of the infinite axial stiffness in the vertical stiffener which has been assumed in the analyses. If the axial stiffness of the stiffener, and hence the tangential restraint on the vertical edge, is less than infinite, then the shear flows will be more uniform, giving rise to a reduced build up of stiffener force. When there is a total lack of tangential restraint, then the shear stress on the boundary will be uniform, and there will be no axial force in the stiffener. This case was also analysed using ASASNL, for the situation where the horizontal edges do not shorten (ie $\epsilon_x'=0$). In addition, the same analysis was carried out with a vertical stiffener having a cross-sectional area equal to 10% of the web cross-sectional area (this figure based on calculations using (24)). The stress-strain curves produced, are shown in figure 2.2, as curves VI and V, respectively. The surprising thing to note is that curves V and VI are almost coincident with curve IIIa. It is apparent that the tangential restraint on the vertical edges has almost no effect on the shear strength of the panel, even though in one limit the vertical edge is prevented from shortening, and in the other limit the edge is totally unrestrained from shortening. A similar effect will be shown later in this section for a different set of boundary conditions.

A particular feature of the boundary conditions assumed in the analyses of (35), was the requirement that tangential strains on the boundaries have to be uniform (or uniformly zero). It has been pointed out that this is anomalous for situations where there are no net direct stresses on the panel. Furthermore, it gives rise to non-uniform axial force effects in the stiffeners (and flanges) which would need to be included in their design, if the panel strengths used in design are based on the boundary members providing these membrane restraint forces.

The use of finite element analyses, however, facilitates the adoption of boundary conditions which do not impose tangential restraint. Although the original intention had been principally to make use of the numerical results of (35) to produce a design model, it was felt that the boundary conditions of (35) represented upper bound assumptions about the tangential restraint offered to the panel by the stiffeners (and flanges). It was therefore decided that new analyses, using a less restraining set of boundary conditions, should be carried out to provide the basis of a design model. In the new set of boundary conditions, all the panel boundaries are assumed to be free from tangential restraint (and are subjected to a uniform shear stress). External boundaries would, in addition, be free of any normal restraint (so that the normal stress will be everywhere zero on the external edge), whereas internal boundaries would be constrained to remain straight while being free to translate such that there will be no net normal force (which will give rise to a self-equilibrating system of normal stresses). It was felt that such boundary conditions would not only offer a

safe lower bound to the actual tangential restraint, they could also simplify the design of the stiffeners and flanges. It seems reasonable to assume that panel shear strengths based on these boundary conditions, do not require either tangential forces or overall axial forces to be included in the design of the boundary stiffeners (and flanges). Neither do they require the boundary stiffening elements to have reserve axial stiffness beyond their resistance to out-of-plane flexure and global force effects. What would be required, of course, is sufficient ductility in the stiffeners to permit any redistribution that may be needed. Verification of this basic assumption about the effect of zero tangential restraint on the design of stiffeners forms part of a separate research project, which is presented in (71).

These boundary conditions have the additional advantage of being consistent with those used in the biaxial compression and lateral pressure studies of (47) to (49), which will be used in chapters 3, 4 and 6.

The edges which are constrained to remain straight will be referred to as 'constrained' edges, whereas the edges which are free of any membrane restraint will be termed 'unconstrained'. The letters C and U will be used as a short-hand notation to denote these boundary conditions, and each of the boundaries of the panel will be given one of these letters, starting with the left hand vertical boundary and going round the boundaries in a clockwise direction. A panel which is constrained on all four edges will have its boundary conditions denoted as 'CCCC'; a panel unconstrained on all four edges will be denoted 'UUUU'; whereas a panel constrained on the vertical edges only will be denoted 'CUCU'. Curves VII, VIII, and IX, on figure 2.2, correspond to these boundary conditions, and are based on analyses carried out using FINAS. The mesh sizes were 8x8, (compared to 6x6 for ASASNL, and 8x8 for the Nxy mesh in the DR analyses) but plate geometries were exactly the same as in the other analyses represented on figure 2.2. Figure 2.11 describes in detail the boundary conditions of square UUUU, CUCU and CCCC panels.

In the absence of tangential restraint on the horizontal edges, and of a net horizontal force on the panel, it is useful to check the effect of the incompressible vertical stiffener on the panel resistance. If the existence of such a stiffener on an otherwise constrained edge is denoted by the letter S, then the panel boundary conditions are denoted by 'SUSU'. Figure 2.12 compares SUSU and CUCU for both a square and a tall 2:1 panel, with a/t=180. Again, zero tangential restraint reduces the panel strength by only two or three percent of the panel strength with infinite tangential restraint. Figure 2.13 compares the vertical shear stress distributions at two strain levels, for the square plates of figure 2.12, at the edge of the plate, and down its

vertical centre-line. Although the shear stress distributions with and without tangential restraint are naturally quite different on the boundaries, the shear stress distributions are almost identical, remote from the boundaries.

The implications for panel strength, of the assumption that internal boundaries remain straight will now be examined. 3:1 CUCU plates which have been subdivided into 3 square panels by suppressing the out-of-plane displacements on vertical sections a/3 apart, have been analyzed for slendernesses of b/t=80, 120 and 180. A mesh size of 24x8 was used, in order to make direct comparison with square plate analyses with 8x8 meshes. The maximum resistances of the multi-panels were 0.982, 0.831 and 0.616 for b/t=80, 120 and 180 respectively, which are slightly greater than the corresponding values for square CUCU panel analyses of 0.972, 0.803, and 0.597, reflecting the influence of rotational continuity at the internal panel boundaries in the multi-panel analyses.

In this section, the implications of the boundary conditions assumed in the finite difference analyses of (35) have been considered. It has been noted that membrane forces were transferred to the boundary members, and it is felt that the need to take this into account in the design of these members is undesirable in a design method. It has also been noted that similar membrane forces are transferred to the boundary members in the tension field models of (19) to (22), and (30), and that in current practice not all of these membrane forces are being considered in the design of the boundary members. Having chosen boundary conditions which do not transfer membrane forces to the stiffeners (and flanges), numerical analyses can now be presented which will form the basis of the design model.

2.2 Numerical Analysis

2.2.1 Numerical Modelling

Before discussing the results of the numerical analyses which were carried out, it is worth describing the numerical modelling which was used, particularly since much effort was expended on its development.

The analyses were carried out using the eight-noded iso-parametric shell element in FINAS, with 2x2 gaussian integration, the stresses being evaluated at 6 stations through the thickness. It was primarily in the area of constraint modelling that the difficulties arose. FINAS currently lacks many of the features which are available in commercial packages. One such feature is the availability of constraint equations, or

some other general method of constraint modelling.

The beam element which is available in FINAS was developed (72) for use as an open-section stiffener in stiffened shell problems. Connecting such a beam to the boundaries, with sufficiently high bending and shear moduli to keep the edge straight will over-constrain the edge, suppressing the shear strains on the boundary. In addition, if such beams were to be applied to all four edges, the moment continuity they would have at the corners would form a rigid Vierendeel panel around the plate. This would clearly not be suitable as a constraint model.

Considerable time and effort was therefore expended on developing constraint models which would be suitable for plates in shear.

A simple axial and transverse spring model was available which could be used in two different ways to model un-rotating constrained boundaries. One way was to set up a rigid beam parallel to the translating boundary, and to connect it to each node on the boundary by high stiffness axial springs, thus keeping the edge straight while de-coupling the shear restraint of the beam from the plate, allowing the plate boundary to strain in shear. A simpler way to use the springs was to connect them end-to-end along the nodes on the edge of the plate, setting their axial stiffness to zero, but giving them a high transverse, or shear, stiffness. (The axial stiffness could also be set high if an incompressible stiffener was to be modelled). The high shear stiffness of the springs constrains adjacent normal displacements of the edge of the plate to be equal. This method of constraint was by far the better conditioned of the two, giving a solution less likely to break down through lack of convergence.

Neither method is suitable for rotating constrained edges. The beam-spring model could in principle be used on rotating edges but turns out to be very ill-conditioned when its stiffness is sufficient to keep the edge straight, whereas the shear-spring would actually suppress rotations. It was therefore necessary to develop a special element for rotating constrained edges.

Two elements were developed for this boundary condition. The first was a two-noded plane frame beam, using simple beam theory. Such elements connected end-to-end keep the edge straight by virtue of their high bending stiffness alone. It was formulated with the option of a pin at either end, to prevent moment continuity at the corners of the panel. The second model was set up as an optional modification to the beam-stiffener element, in association with the author of the beam-stiffener. This model used the finite difference formulation for curvature over three nodes to constrain the middle node to lie on a straight line between the outer

nodes. On its own, this merely produced a rigid three noded link, with pinned ends, so not only were they connected end-to-end along the boundary of the plate, but a second layer of elements was set up which over-lapped the first layer, so that the middle nodes of the overlapping links coincided with the end nodes of the first layer of the links.

For non-rotating straight edges, all four constraint models give the same answers, although with widely varying efficiencies. Figure 2.14 shows a shear stress-strain curve for the b/t=180 CUCU plate with a 6x6 mesh. The right hand constrained edge is simply modelled by suppressing normal displacements, whereas on the left hand edge each of the four constraint models have been used in turn. The curve which is drawn is due to the over-lapping link model, with the results of the other three models shown as data points. It is interesting to note that the two-noded beam element was almost identically conditioned to the shear-spring element and followed almost the same automatically selected load increments. The over-lapping link element was less well-conditioned, with the beam-spring model being the least well-conditioned.

For rotating straight edges, the two-noded beam turned out to be poorly conditioned, whereas the over-lapping link was entirely satisfactory. Obtaining overall good performance from the over-lapping link terminated the development and improvement of the two-noded beam, and this element was no longer used.

Checks were carried out on the constraint modelling such as modelling a plate with only two opposite boundaries constrained, both as CUCU (using shear-springs on the left hand un-rotating constrained edge) and as UCUC (using over-lapping links on both the rotating constrained edges). These analyses gave identical results. Internal checks are also possible. In the CUCU case the left hand edge is modelled using the constraint models, whereas the right hand edge can be modelled simply by suppressing normal displacements (see figure 2.11). This latter condition does precisely and explicitly what is required of the constraint condition, so the fact that the solutions produced are entirely symmetric, indicates that the constraint models are also behaving exactly as required.

The result of this modelling development work was that constrained edges which were not required to rotate were modelled using shear springs, whereas constrained edges which were required to rotate were modelled using the over-lapping links. These analyses can now be discussed.

2.2.2 Numerical Results

The use of the finite element package was built up in stages. First of all, linear eigen analyses were carried out for flat plates subjected to uniform shear. These were compared with the results of buckling analyses using a Fourier series program, based on the Galerkin method, taken with sufficient terms for full convergence. Twelve terms were usually sufficient for convergence but 32 terms were used in general (this being the maximum allowed by the micro-computer memory). This Galerkin program, which includes biaxial compression as well as shear, is included in Appendix A, which sets out the theory.

Different mesh sizes were used in the FINAS eigen runs to enable the mesh-sensitivity to be studied. With sufficient elements the FINAS eigenvalues converged to within 3 significant figures of the Galerkin results. The buckling modes, plotted as contours, were identical. Figure 2.15 plots the ratio of the FINAS eigenvalues to the Galerkin eigenvalues for different mesh sizes, for a square plate in compression, and a square and 2:1 plate in shear.

It can be seen that for compressive buckling in square plates a 4x4 mesh is perfectly converged, whereas for the same degree of convergence in a square plate loaded in shear an 8x8 mesh would need to be used. A 6x12 mesh would give the same accuracy in a 2:1 plate subjected to shear. The requirement for a finer element mesh for square plates in shear than in compression, or for square shear plates than for rectangular shear plates, is due to the more localised bending curvatures which have to be modelled in the buckling mode. Figure 2.16 presents the contours for the first and second buckling modes in shear for square and 2:1 plates. The FINAS and Galerkin eigenvalues are also listed on the figure.

A comparison in the non-linear elastic range of behaviour is made in figure 2.17 between FINAS and the finite difference analyses of (73), of square imperfect plates with all four edges unconstrained. Also shown is the perfect plate post-buckling curve produced in (74) for the same plate, also using finite differences. The FINAS solutions give good agreement, and help to give confidence in the use of FINAS.

Figure 2.18 presents elasto-plastic shear stress-strain curves for a square and long 2:1 CUCU plate, with different mesh sizes. It is clear that many more elements are needed for full convergence in the elasto-plastic analyses than in the elastic buckling analyses. 12x12 elements are needed for convergence at the maximum shear strength of the square plate (compared to 8x8 for the elastic buckling load), and 10x20 is

needed for the 2:1 plate (compared to 6x12). It also appears that even these much finer meshes may not be fine enough to describe the unloading part of the stress–strain curve.

The reason for this is the same as for the differences in figure 2.15. In the elasto–plastic analyses the bending curvatures are even more localized than in the eigen modes, as can be seen by comparing the elasto–plastic buckling modes of figure 2.19 with the critical buckling modes of figure 2.16, and as a result need more elements. The modes of figure 2.19 are for square and 2:1 plates (both long and tall) of slenderness b/t=180 (a/t=180 for the tall plate). The corresponding shear strains in the plate are at approximately once and twice the yield strain. The plate maximum resistance is approximately at the former strain level. The figure also shows that the curvatures become increasingly localized in the post–peak phase of behaviour, so that more elements would be needed for convergence in the unloading part of the stress–strain curve than is needed in the region of the maximum stress.

The same argument applies to the presence of localized stress–gradients, and localized plasticity. Figure 2.20 presents the zones of mid–thickness yielding in the same plates as in figure 2.19. Gauss points (with their corresponding quarter–element) where mid–thickness yield exists, are indicated on this figure.

Principal stresses for these plates, at maximum resistance only, are shown on figure 2.21, both with and without the critical shear stress subtracted from the actual shear stresses. In a similar manner to figure 2.6 the removal of the critical buckling stress enables the post–buckling stress field to be examined, and reveals the same features as in figure 2.6. For all three aspect ratios, inclined tension fields are visible, with the regions outside the tension field containing little post–buckling stress except for the edge compressions along the boundaries. The diagonal tensions are more steeply inclined than the half the angle of the diagonal which is predicted by the Basler model. The tension field widths and inclinations due to Basler's model, and due to the model of (30), are shown on the figure. It may be remarked that tension fields steeper than half the angle of the diagonal can only occur in the tension field model of (22) and (24), by virtue of frame action in the flanges, whereas there are no flanges in the numerical analyses.

As the buckling deformation increases, and the zone of diagonal yielding develops, there comes a point when the ability of the plate to sustain additional shear is lost and the shear capacity of the plate reduces. Meanwhile, the loss of membrane stiffness down the yielded diagonal gives rise to an increase in the average shear strain. However, the off–diagonal regions of the plate are still elastic at their

mid-thickness, and as the shear stress which is being applied to these elastic regions reduces in accordance with the reduction in the applied shear stress, the local shear strain also reduces, even though the overall shear strain is increasing.

This means that the overall shear deformation will be increasingly concentrated in the yielded length of the unconstrained edge, giving rise to the localized boundary deformation seen in figure 2.22. This figure is for the same square plate and strain levels as in figure 2.20. If the applied shear stress is plotted against the average shear strain in the off-diagonal elastic regions (calculated from the deformation of the elastic half of the unconstrained edge), as in figure 2.23, then it can be seen that the local shear strain does in fact reduce.

The localized deformation in figure 2.22 only occurs in Basler-derived tension field models by virtue of plastic hinge mechanisms in the flanges. These hinge mechanisms are used to enhance the shear strength of the panel beyond its critical buckling and tension field capacities in the absence of frame action. It should be noted, however, that the localized panel deformations, which impose the plastic hinges on the flanges, only occur as the panel itself is unloading.

If the panel is constrained to remain straight on all four edges, then there will not be an opportunity for the shear strain to localize in the panel corners adjacent to the tension diagonal. The shear strain in the elastic region will still be reducing, however. As a result, the overall shear strain will also reduce, since the straight edge boundary condition constrains the yielded zone of the horizontal edges to have the same shear deformation as the elastic zone. Figure 2.24 presents stress-strain curves for a constrained square plate with b/t=180 for mesh sizes from 6x6 to 12x12. Although the 10x10 and 12x12 meshes show the reduction in the shear strain which has been described, the shear strain does not reduce with the 8x8 and 6x6 meshes.

Figure 2.25 shows the mid-thickness yield patterns at various strain levels for both the 8x8 and 10x10 meshes. The corresponding strains are indicated on figure 2.24.

Both meshes show localized membrane yield at the corner of the plate in the off-diagonal elastic region, at loads in the region of maximum stress. This permits the overall strain to continue to increase, even though the stress in the plate has begun to reduce. The 10x10 mesh, however, is better able to model local stress gradients and is thus able to represent the corner of the plate becoming elastic again, whereas the coarser 8x8 mesh does not detect this, and maintains yielding in the corner. This corner yield permits the overall strain to continue to increase, forcing plastic shear strains along the boundaries and causing a spread of plasticity along

them. The finer mesh reduces the overall shear strain as buckling proceeds, while giving rise to very large direct strains in the plate. The 10x10 solution has a direct strain nearly twenty times the yield strain, when the shear strain has reduced to the shear yield strain.

Having explored the basic behaviour which is indicated by the numerical analyses, the next task was to carry out a range of shear analyses for aspect ratios from 1 to 5, with slendernesses of b/t=80, 120 and 180, and boundary conditions from UUUU to CCCC. The imperfection used in all cases was the same as that used in (35), which has an amplitude equivalent to that in (24). That is, ripple sinusoidal imperfections having a half-wavelength equal to the shortest plate dimension were used, with an amplitude equal to w_0=b/200. The yield stress was taken to be σ_0=245 N/mm^2, and Young's Modulus, as E=205,000 N/mm^2.

The studies in (35) and (75) indicated that the shear strength was not very sensitive to the mode or amplitude of imperfections. Figure 2.26 shows the 8x8 CCCC result from figure 2.24 with the result of an analysis of the same panel with an imperfection affine to the inclined critical buckling mode. As would be expected this mode gives rise to less stiffness in the early stages of loading, but it has little effect on the maximum stress, or on the overall stress-strain behaviour.

Figure 2.27 shows the result of halving and doubling the w_0=b/200 plate imperfection on the stress-strain response of square CUCU plates with b/t=120 and 180. This supports the observation in (35) that the imperfection sensitivity of shear plates is not great (it is much less than will be seen later for compressed plates), and the question of other imperfection magnitudes was not examined further.

Residual stresses are not readily modelled using FINAS, and at a time when the program was having difficulty in modelling even residual stress-free plates with the desired boundary conditions, it was decided not to include σ_r in the analyses. Furthermore, it was found in (35) and (75), that the shear strength of plates was not very sensitive to residual stresses, a residual stress of σ_r'=0.3 giving rise to only a 5% reduction in strength compared to a plate without residual stresses. When the residual stress was 0.1 σ_0 the shear strength was reduced by only 2%.

Figure 2.18 revealed that a great many elements would be needed in order to produce converged solutions. For a 5:1 plate the 10x50 mesh which would be needed for convergence is totally impractical. A 6x30 mesh however is possible, although even that proves very expensive in terms of computer resource and CPU time. A mesh of this size was analysed on a VAX 782 at ARE, Dunfermline, using

ASASNL, and occupied 30% of the CPU resource over 8 days! The 6x30 mesh was just practical, however, in FINAS on the Imperial College Cyber mainframe.

It was therefore decided to use 8x8 meshes for square plates, and 6x6α (where α is the aspect ratio) meshes for rectangular plates. Results such as those of figure 2.18 then permit mesh correction factors to be inferred. It was found, however, that the 8x8 and 6x12 meshes are fully converged at maximum stress for a b/t=80 plate, which does not develop such highly localized curvatures as the b/t=180 plate. As a result, no correction factor needed to be applied to b/t=80 plates. The correction factor that was applied to b/t=120 plates was approximately inferred by interpolation between the factors at b/t=180 and unity at b/t=80.

Figure 2.28 presents the stress-strain curves which resulted from these analyses, for UUUU, CUCU and CCCC plates. For UUUU and CCCC boundaries there is no difference in behaviour between long and tall panels, but for CUCU boundaries long and tall panels behave differently.

It is worth noting at this point the considerable panel shear post-buckling resistance which can be mobilized even in the absence of any normal or tangential restraint on the panel boundaries. Considering, for example, the square b/t=180 plate which has a critical shear stress of τ_{cr}'=0.378, the maximum stress on the UUUU stress-strain curve is $0.555\tau_0$.

Tension field models can only predict a panel resistance greater than the critical buckling capacity by virtue of externally applied direct forces. The numerical analysis, however, shows that an internally equilibrated diagonal tension field is set up, which is reacted by internal edge compressions, which can be seen on the principal stress diagram of figure 2.29. In this figure the post-critical stress field is displayed by subtracting the critical shear stress from the actual shear stress distribution, in a manner similar to figure 2.6.

This is an interesting comment on the shear model of (31) and (32), where the introduction of normal restraint forces in tension field models is avoided. An alternative shear strength model is suggested which is internally equilibrated, and this is shown to allow panel shear capacities much in excess of the critical shear stress. In (32) a photo-elastic test is carried out of a square panel with flexible flanges (which although they provide little normal restraint, do provide tangential restraint). The shear stress distributions from both the proposed theory and the test demonstrate the concentration of shear stress down the diagonal which results from a diagonal tension field.

Table 2.1a presents the peak stresses from figure 2.28, and Table 2.1b presents these peak stresses reduced by the appropriate mesh correction factors. The values in Table 2.1b will be used as the basis of the empirical design model which will now be presented.

2.3 Design Model

Basler's Tension Field model (19), as corrected in (20), gives the following expression for the shear strength of transversely stiffened web panels of aspect ratio, α=a/b:

$$\tau_u' = \tau_{cr}' + \frac{\sqrt{3}}{2}\left[\sqrt{1+\alpha^2} - \alpha\right](1 - \tau_{cr}') \qquad \ldots 2.1$$

Where $\tau_u' = \tau_u/\tau_0$. In (19), the expression for the critical buckling stress, τ_{cr}, was modified in the low slenderness region, to account for strain hardening. Strain hardening has not been allowed for in the analyses so this modification to the critical buckling stress will not be used in the comparison between the behaviour of the design model and the data. The critical buckling stress to be used in equation 2.1 is therefore the lesser of the theoretical buckling stress and the yield stress. That is:

$$\tau_{cr}' = \frac{k\,\pi^2 E}{12(1-\nu^2)}\left[\frac{t}{b}\right]^2 \frac{1}{\tau_0} \quad ; \quad \geq 1.0 \qquad \ldots 2.2$$

$$\text{where } k = \begin{cases} 5.34 + 4/\alpha^2 & ; \quad \alpha \geq 1 \\ 4 + 5.34/\alpha^2 & ; \quad \alpha < 1 \end{cases}$$

The expression for k is an approximation to the elastic critical buckling factor. Figure 2.30 presents the values of k calculated using the Galerkin program, for both symmetric and anti-symmetric buckling modes, in plates of aspect ratios 1 to 5. The fact that the buckling loads for the first and second modes become very close for rectangular plates can be seen on this figure. Also of interest is the fact that the preferred buckling mode alternates between symmetric and anti-symmetric modes as plates get longer.

The expression for k in equation 2.2 is also shown on the figure, and can be seen to give very good agreement.

On Figure 2.31, equations 2.1 and 2.2 are compared with the CUCU data of Table 2.1b, for b/t=80, 120 and 180. The most striking contrast between the data and the Basler model is the fact that the latter predicts a far greater difference between the strengths of tall and long plates of the same slenderness, than do the data. As a

consequence of this, although the Basler model gives reasonably good agreement with the numerical data for long CUCU panels, it severely overestimates the resistance of tall panels. The Basler resistance of 0.774 for a tall 5:1 b/t=180 panel being almost double the computed resistance of 0.431. Due to the use of the theoretical critical buckling stress (equation 2.2) whenever this is less than the yield stress, without any adjustment in the region of the critical slenderness, the Basler model predicts that a b/t=80 panel of any aspect ratio is fully effective, whereas, according to the analyses, a long 5:1 panel can only sustain 83% of shear yield.

The tension field model due to Dubas (30), defines the inclined tension field by assuming that the corner of the plate contains a rectangular region at yield, with an aspect ratio equal to the panel aspect ratio, whose size is such that its critical buckling stress, given by equation 2.2, is just equal to the yield stress. The shear strength, given by this model, is:

$$\tau_u' = \tau_{cr}' + (1 - \tau_{cr}') \sqrt{\tau_{cr}'} \quad \ldots 2.3$$

Equation 2.3 is also compared with the CUCU data on figure 2.31. Because this model makes no distinction between the boundary conditions that exist on the vertical and horizontal edges of the panel, it does not predict any difference between the strengths of long and tall plates. The tension field widths and inclinations, according to the 2 models, for long and tall 2:1 plates (of b/t or a/t=180) are indicated on Figure 2.32.

The critical buckling stress of equation 2.2 can alternatively be written as:

$$\tau_{cr}' = \left[\frac{\beta_{crit}}{\beta}\right]^2 = \frac{1}{\lambda^2} \quad \ldots 2.4$$

where β is the non-dimensionalized slenderness (β = b/t$\sqrt{(\sigma_0/E)}$), and β_{crit}, the critical slenderness, is the value of slenderness (for a particular aspect ratio) at which the critical buckling stress, calculated from equation 2.2, is equal to the yield stress. λ is the ratio of the actual slenderness to the critical slenderness. Using this notation, equation 2.3 becomes:

$$\tau_u' = \frac{1}{\lambda} + \frac{1}{\lambda^2} - \frac{1}{\lambda^3} \quad \ldots 2.5$$

This single expression applies to plates of any aspect ratio because the effect of aspect ratio is already incorporated in λ, and no other aspect ratio terms are present.

It seems possible that such a polynomial may be used to fit the numerical data for

CCCC and UUUU plates, since there is no distinction between "long" and "tall" panels with these boundary conditons. For instance, figure 2.33 plots against β the CCCC data for square, 2:1 and 5:1 plates, with separate broken lines for each aspect ratio drawn to link the data. When these are re-plotted against λ, in figure 2.34, the square and 2:1 data follow the same curve. However, this does not apply to the 5:1 data, so polynomial functions such as equation 2.5 would need additional aspect ratio dependent terms in order to fit the data. This is also the case for the UUUU data, which are plotted against λ in figure 2.35 in a similar format to figure 2.34.

The solution which has been adopted is to use a simpler polynomial, of the form:

$$\tau_u' = \frac{c_1}{\lambda} + \frac{c_2}{\lambda^2} \qquad \ldots 2.6$$

to fit the data on figures 2.34 and 2.35. Simple linear expressions for the coefficients, c_1 and c_2, have been found, and are plotted against aspect ratio for CCCC and UUUU plates, in figure 2.36. These are, for CCCC plates:

$$\left.\begin{array}{rl} c_1 = & \begin{cases} 1.3 - .05\,\alpha & ;\ \alpha < 5 \\ 1.05 & ;\ \alpha \geq 5 \end{cases} \\ c_2 = & 0.85 - c_1 \end{array}\right\} \qquad \ldots 2.7$$

and for UUUU plates:

$$\left.\begin{array}{rl} c_1 = & \begin{cases} 1.12 - .15\,\alpha & ;\ \alpha < 3 \\ 0.67 & ;\ \alpha \geq 3 \end{cases} \\ c_2 = & \begin{cases} 0.14\,\alpha - .3 & ;\ \alpha < 3 \\ 0.12 & ;\ \alpha \geq 3 \end{cases} \end{array}\right\} \qquad \ldots 2.8$$

It was also decided to make the upper part of the design curve merge smoothly with the yield plateau. This was done by defining a separate function for τ_u' for values of λ less than unity, which merges with the curves given by equations 2.6 to 2.8, at $\lambda=1$, and with the yield stress at $\lambda=0.5$. The four geometric boundary conditions which such a function must satisfy suggested the use of the following equation:

$$\tau_u' = c_3 + c_4\,\lambda + c_5\,\lambda^2 + c_6\,\lambda^3 \quad ;\ 0.5 \leq \lambda \leq 1 \qquad \ldots 2.9$$

The coefficients c_3 to c_6 are defined in terms of the c_1 and c_2 coefficients used in equation 2.6 for $\lambda>1$, as follows:

$$\left.\begin{aligned} c_3 &= -4 + 6\,c_1 + 7\,c_2 \\ c_4 &= 24 - 29\,c_1 - 34\,c_2 \\ c_5 &= -36 + 44\,c_1 + 52\,c_2 \\ c_6 &= 16 - 20\,c_1 - 24\,c_2 \end{aligned}\right\} \quad \ldots 2.10$$

Curves based on equations 2.6 to 2.10 are compared with the data on figures 2.34 and 2.35, and, in general, give good agreement.

Figure 2.37 plots the CCCC, CUCU and UUUU data from Table 2.1b, against aspect ratio for b/t=80, 120 and 180. It is clear that as a tall CUCU plate gets taller, the presence of constraint on the long edges makes the strength of the plate approach that of the CCCC plate. Conversely, as the aspect ratio of the long plate increases the strength approaches that of the UUUU plate. The latter effect occurs for a smaller α than does the former, to the extent that, at an aspect ratio of 2, the strength of a long CUCU plate is almost indistinguishable from that of a UUUU plate. A square CUCU plate has a strength approximately half-way between that of the CCCC and UUUU plates.

These trends in the strength of a CUCU plate, suggest that the strength of CUCU plates could be obtained by interpolating between the corresponding strengths of CCCC and UUUU plates. It is also necessary, however, to consider other combinations of constrained and unconstrained boundaries than CUCU.

Figure 2.38 presents stress-strain curves for an a/b=1, b/t=180 plate with the full range of asymmetric combinations of unconstrained and constrained boundaries - that is, UUCC, UUCU and UCCC, in addition to the UUUU, CUCU and CCCC cases previously presented.

A reasonable basis for an interpolation function would be to use the ratio of the lengths of the constrained and unconstrained boundaries. However, this ratio is the same for a square CUCU plate as it is for a square UUCC plate, and it is apparent from figure 2.38 that the latter plate has a strength much nearer to the UUUU case than is the CUCU plate. A refinement to this postulate, therefore, which is based on the fact that the ultimate shear strength relies on the capacity of the panel corners at either end of the tension field to withstand the tension forces, would be to use the ratio of constraint to unconstraint on the least constrained pair of adjacent boundaries. As a result, the UUCC and UUUC plate would be given the same strength as a UUUU plate, and a CUCC plate would be given the strength of a CUCU plate. This reduces the number of combinations of boundary conditions to only three, and reasonably represents the actual effect of the boundary conditions. Where there are only two adjacent unconstrained edges, and these meet at a compression diagonal (rather than at a tension diagonal), then this case can also be

conservatively deemed to be equivalent to the UUUU case.

The upper bound case is where all edges are constrained. The lower bound case is where there are at least 2 adjacent unconstrained edges, and the intermediate case is where an unconstrained edge only exists between adjacent constrained edges, whether or not it is the only unconstrained edge.

An interpolation function which is suitable for this intermediate case, turns out to be:

$$\rho_1 = \left\{ \begin{array}{ll} \dfrac{1}{1 + 1/\alpha} & ; \alpha \leq 1 \\ \dfrac{1}{1 + \alpha^3} & ; \alpha > 1 \end{array} \right\} \qquad \ldots 2.11$$

If τ_{cu} is the strength of CUCU or CUCC plates, and τ_{cc} and τ_{uu} the strengths of CCCC and UUUU (or UUCC and UUUC) plates, then:

$$\tau_{cu} = \rho_1 (\tau_{cc} - \tau_{uu}) + \tau_{uu} \qquad \ldots 2.12$$

For square plates ρ_1 is equal to 0.5, giving a τ_{cu} strength which is the average of the τ_{cc} and τ_{uu} strengths. τ_{cu} for square plates is plotted against b/t on figure 2.39, where it is compared with the results of numerical analyses, not only for b/t=80, 120 and 180, but also for b/t=60, 90 and 100. The critical slenderness (for mild steel) is b/t=110.6, so this provides a useful check on the use of equation 2.9 for $\lambda < 1$.

Figure 2.40 presents a comparison between the CCCC, CUCU and UUUU data in the same format as in figure 2.37, and the design model. The model can be seen to give good agreement throughout the range of aspect ratios, slendernesses and boundary conditions.

Figure 2.41 presents strength curves suitable for use in design for CCCC plates, long and tall CUCU plates, and UUUU plates for aspect ratios 1,2,3,4 and 5. The strengths are plotted against b/t in this figure, whereas figure 2.42 presents the same curves as a function of λ.

Table 2.2 compares the FINAS data and the proposed design model for CUCU plates of various aspect ratios, with the shear strengths given by a range of different design models (19),(20),(30) and codes (24),(25),(26),(76),(77) & (78).

Of particular interest is the comparison between the proposed method and the 'Simple Post-Critical' and 'Tension Field' methods given in 5.6.4 and 5.6.5 of the

latest draft Eurocode (26). The 'Simple Post-Critical' method is derived from that of (30), whereas the 'Tension Field' method is derived from that of (22). These two models represent the current 'state-of-the-art' in applied shear design models, for webs with transverse stiffeners only.

The former model does not distinguish between long and tall web panels, because it does not rely on the existence of normal boundary forces to develop the panel shear resistance, whereas the latter model does require such forces, as has already been discussed. The 'Simple Post-Critical' gives quite good agreement with the method proposed in this Chapter for tall plates, but is non-conservative for long plates. The 'Tension Field' model, being based on the same concepts as in (19), (20) and (22), implies the existence of external force systems to anchor the tension field, and thus distinguishes between long and tall panels. Whereas the Tension Field model is non-conservative, relative to the data, for tall panels, it is much less so for long panels (for which it is no worse than about 12% non-conservative). The simple post-critical method, on the other hand, gives a good representation of the FINAS data for tall panels, while being non-conservative for long panels. Again, the flange forces due to the anchoring of the tension field are not taken into account.

Nevertheless, the existence of both these models in the one code, does suggest that the proposed method and the well-established tension field model can be usefully offered to the designer as alternatives for full-depth webs. If the designer elects to choose the reduced panel shear strength given by the proposed method then no axial force effects, other than those due to global forces, need be taken into account in the design of the flanges and stiffeners. The design of these elements should, however, take into account their flexural role in preventing out-of-plane displacement at the panel boundaries.

If, on the other hand, the designer chooses the greater panel shear strength given by the tension field model, then all the axial force effects in the flanges and stiffeners, which this enhanced shear capacity relies upon, would then need to be taken into account in the design of the flanges and stiffeners (in addition to their flexural role, and their resistance to global effects), which is likely to result in a heavier stiffener (and probably heavier welding as a result). The option is then given to the designer to make a choice appropriate to the particular circumstance, on economic grounds.

This design model will be used again, in Chapter 5, when the interaction between biaxial compression and shear will be discussed. Before that, it is necessary to develop uniaxial and biaxial compression models. The uniaxial compression model is the subject of the next chapter.

b/t	a/b	β	λ	CCCC	UCUC	CUCU	UUUU
80	1	2.77	0.72	.977	.972	.972	.965
	2		0.88	.925	.912	.896	.892
	3		0.92	-	.895	.852	-
	5		0.94	.875	.875	.832	.830
120	1	4.15	1.09	.835	.803	.803	.772
	2		1.32	.742	.710	.638	.630
	3		1.38	-	.678	.581	-
	5		1.41	.660	.650	.552	.552
180	1	6.23	1.63	.672	.597	.597	.555
	2		1.98	.560*	.530	.450	.442
	3		2.07	-	.496	.390	-
	5		2.12	.490	.461	.361	.361

* mesh size 8x16 rather than 6x12

Maximum Shear Resistance without Mesh Correction

Table 2.1 (a)

b/t	a/b	β	λ	CCCC	UCUC	CUCU	UUUU
80	1	2.77	0.72	.977	.972	.972	.965
	2		0.88	.925	.912	.896	.892
	3		0.92	-	.895	.852	-
	5		0.94	.875	.875	.832	.830
120	1	4.15	1.09	.825	.793	.793	.762
	2		1.32	.718	.687	.618	.610
	3		1.38	-	.656	.562	-
	5		1.41	.640	.629	.534	.534
180	1	6.23	1.63	.652	.578	.578	.537
	2		1.98	.545	.495	.420	.413
	3		2.07	-	.463	.364	-
	5		2.12	.460	.431	.337	.337

Note : UCUC implies constraints on long edges only
CUCU implies constraints on short edges only

Maximum Shear Resistance corrected for mesh size

Table 2.1 (b)

h/t† d/t†	h/d†	Model	FINAS	BS5400	BS2573	BS5950	Basler*	Dubas*	SIA161	Eurocode 3		AASHTO
										(a)	(b)	
80	.20	.875	.875	.839	--	.947	1.0	1.0	.992	.913	.973	.942
	.33	.880	.895	.839	.997	.945	1.0	1.0	.995	.927	.970	.932
	.50	.897	.912	.875	1.0	.951	1.0	1.0	1.018	.953	.976	.931
	1	.957	.972	.982	1.0	.977	1.0	1.0	1.155	1.00	.998	.971
	2	.886	.896	.963	1.0	.945	1.0	1.0	1.018	.953	.967	.882
	3	.857	.852	.935	.997	.921	1.0	1.0	.980	.927	.947	.845
	5	.838	.832	.910	--	.899	1.0	1.0	.963	.913	.931	.818
120	.20	.633	.629	.747	--	.851	.855	.854	.925	.639	.835	.848
	.33	.652	.656	.722	--	.822	.822	.870	.915	.655	.804	.816
	.50	.682	.687	.714	.874	.807	.803	.898	.905	.686	.792	.798
	1	.787	.793	.869	.980	.863	.904	.988	.932	.824	.892	.840
	2	.623	.618	.650	.874	.682	.663	.898	.741	.686	.683	.655
	3	.553	.562	.566	--	.608	.593	.870	.656	.655	.613	.579
	5	.534	.534	.504	--	.551	.543	.854	.637	.639	.561	.519
180	.20	.443	.431	.672	--	.764	.774	.589	.883	.476	.719	.771
	.33	.461	.463	.624	--	.706	.712	.604	.863	.437	.664	.709
	.50	.490	.495	.577	--	.654	.654	.633	.832	.457	.617	.653
	1	.582	.587	.566	.820	.616	.601	.760	.759	.555	.595	.619
	2	.423	.420	.371	--	.421	.408	.633	.544	.457	.410	.406
	3	.357	.364	.304	--	.350	.342	.604	.444	.437	.346	.334
	5	.343	.337	.250	--	.294	.289	.589	.435	.426	.294	.278

* Elastic τ_{cr} assumed, whenever this is less than the yield stress.

(a) Simple Post-Critical Method - 5.6.4 of (26)

(b) Tension Field Method - 5.6.5 of (26)

†d is web depth, h is stiffener spacing. (The quoted slenderness is in terms of the lesser of d and h)

Comparison Between Proposed Model for CUCU Plates and Design Models for Transversely Stiffened Webs

Table 2.2

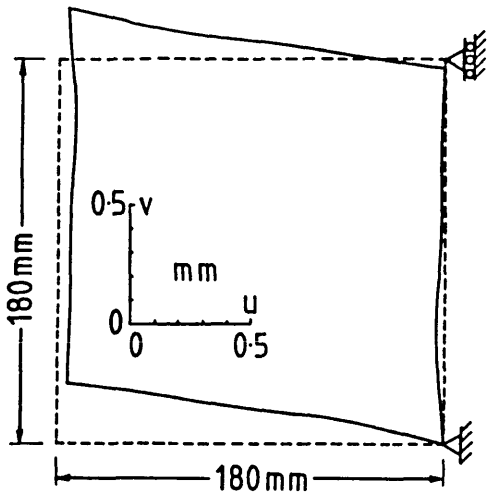

FIGURE 2.1 – Boundary deformation of shear panel, a/b=1, b/t=180, in the absence of any in-plane restraint at the panel boundaries

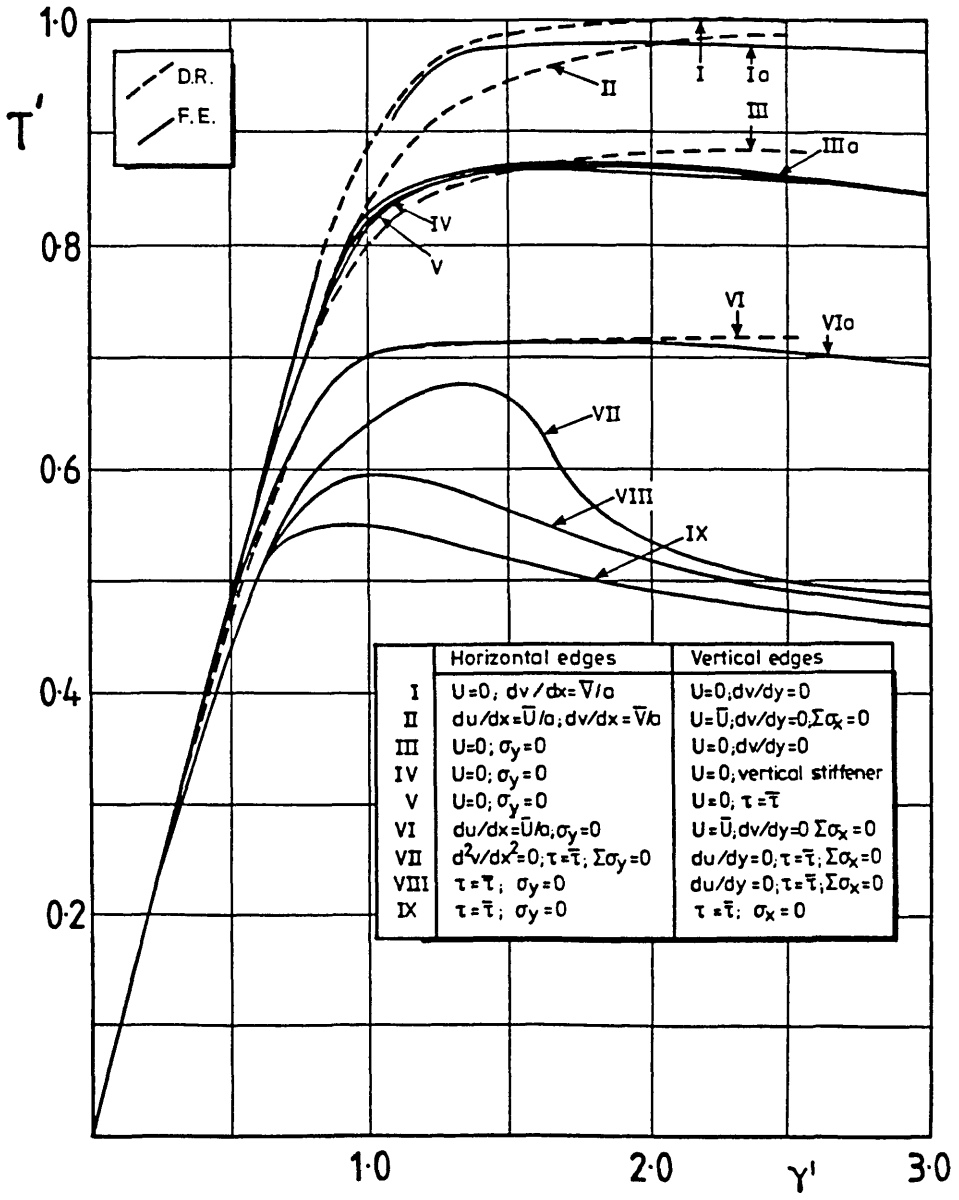

FIGURE 2.2 – Shear stress–strain curves for square simply supported panel, b/t=180 with various in-plane boundary conditions

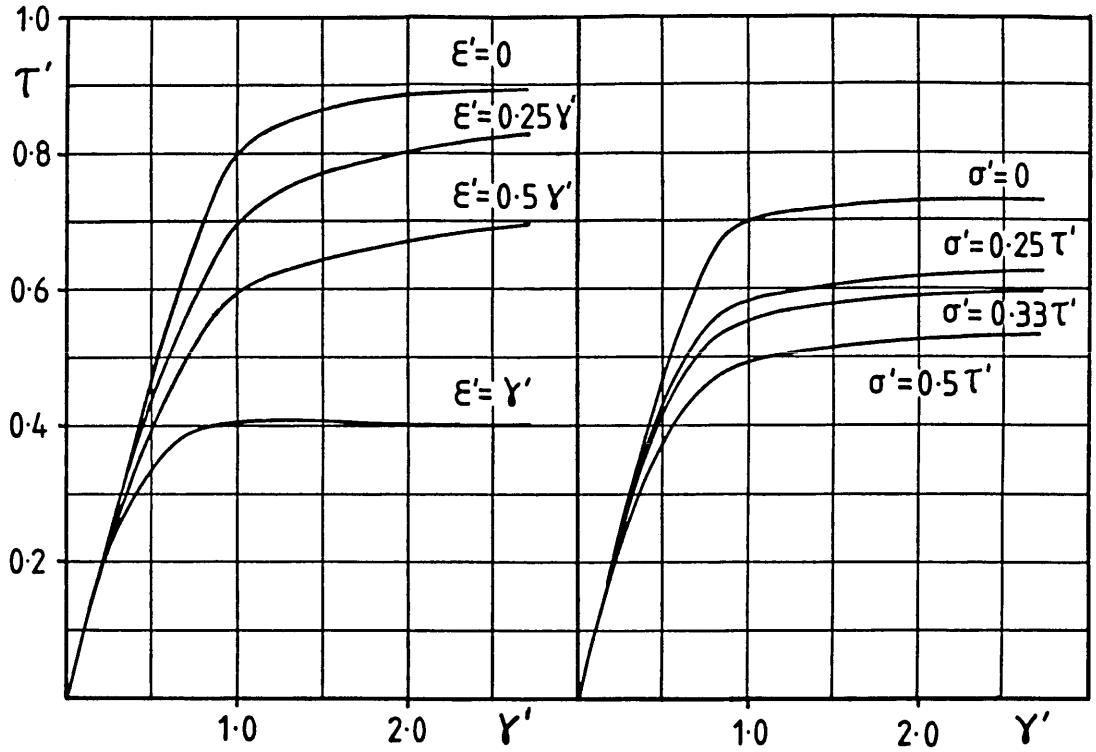

FIGURE 2.3 – Proportional strain stress–strain curves from (35) for various strain ratios, and cross–plotted proportional stress stress–strain curves for various stress ratios – a/b=1, b/t=180

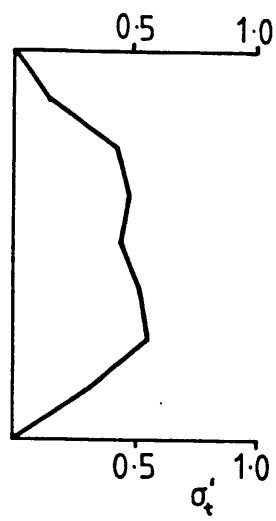

σ_x on vertical edge of unrestrained plate, a/b=1, b/t=180
ϵ_x'=0, γ'=2.5

FIGURE 2.4

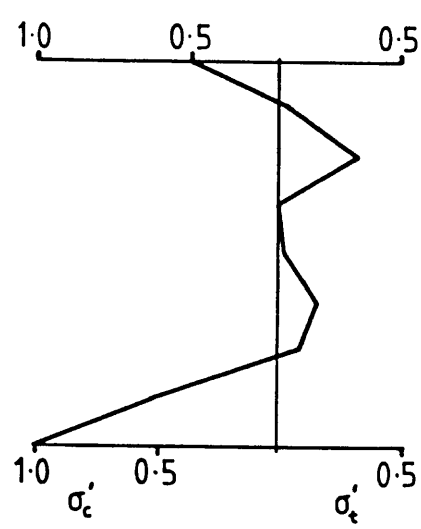

σ_x on vertical edge of unrestrained plate, a/b=1, b/t=180
ϵ_x'=1.25, γ'=2.5

FIGURE 2.5

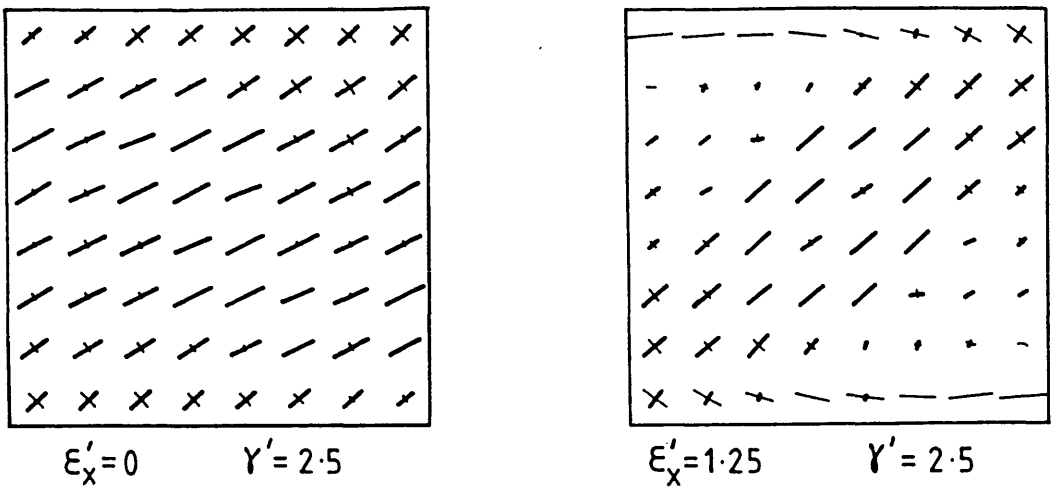

FIGURE 2.6 – Post–critical principal stress distributions for unrestrained plate a/b=1, b/t=180, corresponding to figures 2.4 and 2.5 (heavy line denotes principal tension)

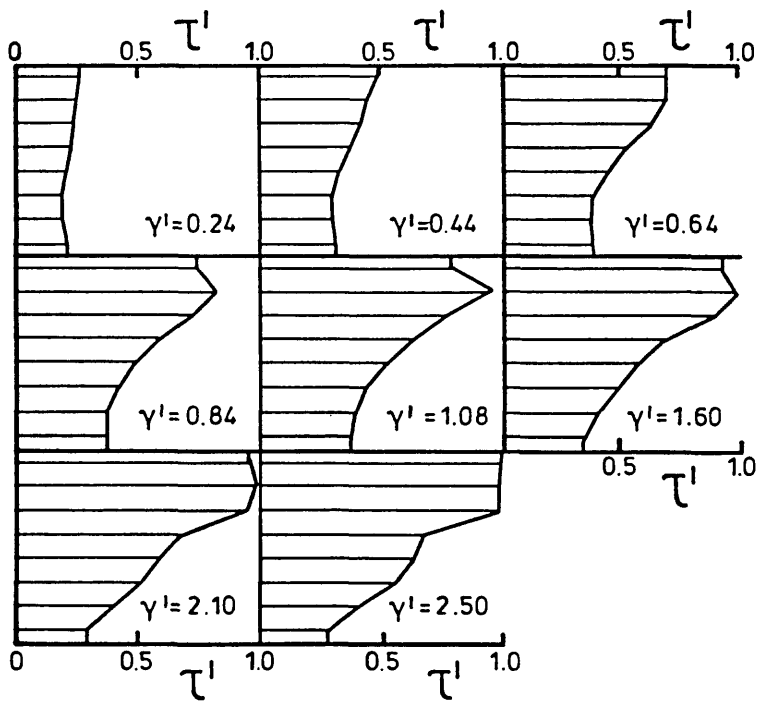

FIGURE 2.7 – Distribution of τ on vertical edge at various levels of applied γ' unrestrained square plate, b/t=180 ($\epsilon_x/\epsilon_0 = 0.5\ \gamma/\gamma_0$)

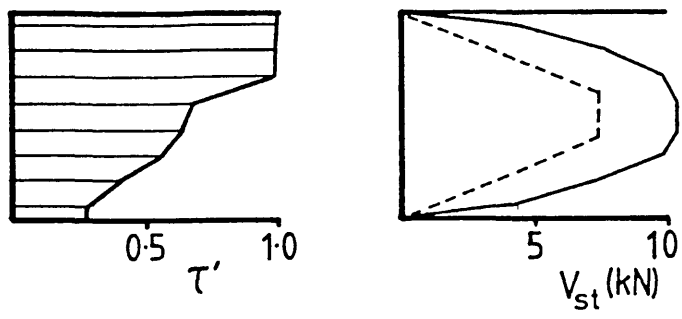

FIGURE 2.8 – Axial force in stiffener, V_{st}, inferred from fig.2.7 at γ/γ_0=2.5 and from Basler's model

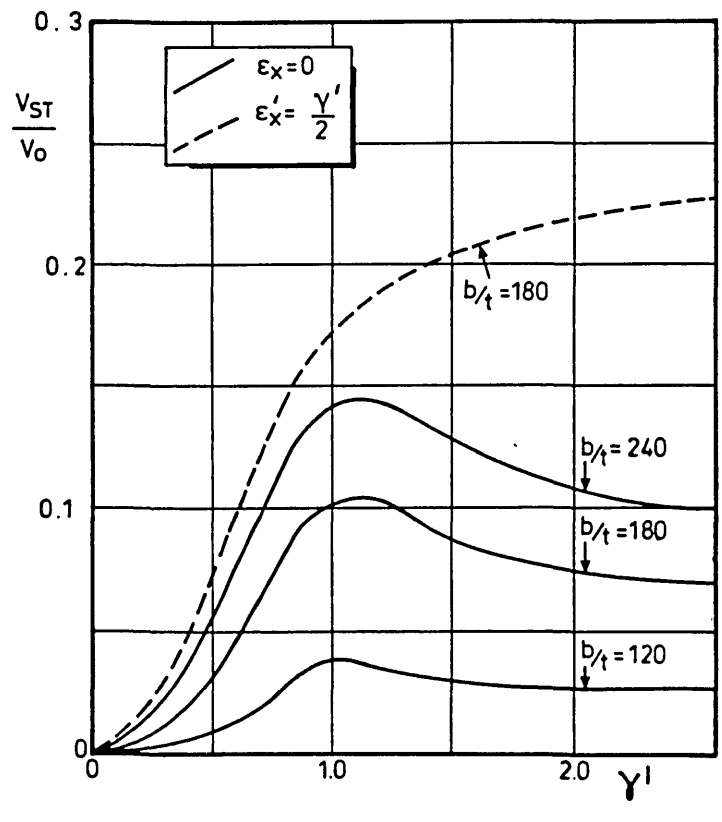

FIGURE 2.9 – Variation in maximum stiffener force with applied γ' from the analyses of (35) for square plates

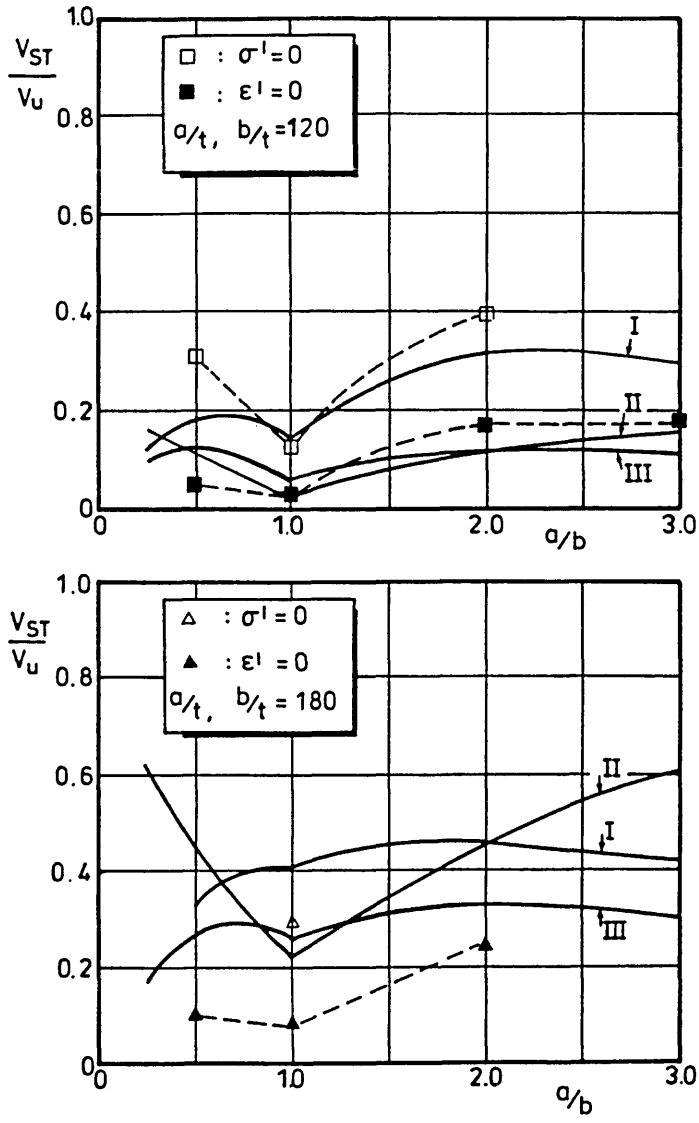

I - BS 5400

II - Dubas

III - Basler

FIGURE 2.10 - Maximum stiffener forces at γ'=2.5, expressed as a fraction of panel shear resistance, compared to BS5400, Basler and Dubas

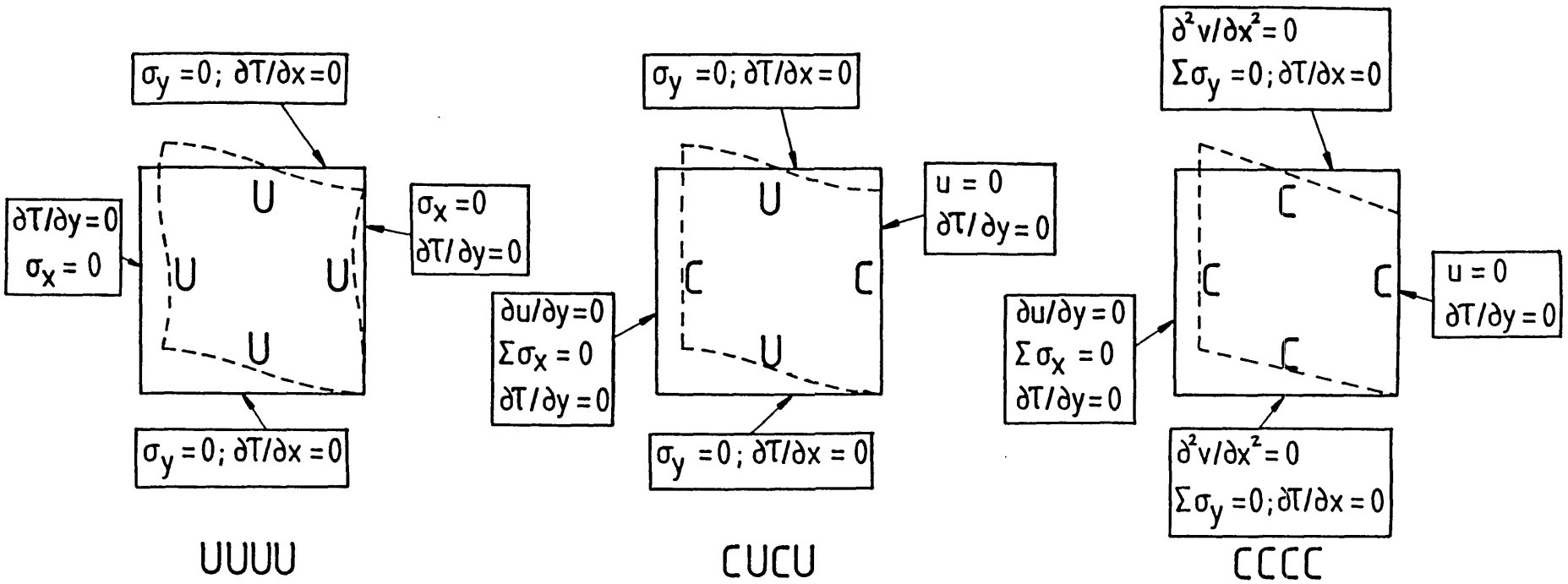

FIGURE 2.11 – **Description of UUUU, CUCU and CCCC in-plane boundary condtions. All edges simply supported**

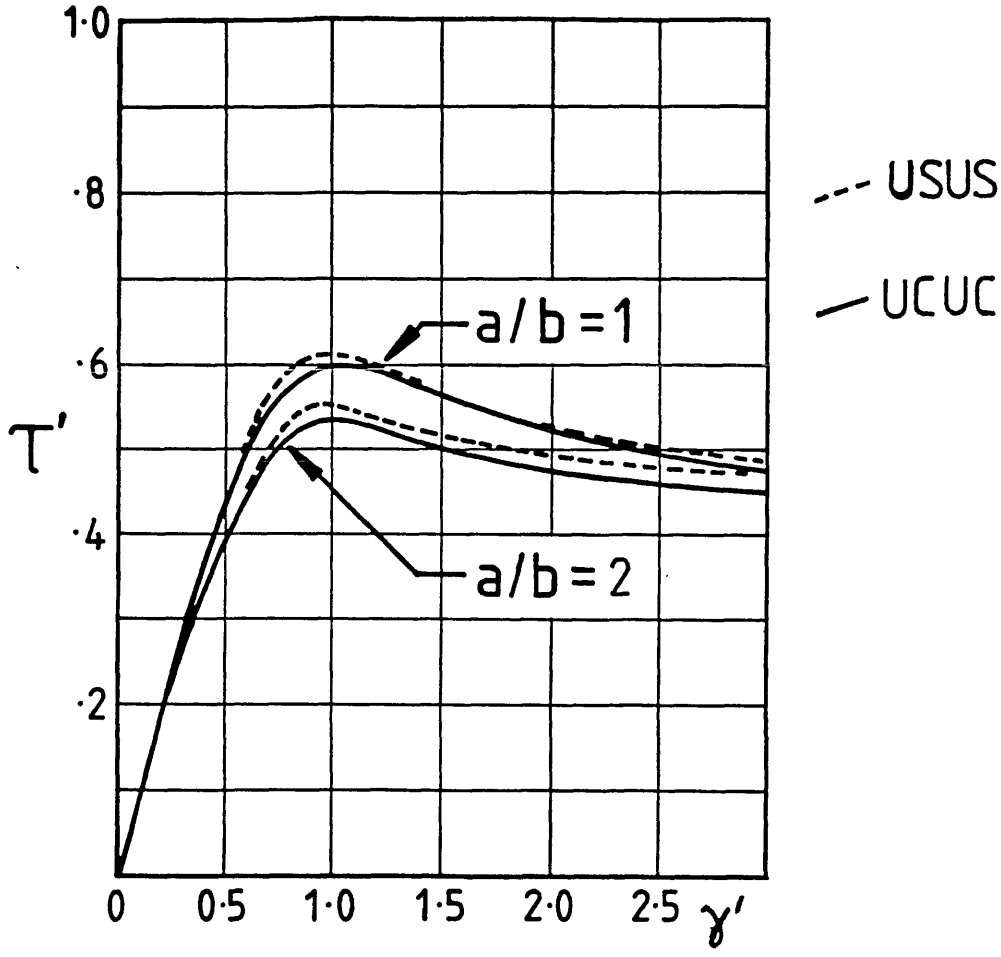

FIGURE 2.12 – Effect of in-compressible stiffener (USUS) on UCUC panel, a/b=1 & 2, b/t=180 (ie stiffener on long boundaries)

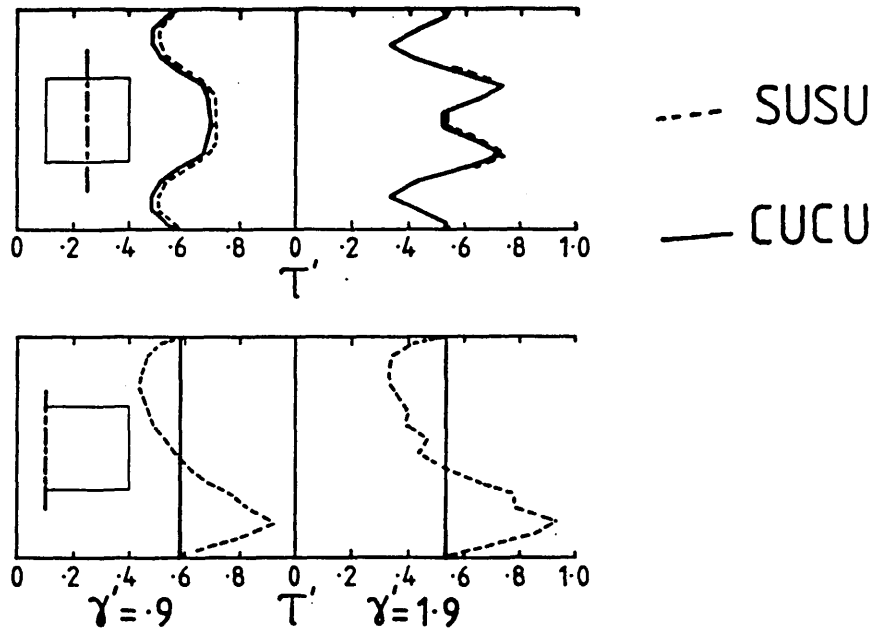

FIGURE 2.13 – Vertical shear distributions for square SUSU and CUCU, b/t=180 panels – on vertical boundary and on vertical centre-line

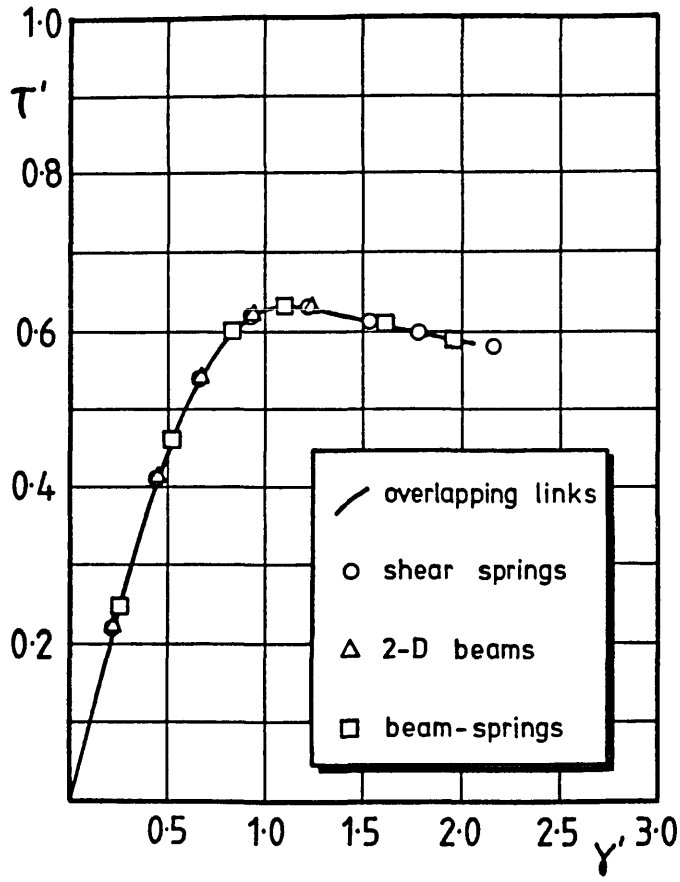

FIGURE 2.14 – Comparison between constraint models $\tau-\gamma$ for a/b=1, b/t=180 CUCU 6x6 mesh

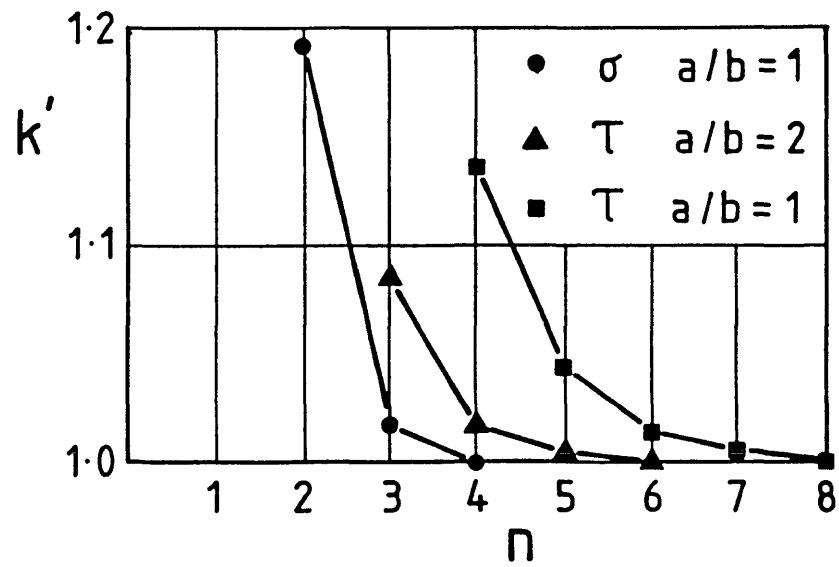

FIGURE 2.15 – Ratio of FINAS eigenvalues, k_f, for different mesh sizes (nxn for a/b=1, and nx2n for a/b=2) to Galerkin eigenvalues, k_g, ($k'=k_f/k_g$)

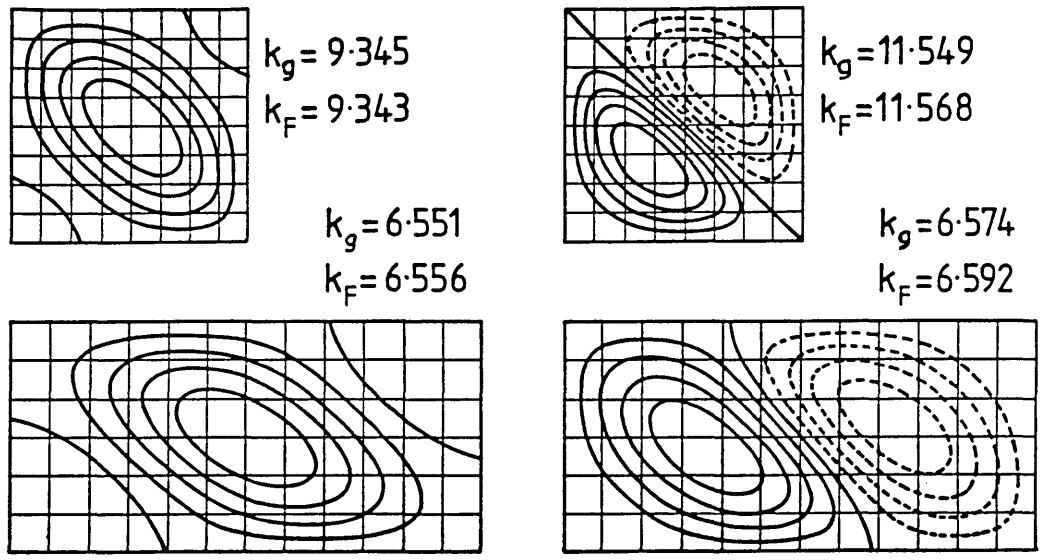

FIGURE 2.16 – First and second elastic critical shear buckling modes for a/b=1 & 2

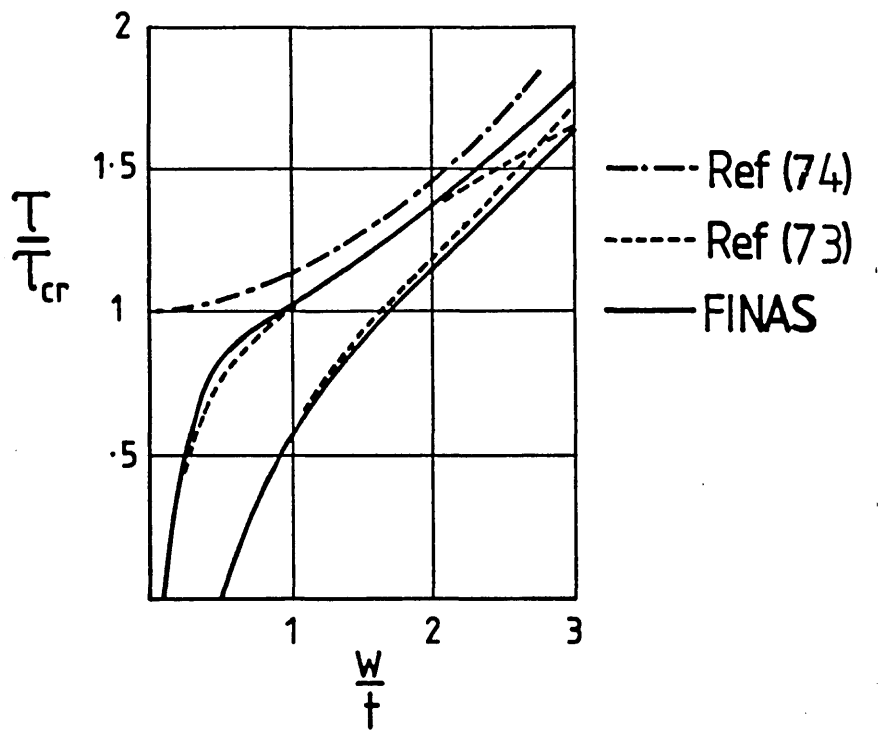

FIGURE 2.17 – Comparison between non-linear elastic behaviour predicted by FINAS, and finite difference analyses in (73) and (74)

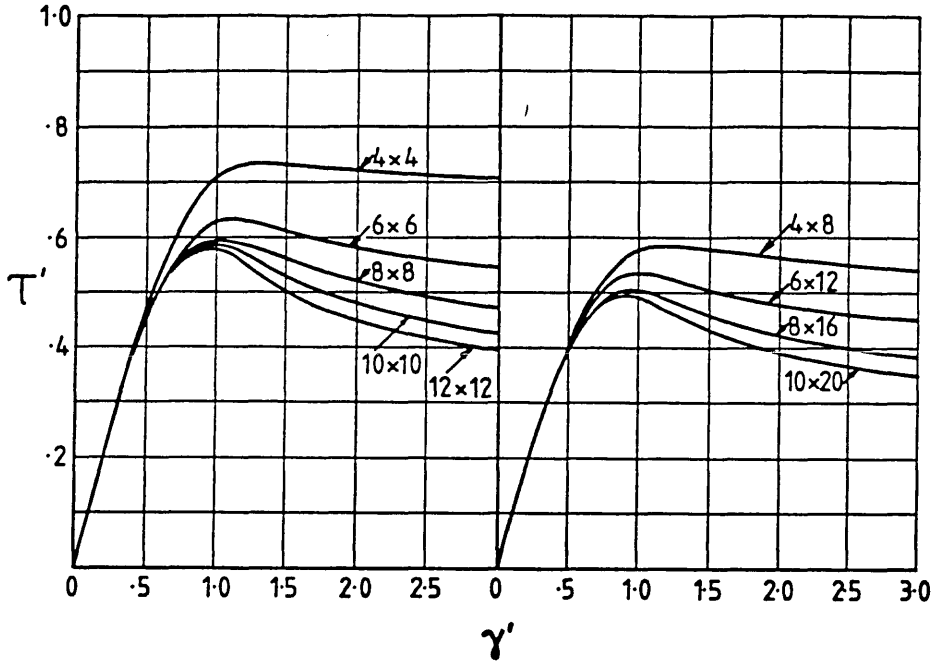

FIGURE 2.18 – Effect of mesh size on $\tau-\gamma$, a/b=1 & 2, b/t=180 UCUC

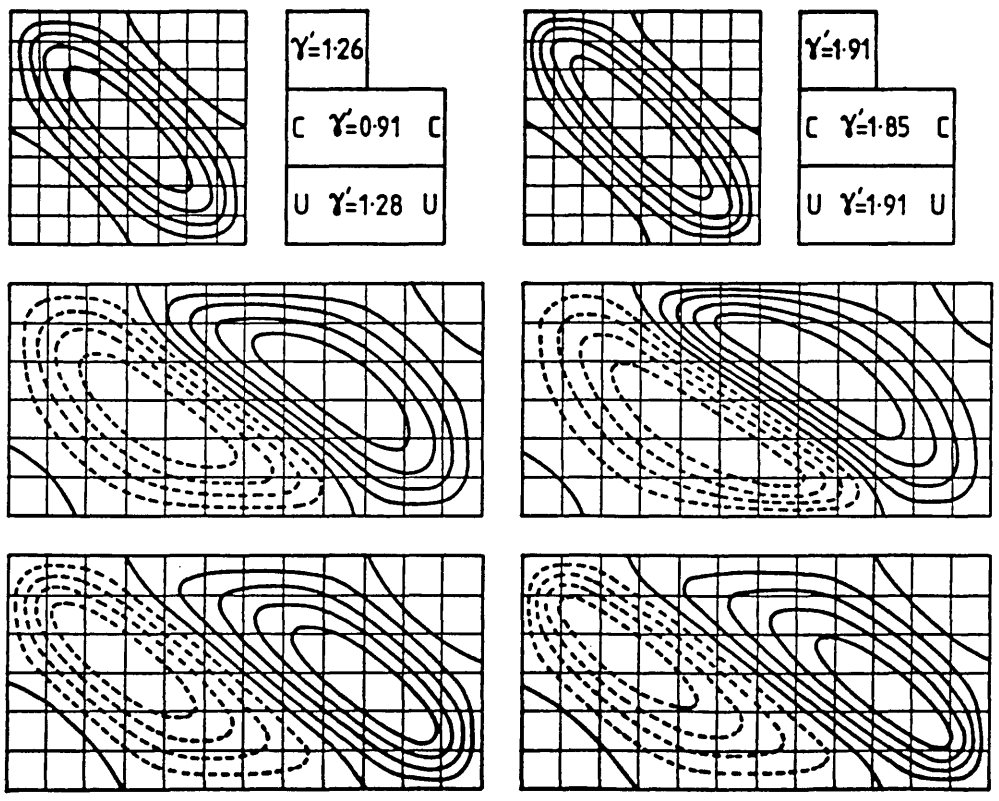

FIGURE 2.19 – Elasto–plastic shear buckling modes from FINAS a/b=1 & 2, b/t=180, CUCU and UCUC

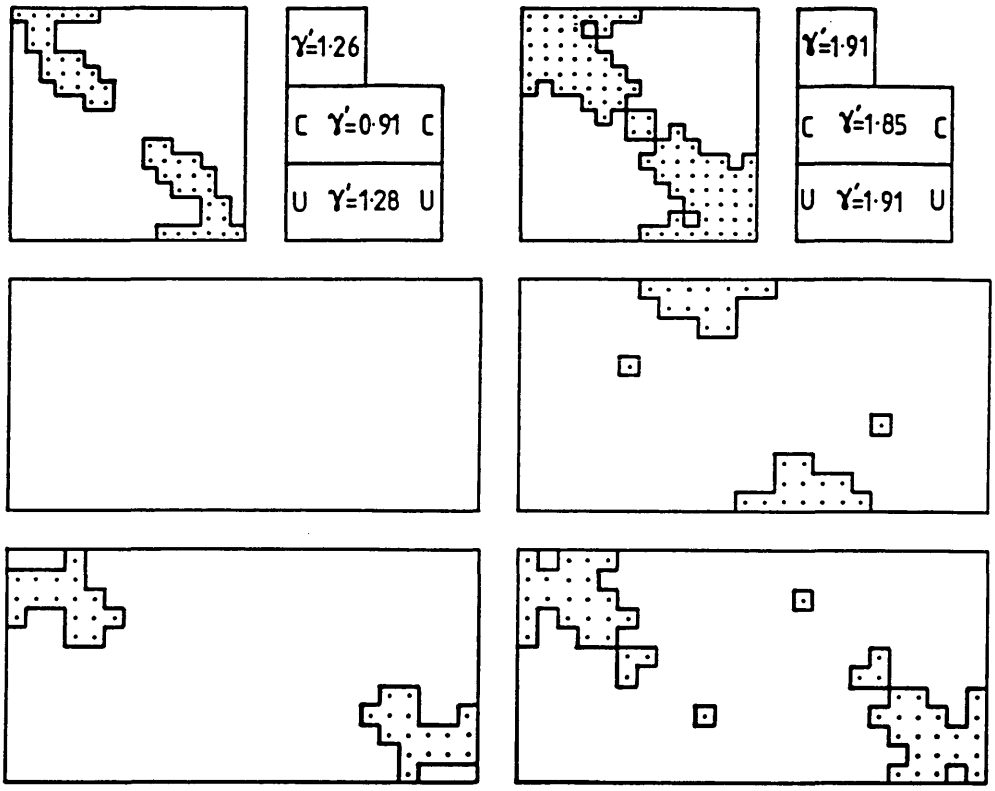

FIGURE 2.20 – Zones of mid-thickness yielding corresponding to fig.2.19 a/b=1 & 2, b/t=180, CUCU and UCUC

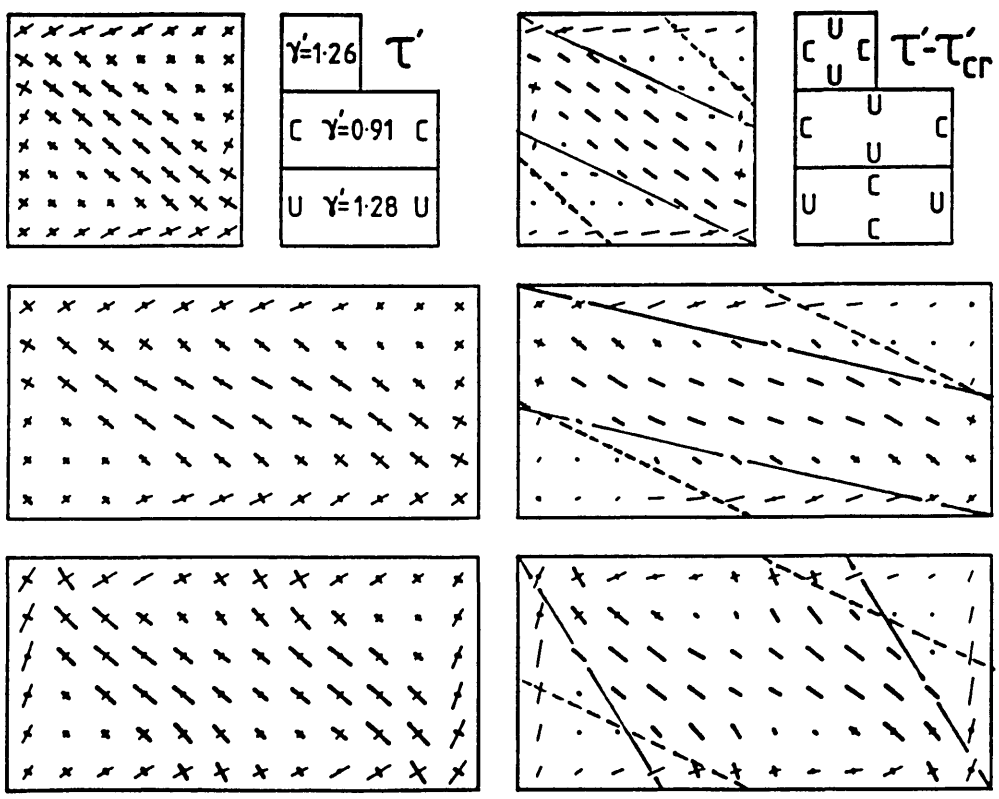

FIGURE 2.21 – Principal stresses corresponding to fig.2.19 (heavy line denotes principal tension) a/b=1 & 2, b/t=180, CUCU and UCUC

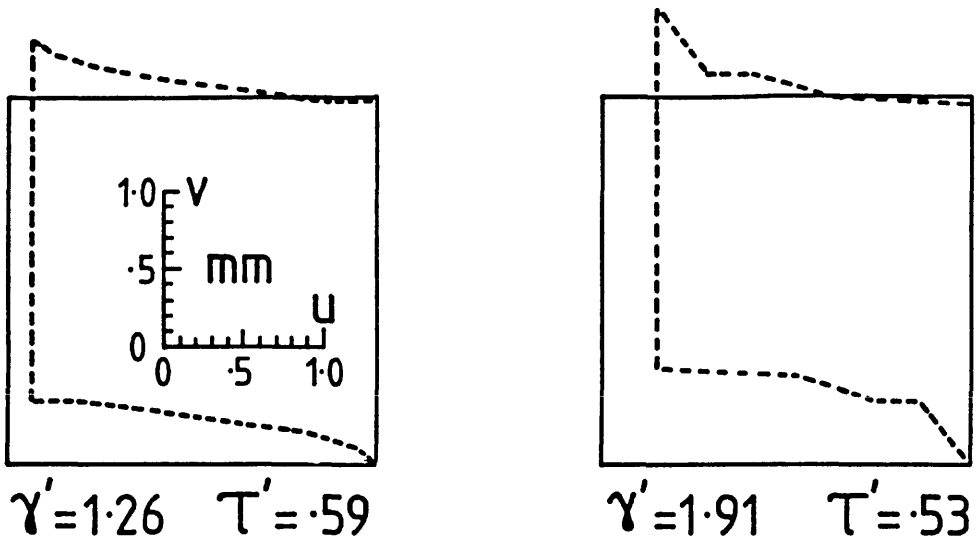

FIGURE 2.22 – Deformation of boundaries in the square panel of fig.2.19

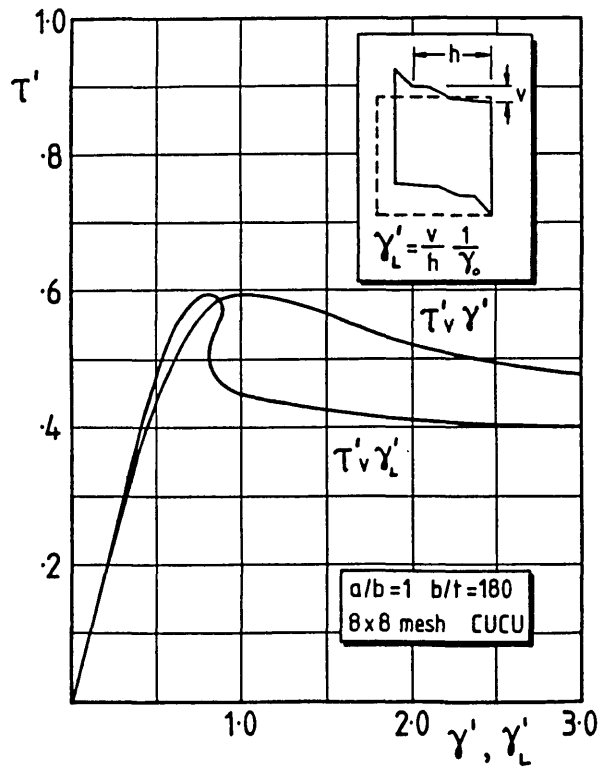

FIGURE 2.23 – Effect of shear strain localization on shear strain in off-diagonal region

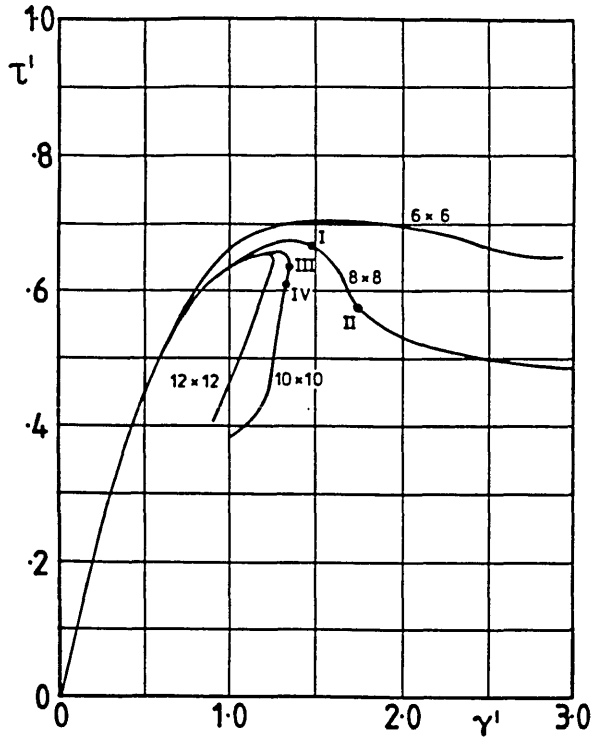

FIGURE 2.24 – $\tau-\gamma$ for CCCC square plate, b/t=180 effect of mesh size

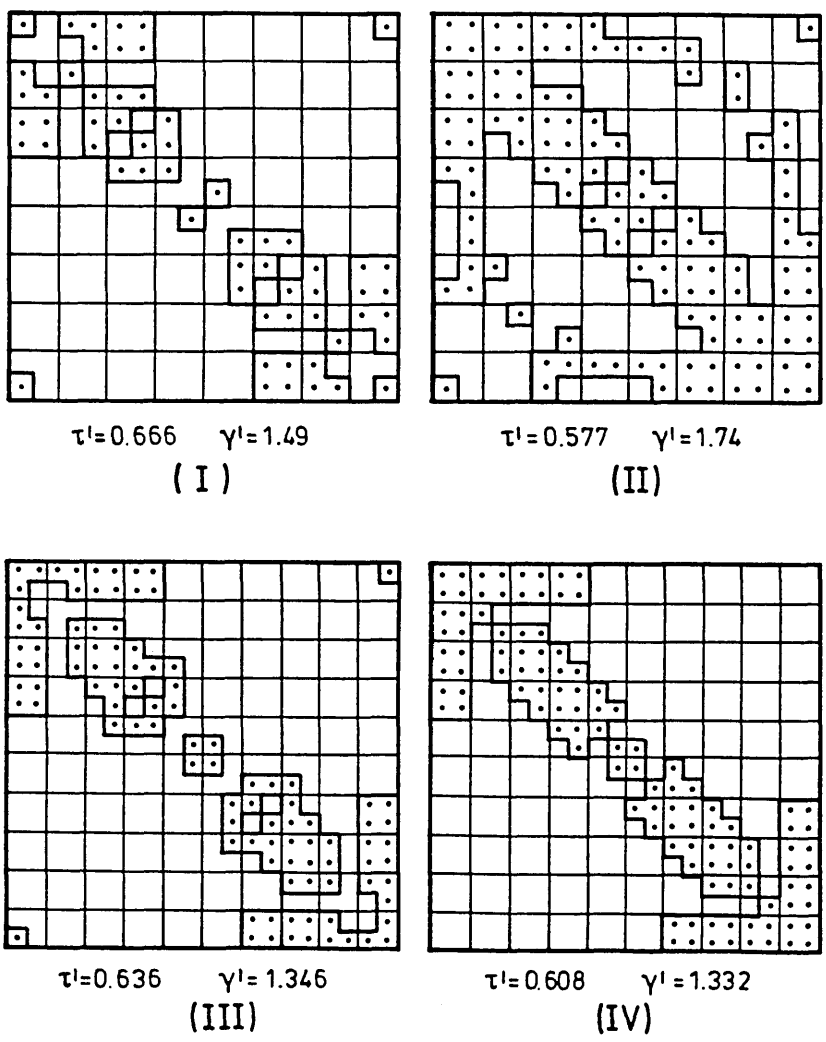

FIGURE 2.25 – Zones of mid-thickness yielding corresponding to points indicated on figure 2.24

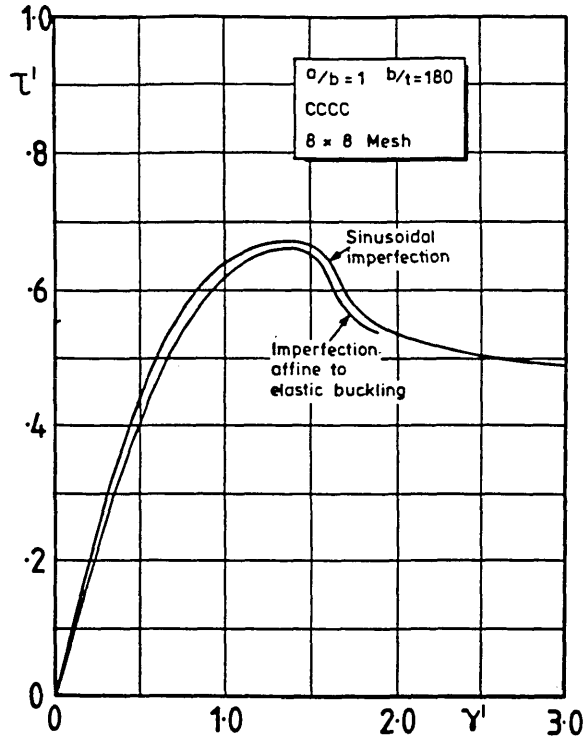

FIGURE 2.26 – Effect of imperfection affine to critical buckling mode
a/b=1, b/t=180 CCCC 8x8 mesh

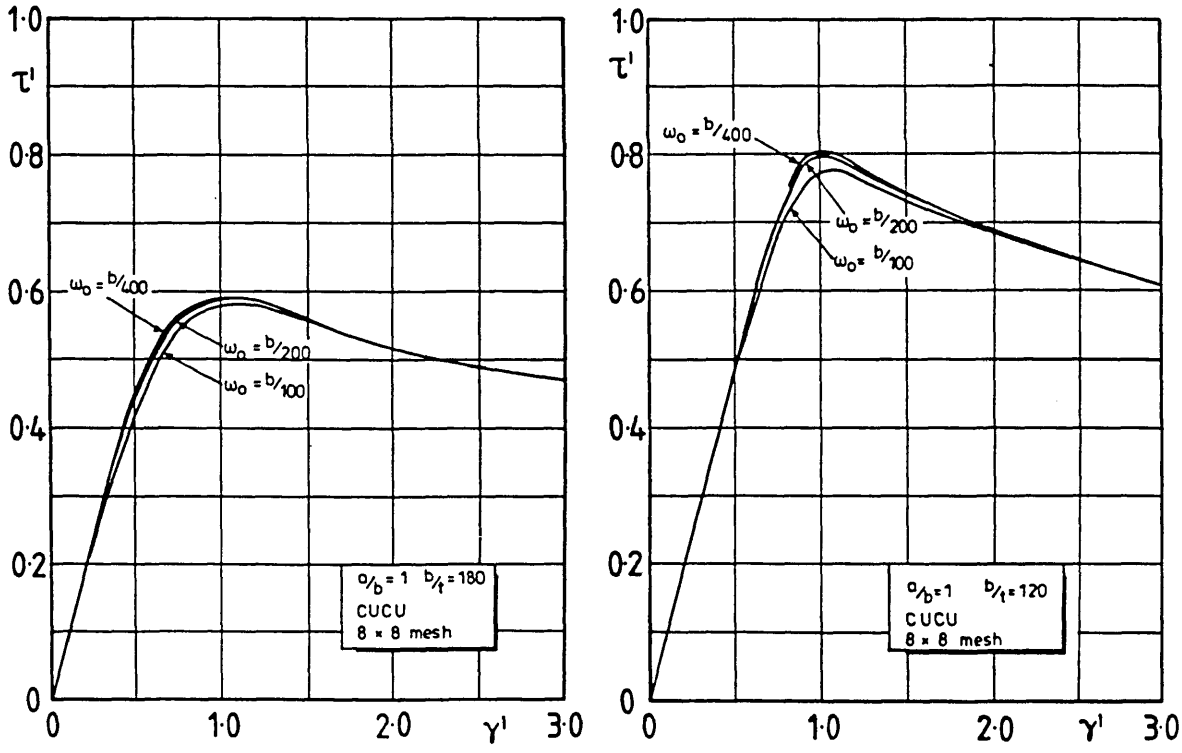

FIGURE 2.27 – Effect of imperfection magnitude on $\tau-\gamma$
a/b=1, b/t=120 & 180, CUCU, 8x8 mesh

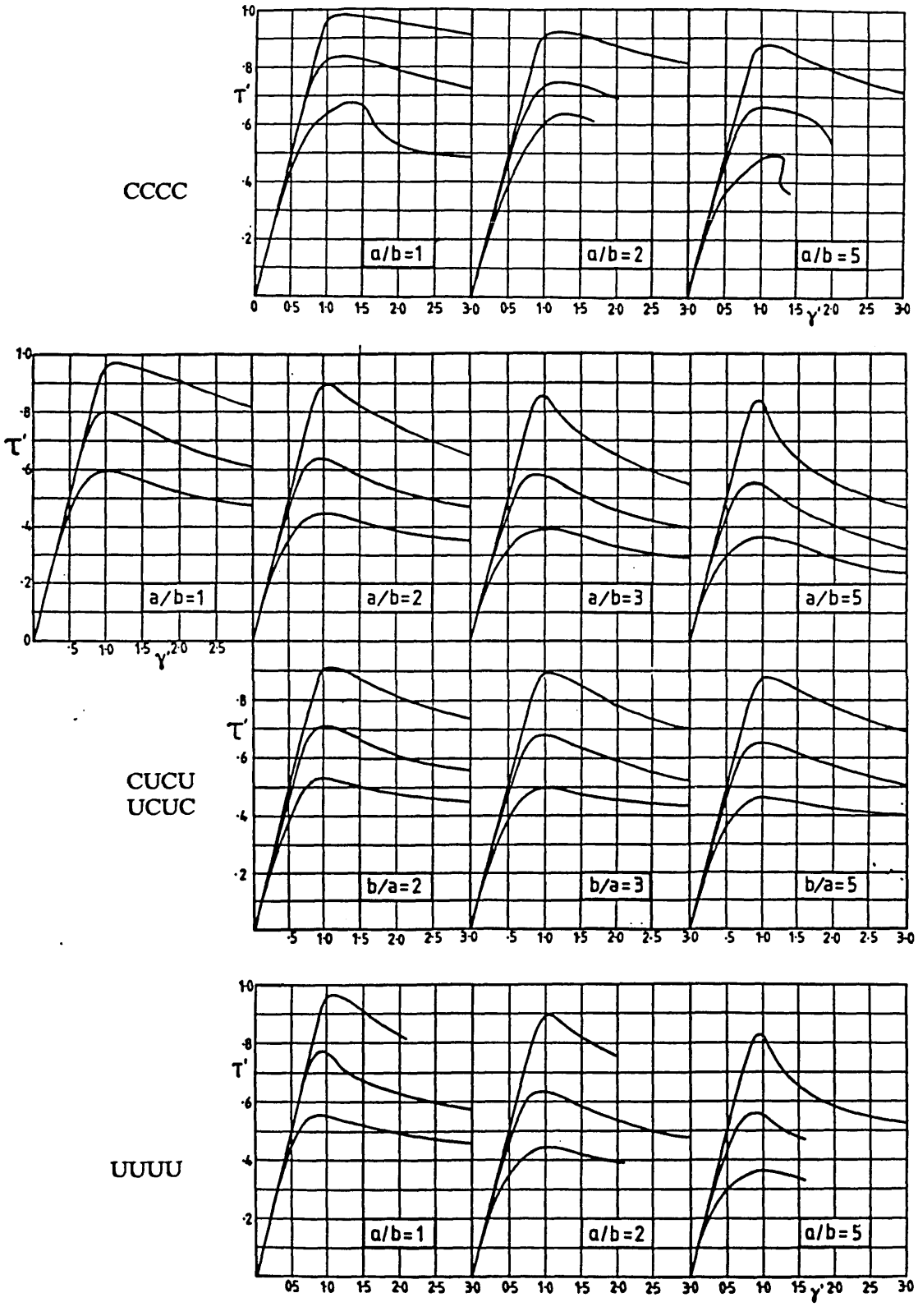

FIGURE 2.28 – Stress strain curves from FINAS, for a/b=1 to 5, b/t=80, 120 & 180 CCCC, CUCU/UCUC, & UUUU

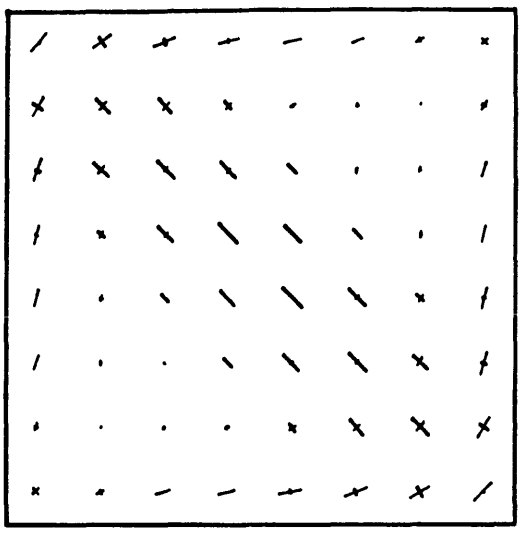

FIGURE 2.29 – Post-critical principal stresses
a/b=1, b/t=180 UUUU at maximum τ

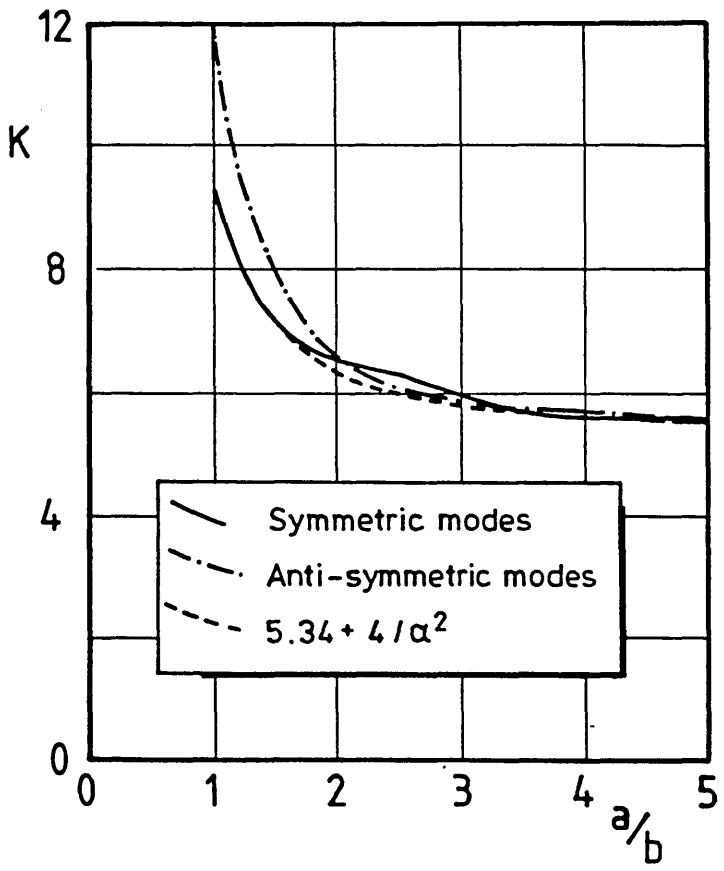

FIGURE 2.30 – Shear buckling coefficient from
Galerkin analysis and equation 2.2

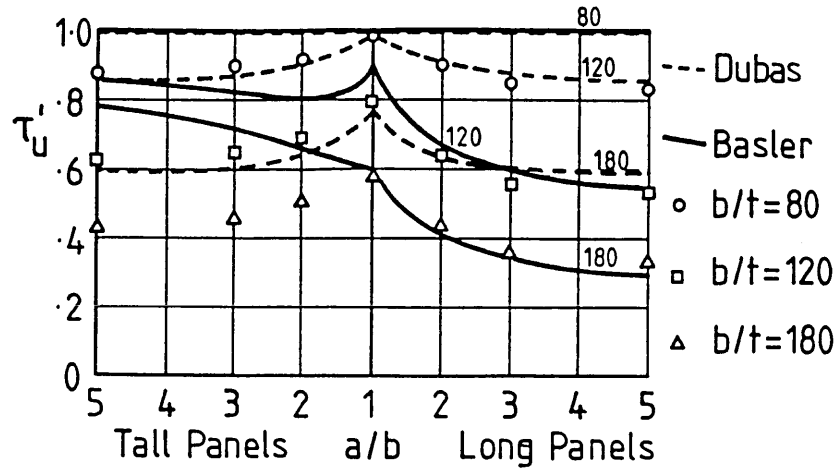

FIGURE 2.31 – Comparison between Basler and Dubas models and numerical data CUCU/UCUC

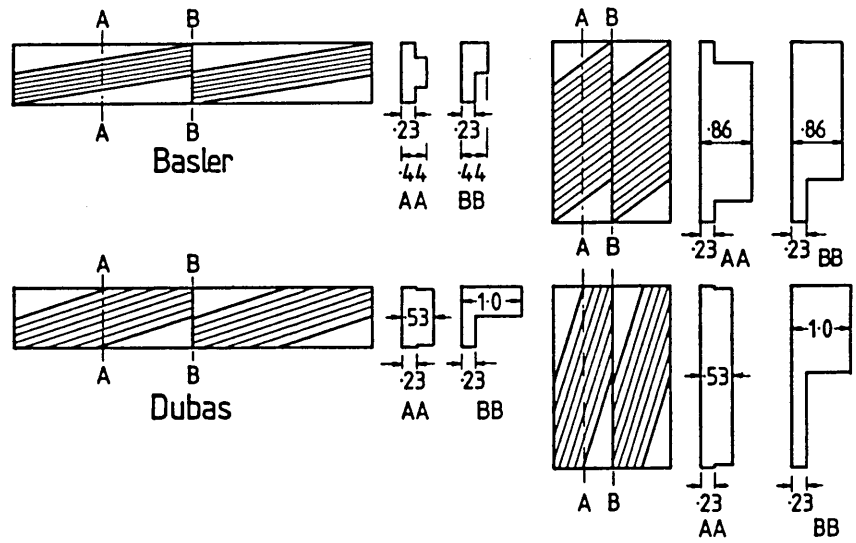

FIGURE 2.32 – Tension field widths and inclinations from Basler and Dubas

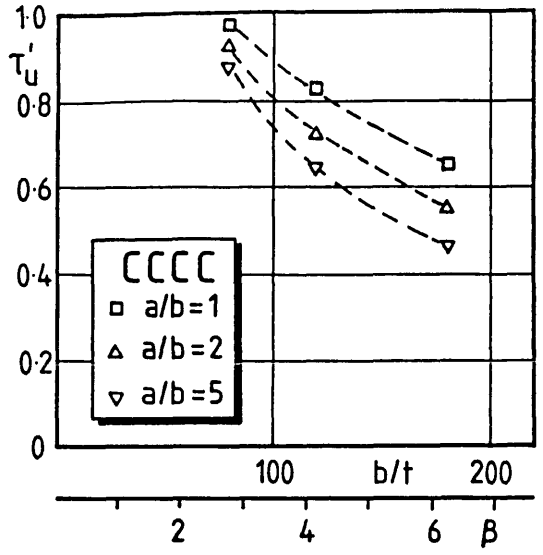

FIGURE 2.33 – CCCC data plotted against β

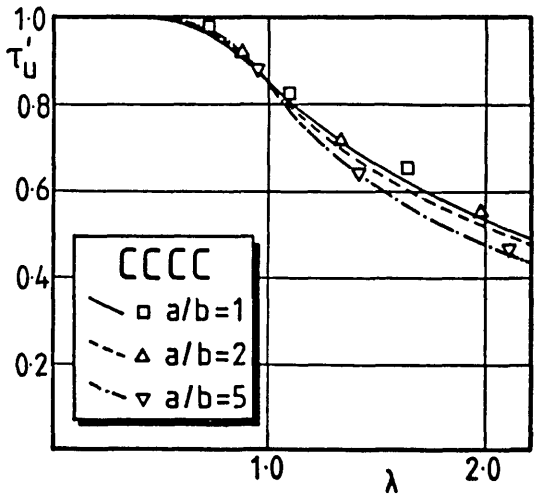

FIGURE 2.34 – CCCC data plotted against λ

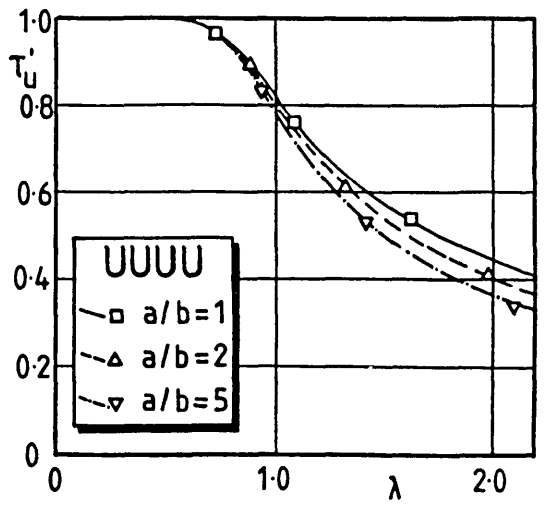

FIGURE 2.35 – UUUU data plotted against λ

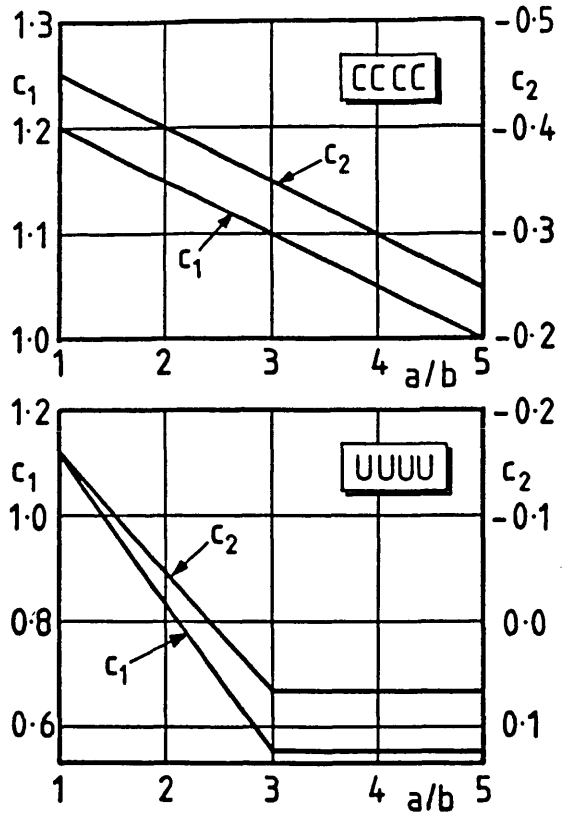

FIGURE 2.36 – Coefficients in equations 2.6 to 2.8

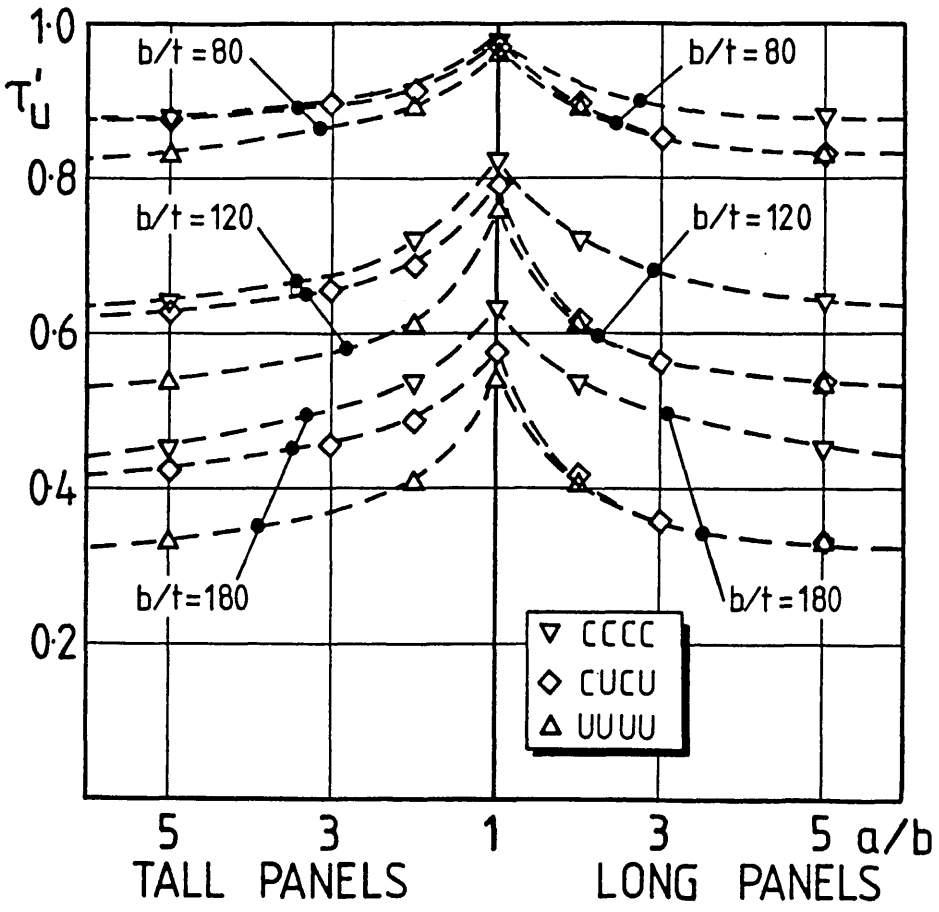

FIGURE 2.37 – Numerical data plotted against aspect ratio for long and tall panels

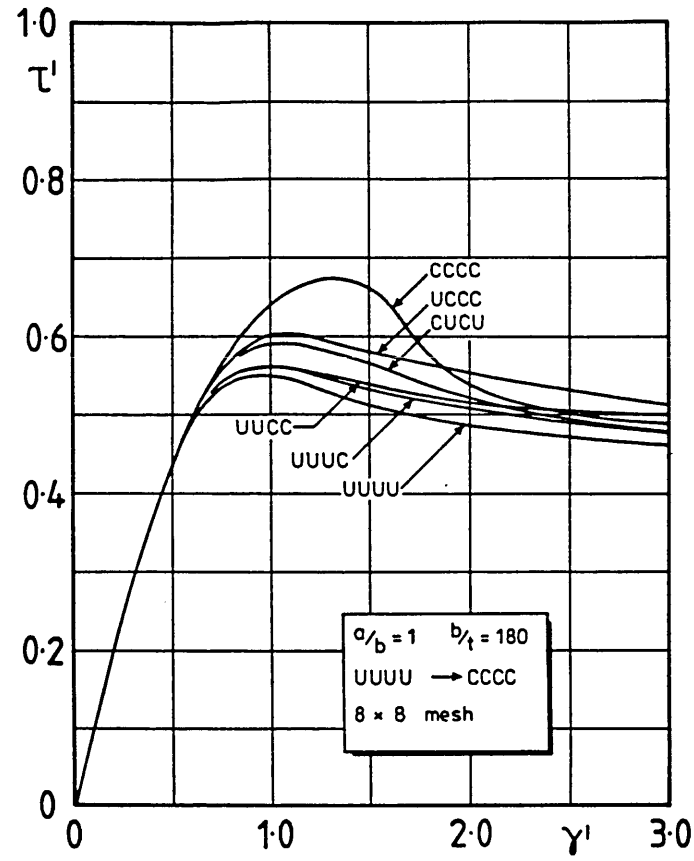

FIGURE 2.38 – $\tau-\gamma$ for all possible combinations of constrained and unconstrained egdes a/b=1, b/t=180 8x8 mesh

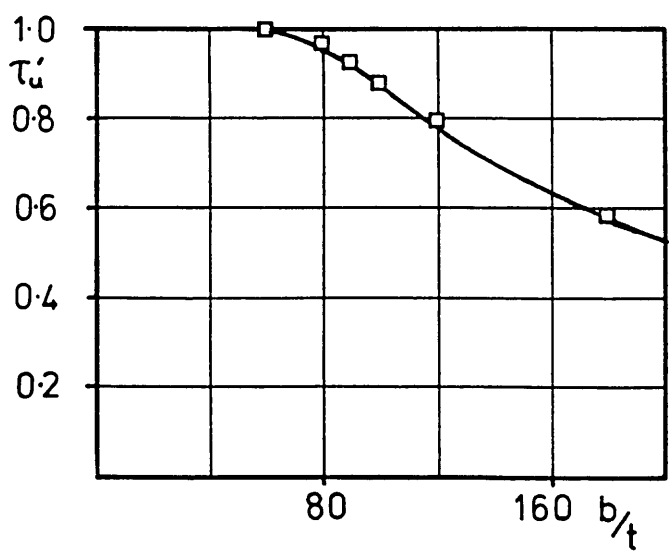

FIGURE 2.39 – Comparison between proposed CUCU model for square plates, and numerical data

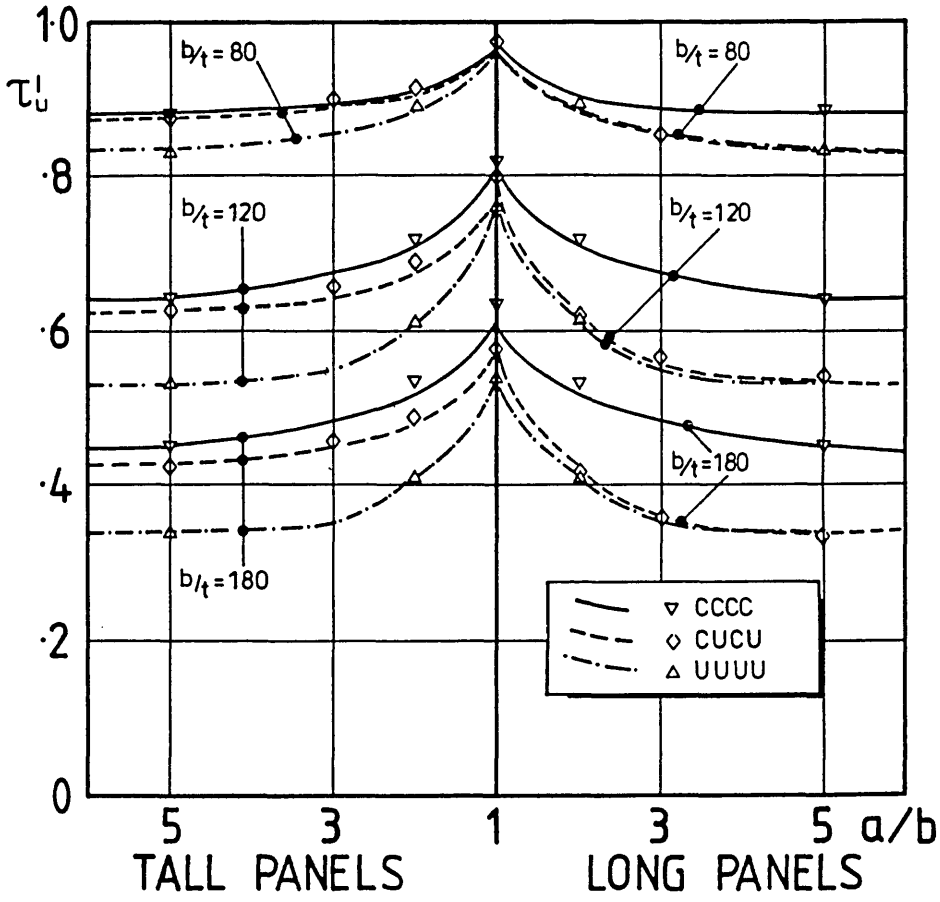

FIGURE 2.40 – Proposed models for CCCC, CUCU/UCUC and UUUU plotted against aspect ratio, and compared to numerical data

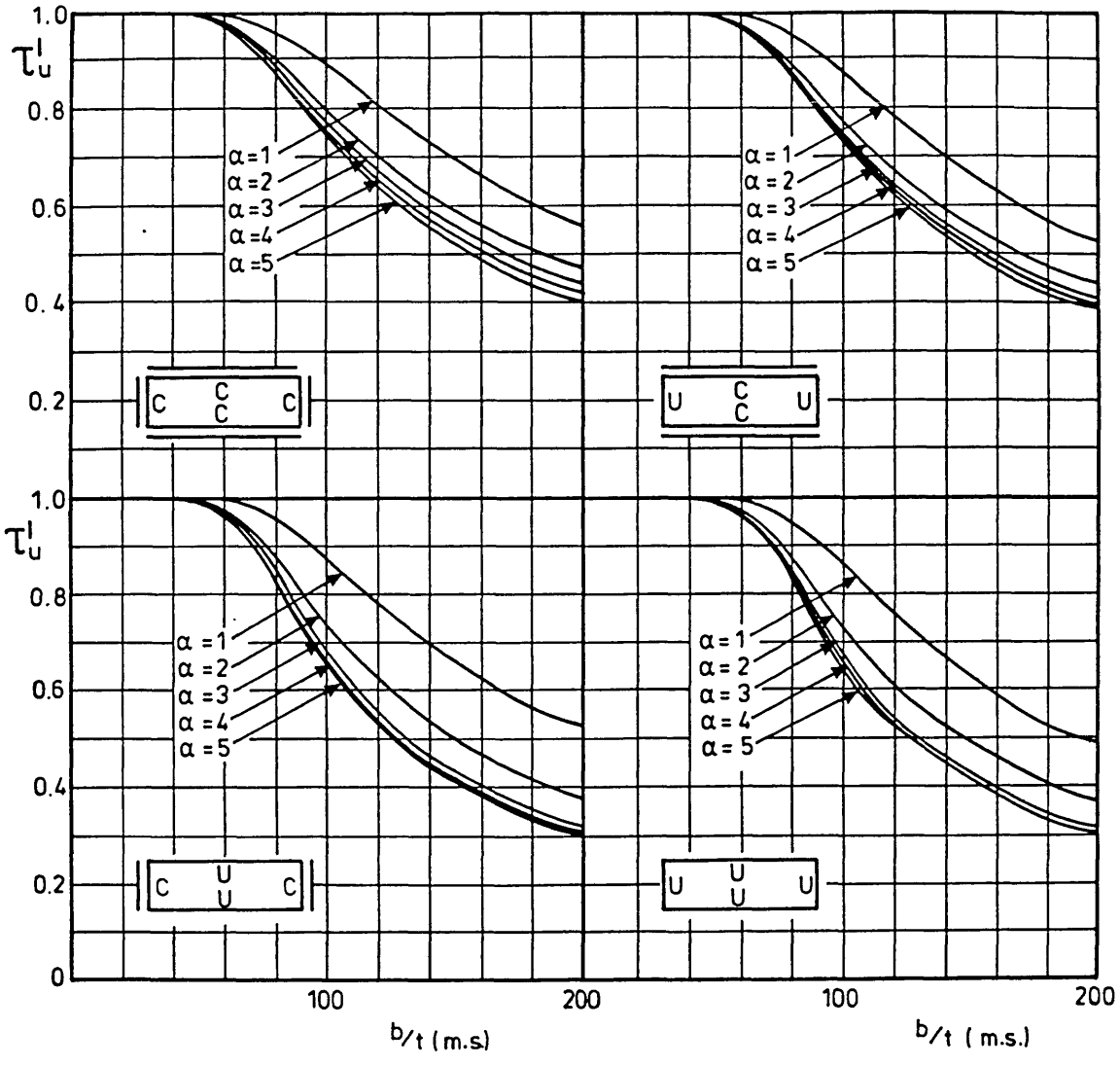

FIGURE 2.41 – Design curves from the proposed model

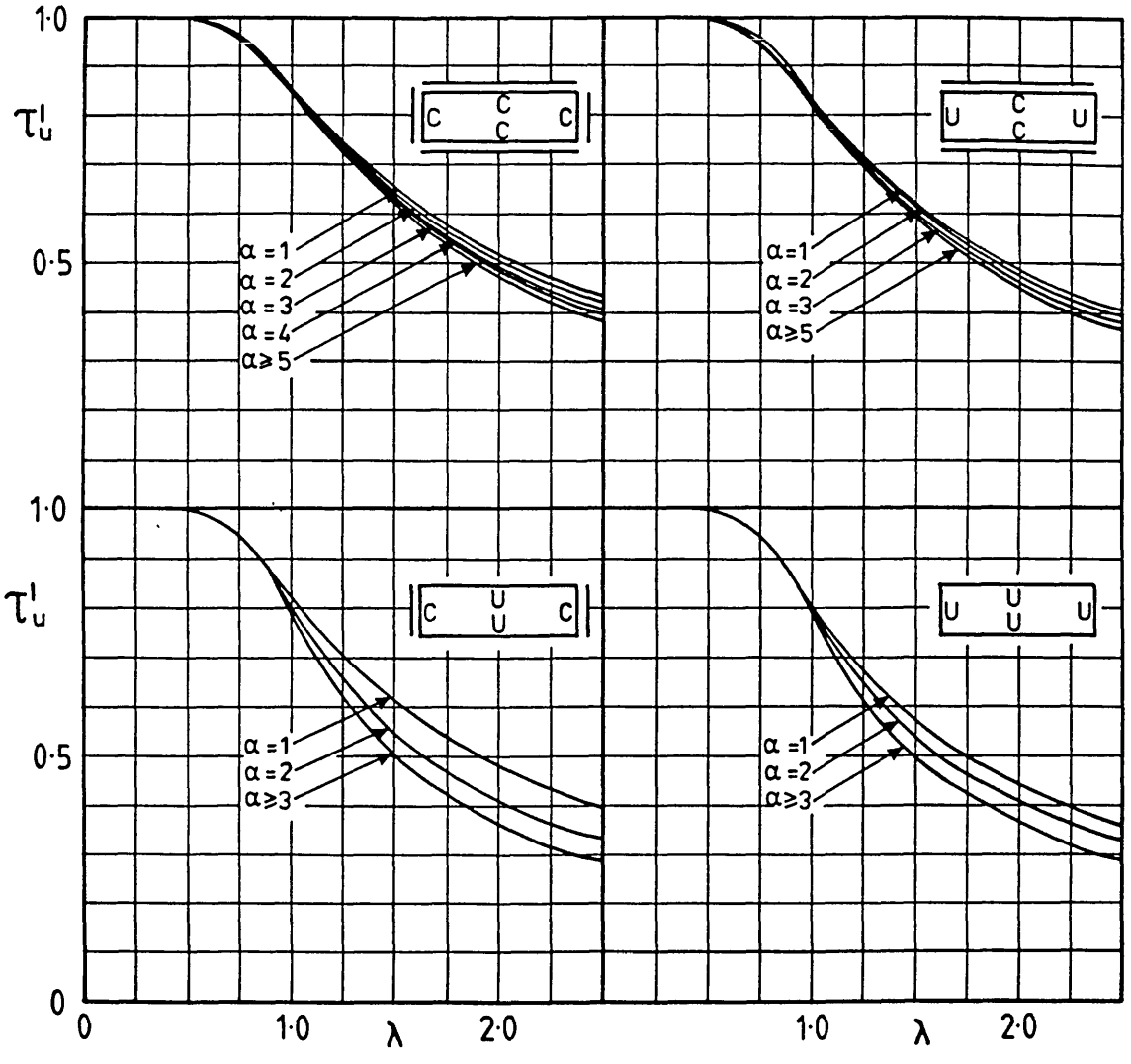

FIGURE 2.42 – Design curves from the proposed model

CHAPTER 3 UNIAXIAL COMPRESSION

3.1 Longitudinal Strength

In later chapters of this thesis design models will be proposed which will describe the strength of plate panels which are subject to various load combinations. These load combinations will include biaxial compression, biaxial compression with shear, and biaxial compression with pressure. A pre-requisite for the development of the load combination models is to have a consistent uniaxial compression model. The purpose of this chapter is to describe such a design model, which will define the uniaxial longitudinal and transverse compressive strength of rectangular constrained plates, based on the results of both published and new elasto-plastic numerical analyses. This first section of the chapter will deal with longitudinal compression.

The constrained boundary condition assumed in this chapter is the same as the constrained boundary used for shear panels in Chapter 2. In that context, the constraint condition required the shear stress applied to the boundaries to be uniform. In the context of compression in plates the shear stress on the boundary has to be uniformly zero, which results from the lack of tangential restraint on the edges.

Most of the data on which this chapter is based were published in (47) to (49), and were obtained from finite difference multi-layer elasto-plastic analyses, using the Dynamic Relaxation method. All three references were for plates subject to biaxial compression, with (47) and (48) also including lateral pressure. In a similar manner to the Dynamic Relaxation analyses of (35), for plates in shear, which were referred to in the previous chapter, the in-plane loading was applied as boundary displacements in fixed proportion to one another. As these proportional biaxial strains were increased, then the ratio of biaxial stresses applied to the plate varies. Interactions were drawn as outer envelopes to the resulting σ_x-σ_y trajectories, and the uniaxial strengths inferred from (47) to (49) are obtained from the end-points of these interactions. The results of some direct uniaxial loading analyses were also presented in (49), and these will be described later. Furthermore, additional uniaxially stressed analyses, using FINAS, have been carried out as part of the present work.

The bulk of the analyses in (47) to (49) were for square and 3:1 rectangular plates, with a few 1.5:1, 2:1 and 5:1 plates in addition. The out-of-plane imperfection assumed in the analysis of rectangular plates was composed, in general, of the buckling mode of the panels when subjected to transverse compression, with an

additional, but secondary, component of the buckling mode due to longitudinal compression. The magnitude of the latter mode component was one half that of the former component. The imperfection mode for 3:1 plates is illustrated in Figure 3.1.

In this way, a single plate imperfection can be used to analyse rectangular plates with biaxial loads ranging from predominantly transverse compression to predominantly longitudinal compression, with a reasonable expectation that the panel will be able to develop the different modes preferred towards the ends of the biaxial compression interaction.

Furthermore, an imperfection profile broadly of this type is also the likely mode due to the fabrication process. The main features of the process by which the mode is formed are the "draw down" due to angular shrinkage of the cross-section of the longitudinal welds , and also a degree of longitudinal compressive buckling in the plate caused by the longitudinal shrinkage of these welds. There will also be a contribution to the imperfection profile from transverse compressive buckling, caused by the shrinkage of the welds on the short edges of the panel, but this effect may not be very great for rectangular plates.

However, there is a possibility (at least for reasonably slender plates) that the single half-wave "hungry horse" component of the as-welded mode may be substantially shaken out if the panel is subjected to repeated cycles of longitudinal compression. This would require there to be sufficient of the "ripple" mode component in the as-welded imperfection for this mode to amplify when load is applied. If the buckling deformation that occurs when load is applied is sufficient to cause at least surface yielding then when the load is removed there will be an increased component of the ripple mode in the initial imperfection prior to the next cycle of loading. This could give rise to a cumulative "shaking-in" of the affine imperfection, and a shaking out of the as-welded mode, with repeated applications of load, so that for later cycles of load the out-of-plane imperfection is closer to the preferred mode. A long plate with a preferred mode imperfection will behave like a square plate, as demonstrated in (79), and will be weaker than the same plate with a significant hungry horse component of imperfection. In (80) are reported the results of cyclic compression tests of long panels which showed a loss of compressive capacity after several load cycles. It is not reported, however, whether this was associated with mode change effects.

Even if this shaking-in effect didn't occur, it only requires the as-welded profile to have less of the hungry horse mode relative to the ripple mode than is assumed in the analyses of (47) for the results of the analyses to be non-conservative.

As-welded profiles are notoriously variable, and although the principal contributions to these profiles are as described above, their relative magnitude is crucially dependent on the welding process, as well as on the initial plate fairness.

Since the assumption of a composite mode can lead to non-conservative estimates of longitudinal strength relative to square plate strengths, it might be safer to make the assumption that the imperfection is in the preferred mode, that is, the critical buckling mode. A caveat to this assumption will be discussed in section 3.3.

The maximum displacement in the imperfection mode used in (47) to (49) is given by $w_0/t=0.1\beta^2$, ($\beta=b/t\sqrt{(\sigma_0/E)}$), whereas in (35) the plate imperfection had a magnitude given by 0.145β, which for mild steel results in $w_0=b/200$. The strength rules of the current UK bridge code, (24), assume this latter level of imperfection, (the analysis of (35), for instance, is the basis of the BS5400 rules for longitudinally stiffened webs). However, the difficulty which arises when trying to measure real plate imperfection profiles is to identify the contribution to the total imperfection from the ripple mode assumed by the design rules. Since for longitudinally loaded plates it will be an excessive magnitude of the ripple component which will reduce the plate strength, the tolerance specification sets out to measure the amplitude of the ripple by using a gauge length inherited from the so-called Merrison rules (81). These rules required a gauge length twice as long as the shorter panel dimension, b, to be used in the longitudinal direction of panels longer than 3:1. Figure 3.2 reproduces the diagrams explaining the use of the gauge from Table 23.1 of (81). The logic of using a gauge length of 2b for panels longer than 3:1 is that it is only for such panels that 2 distinct peaks can occur in the imperfection mode which is affine to longitudinal buckling. The plate deformation measured relative to this gauge will identify not the ripple amplitude but its double-amplitude, that is the measurement from peak to trough of the periodic wave (= $2\ w_0$). The equivalent plate with only a ripple imperfection will therefore have a ripple amplitude, w_0, equal to one half the gauge tolerance. Figure 3.3 plots one half of the gauge tolerance due to Merrison, as w_0/b against b/t for long plates. Since the Merrison tolerance is a function of plate thickness for plates less than 25 mm thick, it is plotted on the figure for thicknesses of 10, 15, 20 and 25 mm.

The basis for the tolerance rules for plates shorter than 3:1 is not clear. In these plates the gauge length is taken to be the long panel dimension, which for square plates, at least, identifies an imperfection of the same wavelength and amplitude as for plates longer than 3:1. For intermediate aspect ratios, however, what is being measured by such a gauge length is not obvious. Firstly, there is a 50% increase in w_0 magnitude at aspect ratio 3, which was corrected in BS5400 by defining the

change-over in gauge-lengths to occur at aspect ratio 2, rather than 3. However, the justification of the long gauge length is that it can pick out the amount of ripple imperfection in a complex imperfection profile, by spanning between adjacent peaks (or troughs). This it clearly cannot do for plates shorter than about 2.5:1, except for ripples of much shorter wavelength than the critical mode. A better approach might be to use a gauge length equal to b for panels less than 3:1. No discontinuity will then exist at 3:1, and a reasonable indication of the degree of ripple mode would still be obtained. Even so, it is still a rough and ready measure, which would certainly benefit from calibration with real imperfection profiles, with Fourier analysis of the profiles identifying the actual amount of the critical buckling mode, carried out in a similar manner to that reported in (4).

The BS5400 tolerance for mild steel is also shown on figure 3.3, and it can be seen that it is not only more simply defined than Merrison, but it is also set at a higher level found to be representative of good bridge fabrication practice in the UK. The offshore DNV rules (63), require imperfections to be not greater than w_0=b/100, reflecting the generally greater imperfections found in ship and offshore structures than in bridges. This imperfection magnitude is also shown on the figure.

On figure 3.3, it can be seen that w_0=b/200 and $w_0/t=0.1\beta^2$ intersect at b/t=42 (for σ_0=245 N/mm^2). Since the critical slenderness (for the same steel) is b/t=55, it follows that where the magnitude of imperfection is likely to have a significant influence on plate compressive strength (in the imperfection sensitive region, that is in the vicinity of the critical slenderness) there is not a great deal of difference between the two w_0 specifications. They are at their most divergent at slendernesses remote from the imperfection sensitive range.

Figure 3.4 presents results published in (82) for compressive strength of square plates with b/t=40, 60 and 80. These results were obtained using an earlier version of the Dynamic Relaxation program referred to already in this chapter, but one which relied on a single layer idealisation of plate yielding. The maximum compressive strength of plates with different levels of w_0 and residual stress are plotted against w_0/b, and curves drawn through to fit these points.

Included on this figure are the result of 3 FINAS analyses with w_0=b/200 and no residual stress, and the end-points of the square plate interaction curves for the same slendernesses from (48), (for which $w_0/t=0.1\beta^2$ and the residual stress was 0.2 σ_0). The format of this figure allows the various results to be compared with one another, notwithstanding the differences in w_0 and σ_r, and it can be seen that the three different analyses all agree with one another very well.

Also indicated on the figure are the w_0=b/200 and 0.1 β^2 imperfection levels, which demonstrate that if the residual stresses are in the region of 0.15 to 0.3 σ_0 then there is only a 1-2% difference in panel strength as a result of the different w_0 specification magnitudes.

This observation can be used to justify use of the analyses of (47) to (49) to formulate a design model even when the imperfection magnitude is specified to be not greater than w_0=b/200.

It has already been mentioned that the DR program applied load as proportional strains. In Chapter 2, proportionally stressed stress-strain curves were inferred from proportional strain data (presented as figure 2.3) by a process of interpolation, described in Section 2.1. It is possible to use the same procedure with the biaxial straining data, and this has been carried out for a/b=1, b/t=60, to produce the proportionally stressed biaxial stress-strain curves of figure 3.5.

Proportional stress solutions for the same plate with uniaxial stress, and biaxial stresses in the ratios of 1:1 and 2:1, have been directly calculated using FINAS, but without residual stresses, and these are also shown on figure 3.5. The influence of residual stresses on compression stress-strain curves has been described in (82) and (83). The initial loading and later un-loading parts of the stress-strain curve are expected to be only slightly affected by residual stress. The main influence of residual stress is to truncate the peak area of the stress-strain curve for σ_r=0, due to a sudden reduction in tangent modulus in the loading part of the curve. This can be seen in figure 3.5. Apart from this expected cause for disagreement between the cross-plotted Dynamic Relaxation results and FINAS, there is very good agreement between the two analyses. It should be pointed out that the equal biaxial stress case does not need to be cross-plotted from the Dynamic Relaxation analyses since equal biaxial straining is the same as equal biaxial stressing for a diagonally symmetric plate.

This good correspondence between the finite difference solutions modified by cross-plotting, and the proportionally stressed finite element analyses, was already noted in Chapter 2 for shear loading.

Figure 3.6 summarizes the maximum strength longitudinal compression data from (47) to (49), plotted against slenderness. The longitudinal compression end-points of 3:1 plate interaction curves are compared with the end-points of the square plate interaction curves and it is clear that the longitudinal strength of a rectangular plate

with a composite imperfection mode is greater than that of a square plate, for slendernesses in the imperfection sensitive range ($40 \leq b/t \leq 60$). In (49), a modification to the Dynamic Relaxation program was used which allowed the case of pure uniaxial compression to be analysed. The constraint condition on the unloaded edges was incorporated in the analysis by iteratively solving the amount of draw-in of those edges such that the net stress on them is close to zero. The data which were produced in this way for square plates are also shown. These data are generally slightly higher than the equivalent square plate interaction end-points, due to residual stress only being applied in the direction of loading in the uniaxial cases, whereas residual stresses were applied in both longitudinal and transverse directions in the biaxial straining cases.

The result of a FINAS analysis of a square plate with b/t=180, but without residual stress, is also shown in order to extend the range of the solutions. At this slenderness, residual stresses will have an insignificant effect on maximum strength.

For the reasons already described, the square plate interaction end-points, augmented by FINAS results, will be used as the basis of an empirical design function for longitudinal compressive strength.

The simplest approach to a design function is to say that the strength of the plate is given by visualizing an effective width of plating which does not vary with slenderness. That is, as the plate is made wider, the same amount of effective plate is assumed to exist, with the additional plate material deemed to have no effect on the net force which the plate can resist (there will, of course, be a reduction in average stress commensurate with the increase in total plate cross-sectional area). Such a rule was proposed in (84), and results in an expression of the form:

$$\sigma_{xu}' = f(\frac{1}{\beta}) \qquad \ldots 3.1$$

where $\sigma_{xu}' = \sigma_{xu}/\sigma_0$. This type of expression is also used in Table 8 of the latest UK steel building code, BS5950 (25), to define the strength of slender compression elements of a cross-section. This form of equation was developed further (85)-(87) by including a 2nd order term to give better agreement with test results, and since the critical buckling stress of the plate, which must have some influence on plate behaviour, is itself a 2nd order term, there is also an intuitive basis for its inclusion. This can be written as:

$$\sigma_{xu}' = f(\frac{1}{\beta}, \frac{1}{\beta^2}) \qquad \ldots 3.2$$

In (88) a constant term was added to equation 3.2, whereas in (51) a 3rd order term was added, once again justified empirically. It is found that very good agreement with the data of figure 3.6 requires both a constant and a third order term to be included in the design equation. This results in:

$$\sigma_{xu}' = 0.23 + \frac{1.16}{\beta} - \frac{0.48}{\beta^2} + \frac{0.09}{\beta^3} \quad \ldots 3.3$$

and this is shown on figure 3.6. An equation of this form was also found in (89) to give a good representation of the mean minus two standard deviations curve, based on 383 experimental results. Equation 3.3 has only been justified up to b/t=180 and should not be used without further verification for higher slendernesses. A particular point to note is that due to the inclusion of the constant term, equation 3.3 is asymptotic to σ_{xu}'=0.23, not to zero. As an alternative, simpler equations without the constant term, and even without the cubic term (ie in the form of equation 3.2), could be used, but at the expense of accuracy in the practical range of slendernesses. Since a principal purpose of the uniaxial model which is proposed in this chapter is to provide a reasonably accurate input to the interaction models, which will be proposed in later chapters, so that they can be compared with the numerically derived interactions, then the more complicated, but more accurate, expression of equation 3.3 will be used.

Although the shear resistance model which was proposed in the previous chapter merged with the shear yield stress in the low slenderness region, it is not proposed to incorporate a similar feature in the compression resistance model. Clearly the value of σ_{xu}' predicted by equation 3.3 can only be used to define the uniaxial compression resistance when it is less than unity. However, it will be seen in the following chapter, that values of σ_{xu}' greater than unity (as predicted by equation 3.3) will be useful when discussing biaxial compression interactions.

Equation 3.3 is compared in Figure 3.7 with current design models of plate compressive strength (24),(63) and with mean and lower bound strength curves from (88), which are drawn through a more recent summary of experimental data than (89). The lower bound experimental curve of (88) cannot be merely due to the worst possible combination of w_0 and σ_r, since the experimental curves are at their most divergent remote from the imperfection sensitive region. A possible explanation of this divergence will be suggested later in this chapter, in section 3.4.

3.2 Transverse Strength

In (49) the transverse strength of rectangular plates was also considered. Interaction end-point data were again compared to direct uniaxial loading cases, with the same difference between the residual stress fields applied to uniaxially and biaxially loaded rectangular plates, as for square plates. The consequent disagreement between the interaction end-points and the uniaxial data is less than for square plates, as can be seen in figure 3.8 which plots both types of data for square and 3:1 plates, but this is to be expected since the absence of a residual stress perpendicular to the direction of loading will have less influence on transversely loaded rectangular plates than on square plates. A particular point to be noted about the residual stress assumptions used in (47) to (49), is that the transverse residual stresses were calculated on the assumption that the residual tensile yield block along the short edges of the panel are only half the width of the residual tensile yield blocks along the long edges of the panel. This means that a transverse residual compression of $0.0286\sigma_0$ was used for 3:1 plates. For biaxially loaded plates this would be in conjunction with a longitudinal residual compression of $0.2\sigma_0$.

Figure 3.9 shows the profiles at peak load of the additional out-of-plane deflection along the longitudinal centre-line of 3:1 plates with b/t=40, 60 and 80, primarily loaded in the transverse direction. It can be seen that the plate deformation is approximately constant over the middle portion of the plate with the double curvature concentrated towards the ends of the plate.

In (60) and (90) a design model for transverse strength is used where the central portion of the plate which is deforming with single curvature is idealised as a series of transverse struts, and the doubly curved end regions are idealised as the two halves of a square plate subject to uniaxial compression. This idealisation is illustrated in figure 3.10.

If σ_c is the strut strength, then this idealisation results in a transverse strength of the panel given by:

$$\sigma_{yu} = \sigma_c + \frac{b}{a} (\sigma_{xu} - \sigma_c) \qquad \ldots 3.4$$

where σ_{xu} is the square plate strength from equation 3.3. In order for this model to be used, a suitable strut strength curve needs to be defined. The aspect ratios analysed in (49) included infinity, this analysis being based on a plate-strip strut analysis, consistent with the rectangular plate analyses.

Perry's analysis (91) of imperfect struts, when applied to a plate strip gives:

$$\frac{\sigma_c}{\sigma_0} = \frac{(1 + (1+6(w_0/t))\sigma_e')}{2} - \sqrt{\left\{\frac{1 + (1+6(w_0/t))\sigma_e'}{2}\right\}^2 - \sigma_e'} \quad . . 3.5$$

where $\sigma_e' = \frac{\pi^2 E}{12(1-\nu^2)}\left[\frac{t}{b}\right]^2 \frac{1}{\sigma_0}$

which is based on the extreme compressive fibre reaching yield. However, it is possible to make a simple adjustment to equation 3.5 to take into account the residual compression stress which acts at right angles to the direction of the strut compression, which will have the effect of increasing the extreme fibre stress needed to cause yield (since a state of biaxial compression will exist). σ_0 in equation 3.5 should therefore be replaced by σ_{0r}, in accordance with Von Mises, such that:

$$\sigma_{0r} = \frac{\sigma_0}{2}\left\{\sigma_r' + \sqrt{4 - 3\,\sigma_r'}\right\} \quad . . . 3.6$$

Since σ_r' is 0.2 in the analyses of (47) - (49), then σ_{0r}/σ_0 is 1.08.

The strut strength given by equations 3.5 and 3.6 is plotted against b/t on figure 3.11, where it is compared to the data of (49). There is very good agreement between equations 3.5 and 3.6 and the data for b/t=110, 80 and 60, whereas for more stocky plates the curve is increasingly conservative as the slenderness is reduced, until at b/t=20 it predicts a strength of 0.74, compared to 0.84 from (49).

An alternative approach to the strut curve would be to use a polynomial function which will be less conservative in the stocky plate region while still giving good agreement with the slender plate data. Such a function is:

$$\frac{\sigma_c}{\sigma_0} = \frac{0.025}{\beta} + \frac{0.641}{\beta^2} - \frac{0.188}{\beta^3} \quad . . . 3.7$$

and this is shown as a broken line on figure 3.11. This now gives a strut strength of 0.81 for the b/t=20 case, compared to 0.84 from the data, and 0.74 from equations 3.5 and 3.6.

Equations 3.3 to 3.6 have been used to produce strength versus slenderness curves for aspect ratios 1, 1.5, 2, 3, 5 and infinity, in figure 3.12(a). The numerical data of (49) are also shown on this figure for comparison. Figure 3.12(b) is the same plot using equation 3.7 instead of equations 3.5 and 3.6. The conservatism of the strut models in the stocky plate region, can be seen to have an influence on the predicted strengths of rectangular plates in that region, but both models do give, in general, a good agreement with the numerical data throughout the range of aspect ratios and

slendernesses. Any discrepancies are such that the design models are conservative. Furthermore, most of the data which are under-predicted by both models are based on uniaxial compression analyses in which residual stresses were only applied in the direction of loading.

If the transverse strength model and the data are plotted against the inverse of aspect ratio, as in figures 3.13 (a) and (b), then an important feature of the behaviour becomes apparent. The design model produces for each slenderness a straight line between the transverse strength of an infinitely long plate as given by equations 3.5 and 3.6 (in figure 3.13(a)), or by equation 3.7 (in figure 3.13(b)), and the transverse strength of a square plate as given by equation 3.3. The data also follow the straight lines very closely.

Also shown are FINAS results for b/t=180 to extend the range of the comparison between model and data. Again, the lack of residual stress in the FINAS solutions is insignificant at this slenderness, as is the four-fold increase in imperfection magnitude from the b/200 used in the analysis to $0.1\beta^2$ used in (47) - (49). Even at b/t=80, figure 3.4 tells us that such a difference would only give rise to a 6-7% reduction in strength.

It is instructive to plot the critical buckling factor, k_y, for transverse compression in plates of aspect ratios from infinity to unity, in a similar format to figure 3.13. This is shown on figure 3.14, and gives a parabolic relationship between critical buckling stress and aspect ratio, in contrast to the linear relationship between strength and aspect ratio which is evident in the previous figure. It is possible, however, to calculate a pseudo-critical buckling factor where the elastic critical factors appropriate to square pseudo-plates (k_y=4) are applied to the end regions of the plate, and the Euler buckling factor (k_y=1) is applied to the remainder of the plate, and these factors amalgamated to produce the average k_y. This results in the straight broken line shown on figure 3.14. It is also instructive to consider the effect of assuming that the end regions make up a pseudo-plate longer than square. As an example, assuming the end regions made up a pseudo-plate of a/b=1.5 produces the chain straight line between aspect ratios infinity and 2/3, together with the critical buckling parabola between aspect ratios 2/3 and unity.

The linear relationship between transverse strength and aspect ratio produced by the design model on figure 3.13 is therefore a consequence of assuming the end regions of the plate make up a square pseudo-plate. The fact that the numerical data also lie on straight lines would seem to suggest that the plate deformation profiles in the numerical analyses agree with the idealised profile used by the design model. This,

however, is not the case, as seen in figure 3.8, since the effect of membrane stresses on the deformation profile diminishes as the plate slenderness reduces, so that the deformation profile tends towards the sinusoidal critical buckling profile for the least slender plates. As a result, the end regions of the deformation profiles of figure 3.8 make up pseudo-plates which vary in aspect ratio, being increasingly longer than square for the least slender plates.

There is an apparent anomaly between the numerical data which follows the straight line implied by square pseudo-plates, and the deformation profiles which show end regions making up pseudo-plates longer than square for the least slender plates. The explanation for this, could be that the reduction in the local transverse stress that can be sustained by the end regions, when these are longer than square, is being offset by the reduction in the proportion of the plate which only sustains the much lower strut buckling stress. In any event, the use of square pseudo-plates in the design model is justified by the agreement this gives with the trends of the numerical analyses.

This question of deformation profiles will be raised again, in Chapter 4, where it will be seen to have a consequence for the shape of biaxial compression interaction curves.

3.3 Minimum Strength Consideration

In section 3.1 the use of longitudinal compression data obtained for rectangular plates with composite w_0 modes was rejected in favour of using square plate compression data. The justification was that the analysis of a square plate was equivalent to the analysis of a rectangular plate with an imperfection affine to longitudinal compressive buckling, and that affine imperfections are to be preferred since these will give a lower strength than the non-affine imperfections of (47) - (49).

However, it was pointed out in (92) and (93) that imperfections in the critical buckling mode will not necessarily give the lowest strength. In (93), compressive strengths were tabulated for plates of aspect ratios between 0.4 and 1.0, for slendernesses between b/t=27.5 and 96, with various magnitudes of w_0 and residual stresses. For consistency with the notation of this thesis (in which a is always the long dimension of the plate), these compressive strengths will need to be described as transverse compressive strengths of plates with a/b from 1 to 2.5 (=1/0.4), whose slendernesses are expressed in terms of the long panel dimension as a/t (=27.5 to 96). Interpolating between the data to find the strengths when σ_r'=0.2 and

w_0=a/200, enables figure 3.15 to be plotted. It can be seen from this figure that, with the exception of the a/t=27.5 case, the aspect ratio for minimum strength decreases continuously as slenderness is increased, from around 0.8 at a/t=41 to less than 0.6 at a/t=96. The trend reverses, however, at a/t=27.5, for which the weakest aspect ratio is in the region of 0.5 to 0.6.

The design model of the previous sections can also be used to produce a similar type of plot to figure 3.15. b/a is reduced from unity, while keeping a/t constant, and the transverse strength, σ_{yu}, is calculated from equation 3.4 (with equations 3.3 and 3.7). This is equivalent to calculating the longitudinal strength of plates of aspect ratios reduced below unity, of constant slenderness, b/t, and is plotted on figure 3.16. The polynomial strut curve of equation 3.7 is used in the derivation of this figure, rather than equations 3.5 and 3.6, since this gives better agreement with the data throughout the slenderness range.

It is clear that the design model also shows a reduction in strength as panels become shorter than square, and that the aspect ratio for minimum strength decreases with increasing slenderness in a manner similar to figure 3.15 (excluding the b/t=27.5 result). At b/t=30 the weakest aspect ratio is 0.95, but at b/t=180 it is 0.45. The locus of minimum strengths has also been shown on figure 3.16. The trend in the aspect ratio for minimum strength which is displayed by the design model is continuous, and, unlike the trend shown on figure 3.15, it does not reverse. Indeed, for very stocky plates the design model suggests that square plates give the least strength, and it may be that the minimum strength aspect ratio of a/b=0.5–0.6, for b/t=27.5, is erroneous. It seems possible that the extent of plasticity at maximum resistance made convergence difficult to achieve, although no comment is made on this in (93).

An additional means of investigating this phenomenon is to use a simple elastic analysis of uniaxially loaded constrained plates with a first yield criterion of failure. The analysis is a subset of the biaxial compression and lateral pressure analysis of Appendix B, which is discussed in section 6.1 of Chapter 6. The particular solution for uniaxial compression, which is rendered by the more general solution, is simple and concise and is the same as that described in (94), for instance. The analysis assumes that the profile of both the initial imperfection and the displacement under load is given by a single sinusoidal function. If w is the additional out-of-plane displacement then the ratio between the additional displacement and the initial imperfection is given by $k=w/w_0$. The average uniaxial stress, $\bar{\sigma}_x$, is related to k by:

$$\bar{\sigma}_x = \frac{k}{1+k}\sigma_{cr} + \left\{\left[\frac{a}{b}\right]^2 + \left[\frac{b}{a}\right]^2\right\}\frac{\pi^2 E}{16}\left\{\frac{w_0}{b}\right\}^2(k^2 + 2k) \quad \ldots 3.8$$

σ_{cr} is the critical buckling stress. The stresses at the mid-length of the unloaded edge are:

$$\left.\begin{aligned} \sigma_{xe} &= \bar{\sigma}_x + \frac{\pi^2 E}{8}\left\{\frac{w_0}{a}\right\}^2 (k^2 + 2k) \\ \sigma_{ye} &= -\frac{\pi^2 E}{8}\left\{\frac{w_0}{b}\right\}^2 (k^2 + 2k) \end{aligned}\right\} \quad \ldots 3.9$$

Figure 3.17 shows the results of incrementing k in equation 3.8, and applying the Von Mises Yield criterion to σ_{xe} and σ_{ye} in equation 3.9 until the level of average stress is found that causes first membrane yield. Slendernesses between 20 and 180 have been analysed in this way, and the locus of the weakest strengths is also indicated. It can be seen from the figure that, even with this simple application of a well-established relationship between uniaxial compression and out-of-plane displacement there is a reduction in strength indicated for plates shorter than square, although the magnitude of the reduction is not great. None the less, at b/t=180 the weakest aspect ratio is less than 0.7.

This phenomenon was shown in (92) and (93) to result from the conflicting influences of an increasing critical buckling stress and a decreasing post-buckling stiffness as plates became shorter than square. The former effect results in a stiffer plate in the early stages of loading where little buckling has occurred, whereas the latter effect reduces the stiffness after significant buckling has taken place. For a reasonably slender plate just shorter than square the reduction in post-buckling stiffness gives rise to a weaker plate than the equivalent square plate, but as the plate becomes even shorter the critical stress becomes so high that post-buckling effects are not given the opportunity to influence the plate behaviour, and the plate strength increases. The weakest aspect ratio will depend on b/t, w_0 and σ_r.

The implications of this phenomenon for longitudinally compressed rectangular plates need to be considered. A perfect, or near-perfect, longitudinally compressed rectangular plate will buckle in the critical buckling mode, and this mode will quickly amplify in the immediate post-buckling phase. The development of this mode in the early stages of loading is very likely to preclude the development of shorter modes at higher load levels.

An imperfect plate is likely to contain a significant amount of the longitudinal compression square buckling mode in its initial imperfection, as explained in section 3.1, and as reported from ship surveys in (5), for instance. At low load levels this mode will amplify more readily than any of the other modal components, so that at higher load levels, once again, snap through to a shorter wave mode may be

precluded.

Figure 3.18 presents stress-strain curves for a 3:1 plate with b/t=80, with various imperfection modes, calculated using FINAS. Figure 3.19 shows the total out-of-plane deformation profiles at various stages of loading, for the plate with an imperfection in the elastic critical mode, w_{03}. This mode, having readily amplified in the early stages of loading, persists without any sign of mode-change at all load levels.

Snap-through to shorter wave-length modes can occur, however, if the initial wavelength consists purely of a longer wavelength than critical. Figure 3.20 shows the deformation profiles for w_{01} at various levels of loading. In this case the single half-wave buckling mode snapped through to a five half-wave mode, and not to the three half-wave mode. A similar effect was observed in 4:1 plates in (79).

One might expect the stress-strain curve of the w_{01} case, after it had snapped through to an m=5 mode, to converge at large strains with the stress-strain curve for the w_{05} case. There is a degree of convergence apparent in figure 3.18, but the w_{01} stress-strain curve is still slightly above the w_{05} stress-strain curve in the unloading region. An important aspect of the different analyses which may account for the lack of complete covergence is the difference in the finite element mesh sizes used in the two cases. The w_{01} case had a 12x4 mesh whereas the w_{05} case had a 15x5 mesh. After snap-through the former case has 2.4 elements to the half wave of buckle whereas the latter case has 3 elements to the half-wave of buckle, which difference gives rise to the higher stress for a given strain in the w_{01} solution.

In the numerical data investigated in the current work, there is no evidence of "snap-through" from the mode preferred at lower load levels to the shorter wavelength mode preferred at higher load levels, and the writer is not aware of any other evidence that it occurs in this kind of situation. Nevertheless, it might be that the phenomenon could occur for plates much more slender than investigated herein (for which the weakest aspect ratio will be very much shorter than square than in the present analyses).

Real imperfection profiles, however, even though they are likely to contain a significant ripple imperfection, will not be perfectly regular and will always contain some asymmetry. Similarily, the plate material properties will also contain some irregularities, and will not be uniform throughout the plate. This means that, although all of the ripple half-waves will amplify under longitudinal compression, surface yielding will first occur at the crest of only one of the ripple half-waves.

The plate will still, of course, be able to sustain additional load, so that all of the half-waves will continue to amplify as the load is increased, and provided the initial imperfection was not irregular to the point of containing a substantially local imperfection, then some yielding will also occur at the crests of the other half-waves. None the less, the initiation of yield at only one crest will further emphasize the buckling displacement of that half-wave relative to the others. The maximum resistance of the plate as a whole will be limited to the maximum capacity of this most heavily deformed (and yielded) half-wave, and when this has been exhausted the applied compression will begin to unload, even though the local buckling displacement will still continue to increase. However, since the remaining half-waves had not yet reached their maximum capacities, then the buckling displacement in these half-waves will diminish as the loading reduces. As a result, the buckling displacement will become increasingly localized (developing into a folding mechanism) which will be less constrained against changing its wavelength by the rest of the plate than it was when all the buckle half-waves were amplifying significantly, so that it may begin to shorten as it continues to buckle. The plate will also become increasingly anisotropic, due to yielding, which will provide an additional reason for the wavelength to shorten at this stage.

This effect may be expected not to have a significant effect on the behaviour of the plate before its maximum strength is achieved, unless (as has been mentioned) the imperfection was predominantly composed of a local buckle, in which case the adjacent ripple half-waves will not have amplified sufficiently to constrain the principal half-wave against changing its wavelength. Where such a local plate imperfection, or dent, exists then the strength of the plate will be reduced compared to its strength when the plate has a critical buckling imperfection, as was demonstrated in (79). Furthermore, this reduced strength was shown to be approximately the same as the strength of the short plate of aspect ratio equal to that of the dent. It is apparent, then, that where a plate has a likelihood of local indentations, perhaps due to impact damage, then the compressive strength will be reduced in accordance with a deformation shorter than the plate width. For this situation, the design model should be used to find the weakest aspect ratio, in order to find the minimum strength of the panel.

3.4 Sensitivity to Imperfections

Although a strength model used in design has to relate to the imperfection limits specified in the fabrication of the structure, or to the quality of workmanship which is anticipated, it is often useful to be able to quantify the effect of exceeding the

limiting, or anticipated, imperfection. Alternatively, it may be useful to know what benefit will accrue from tighter quality control procedures. It is also important to be able to quantify the effect of imperfections both greater than and less than specified when assessing structures in-service.

In any consideration of imperfection profiles, it is necessary to have an appreciation of the forces applied to the panel, and of the influence of imperfection profiles on the panel's resistance to those forces. The use of long gauge lengths in rectangular panels which was discussed in section 3.1 assumes that these panels are longitudinally loaded. Clearly for transversely loaded panels where it is the "hungry horse" type of mode which will be critical, a different approach to imperfection measurement is required, possibly using transverse gauges.

The tendency for preferred imperfection profiles to be "shaken in" to slender plates during their service life has already been mentioned in section 3.1. As a result, in a transversely loaded rectangular panel the as-welded "hungry horse" mode will be emphasized by its loading, whereas in a longitudinally loaded panel of the same geometry, this mode will be shaken out.

Deterministic or probabilistic design methods, based on surveys of ship structures which fail to recognize this potential correlation between loading direction (or type) and affinity of in-service imperfection profiles, could result in optimistic estimates of panel strength.

Despite the considerable difficulties of making sensible assessments of imperfection profiles, they are much less than the potential difficulties raised by residual stresses. Techniques for measuring residual stress either during construction or when assessing structures in-service, are very involved and are not feasible as part of a general programme of quality control or structural assessment (other than in exceptional circumstances).

Although there will be a tendency for residual stresses to reduce during the service life of a structure, such a reduction could not be relied upon in determining panel strength. It may be that it will be useful to make use of such a reduction if there has also been an increase in panel imperfection during the service life. Such an increase in imperfection would have to be taken into account as a result of its deleterious effect on panel resistance, and it may then be useful to try and offset this by taking account of the beneficial effect of the reduced residual stress. This reasoning, for instance, justifies the treatment of residual stress and plate imperfection as independent variables in (7), and also the inverse correlation between the

magnitudes of residual stress and plate imperfection assumed in the analysis of (51).

However, it would require a great deal of confidence in the degree of reduction of residual stress before its beneficial influence could be relied upon, and as a result of the relative difficulty in measuring residual stresses in completed structures there is not sufficient data on the reduction of residual stress during service life to give this degree of confidence. Furthermore, it was pointed out in (95), that for the same class of ship (RN frigates) there did not appear to be a significant increase in panel imperfections, compared to as-fabricated imperfections, during the service life of the structure, so such increase as there may be cannot be said to be general.

As a result of this reasoning, it is reasonable to make the simplifying assumption that there exists a general correlation, for a given slenderness, between higher imperfection levels and higher residual stresses. In other words, the higher the welding residual compressions are, the more buckling deformation (and hence w_0) will have occurred in the plate due to the cooling of the weldment. If a plate with a large out-of-flatness did have low levels of residual stress (due to in-service overload causing a permanent set together with a shaking out of the residual stress as discussed above), then it will, at least, be safe to assume that the larger imperfection is correlated with a larger residual stress. On the other hand, a plate with little out-of-flatness (relative to its thickness) is very unlikely to have significant residual stresses unless its slenderness is such that residual compressions don't cause buckling. The maximum resistance of such a plate will be very nearly the yield stress and almost any level of residual stress will have little effect on the maximum strength of the panel.

This approach corresponds to the adoption of upper and lower bound (and mean) combinations of w_0 and σ_r which are used to identify the upper bound, mean and lower bound curves from a wide range of experimental data in (88). The reasoning also justifies the correlation between the residual stress and imperfection magnitudes used in the calculation of uniaxial strength curves in (49), where "slight" w_0 is paired with "slight" σ_r, "average" w_0 with "average" σ_r, and "severe" w_0 with "severe" σ_r, the magnitudes of each being based on ship surveys reported in (3), (86) and (95). The w_0 magnitudes were $0.025\beta^2$, $0.1\beta^2$ and $0.3\beta^2$, and the σ_r/σ_0 magnitudes were 0.05, 0.2 and 0.4. Although the w_0 magnitudes are expressed as a function of slenderness, it may be noted that the residual stress magnitudes are deemed not to vary with slenderness. For very slender plates, at least, (where the assumed residual stress level may be greater than the compressive strength of the plate) this assumption will not be valid. This point will be discussed in Chapter 6, however, where an additional constraint on imperfection assumptions will be introduced.

In (49) are presented numerically derived strength curves for longitudinal and transverse compression on 3:1 plates from b/t=20 to 110, for the 3 pairs of w_0 and σ_r magnitudes listed above. Although it has been decided not to use the rectangular plate longitudinal compression data in the present work (due to non-affine imperfections), the strength enhancement which they predict relative to square plate strengths is slight for b/t=80 plates, and is likely to be even more slight for the b/t=110 plate, so in this latter case (where there are no square plate data) the longitudinal compression points can be used. For the other slendernesses the square plate analyses of (47) and (48) included the same combinations of w_0 and σ_r and provide a more suitable basis for longitudinal strengths.

Figure 3.21 plots the appropriate slight and severe data from (47)-(49) for square and 3:1 plates, plotted against slenderness. Equations analogous to equation 3.3 can be used to fit the square plate data, giving:

$$\left.\begin{aligned} \frac{\sigma_{xu}}{\sigma_0}\ (\text{severe}) &= 0.24 + \frac{1.06}{\beta} - \frac{0.54}{\beta^2} + \frac{0.14}{\beta^3} \\ \frac{\sigma_{xu}}{\sigma_0}\ (\text{slight}) &= 0.22 + \frac{1.40}{\beta} - \frac{0.60}{\beta^2} + \frac{0.09}{\beta^3} \end{aligned}\right\} \quad \ldots\ 3.10$$

The compression strength curves of equations 3.10 are plotted on the figure as solid lines. The benefit of the modified Perry model of equations 3.5 and 3.6, notwithstanding its greater conservatism for very stocky plates relative to the polynomial strut curve of equation 3.7, is that it made explicit allowance for w_0 and σ_r. As a result, the Perry model has been used with the appropriate slight and severe levels of both to produce the "slight" and "severe" strut curves which are also shown as broken lines on figure 3.21. The transverse strength curves, for 3:1 plates with "slight" and "severe" imperfections, produced by combining the appropriate strut curve with equations 3.10 and 3.4, are also indicated on the figure (as chain lines). These transverse strength curves give satisfactory agreement with the 3:1 plate data from (49).

It is clear, therefore, that not only could the transverse strength of rectangular plates with average imperfections be estimated on the basis of square plate and strut strengths, but also the strength of rectangular plates with low and severe imperfections can be estimated in the same way.

At this point it is possible to re-examine the mean and lower bound experimental curves of figure 3.6, which are reproduced on figure 3.22. It will be appropriate to compare the severe imperfection model with the lower bound experimental curve, but it will also be appropriate to assume that such lower bound experimental results were

imperfect in such a way as to permit short wave or localised buckling sufficient to cause minimum strength. As a result, the average imperfection model applied to plates with square buckling modes, and the severe imperfection model applied to plates buckling in the weakest aspect ratio for a particular slenderness have been included on figure 3.22. It is evident that these design models produce reasonably similar curves to the experimentally-defined curves when account is taken of imperfection mode and magnitude.

3.5 Strain Limitation

The maximum stress that can be sustained by a panel is commonly used as the definition of design strength. This maximum stress is achieved at magnitudes of average direct strain in the plate which can vary from about yield strain to more than twice yield strain, depending on initial imperfections and residual stresses, and on aspect ratio and slenderness.

It is important to recognize that this strength criterion can impose on the stiffeners (or flanges) a requirement to maintain their flexural stiffness well into the regime of axial plastic straining. A less onerous requirement is demanded of the boundary members if the panel strength is defined as being the average stress in the panel when the boundaries shorten by an amount equivalent to the yield strain. This has the additional benefit of providing a basis for a first estimate of the compressive strength of multi-panel assemblages as a prelude to computer analyses which incorporate complete representations of panel load-shortening curves, as in (11)-(15). Maximum stress definitions of strength could not be used in this way, since some panels will be unloading while others have not yet reached their maximum strength.

Although the uniaxial stress that can be sustained by a panel at $\epsilon_x'=1$ can be interpolated from the stress-strain curves of (47), these stress-strain curves are limited to b/t=40, 60 and 80, and not all of these slendernesses are analysed for all the imperfection levels. A generalized method of predicting the stress sustainable at yield strain, based on the much wider body of maximum strength data together with the few yield strain points that can be interpolated, is therefore required. Such a method will now be presented.

The elastic model of equations 3.8 and 3.9 can be used to produce approximate stress-strain curves, in a manner somewhat similar to, but simpler than, the method of (83). In the loading part of the stress-strain curve the average stress in the panel is given directly by equation 3.8, whereas the non-dimensional average strain, ϵ_x/ϵ_0,

is given by the edge stress, σ_{xe}, from equation 3.9, divided by σ_0. This is illustrated on figure 3.23, where $\bar{\sigma}_x/\sigma_0$ and σ_{xe}/σ_0 are plotted against ϵ_x/ϵ_0. The effective width ratio of the panel, defined as the average stress divided by the edge stress, is given by $\bar{\sigma}_x/\sigma_{xe}$ from equations 3.8 and 3.9. This is also illustrated on figure 3.23. In (83) it was shown that an elastically derived effective width, such as this, also served as a very good approximation to the effective width in the unloading part of the stress–strain curve, even though σ_{xe} (from equation 3.9) will be greater than σ_0. This effective width, plotted against ϵ_x/ϵ_0, intersects with the $\bar{\sigma}_x$ curve at the yield strain. The stress–strain curves that are produced by using $\bar{\sigma}_x$ from equation 3.9 up to $\epsilon_x'=1$, and $\bar{\sigma}_x/\sigma_{xe}$ for $\epsilon_x'>1$ are shown on figure 3.24 for square plates with b/t=40, 60 and 80, and $w_0/t=0.1\beta^2$.

The effect of residual stress on stress–strain curves has already been briefly described. The reduction in tangent modulus caused by residual stress will occur approximately at a level of stress given by the maximum stress in the absence of residual stresses less the residual stress level. A straight line can be drawn from this point on the loading part of the stress–strain curve to meet the un–loading part at twice yield strain. This is shown on figure 3.24 for $\sigma_r'=0.05$, 0.1, 0.2 and 0.3. This modification to the residual–stress–free stress–strain curves will be exactly correct for un–buckling plates (with rectangular residual stress fields), and is a reasonable simplification of the behaviour of buckling plates, producing stress–strain curves similar in appearance to those of (82) and (83). The influence of residual stress on the initial part of the stress–strain curve could be modelled fairly simply with this elastic model (in a similar manner to the inclusion of residual stresses in the elastic pressure model of Chapter 6), but the effect on the stress–strain curve is slight and certainly un–important for the present purpose.

It can be seen from figure 3.24 that one effect of significant levels of residual stresses in this simple model is to change the strain at maximum stress from yield strain to twice yield strain. Levels of σ_r' less than 0.1, however, may not change the strain at maximum stress significantly from $\epsilon_x'=1$. This effect of residual stresses is also illustrated in (82). It also follows from this that most of the influence of residual stresses on the maximum compression resistance of the panel occurs for levels of residual stress less than about $0.1\sigma_0$, as was first pointed out in (96).

For the case with $\sigma_r/\sigma_0=0.2$, the maximum stresses from the numerical data are plotted at the strain at maximum stress from the elastic model, and give very good agreement. The uniaxial stresses at $\epsilon_x'=1$ have been interpolated from the data of (48) and are 0.785, 0.58 and 0.475 times the yield stress for b/t=40, 60 and 80 respectively. These are plotted on the figure at $\epsilon_x'=1$, and also give good

agreement.

The elastic model can be improved by making use of the previously described maximum strength models, to stretch the stress-strain curve produced by the elastic model in the vertical direction, so that the maximum stress agrees with the maximum strength model. This scaling should be applied to the basic elastic stress-strain curve and not to the residual stress modification, since the residual stress must remain at its specified value in the scaled stress-strain curve. If σ_1 is the elastic stress at $\epsilon_x'=1$ (ignoring residual stresses) and σ_2 is the elastic effective width at $\epsilon_x'=2$, then the scaling factor, ρ, say, is given by:

$$\rho = \left\{ \begin{array}{lll} \dfrac{\sigma_{xu} + \sigma_r}{\sigma_1} ; & \text{if} & \dfrac{\sigma_{xu}}{\sigma_{xu} + \sigma_r} \geq \dfrac{\sigma_2}{\sigma_1} \\ \dfrac{\sigma_{xu}}{\sigma_2} ; & \text{if} & \dfrac{\sigma_{xu}}{\sigma_{xu} + \sigma_r} < \dfrac{\sigma_2}{\sigma_1} \end{array} \right\} \quad \ldots 3.11$$

The stress on the loading part of the stress-strain curve at which the tangent modulus is suddenly reduced due to residual stresses, is therefore:

$$\sigma_i = \sigma_1 - \frac{\sigma_r}{\rho} \quad \ldots 3.12$$

and the non-dimensionalised strain at which this occurs, denoted by ϵ_i', is found by following the stress-strain curve until $\bar{\sigma}_x=\sigma_i$. The stress at yield strain, taking into account residual stresses, which we may denote as $\sigma_{1(r)}$ is given by:

$$\sigma_{1(r)} = \rho \left[\frac{(1 - \epsilon_i')}{(2 - \epsilon_i')} (\sigma_2 - \sigma_i) + \sigma_i \right] \quad \ldots 3.13$$

This process has involved using the maximum strength design curve to empiricize a simple elastic stress-strain model, and then to use this elastic model to find the stress at yield strain. Considering again figure 3.24 it is clear that ρ for the three cases shown will not vary greatly from unity since the un-empiricized elastic model, with the described modifications for residual stress, already agrees very well with the data.

The elastic model with the appropriate slight, average and severe w_0 and σ_r levels can be used with the maximum strength design models of equations 3.3 and 3.10 to calculate the compressive resistance at yield strain of square plates with the three imperfection levels. These yield strain compression curves are plotted against slenderness on figure 3.25 (as broken lines) where they can be seen to have plateaus at various stresses less than yield. Consideration of an un-buckling plate will show that, if residual stresses exist, the average stress at yield strain will always be less than the yield stress. As a result the yield strain resistance curves of figure 3.25 will be truncated by a stress, σ_m, which depends on the magnitude of the residual stress,

and (for rectangular stress blocks) is given by:

$$\sigma_m' = \frac{1}{1 + \sigma_r'} \quad \ldots 3.14$$

This gives maximum values of strength for the 3 residual stress levels of σ_m'=0.715, 0.833 and 0.952, which agree with the plateaus on the figure. It can be seen, therefore, that one implication of the yield strain limit is that a plate with residual stresses can never be said to be fully effective (at yield strain), however stocky the plate is, since the stress at yield strain will always be less than the yield stress by an amount which depends on the level of residual stress in the plate. It is for consideration whether this restriction on the effective-ness of panels normally considered to be fully effective, should be relaxed, perhaps on the grounds of the enhanced stability of such stocky plates, but it will be assumed in the remainder of this thesis that the restriction on yield strain resistance given by equation 3.14 should be taken into account, in order for its implications to be clearly demonstrated.

Also shown on figure 3.25 are the compression resistances at ϵ_x'=1 interpolated from the curves of (47). It can be seen that these numerical data points agree very well with the elastically derived adjustments to the maximum strength models. This agreement gives some confidence in using equation 3.13 to produce an estimate of the resistance at yield strain. However, it is not really practical for design use to require the buckling displacement, given by k, to be incremented in order to find the design resistance. Simple inverse polynomial curve fits have therefore been calculated which more closely fit the three sets of data, but using their relationship to the elastically adjusted curves to extend the range of the curve fit. These turn out to be:

$$\left.\begin{aligned}
\frac{\sigma_{xu}}{\sigma_0}\ (\text{slight}) &= 0.17 + \frac{1.48}{\beta} - \frac{0.73}{\beta^2} + \frac{0.14}{\beta^3} < 0.952 \\
\frac{\sigma_{xu}}{\sigma_0}\ (\text{average}) &= 0.08 + \frac{1.21}{\beta} - \frac{0.40}{\beta^2} + \frac{0.05}{\beta^3} < 0.833 \\
\frac{\sigma_{xu}}{\sigma_0}\ (\text{severe}) &= 0.08 + \frac{0.78}{\beta} - \frac{0.22}{\beta^2} + \frac{0.05}{\beta^3} < 0.715
\end{aligned}\right\} \quad \ldots 3.15$$

These functions are plotted as solid lines on figure 3.25.

The square plate curves of equations 3.15 can be used with the strut curves of equations 3.5 and 3.6 (or of equation 3.7 for "average" plates) to find transverse strengths at ϵ_y'=1 of rectangular plates, even though the strut curve makes no reference to strain limits. When this is carried out for 3:1 plates with b/t=40, 60 and 80, with "average" imperfections, it gives values of 0.43, 0.28 and 0.21 respectively, which agree very well with the corresponding values interpolated from

the numerical results, which are 0.45, 0.28 and 0.215. It is suggested, therefore, that the strut curves given previously, by equations 3.5 and 3.6, or 3.7, be used with the strain limit square plate strengths given by equations 3.15 to calculate the transverse compressive resistances (at $\epsilon_y'=1$) of rectangular plates, in accordance with equation 3.4.

These transverse compressive resistances (at $\epsilon_y'=1$) have been calculated for square, 3:1 and 10:1 plates, and are plotted against slenderness in figure 3.26. The proposed model is compared, on the figure, with the design models of (24) and (63). The latter model gives a compression capacity equal to the critical buckling stress, unless it is above 50% of yield, in which case the design strength is reduced below the critical stress by a function which rounds off the shoulder between the critical buckling curve and the yield plateau. It is clear from the figure that there is a wide divergence in the transverse compressive strengths predicted by existing design models, and that for different aspect ratios and slendernesses the existing models may be significantly conservative or non-conservative relative to the proposed yield strain model.

Having developed design models for uniaxial compression, the treatment of biaxial compression will now be described in the next chapter.

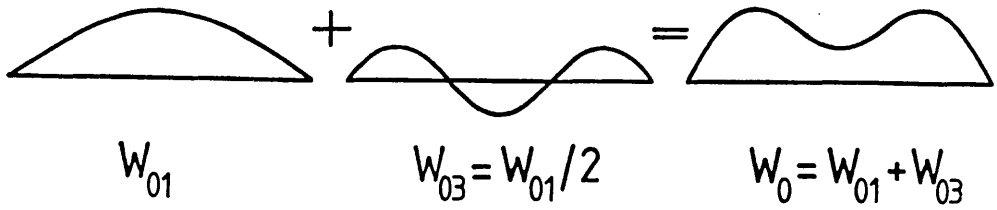

FIGURE 3.1 - Imperfection mode for 3:1 plates

FABRICATION TOLERANCES FOR PLATE PANELS

MODE OF DEFORMATION	TOLERANCE
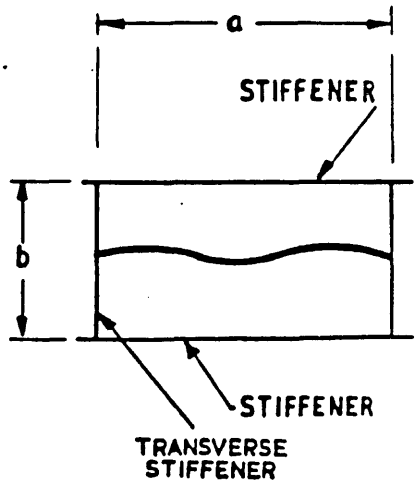	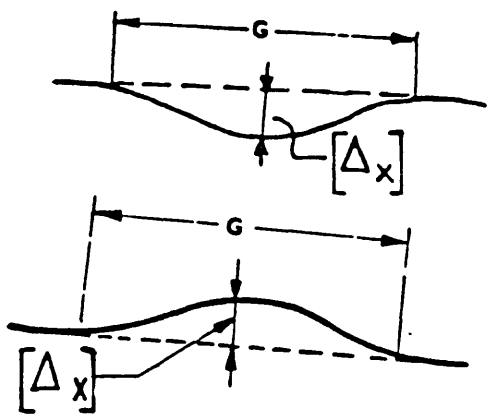

$$[\Delta_x] = \frac{G}{30t}\left(1 + \frac{b}{5000}\right) \text{ mm FOR } t < 25\text{mm}$$

$$\text{or } [\Delta_x] = \frac{G}{750}\left(1 + \frac{b}{5000}\right) \text{ mm FOR } t \geq 25\text{ mm}$$

but in no case less than 1·0mm in flange and diaphragm panels and in unrestrained web panels in compression; and not less than 3·0mm in other web panels.

TOLERANCE GAUGE LENGTHS

The following gauge lengths are to be used in determining the imperfections in plate panels and stiffeners:

Plate Panels:

For $[\Delta_x]$ use G = 2b, for long panels where a > 3b (Figure A23.1) and G = a, for wide panels where a < 3b (Figure A23.2).

where a = The length of the longer side of a plate panel,

b = The length of the shorter side of a plate panel,

FIGURE 3.2 - Gauge length recommendations from Table 23.1 of ref.(81)

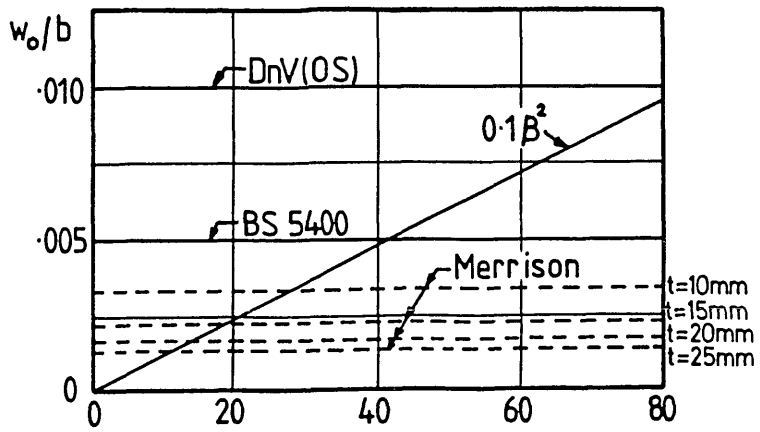

FIGURE 3.3 - Various imperfection specifications - b/t<80

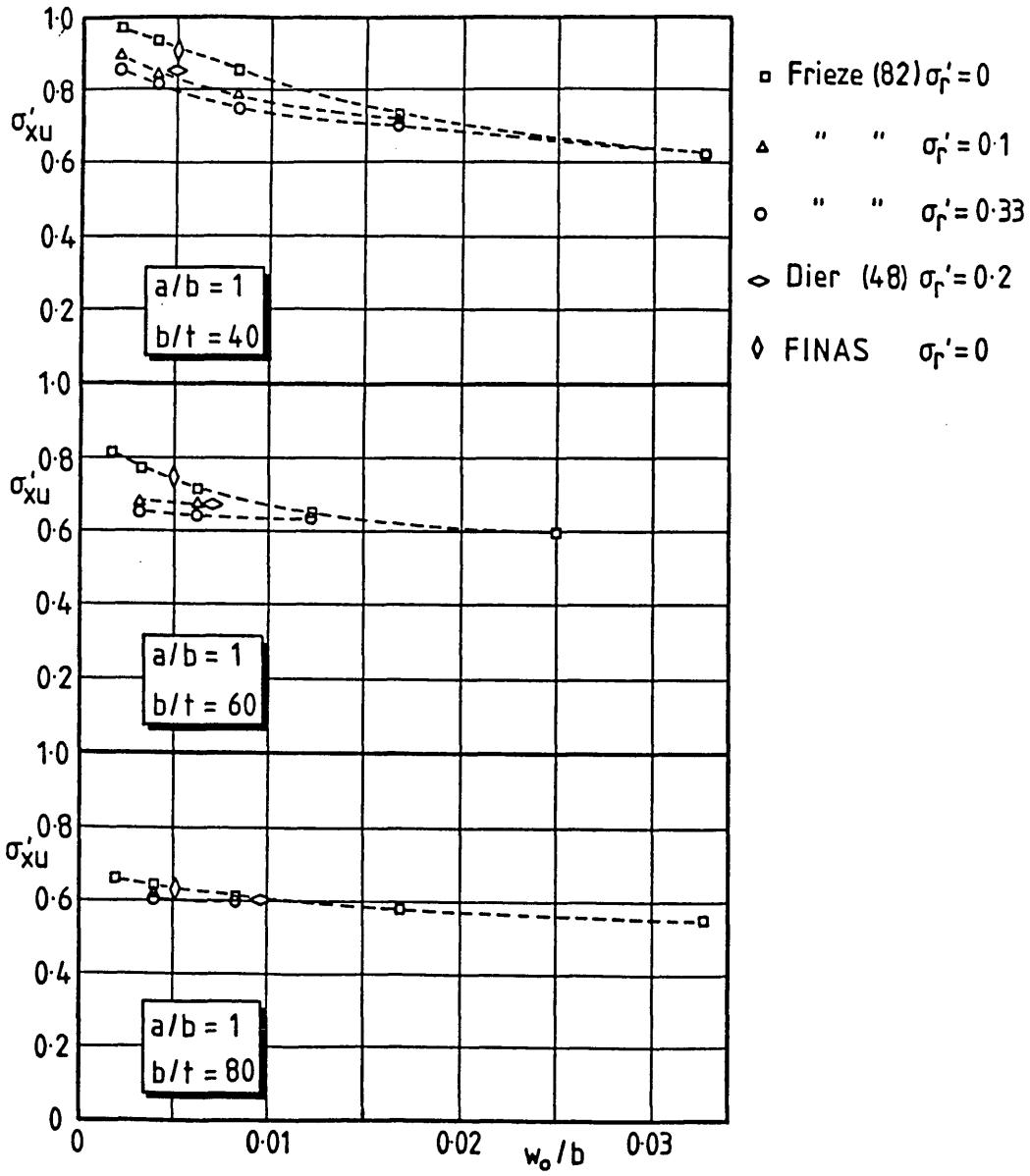

FIGURE 3.4 - Compressive strength for various w_0 and σ_r - from ref.(82)

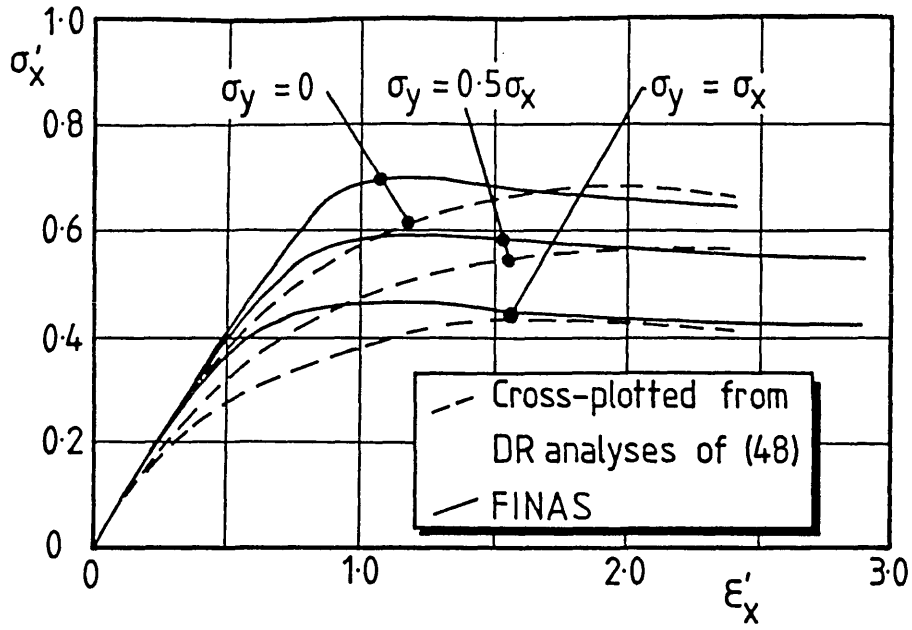

FIGURE 3.5 - Comparison between cross-plotted stress-strain curves and proportionally stressed stress-strain curves from FINAS a/b=1, b/t=60

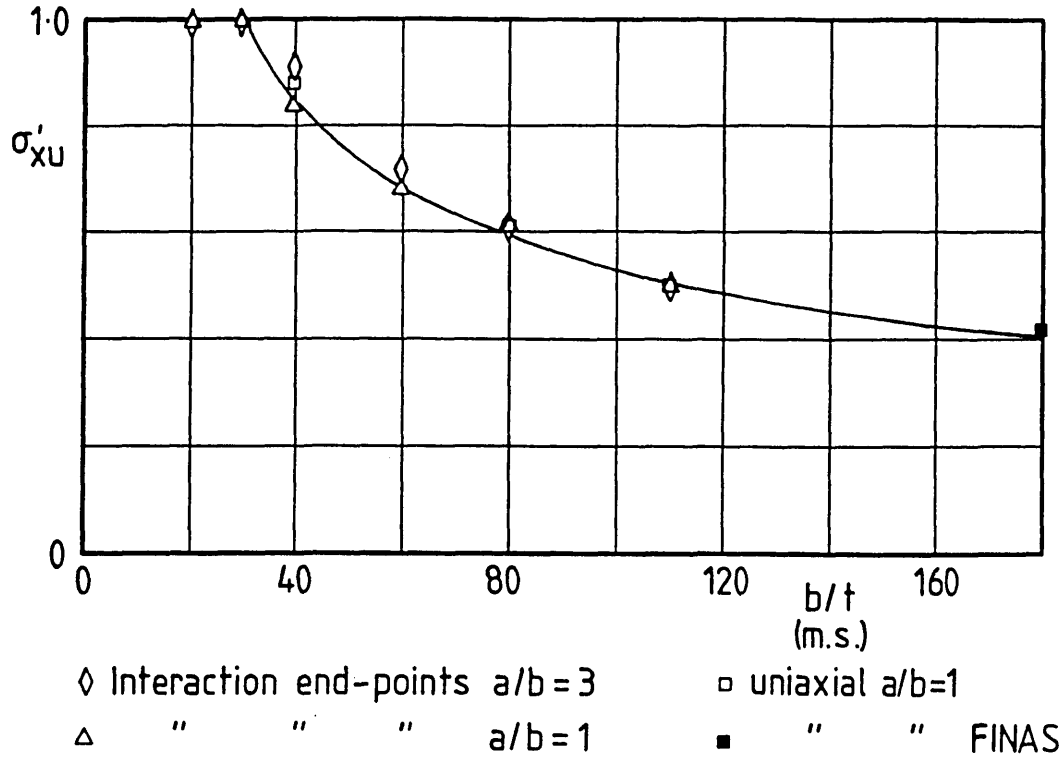

FIGURE 3.6 - Longitudinal compression numerical data compared to eq.3.3

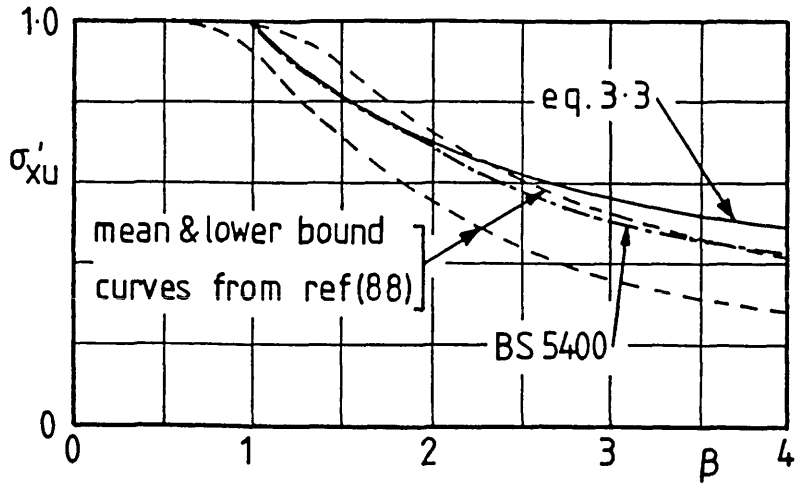

FIGURE 3.7 - Equation 3.3 compared to BS 5400 and experimental curves

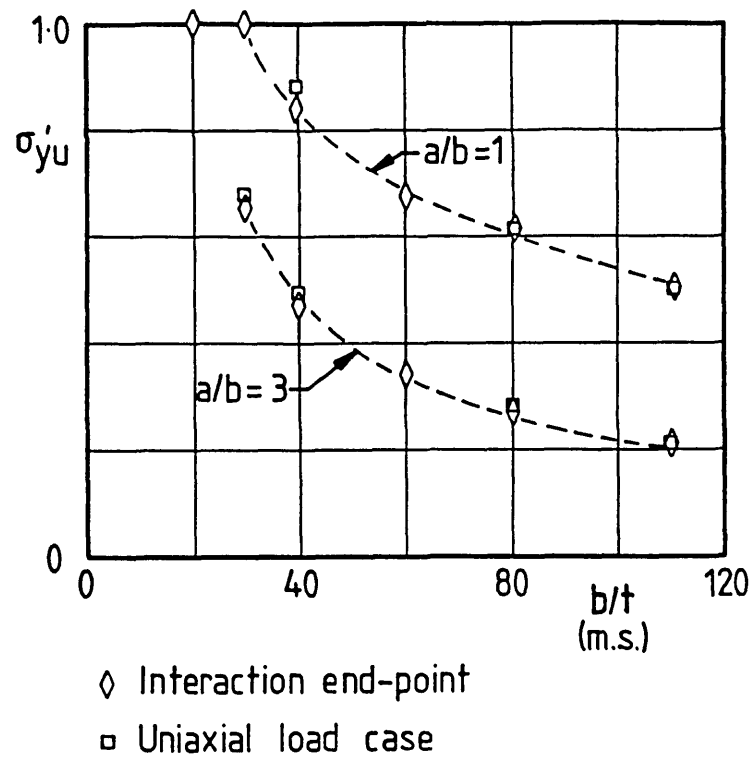

FIGURE 3.8 - Comparison between uniaxial compression analyses and interaction end-points - a/b=1 & 3

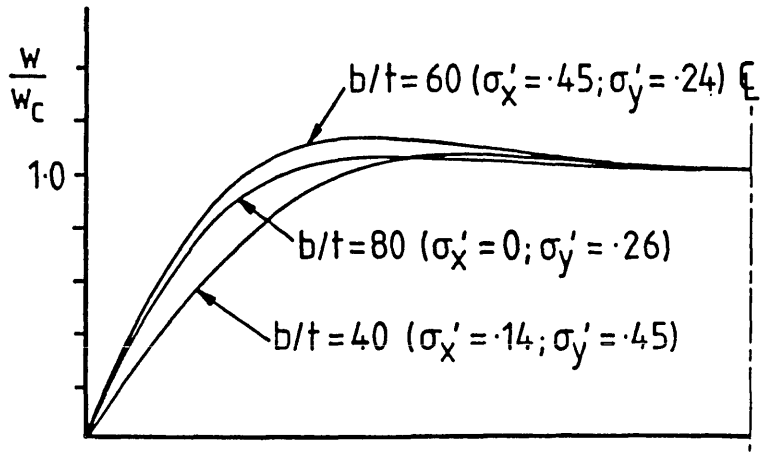

FIGURE 3.9 - Buckling mode profiles at peak load from proportional strain load cases in 3:1 plates

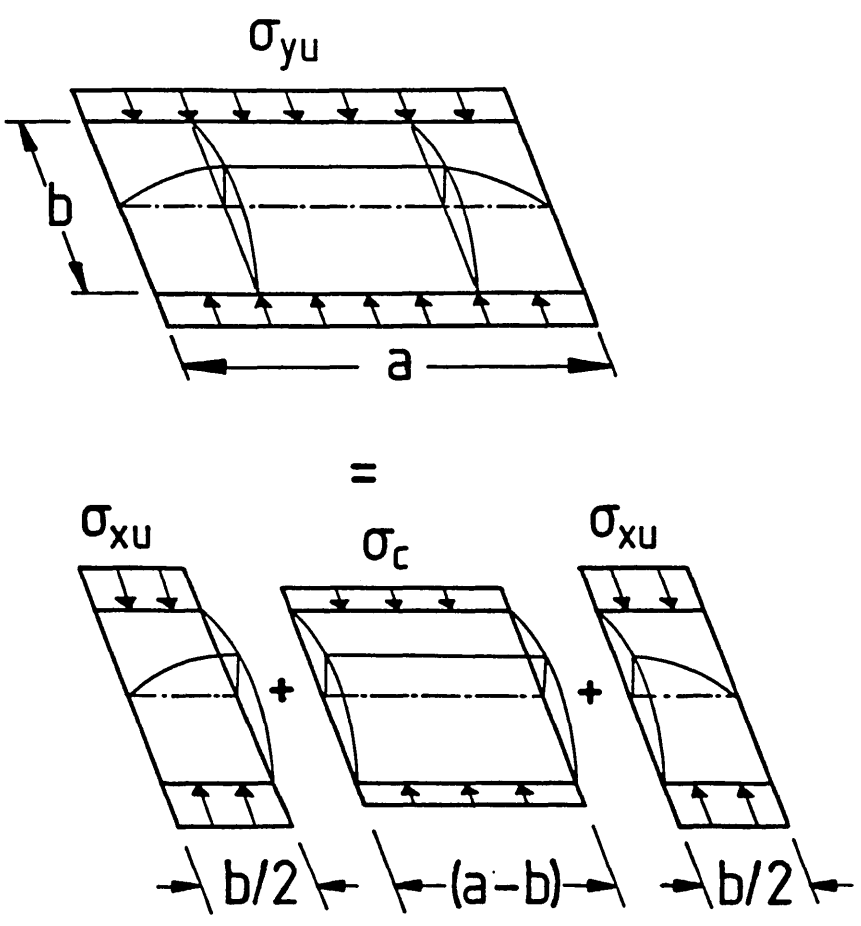

FIGURE 3.10 - Conceptual model for transverse strength for a/b>1

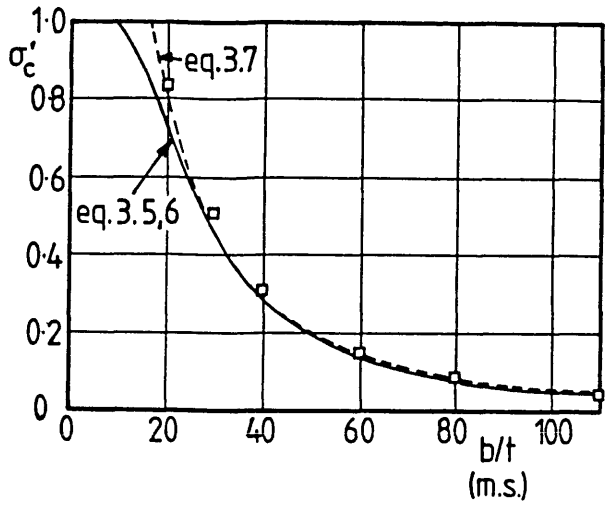

FIGURE 3.11 - Proposed strut design curves compared to numerical data

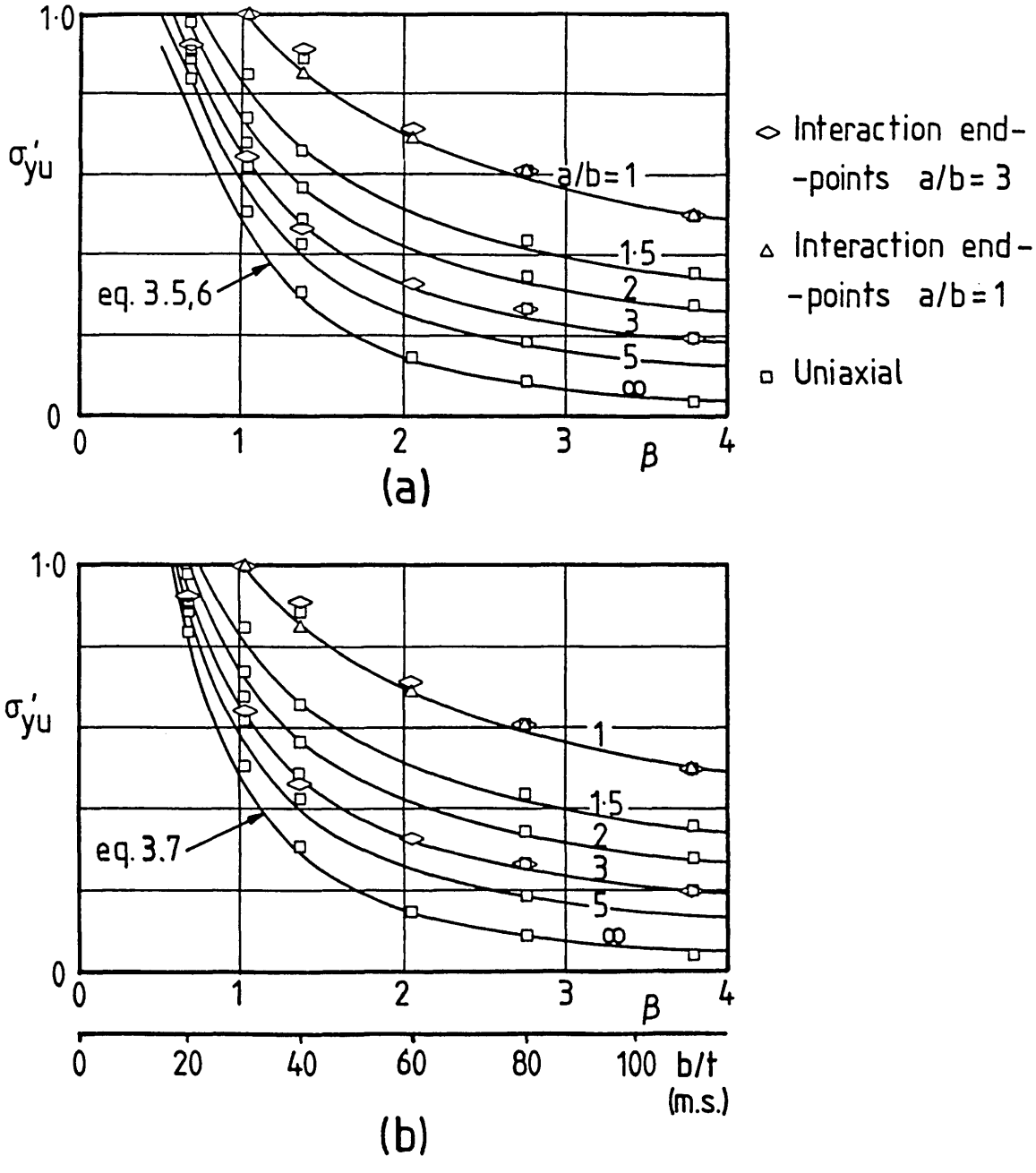

FIGURE 3.12 - Design model for transverse strength cf numerical data

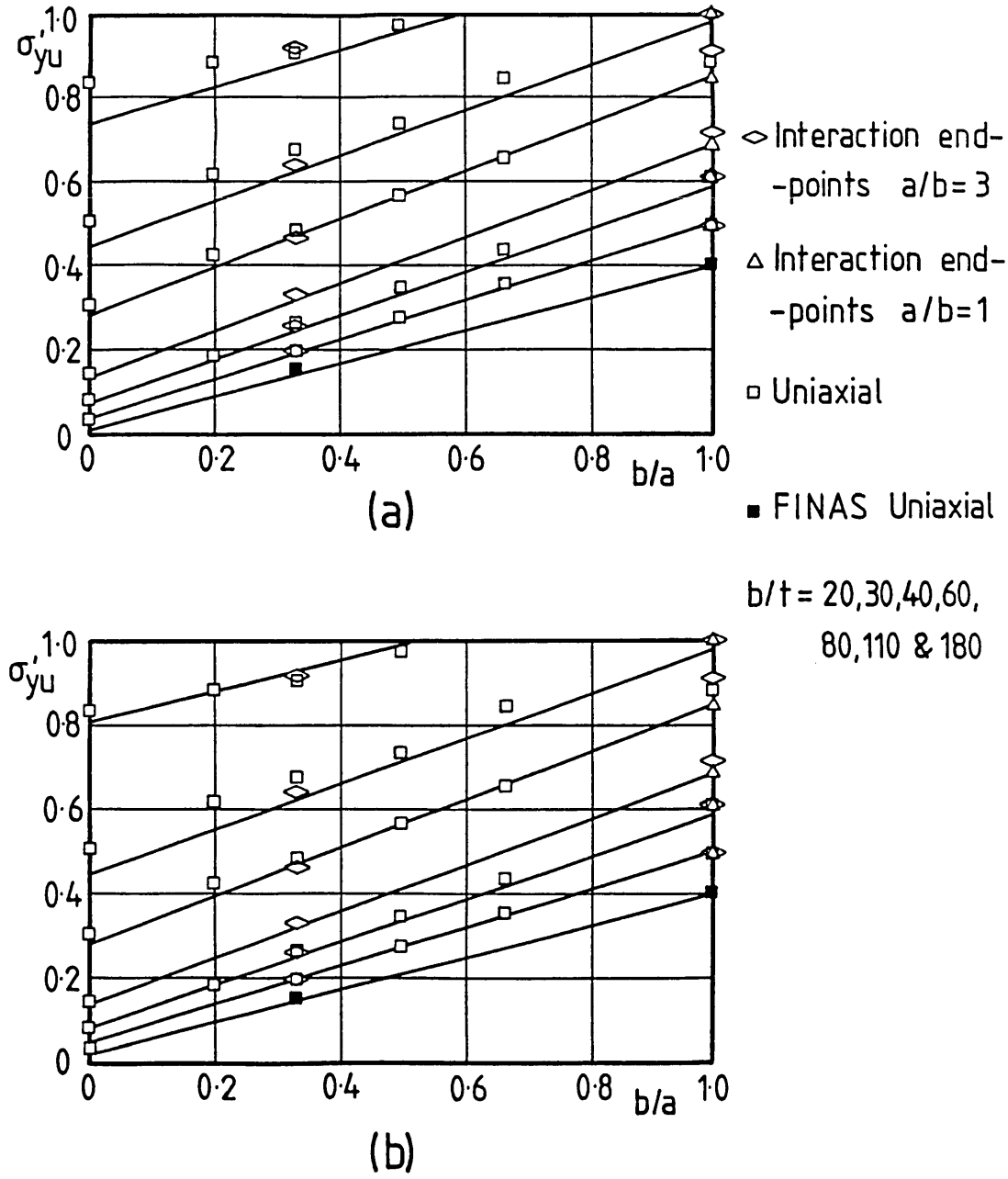

FIGURE 3.13 - Design model for transverse strength cf. numerical data

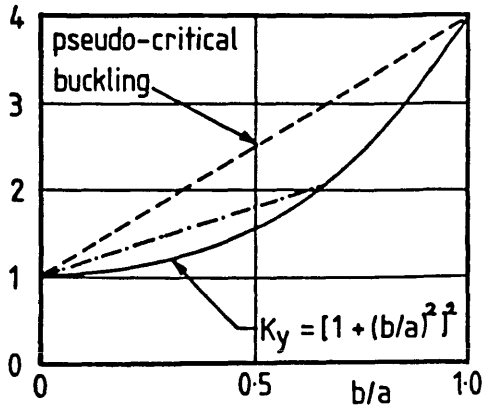

Critical & pseudo-critical buckling for transverse compression

FIGURE 3.14

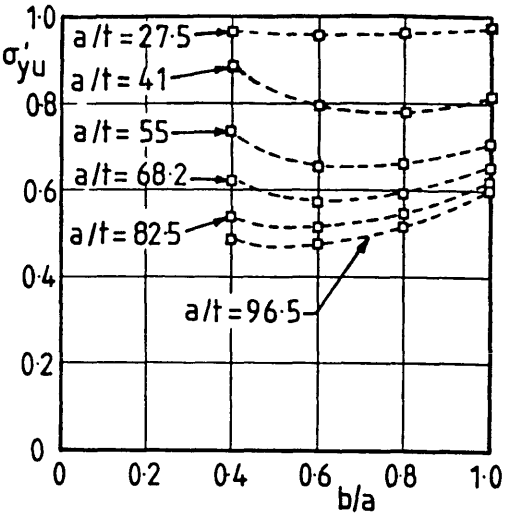

Compressive strength of short plates from reference (93)

FIGURE 3.15

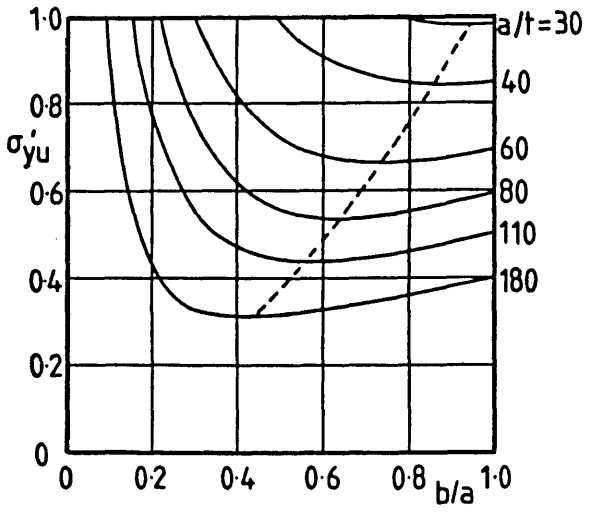

Compressive strength of short plates from proposed design model

FIGURE 3.16

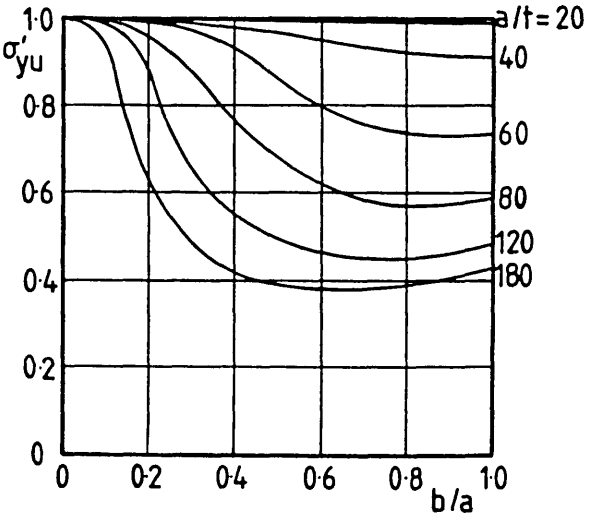

Compressive strength of short plates from elastic analysis with mid-length edge yield criterion

FIGURE 3.17

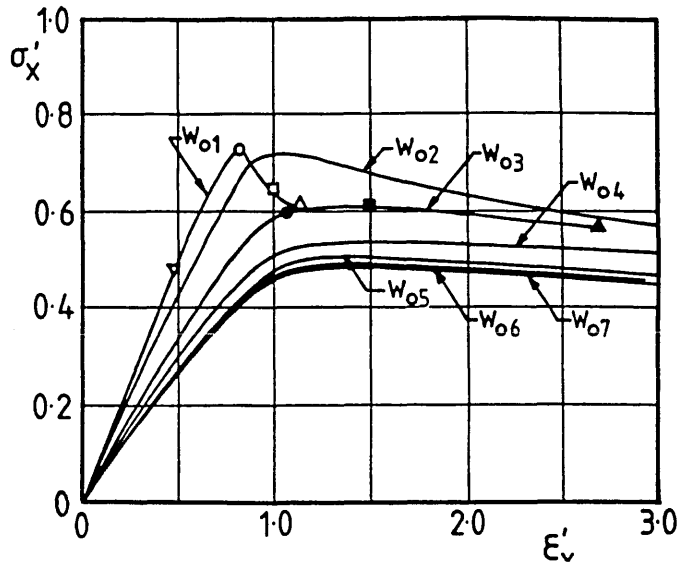

FIGURE 3.18 - Compressive stress-strain curves for a/b=3, b/t=80 with various modes of imperfection

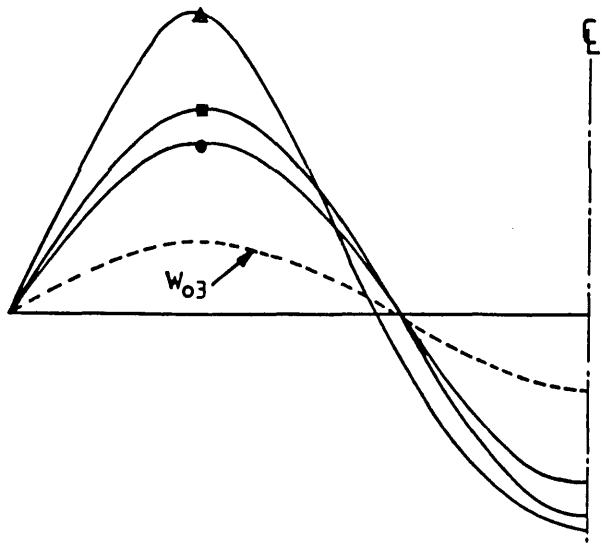

FIGURE 3.19 - Total out-of-plane displacement for w_{03} from fig.3.18

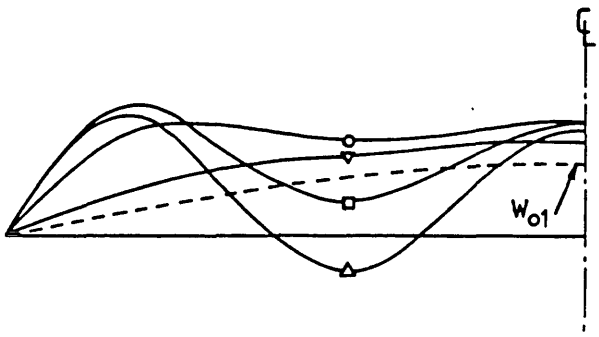

FIGURE 3.20 - Total out-of-plane displacement for w_{01} from fig.3.18

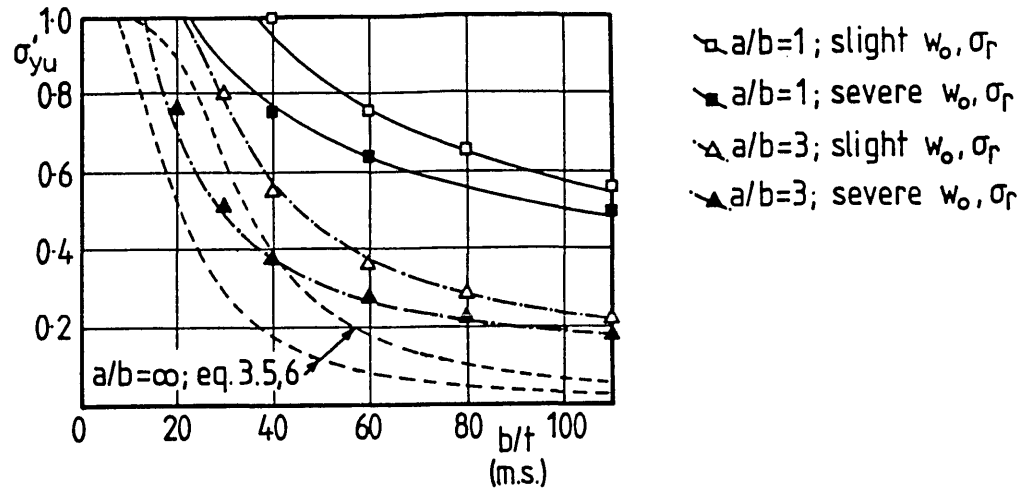

FIGURE 3.21 - Transverse compressive strength data for square and 3:1 plates with "slight" and "severe" imperfections - compared to model based on eq.3.10

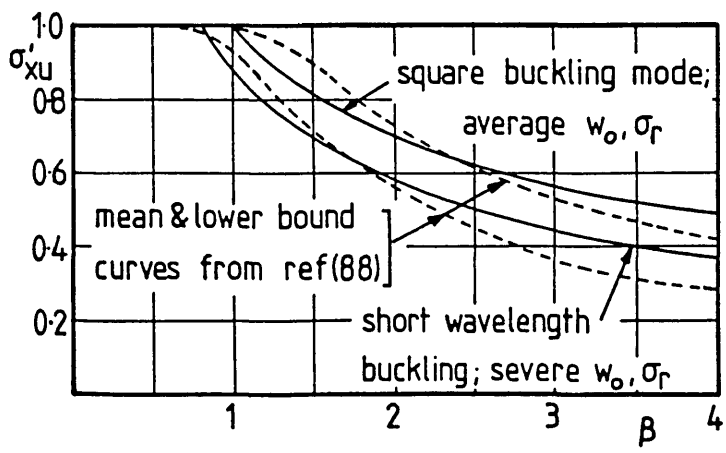

FIGURE 3.22 - Experimental mean and lower-bound curves from (88) - compared to proposed model

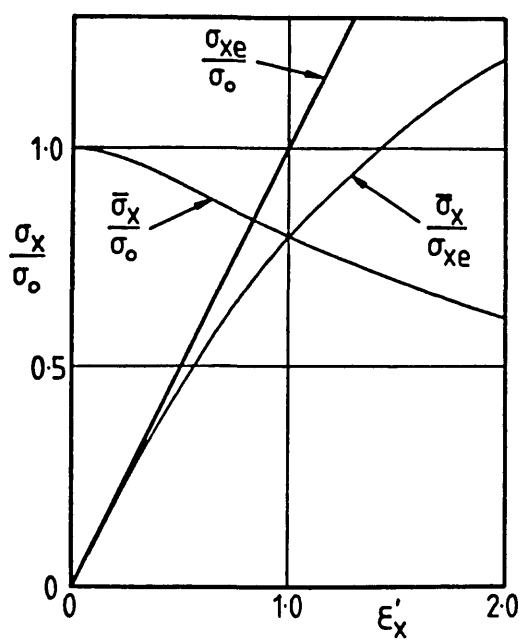

FIGURE 3.23 - Constituents of stress-strain modelling

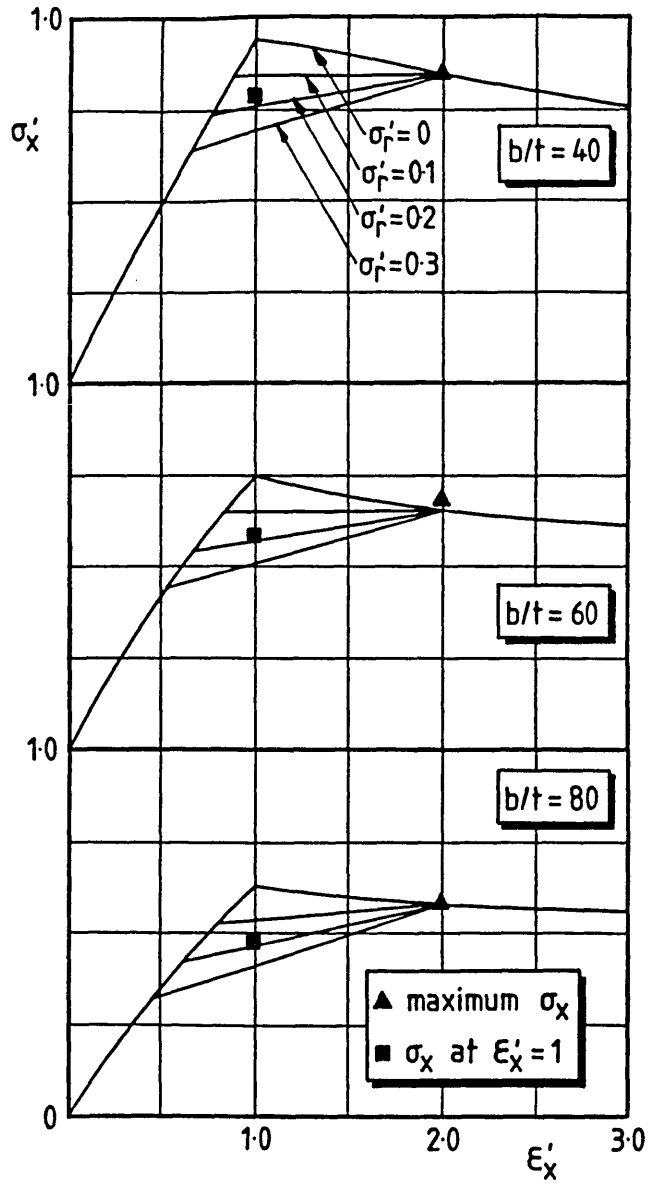

FIGURE 3.24 – Elastically–derived stress–strain curves for a/b=1 $w_0/t=0.1\beta^2$ – compared to data from (48) for $\sigma_r'=0.2$

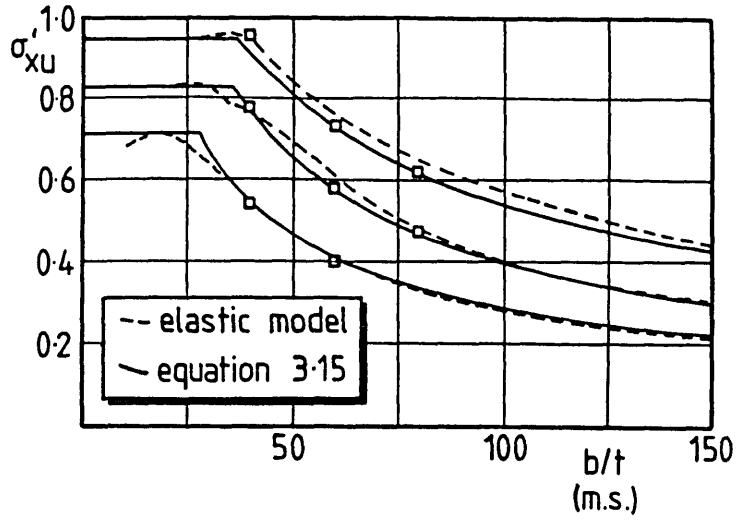

FIGURE 3.25 – Uniaxial longitudinal compressive resistance at $\epsilon_x/\epsilon_0=1$ ($w_0/t=0.025\beta^2$, $0.1\beta^2$, $0.3\ \beta^2$; $\sigma_r'=0.05$, 0.2, 0.4)

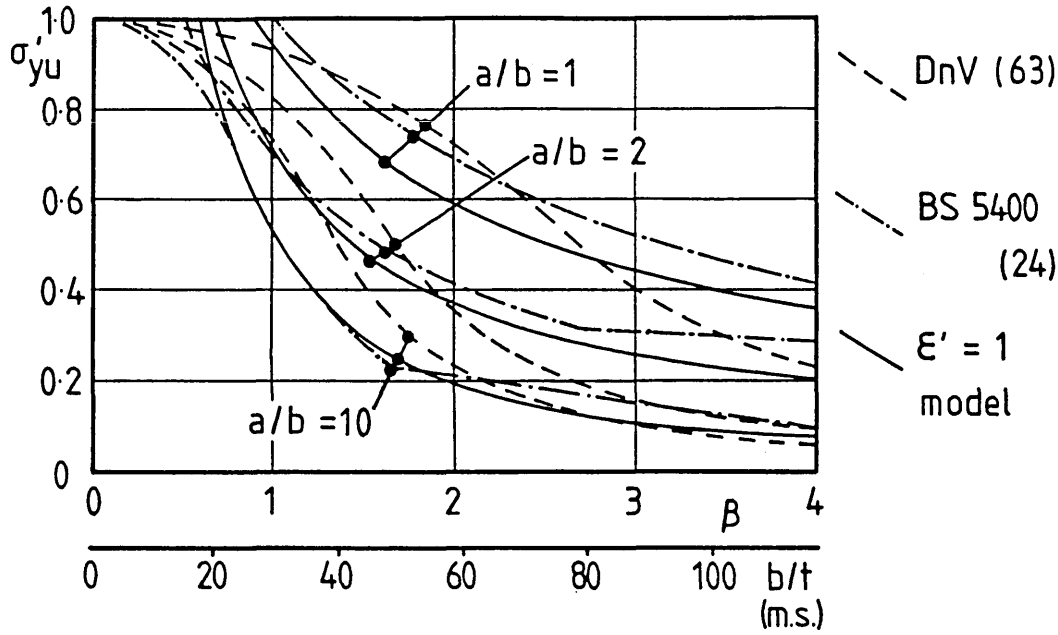

FIGURE 3.26 - Comparison between yield strain model for "average" imperfections, and design models from (24) and (63) for transverse compression - a/b=1, 2 and 10

CHAPTER 4 BIAXIAL COMPRESSION

4.1 Critical Buckling

In this chapter, the uniaxial models of the previous chapter will be used in the development of a design model for biaxial compression applied to rectangular constrained plates. Before developing this model, some of the concepts that will be used can be introduced using critical buckling as the basis.

Figure 4.1 shows the biaxial compression linear buckling interactions for square and 3:1 plates, which are plotted in terms of the non-dimensional critical buckling coefficients, k_x and k_y. For rectangular plates the interaction is made up of the inner envelope of intersecting interactions for different modes of buckling. On the figure the net interaction formed by this inner envelope is shown as solid lines and the remainder of the interactions as dashed lines.

In figure 4.2, the net interactions are re-plotted in dimensions of stress for square and 3:1 plates of various slendernesses, the interactions being drawn in conjunction with the Von Mises yield ellipse.

The uniaxial compressive strength formulation of equation 3.3 is truncated by the yield stress in the low slenderness region. Although the calculated compressive strengths in this region which are greater than the yield stress have no physical validity as uniaxial strengths, nor any numerical basis, they may be useful as the imaginary end-points of strength interactions which are only partially within the Von Mises ellipse. To illustrate this, figure 4.3 scales the critical buckling interactions of figure 4.2 to end at the longitudinal and transverse strengths predicted by equations 3.3 and 3.4 for b/t=20, 40 and 60, whether or not these strengths are less than the yield stress.

The elasto-plastic finite difference analyses of (47) - (49) have already been described in Chapter 3, in the context of uniaxial compression. Much of the uni-axial compression data produced in (49) was as part of biaxial compression studies, presented as a wide range of interaction curves mainly for square and 3:1 plates. These interactions were produced as the outer envelopes to σ_x-σ_y trajectories for proportionally strained panels, and therefore represent the maximum biaxial stresses sustained by proportionally stressed panels. The interactions are reproduced here as figure 4.4. An additional square plate curve has been added, this being the result of FINAS analyses of a b/t=180 plate. These FINAS anaylses did not include

residual stress but at this slenderness residual stress does not have a significant effect on the maximum resistance of the panel.

For both square and 3:1 plates, the biaxial strength interactions for the stockiest plates are truncated by the Von Mises ellipse, as was the case for the critical stress curves discussed above.

Figure 4.5 shows the interaction at yield strain for a 3:1 plate with b/t=60, in more detail, and the plate buckling modes at different points on the interaction are indicated. It can be seen that the strength interactions are similar to the critical interactions in being composed of the inner envelope of intersecting interactions for different modes. The more horizontal part of the interaction corresponds to an m=1 mode. Just as for critical stress interactions, this mode presists, not only for predominantly transverse compression, but even for cases with more longitudinal compression than transverse. Only when the longitudinal compression is greater than about 4.6 times the transverse compression, in the steep part of the interaction curve, does the longitudinal buckling mode, m=3, persist. In the case of critical stresses, the m=3 mode is preferred over the m=1 mode when σ_x is greater than 3.5 times σ_y. The intermediate m=2 mode was precluded by the numerical analysis.

The above observations will be incorporated in the design model which will be proposed in this chapter. The development begins with a consideration of square plates.

4.2 Square Plates

When discussing biaxial compression interactions it will be useful to adopt the terminology of convexity and concavity of interaction shapes. An interaction which lies outside a straight line drawn between its uni-axial compression end-points will be termed convex; that is, the safe design space defined by the interaction has a convex boundary (as viewed from outside the interaction). Similarily, an interaction which lies within the straight line drawn between its end-points will be defined as a concave interaction.

Given this terminology, the square plate critical buckling interaction of figure 4.1, being a straight line, is neither concave nor convex, whereas the strength interactions of figure 4.4 are all convex. It is also clear from figure 4.4 that the convexity of the strength interactions reduces as the slenderness increases, in a manner which suggests that the straight line of the critical interaction could be a lower bound.

However, solutions for panels more slender than b/t=180 have not been found.

A well established expression for the biaxial compressive strength interaction for square plates (for instance in (46) - (49)), which can give a continuous series of convex and concave curve shapes including the straight line and the Von Mises ellipse, is:

$$\left[\frac{\sigma_x}{\sigma_u}\right]^2 + \eta\left[\frac{\sigma_x}{\sigma_u}\right]\left[\frac{\sigma_y}{\sigma_u}\right] + \left[\frac{\sigma_y}{\sigma_u}\right]^2 = 1 \qquad \ldots 4.1$$

Where σ_u is the uniaxial compression end-point of the interaction. The convexity of the interaction curve is varied by changing the coefficient η, on the cross-product term of the equation. For instance, a value of η=2 will give a straight line, η=0 will give a circle, and η=-1 will give the Von Mises ellipse.

In (46) η was defined to vary with slenderness so that the interaction shape changed from a straight line at infinite slenderness to slightly greater than the Von Mises ellipse at zero slenderness. At the same time, the end-points of the interactions did not exceed the yield stress at low slenderness.

The model proposed in (49) takes a quite different approach in which η is kept at a constant value of 0.45 (so giving a constant shape of interaction) but in which the end-points of the interaction are allowed to be greater than the yield stress. When the end-points are greater than the yield stress, the net interaction is produced by intersecting the curve given by equation 4.1 with the Von Mises ellipse. No guidance was given, however, on what the values of the end-points should be when they exceed σ_0.

The same authors adopted a different approach in the earlier report (48) where they were primarily concerned with the changing biaxial interaction as pressure is applied and were considering a smaller range of slendernesses (b/t = 40, 60 and 80). The model proposed therein allowed the interaction shape to change by employing a quadratic function of slenderness to define η for square plates (and by defining discrete values of η for the three slendernesses for 3:1 plates). The proposed uniaxial strength model allowed the end-points to exceed the yield stress.

All three existing definitions of η (for square plates) are compared on figure 4.6 with η values deduced from the numerical data. The η values from the numerical data are deduced from the uniaxial and equal biaxial strengths, and where the interaction curves are only partially within the Von Mises ellipse two values of η are deduced from the data. The first, which is directly relevant to (46), would be used to define

an interaction whose end-point would never be greater than the yield stress, and can be deduced from the relationship between the equal biaxial stress and the yield stress. The second value of η is appropriate to an interaction shape which had uniaxial compression end-points greater than yield and which would be intersected by the Von Mises ellipse, as in the models of (47) - (49). This value of η is found by simultaneous solution of equation 4.1 on the 45 degree line and at the point at which the interaction meets the Von Mises ellipse.

The quadratic variation in η of (48) is seen to be inappropriate for slendernesses outside the b/t=40 to 80 range for which it was derived, and this will presumably have prompted the later suggestion of the same authors to maintain η constant when the wider range of data had become available.

The approach suggested here, is first to define the biaxial strength, σ_b, of a square plate with equal σ_x and σ_y, as a function of slenderness. This is done in a similar empirical fashion to that used for uniaxial strength, by measuring the values of the interaction curves on the $\sigma_x=\sigma_y$ line and plotting them against slenderness in figure 4.7.

An inverse polynomial fit is obtained of a similar form to equation 3.3 (but without a constant term, which is not needed in this case):

$$\frac{\sigma_b}{\sigma_0} = \frac{1.27}{\beta} - \frac{0.89}{\beta^2} + \frac{0.30}{\beta^3} \qquad \ldots 4.2$$

but σ_b is not allowed to be less than 0.5 σ_{xu} (defined in equation 3.3). This restriction is to ensure that the interaction produced is never concave, within the valid range of slendernesses (b/t$\leq$180 for mild steel, $\beta\leq$6.22).

If an interaction of the form of eqn 4.1 is adopted, then η can be defined in terms of the uniaxial and biaxial strength models, as it was when deducing the values of η from the numerical curves for figure 4.6.

$$\eta = \left[\frac{\sigma_u}{\sigma_b} \right]^2 - 2 \qquad \ldots 4.3$$

Interaction curves produced by equations 3.3, 4.1 (setting σ_u to σ_{xu} from equation 3.3), 4.2 and 4.3 are presented in figure 4.8, where they are compared with the elasto-plastic curves of (49).

The variation of η with slenderness given by equations 3.3, 4.2 and 4.3 is compared with the previous models in figure 4.6.

4.3 Rectangular Plates

In Chapter 3, the non-affinity of the assumed imperfection in (47) - (49) was discussed. This non-affinity was particularly with respect to the buckling mode for longitudinal compression, and it was shown to give higher longitudinal compressive strengths in 3:1 plates than would occur if the imperfection had the form of three half sine waves. It was explained why the writer favours the use of affine imperfection assumptions.

A 3:1 plate with only the three half sine wave imperfection mode (w_{03}), buckling in the same mode due to longitudinal compression, can be expected to respond to moderate amounts of coexistent transverse compression in the same manner as would a square plate. This suggests that the effect of the non-affine imperfection mode on the rectangular plate interactions of figure 4.4 can be eliminated by using the square plate interaction curves to represent that part of the interaction appropriate to the 3:1 plate buckling in the m=3 mode. Figure 4.9 shows the 3:1 plate interactions modified in this way. This modification will be used in the rest of this chapter.

An important difference between the shapes of the strength interactions for square and rectangular plates is that rectangular plate interactions are asymmetric. However, if the strength interactions for 3:1 plates are non-dimensionalised (so that they end at unity at their ends), the asymmetry is reduced to some extent, as observed in (46) and (49). This is shown in figure 4.10.

Also on this figure is the critical interaction non-dimensionalised in the same way as the strength curves. It should be noted that, whereas for square plates the form of the critical interaction was a lower bound to the strength interaction curves (for the range of slendernesses analyzed), this does not apply to rectangular plates.

The reduction in asymmetry which is evident from figure 4.10 was used in (49) to justify the proposal that equation 4.1 should be used as an interaction function for rectangular plates, even though that equation is symmetric. The qualification was made that η should be adjusted to make the symmetric function safe, but no specific guidance was given on what η should be.

In (46), on the other hand, the asymmetry of 3:1 plate interactions was explicitly modelled by changing the exponent on the σ_x stress term to unity, and using a constant value of η equal to -0.25. This produces a parabolic shape of interaction which is invariant with slenderness. This model is shown as a chain line on figure 4.10. For plate aspect ratios between square and 3:1 an interpolation procedure was

proposed. DnV (63) and BS5400 (24), on the other hand, specify a circular interaction curve, which is shown as a broken line on figure 4.10.

Although the critical buckling interaction for the 3:1 plate also has an asymmetric shape, this asymmetry arises from the intersection of interactions which (being straight lines) are themselves symmetric when non-dimensionalised to their respective end-points. The asymmetry of the critical buckling interaction arises, therefore, due to changes in buckling mode. This suggests an approach to the interaction modelling which may be more promising than the previous approaches.

If the strength interaction can be produced for a rectangular plate deforming in only one mode, whether or not that would be the preferred mode at all points on the interaction, then, since every point on the interaction is for the same mode, it seems reasonable to expect its non-dimensionalised form to be much more symmetric than the preferred net interaction. The uni-axial model of chapter 3 can be used to predict both longitudinal and transverse compression end-points for such an interaction, for any mode shape. There is good numerical support and conceptual basis for the transverse compression end-points, but much less so for longitudinal compression end-points, for buckling modes longer than square. Nonetheless, since the approach would require all the interactions for the various buckling modes to be intersected, these non-preferred longitudinal compression end-points will generally be well outside the net strength interaction that is produced, so inaccuracy in their values may not have a significant effect on the net interaction. Interactions defined by:

$$\left[\frac{\sigma_x}{\sigma_{xu}}\right]^2 + \eta\left[\frac{\sigma_x}{\sigma_{xu}}\right]\left[\frac{\sigma_y}{\sigma_{yu}}\right] + \left[\frac{\sigma_y}{\sigma_{yu}}\right]^2 = 1 \quad \ldots 4.4$$

are symmetric when non-dimensionalised, and can be applied to each of the modes with the appropriate values of σ_{xu} and σ_{yu} calculated from equations 3.3 to 3.7.

For the square buckling mode (for instance m=3 in a 3:1 plate) η has already been defined using the biaxial compression model in section 4.2. For the non-square modes which equation 4.4 needs to be applied to, it is reasonable to expect that the interactions will also be convex to a degree that depends on slenderness. A simple postulate, therefore, is to use the same value of η that is used for the square buckling mode. This postulate is compared with the curves of figure 4.9 in figure 4.11 where it is seen to give non-conservative interaction curves in the transverse compression region, especially for the slender plates.

None the less, the approach could be adjusted to make it work reasonably, by

modifying the value of η for the non-square modes. One simple change would be to assume that the η which is used for these modes is based not on b/t but on λ_b/t, where λ_b is the longer half wavelength of buckling mode. This amounts to calculating a value of η for a square plate whose slenderness is found by multiplying the actual plate slenderness by the aspect ratio of the buckling mode being considered. This approach is compared with the curves of figure 4.9 in figure 4.12. Clearly, the approach has some promise and, with refinement could be a significant improvement on existing methods.

However, a quite different model is proposed in this chapter. The proposal will have the advantage of being based on a conceptual model of the behaviour of the plate. Moreover the model will be readily extended to include lateral pressure in Chapter 6.

The basic principle of the model is simple to state. Just as transverse compressive strengths were obtained by partitioning the transversely loaded plate into end-regions which together made up a square plate with the remaining central portion acting as a transverse strut, so the separate biaxial interactions appropriate to these partitions should be amalgamated to produce their net effect on the plate. This approach is suggested by plate deformation modes which concentrate the double curvature deformation at the ends, with the remaining central portion deforming in a prismatic fashion, as idealised in figure 4.13. Interactions should be produced in this way for the sub-panel given by a half-wavelength of each of the possible modes, and their inner envelope used as the net interaction.

The biaxial interaction for the end-regions is the square plate interaction of section 4.2 (with η calculated from equation 4.3). The strut-like capacity of the central region, however, is unaffected by coincident longitudinal stresses, so that there is no interaction between the transverse stress in the central region and the longitudinal stress. This effect is also evident from the critical buckling interaction for infinitely long plates, for which the m=1 line is horizontal through the equivalent of the Euler load, at k_y=1. The trend to a horizontal m=1 line for infinitely long plates can be seen in the buckling interaction for 10:1 plates, for instance, which is shown in figure 4.14.

The interaction which is then applied to the half-square end-regions of the sub-panel is, therefore, given by:

$$\left[\frac{\sigma_x}{\sigma_{xu}}\right]^2 + \eta\left[\frac{\sigma_x}{\sigma_{xu}}\right]\left[\frac{\sigma_{y1}}{\sigma_{xu}}\right] + \left[\frac{\sigma_{y1}}{\sigma_{xu}}\right]^2 \leq 1.0 \qquad \ldots 4.5$$

where $\sigma_{y1} = \sigma_c + \alpha_b (\sigma_y - \sigma_c)$

σ_{xu} is from Chapter 3 (equation 3.3 for maximum resistance, for instance). It should be noted that the numerator σ_{y_1} in equation 4.5 is not the average applied transverse stress, but the local transverse stress, deduced from equilibrium, which is applied to the end-regions of the sub-panel, given the average applied transverse stress, σ_y, and the strut capacity, σ_c (from equations 3.5 to 3.7). It should also be noted that, whereas σ_{xu} and η will not vary with α_b, σ_{y_1} will. Consideration of equation 4.5 will show that the square plate interaction model of the previous section will result when α_b is set to unity.

The analysis is repeated for all possible values of the buckling mode aspect ratio, α_b (given by the buckle half-wavelength divided by the plate breadth b), between 1 and the plate aspect ratio, α, and the least value of σ_x determines the preferred mode. The value of 1 for α_b can only be applied, of course, if the plate aspect ratio is an integer.

The net interactions which result from this model are compared on figure 4.15 with the particular interactions presented in (47) - (49) for 2:1, 3:1 and 5:1 panels for which biaxial interactions have been produced in (47) - (49). The figure shows that the model corresponds very well with the interactions which result from numerical analysis. The square plate comparison included in this figure is the same as in figure 4.8, but it is repeated here for completeness.

A feature of the model, not apparent from figure 4.15, is that for any rectangular plate, whatever its aspect ratio or slenderness, all the component interaction curves for the various buckling modes intersect at the same point. For example, the interaction curves for a 5:1 plate with b/t=60, for modes from m=1 to m=5 are shown in figure 4.16. As can be seen, the net interaction is produced by the m=1 and m=5 modes only.

In (97) it was suggested that the intermediate (m=2) mode in 3:1 plates could, in fact, be ignored. This was based on elasto-plastic studies similar to those in (47) - (49). The effect of composite imperfection modes containing amounts of both w_{01} and w_{02} was compared to the effect of imperfection modes containing w_{01} and w_{03}. However, only a few slendernesses were analysed, and imperfection modes predominantly, or wholly, w_{02}, were not considered.

It has already been seen in figure 4.1 that the m=2 mode does contribute a small part to the critical stress interaction. It is possible to apply the plate partition basis of the above biaxial interaction model to the critical stresses, by amalgamating the

critical buckling interactions for the various regions of the plate, in the same way that the strength interactions were amalgamated in figures 4.15 and 4.16.

The critical interaction for the prismatic (strut-like) part of the plate is a constant k_y=1 for any k_x, and the critical interaction for the square plate that makes up the end regions is given in figure 4.1a. These are combined for a 3:1 plate in figure 4.17, where it can be seen that the interactions corresponding to the various buckling modes all intersect at the same point, in a similar way to the strength interactions. The same thing occurs if the calculation is repeated for other rectangular plate aspect ratios.

It is worth observing that, although the critical stress interaction was not a lower bound to the strength interactions, the interaction of figure 4.17, based on more realistic plate deformation profiles than the critical buckling modes, is much closer to a lower bound to the strength interactions.

Although the plate deformation profile implied by the biaxial interaction is a more realistic representation of the deformations of slender plates (at maximum load), it has already been pointed out in Chapter 3 that the assumed profile is less representative of the actual deformation profile of stocky plates which will tend more towards the sinusoidal critical buckling mode. Figure 4.18 shows the deformation profiles under uniaxial transverse compression of 3:1 plates of various slendernesses obtained from FINAS analyses. All the profiles are normalised to have the same central displacement on this diagram by plotting w/w_c (where w_c is the central displacement), and the sinusoidal critical buckling mode is also shown. It is clear that the critical buckling mode is reasonably representative of the deformation profiles of only the most stocky plates.

It is possible to use figure 4.18 to judge how much of the plate deforms in a doubly curved fashion, and how much in a prismatic fashion. The aspect ratios, α_p, of the doubly curved end regions are measured from figure 4.18, and plotted against slenderness in Figure 4.19.

The coefficient, α_p, had previously been assumed to be equal to unity, in deriving equation 4.5 and figure 4.15, but an alternative would be to define α_p as a function of slenderness, based on the data of figure 4.19. Such a function would be:

$$\alpha_p = \frac{2.5}{\beta} \quad ; \leq 1 \qquad \ldots 4.6$$

This function is plotted on figure 4.19 and agrees quite well with the inferred data

points.

It was shown in Chapter 3 that despite the variation in deformation profile with slenderness, the transverse strength model of equation 3.3 proved to be just as suitable for stocky plates as it was for slender plates. It was explained that the effect of a reduction in the proportion of the plate which acts as a strut could be balanced by the reduction in the transverse strength of the plate-like end regions when these are longer than square, and the linear trends in the numerical data presented in figure 3.13 provided some evidence for this to be occurring.

However, in the case of biaxial loading, the coexistent longitudinal compression will have an influence on a larger proportion of the rectangular plate if the end regions are longer than square than it would if the end-regions made up a square plate only, and this could have an influence on the biaxial compression interaction of the plate as a whole. As a result, although it is not proposed that equation 4.6 should change the way that the transverse strength is calculated, it is proposed that the biaxial interaction model take equation 4.6 into account. (In fact, since transverse uniaxial compression is only a special case of biaxial compression, equation 4.6 is, in principle, being applied to transverse compression also. However, since the transverse resistance of end regions which are longer than square, in accordance with α_p from equation 4.6, will itself be made up of the transverse resistance of square end regions with a strut like portion, then equation 4.6 makes no difference to the calculation of uniaxial transverse compression resistance. There is, therefore, no inconsistency between the assumptions of Chapter 3 and Chapter 4).

As a consequence of equation 4.6, the interaction curve which is applied to the end regions of the plate, when these end regions are longer than square (that is for $\beta<2.5$ - b/t<72 for mild steel), should have the same non-dimensionalised form as the biaxial interaction for the square plate with the same slenderness. That is, the same value of η should be used, but the interaction is re-scaled in the x and y directions to end at the σ_{xu} and σ_{yu} end-points appropriate to a plate of aspect ratio, α_p. This approach to the biaxial interactions for the doubly curved end regions is identical to the approach used for the whole plate in figure 4.11.

The strut buckling interaction (ie a strut buckling capacity unaffected by longitudinal loading) is the same as was used previously, but it is now applied to a smaller proportion of the plate. The interaction given by equation 4.5 now becomes, in this more sophisticated model:

$$\left[\frac{\sigma_x}{\sigma_{xu1}}\right]^2 + \eta\left[\frac{\sigma_x}{\sigma_{xu1}}\right]\left[\frac{\sigma_{y1}}{\sigma_{yu1}}\right] + \left[\frac{\sigma_{y1}}{\sigma_{xu1}}\right]^2 < 1.0 \qquad \ldots 4.7$$

where $\sigma_{xu1} = \sigma_{cp} + \alpha_p (\sigma_{xup} - \sigma_{cp})$

$\sigma_{yu1} = \sigma_c + (\sigma_{xu} - \sigma_c)/\alpha_p$

$\sigma_{y1} = \frac{\alpha_b}{\alpha_p} \sigma_y + \left[1 - \frac{\alpha_b}{\alpha_p} \right] \sigma_c$

σ_{xup} and σ_{cp} are calculated from the σ_{xu} and σ_c models of Chapter 3 (equations 3.3, and 3.7 for instance), for an increased slenderness given by $\alpha_p\beta$.

Figure 4.20 demonstrates the effect of using equation 4.6, to define the aspect ratio of the end regions of the plate, on the critical stress interactions of figure 4.17, for β values of 2.5, 2 and 1. The effect is to introduce increasing amounts of the intermediate (m=2) mode as β reduces and α_p increases. The theoretical critical buckling interaction is also shown on the figure as dashed lines.

Figure 4.21 shows the maximum strength interactions (derived from equations 4.6 and 4.7, with 3.3, 3.4, 3.7, 4.2 and 4.3) for 3:1 plates having b/t=20, 30 and 40 (β=.69, 1.04 and 1.38), with the interactions for the m=1,2 and 3 modes clearly indicated. This figure demonstrates that, although increasing amounts of the intermediate (m=2) mode are included in the net interaction as the slenderness reduces and the aspect ratio of the doubly curved end-regions increases, the effect of the intermediate mode is less than in the critical buckling interactions of the previous figure.

Figure 4.22 presents the results of this refinement of the model, using the same analysis as in figure 4.21,for the same range of aspect ratios and slendernesses as figure 4.15. The effect of the refinement and of the intermediate modes is fairly minor and the design model still agrees very well with the numerical analyses, over the whole range of plate geometries. The analyses of (48), however, do not allow us to verify the degree of influence of the intermediate mode on the net interaction.

It is now possible to produce a much wider range of interaction curves which could be used for design at maximum resistance. Figure 4.23 presents biaxial strength interactions for a/b=1, 1.5, 2, 3, 5 and 10, and b/t from 18 to 180.

Yield Strain Resistance

In the previous chapter an alternative longitudinal uniaxial strength formulation was given which defined the strength as the stress sustained by the panel at a level of boundary displacement equivalent to yield strain. This was shown to lead to a transverse strength model which accurately predicted the transverse strength of 3:1

plates at $\epsilon_y'=1$.

For a biaxial compression model to be defined at a yield strain limit, an additional biaxial compressive strength function is needed for equal biaxial stresses on a square plate at $\epsilon_x'=\epsilon_y'=1$. This then replaces equation 4.2. Again referring to the stress–strain curves published in (48), the biaxial strengths at yield strain for square plates with b/t=40, 60 and 80 are 0.52, 0.38 and 0.31 times the yield stress respectively. The following empirical definition of biaxial strength yields corresponding values of 0.53, 0.38 and 0.30:

$$\frac{\sigma_b}{\sigma_0} = \frac{0.937}{\beta} - \frac{0.32}{\beta^2} + \frac{0.053}{\beta^3} \quad \ldots 4.8$$

The yield strain definitions of uniaxial and biaxial strength of square plates could then be used in the refined biaxial compression model to produce a revised set of design curves analogous to figure 4.23. The maximum biaxial resistances of figure 4.23 were truncated by the Von Mises ellipse, since the maximum biaxial resistance for an unbuckling plate will lie on this ellipse. This is true even when there are residual stresses in the plate. However, it was shown in Chapter 3 that the uniaxial panel resistance at yield strain will always be less than the yield stress if residual stresses exist. Equation 3.14 expressed the stress at yield strain in an unbuckling plate as a function of the residual stress level. This provided a cut–off to the yield–strain design curves of equations 3.15.

When considering biaxial stress, a similar issue arises. By virtue of a biaxial residual compression of $0.2\sigma_0$ in the central area of a square plate then the unbuckling plate will only remain elastic in the presence of biaxial average stresses σ_x and σ_y until the stresses in the central part of the plate (which are σ_x' + 0.2, and σ_y' + 0.2) reach the Von Mises ellipse.

This is shown on figure 4.24 for the particular biaxial load case with σ_y = 0.5 σ_x, as an example. When the stresses in the central area of the plate reach the Von Mises ellipse, the average stresses will have reached a point on figure 4.24 produced by translating the Von Mises ellipse by σ_r'=0.2 in the x and y directions. This translated Von Mises ellipse is shown as curve II on figure 4.24. The strains in the plate at this point can be obtained from Hooke's Law.

If the load is increased further, then eventually the residual tensile yield stress at the edges of the plate will be overcome, and a state of uniform biaxial compression on the yield surface, will be attained in the plate. The Von Mises yield ellipse is shown as curve I on the figure. If, as an approximation, it is assumed that the

strain in the plate when the Von Mises yield ellipse is reached is at twice yield in the primary loading direction, then the stress-strain curve of figure 4.25 can be produced (this being for the particular example of $\sigma_y = 0.5\ \sigma_x$). The stress at which there is a reduction in the tangent modulus is given by the intersection of the $\sigma_x - \sigma_y$ line on figure 4.24 with curve II, and the strain is given by Hooke's Law. Figure 4.25 can then be used to approximately predict the average stress in the plate when the strain is at yield. This point is indicated on figure 4.25, and is at a value of $\sigma_x' = 0.976$. This point is also shown on figure 4.24. The same calculation has been carried out for all stress ratios to produce the stresses at yield strain, and these are drawn as curve III.

It can be seen that the uniaxial end-point of curve III is at approximately 0.89, which is greater than the 0.833 predicted by equation 3.14, due to the equal biaxial residual stress field taken into account in curve III. However, a long rectangular plate will have much less transverse residual compression stress than the square plate, and will, as a result, produce a curve on figure 4.24 which will end much closer to the 0.833 of equation 3.14. It is therefore proposed that, just as the yield strain uniaxial resistance of equation 3.15(b) was truncated at a stress of $0.833\sigma_0$, so the biaxial resistance should be truncated by a Von Mises type of ellipse of reduced radii, such that it ends at 0.833 on the uniaxial stress axes. That is, the interactions produced by the design model of this chapter, using yield strain definitions of resistance, should be truncated by:

$$\sigma_x^2 - \sigma_x \sigma_y + \sigma_y^2 = 0.7\ \sigma_0^2 \qquad \ldots 4.9$$

Equation 4.9 is shown on figure 4.24 as curve IV, and falls within the curve predicted by the approximate analysis of unbuckling plates. Interaction curves at yield strain can now be produced, incorporating the cut-off given by equation 4.9, and these are presented as figure 4.26. Figure 4.27 compares the biaxial interactions for square and 3:1 plates with b/t=30, 60 and 90, with the design interactions from (24) and (63).

The ease and simplicity with which these alternative strength formulations have been incorporated into the design model for biaxial interaction curves demonstrates that the approach can readily be adapted to alternative strength formulations defined in codes of practice. Provided that the basic components of the method are available (uniaxial and equal biaxial strength functions for square plates, and a suitable column curve), then interaction curves for biaxial compression in plates of any aspect ratio can be produced. If necessary, the relationship between the uniaxial and biaxial models presented here could also be used in order to define η, in the more typical situations

where a uniaxial plate buckling curve and strut curve are available but a biaxial compression curve is not.

In Chapter 6 the model will be extended further to include lateral pressure.

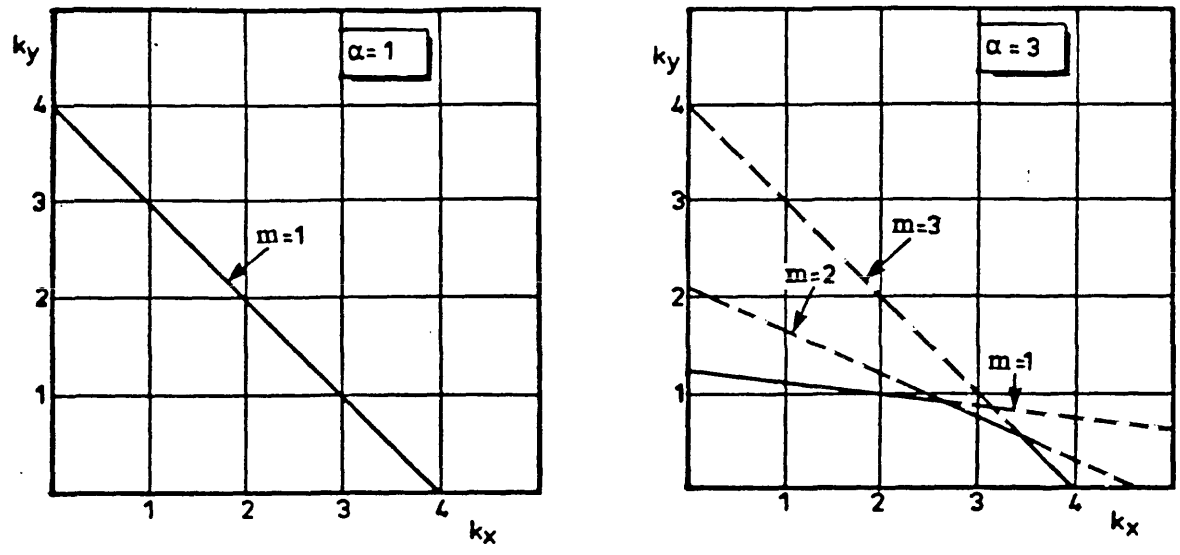

FIGURE 4.1 – Biaxial compression critical buckling coefficients a/b=1 & 3

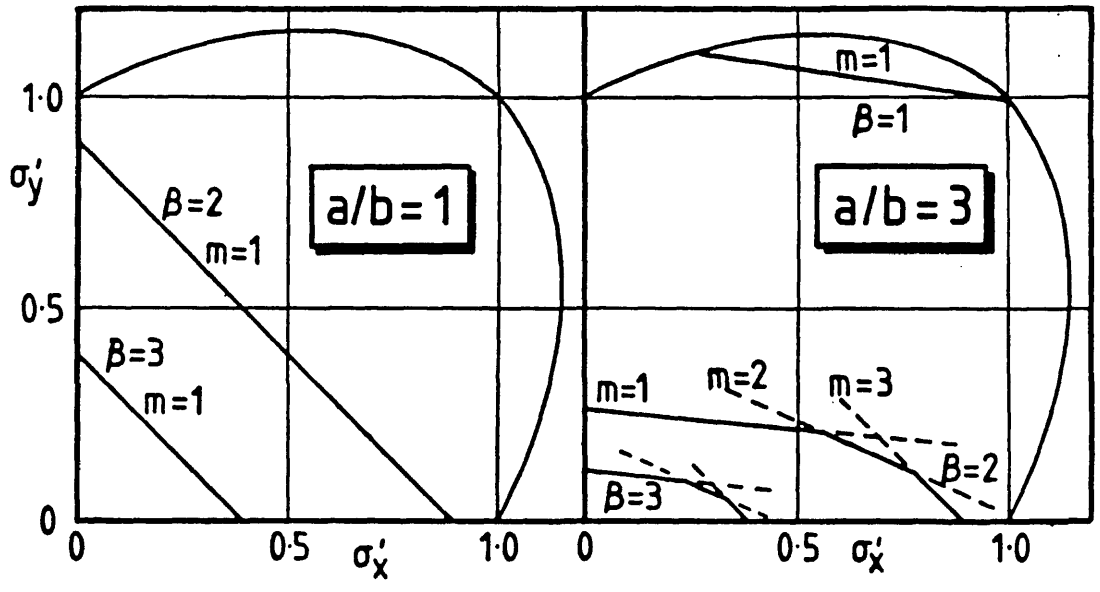

FIGURE 4.2 – Biaxial compression critical buckling stress interactions drawn within the Von Mises ellipse

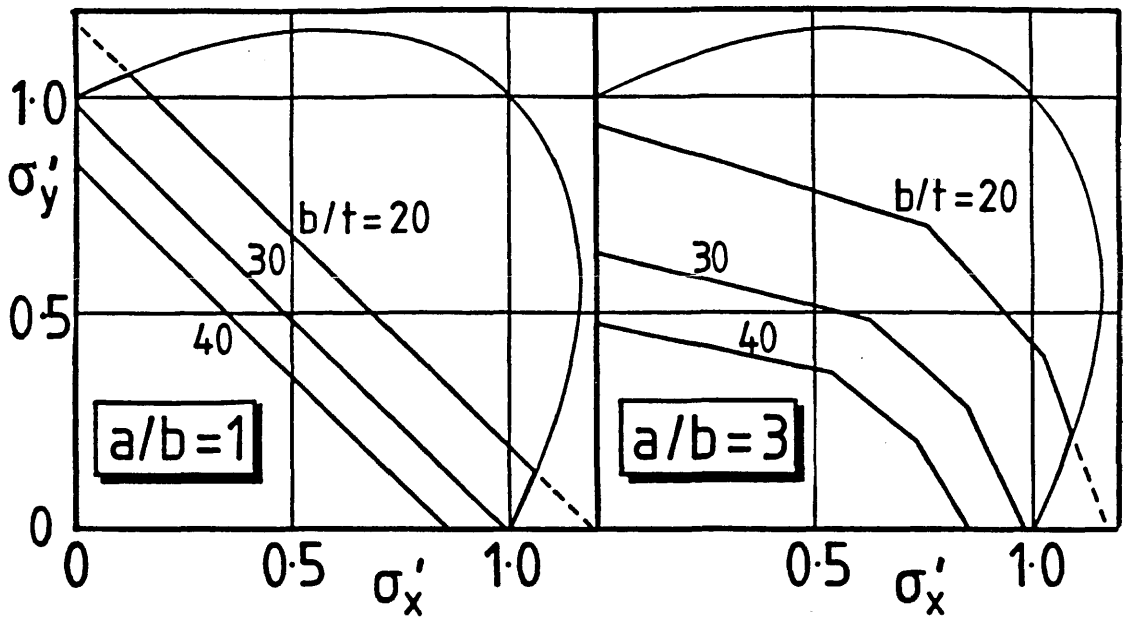

FIGURE 4.3 – Critical interactions scaled to end at σ_{xu} and σ_{yu} from eq.3.3 & 3.4

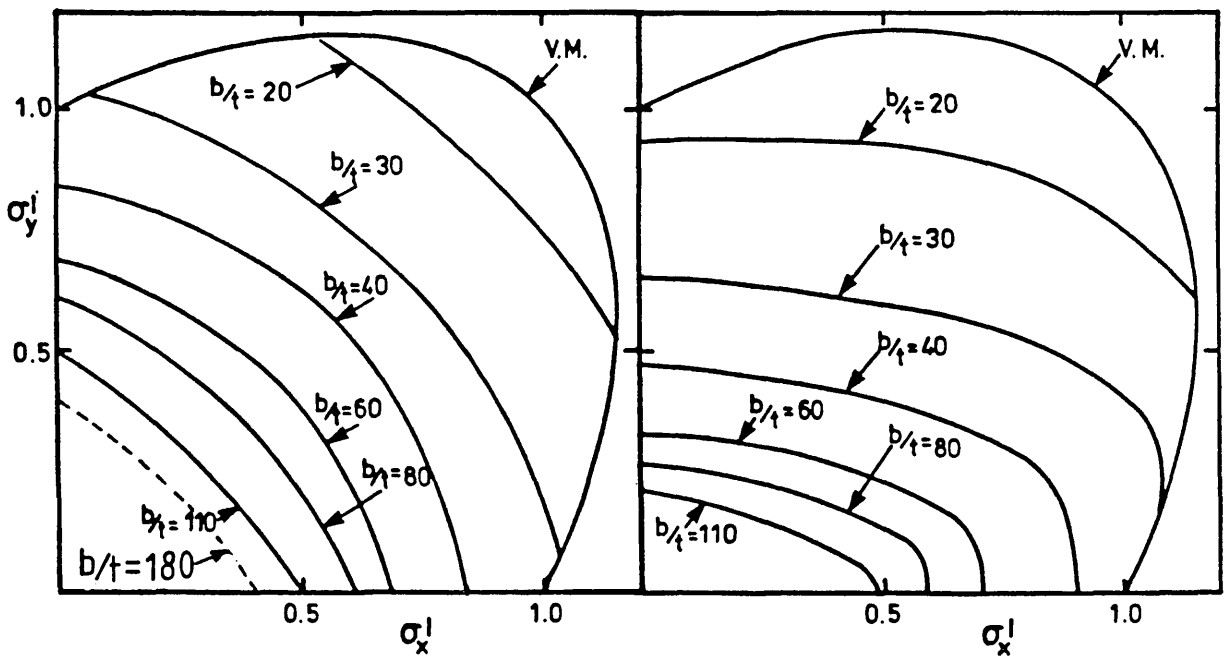

FIGURE 4.4 – Maximum resistance biaxial interaction for square and 3:1 plates from (49), with the result of a FINAS analysis for a/b=1, b/t=180

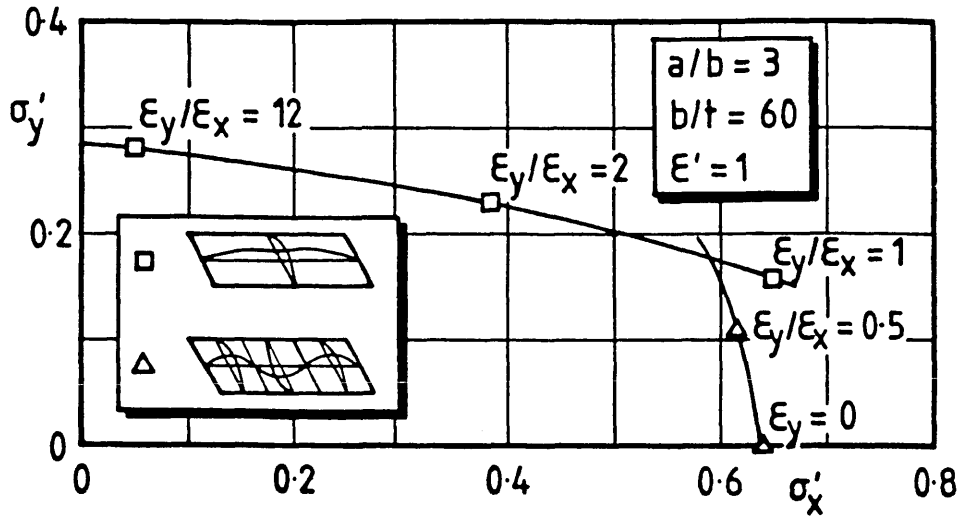

FIGURE 4.5 – Plate buckling modes at various positions on the biaxial interaction for a 3:1 plate, b/t=60, from the data produced for (47)

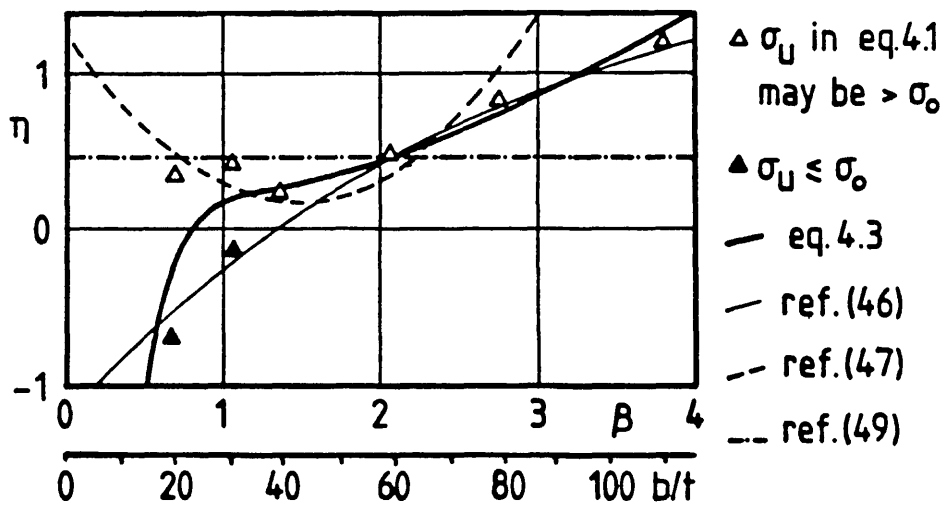

FIGURE 4.6 – Cross-product coefficient, η, from analyses of (49) compared to existing and proposed models

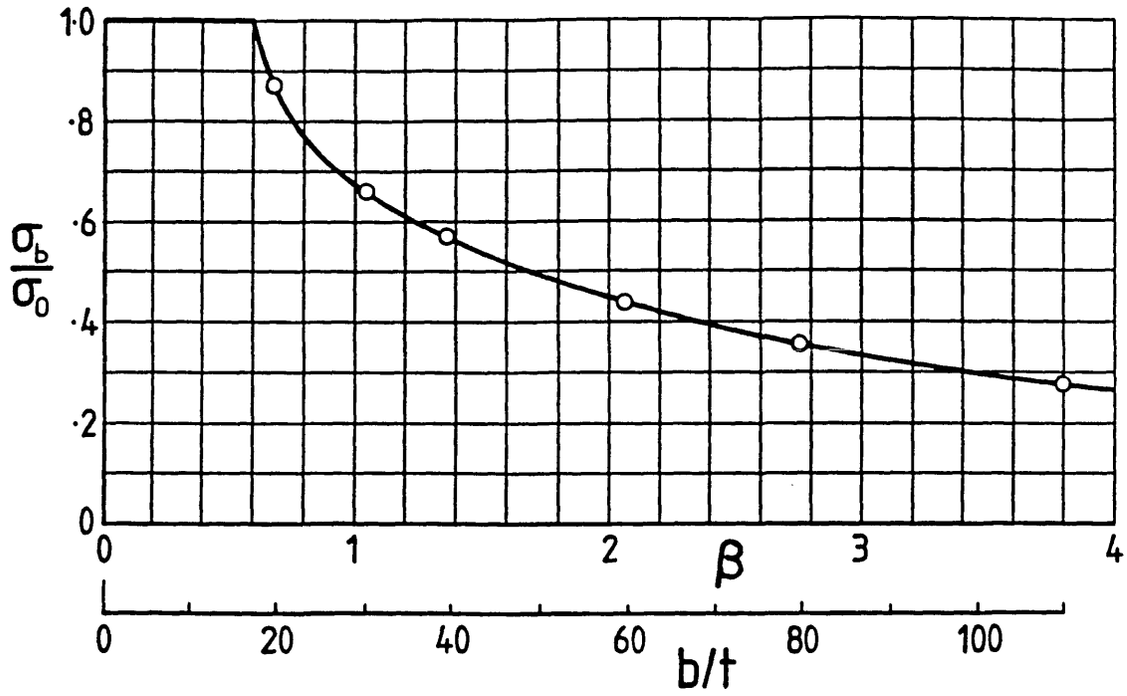

FIGURE 4.7 – Maximum biaxial resistance ($\sigma_x = \sigma_y$) from eq.4.2, cf. data from (49)

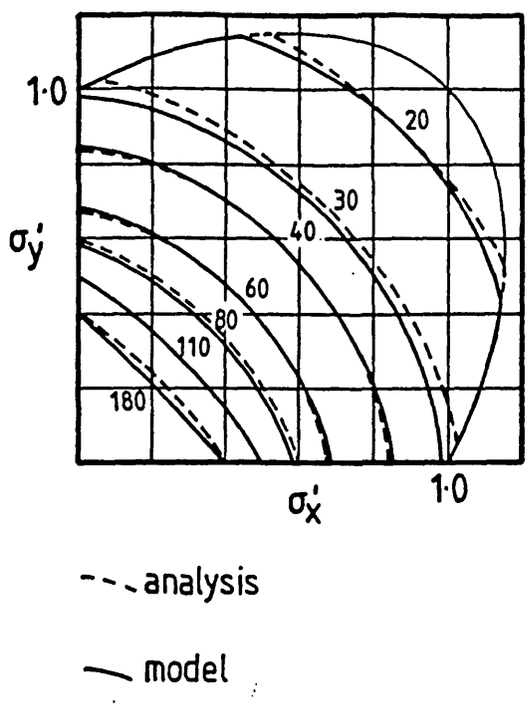

FIGURE 4.8 – Biaxial compression in square plates

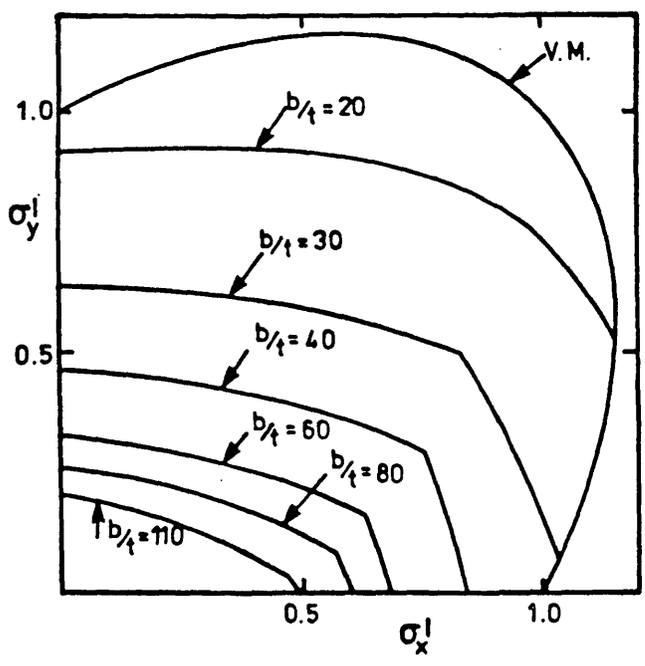

FIGURE 4.9 – Biaxial interactions for 3:1 plates, from (49), modified by square plate interactions

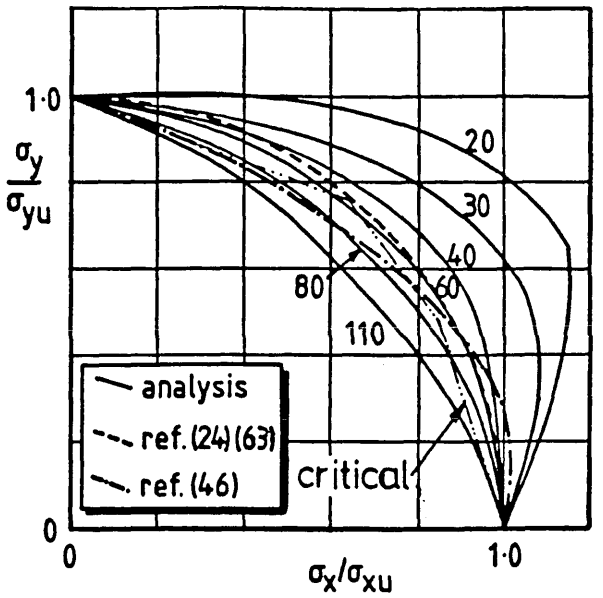

FIGURE 4.10 – Normalized biaxial interactions for 3:1 plates, from fig.4.9 compared to critical buckling interaction & existing models

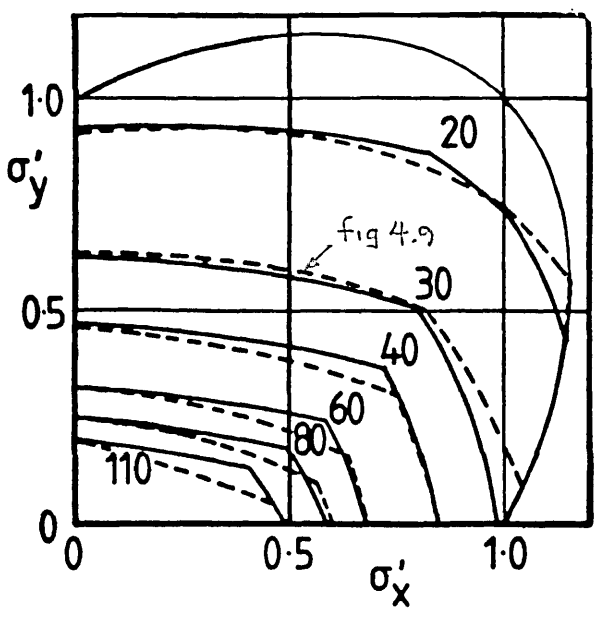

Simple design postulate compared to fig.4.9

FIGURE 4.11

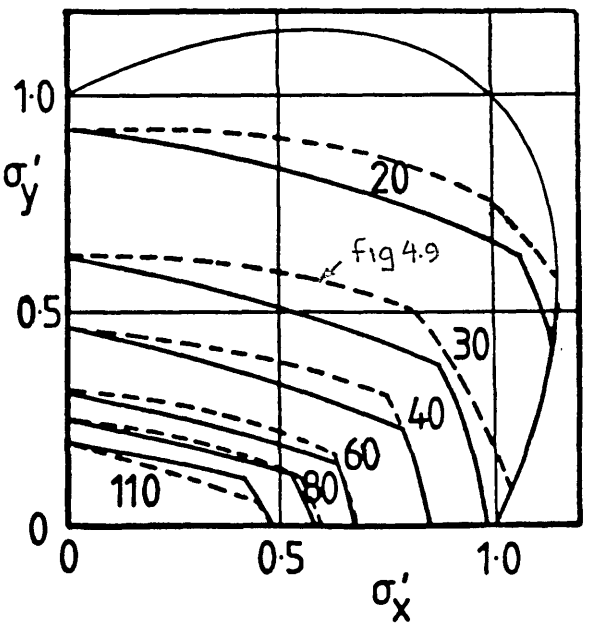

Revised simple design postulate compared to fig.4.9

FIGURE 4.12

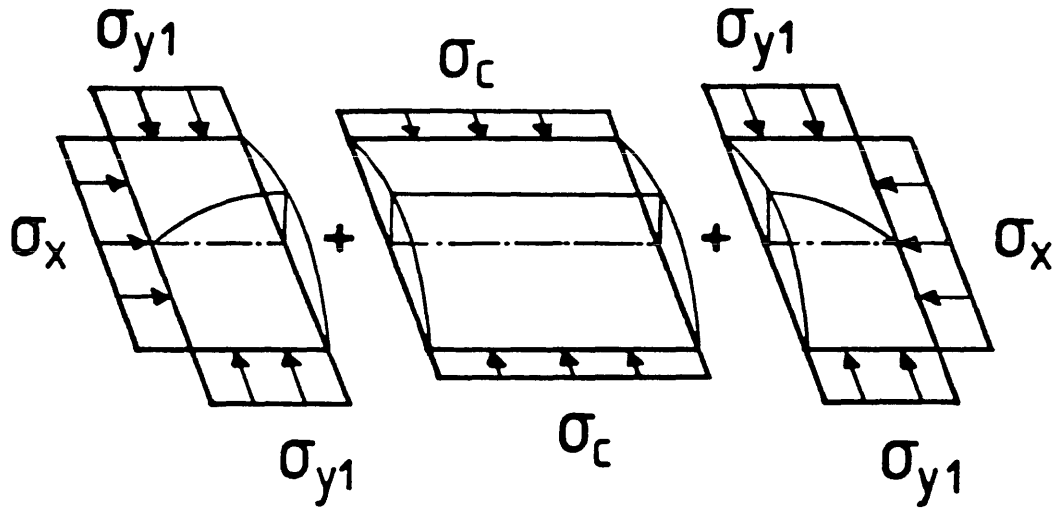

FIGURE 4.13 – Conceptual model for biaxial compression in rectangular plates

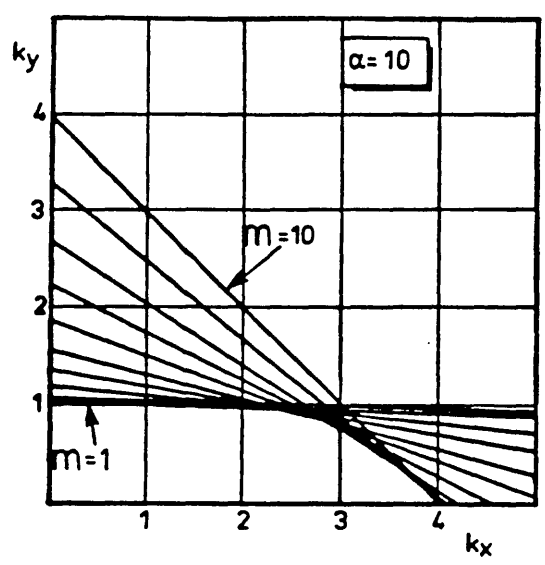

FIGURE 4.14 – Biaxial compression critical buckling interaction – a/b=10

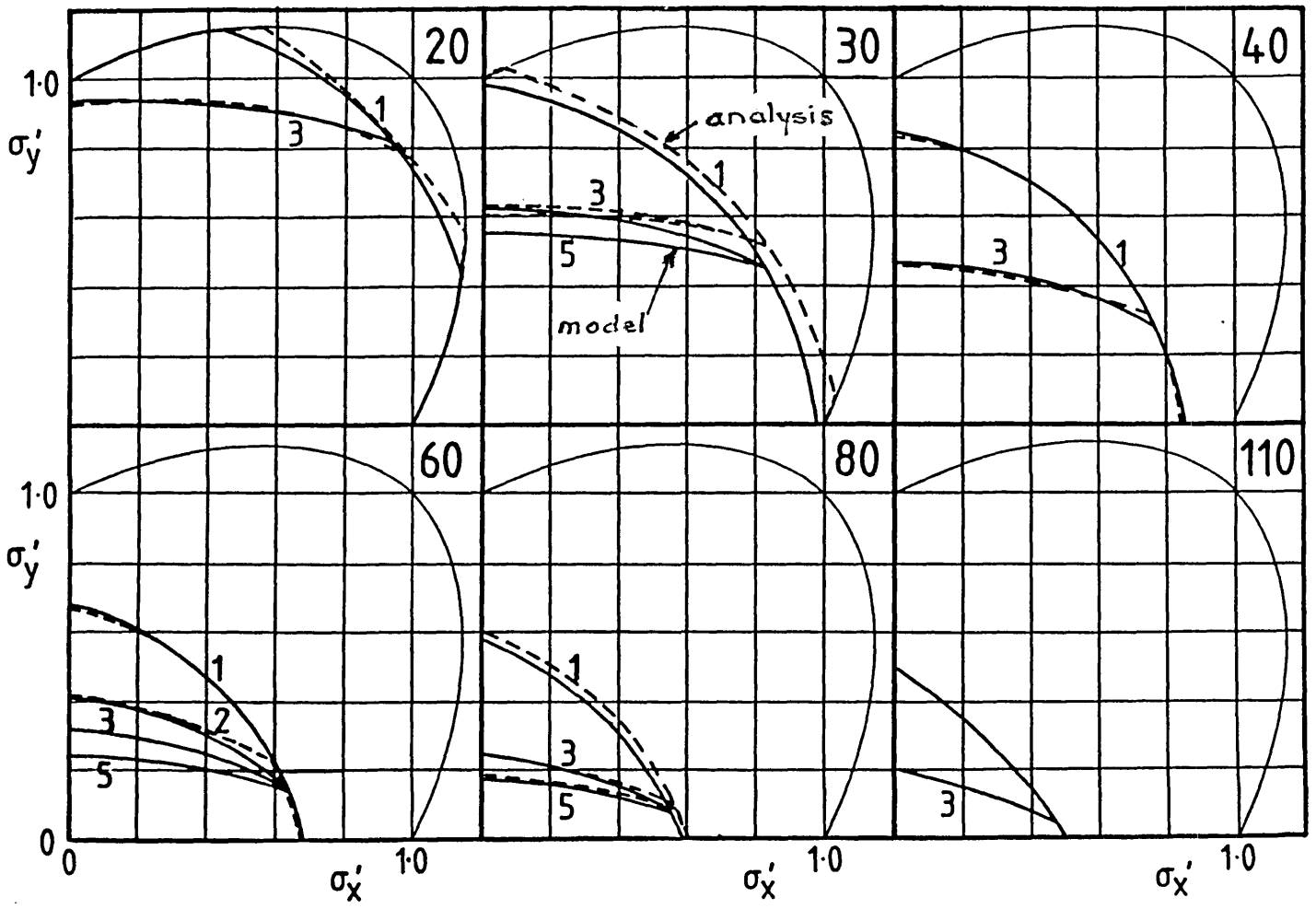

FIGURE 4.15 – Proposed design model for biaxial compression maximum resistance compared to analyses of (49) – b/t=20 to 110, various a/b

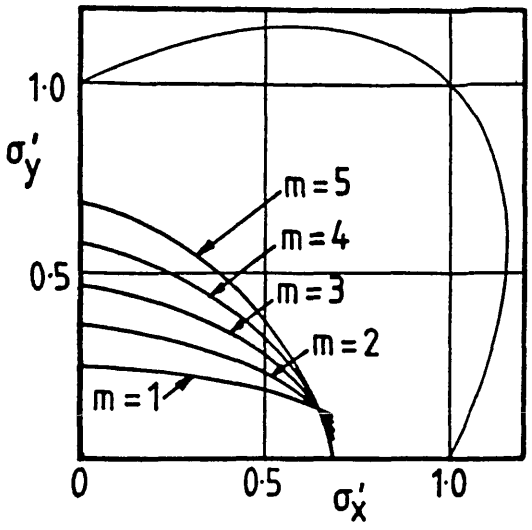

Biaxial compression design model showing effect of each possible mode – a/b=5, b/t=60

FIGURE 4.16

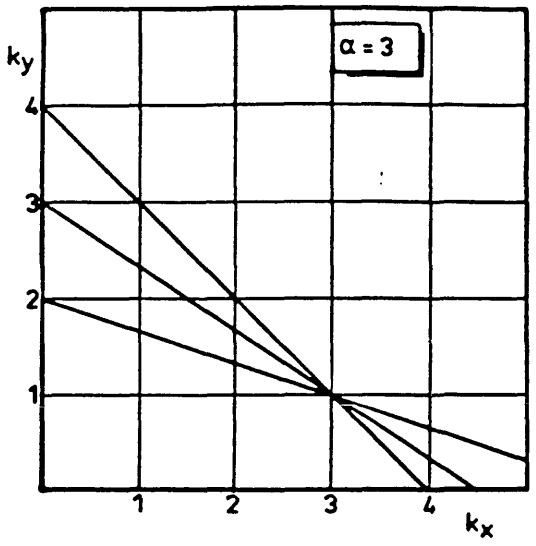

Pseudo-critical buckling – a/b=3

FIGURE 4.17

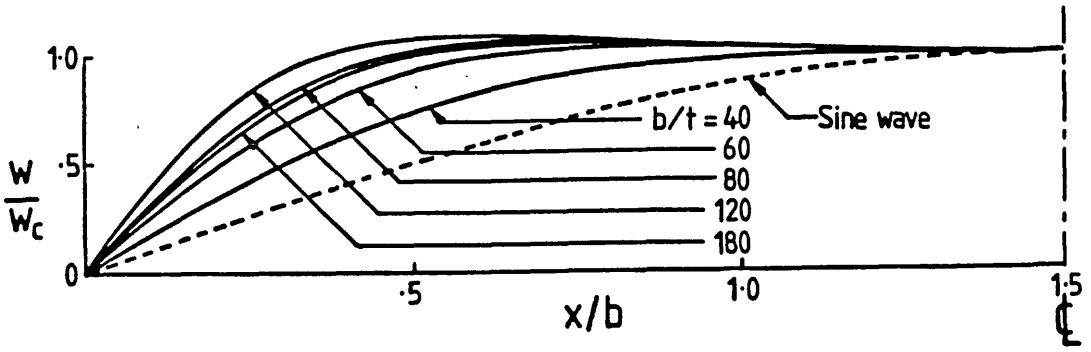

FIGURE 4.18 – Buckling deformation profiles for 3:1 plates in transverse compression

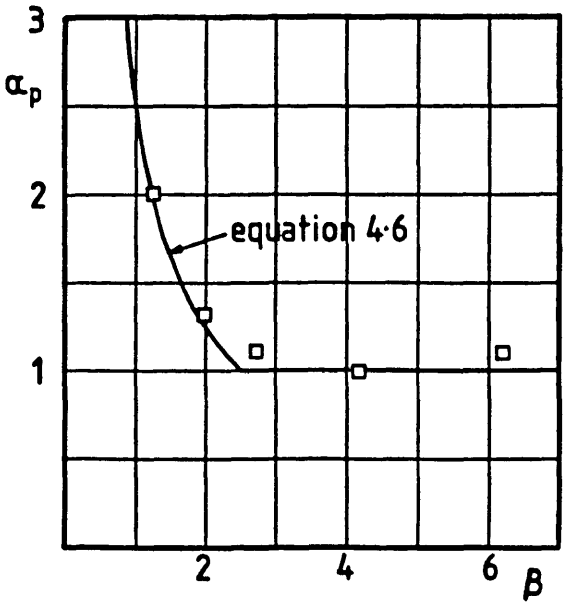

FIGURE 4.19 – Aspect ratio, α_p, of the doubly-curved end-regions in the conceptual model, inferred from fig.4.18, and compared with eq.4.6

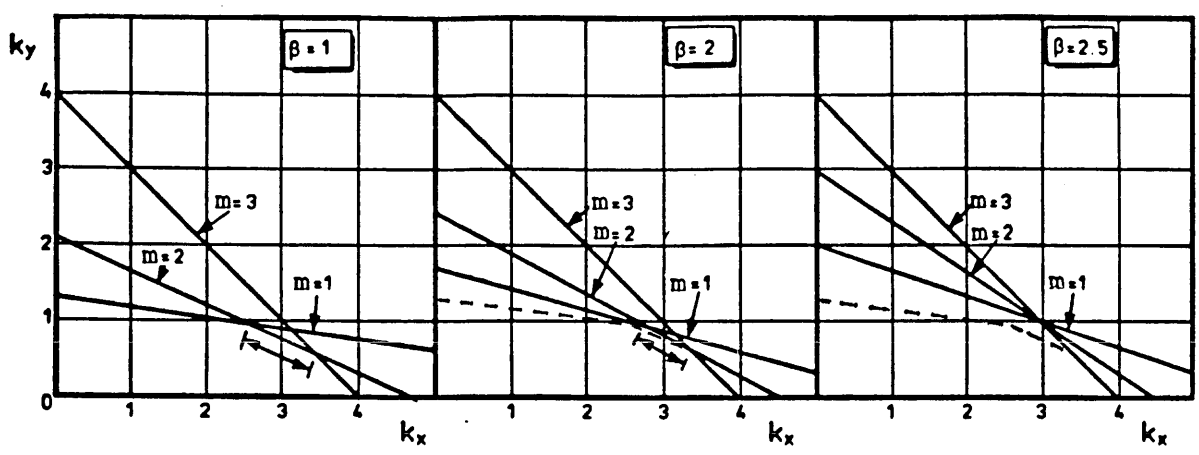

FIGURE 4.20 – Influence of eq.4.6 on pseudo-critical buckling interactions – showing variation in significance of m=2 buckling

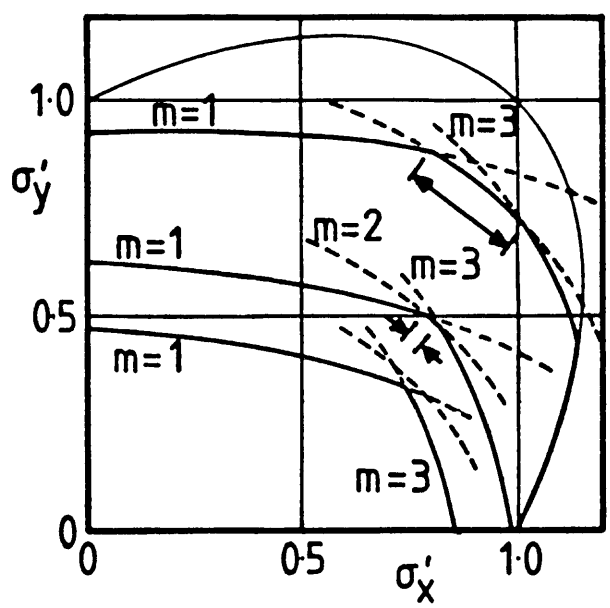

FIGURE 4.21 – Influence of eq.4.6 on maximum resistance biaxial interactions – showing variation in significance of m=2 buckling
a/b=3, b/t=20, 30 & 40

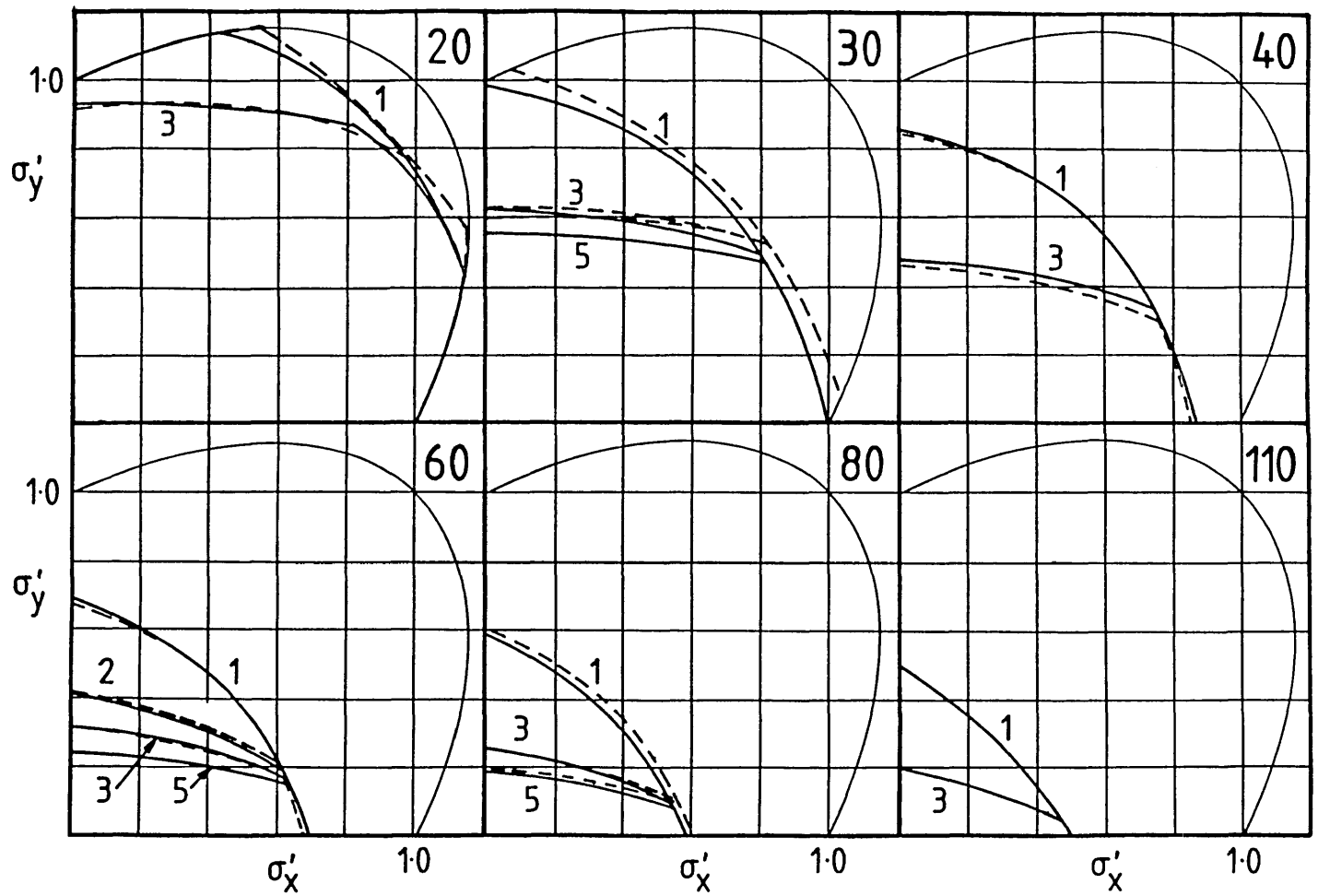

FIGURE 4.22 – **Proposed design model for biaxial compression maximum resistance, incorporating eq.4.6, compared to analyses of (49) – b/t=20 to 110**

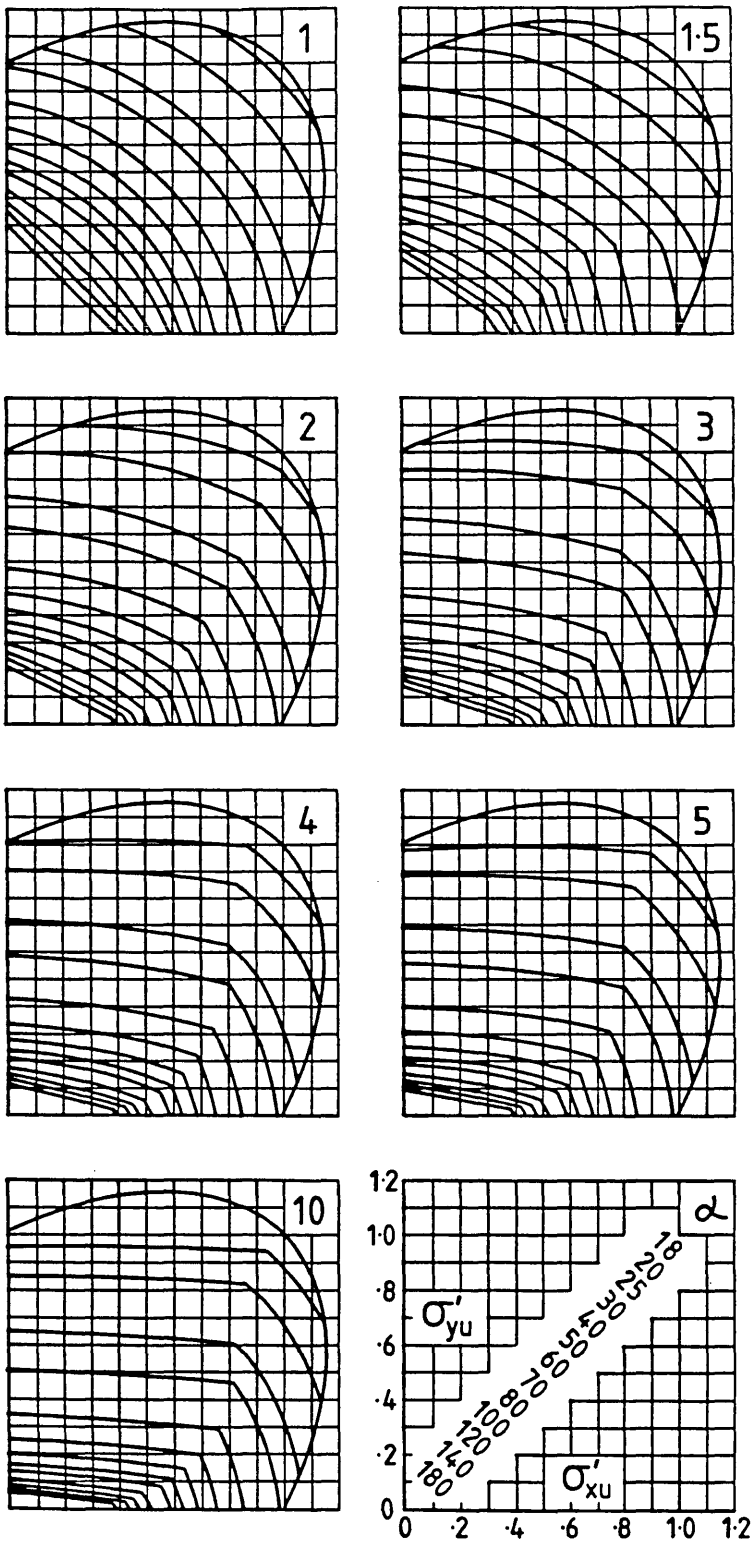

FIGURE 4.23 – Design curves from proposed biaxial compression maximum resistance model

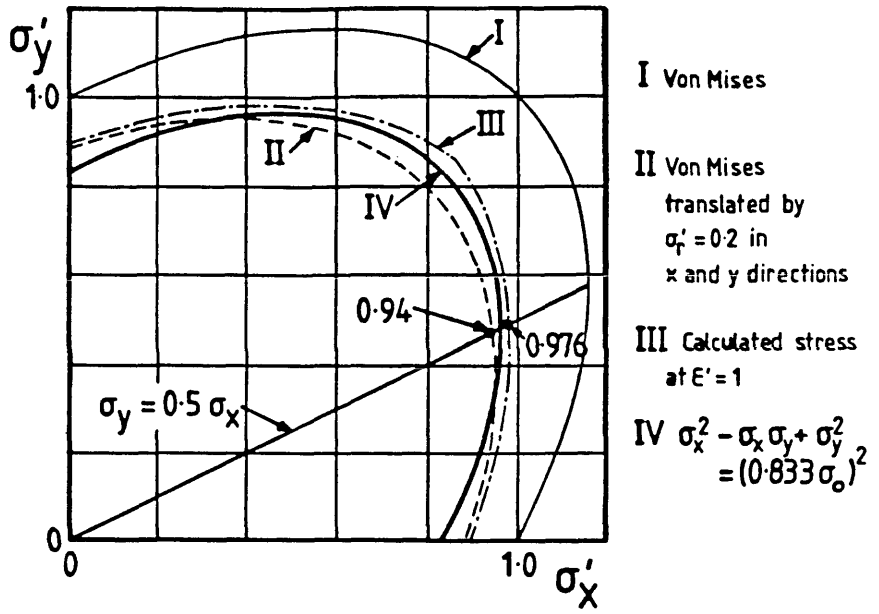

FIGURE 4.24 – Effect of biaxial residual stress on stress at yield stress in an unbuckling plate subject to biaxial compression

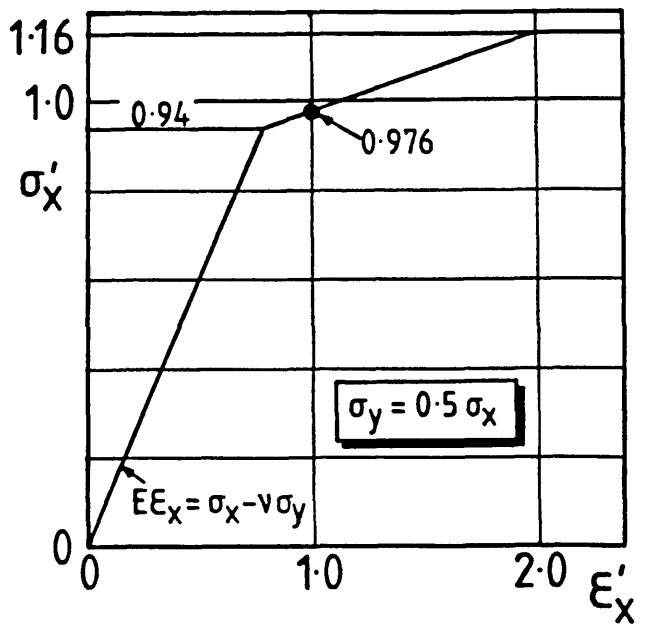

FIGURE 4.25 – Effect of biaxial residual stress on stress–strain curves for an unbuckling plate subject to biaxial compressions, corresponding to line on figure 4.24

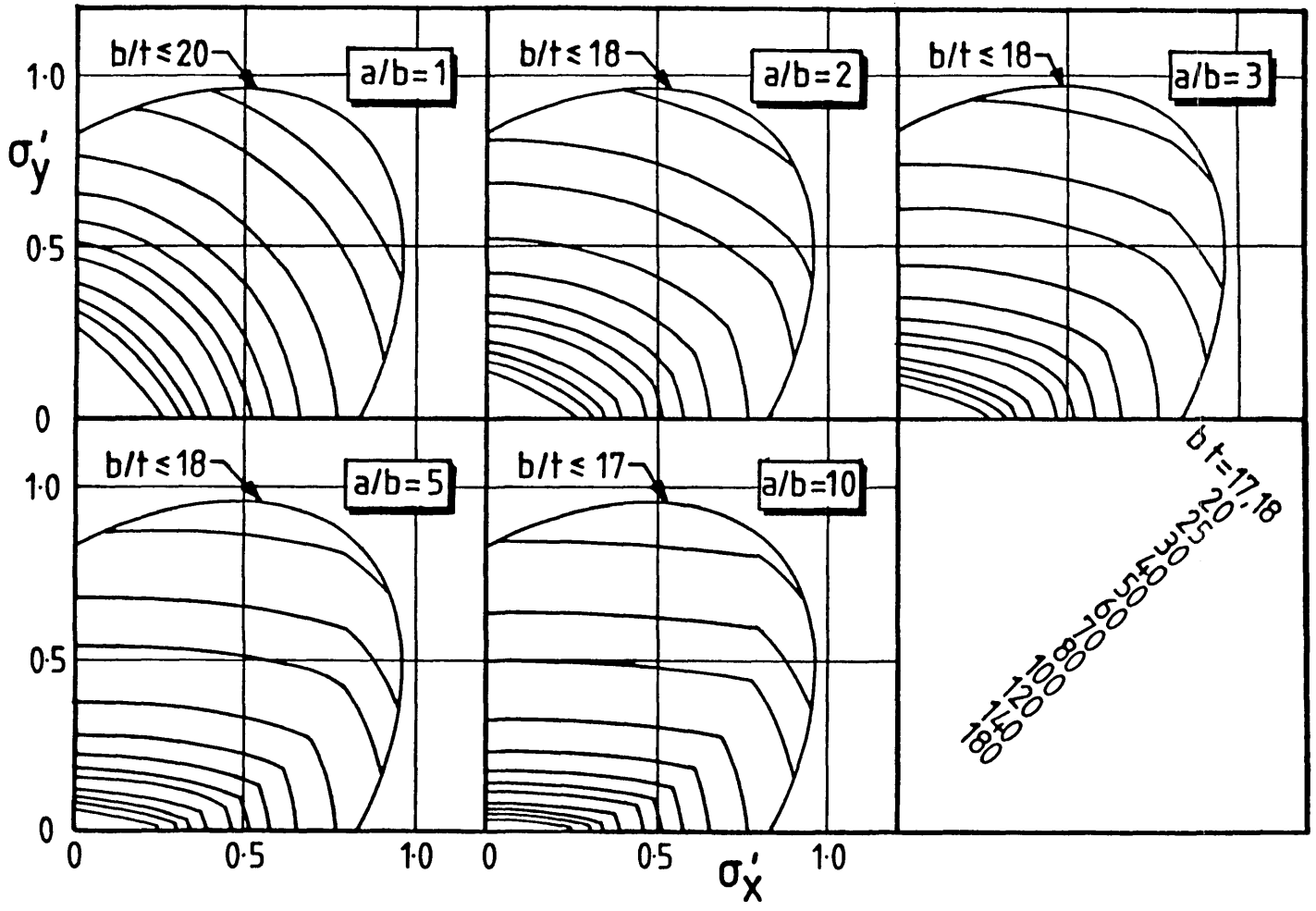

FIGURE 4.26 – Design curves from proposed biaxial compression yield strain resistance model

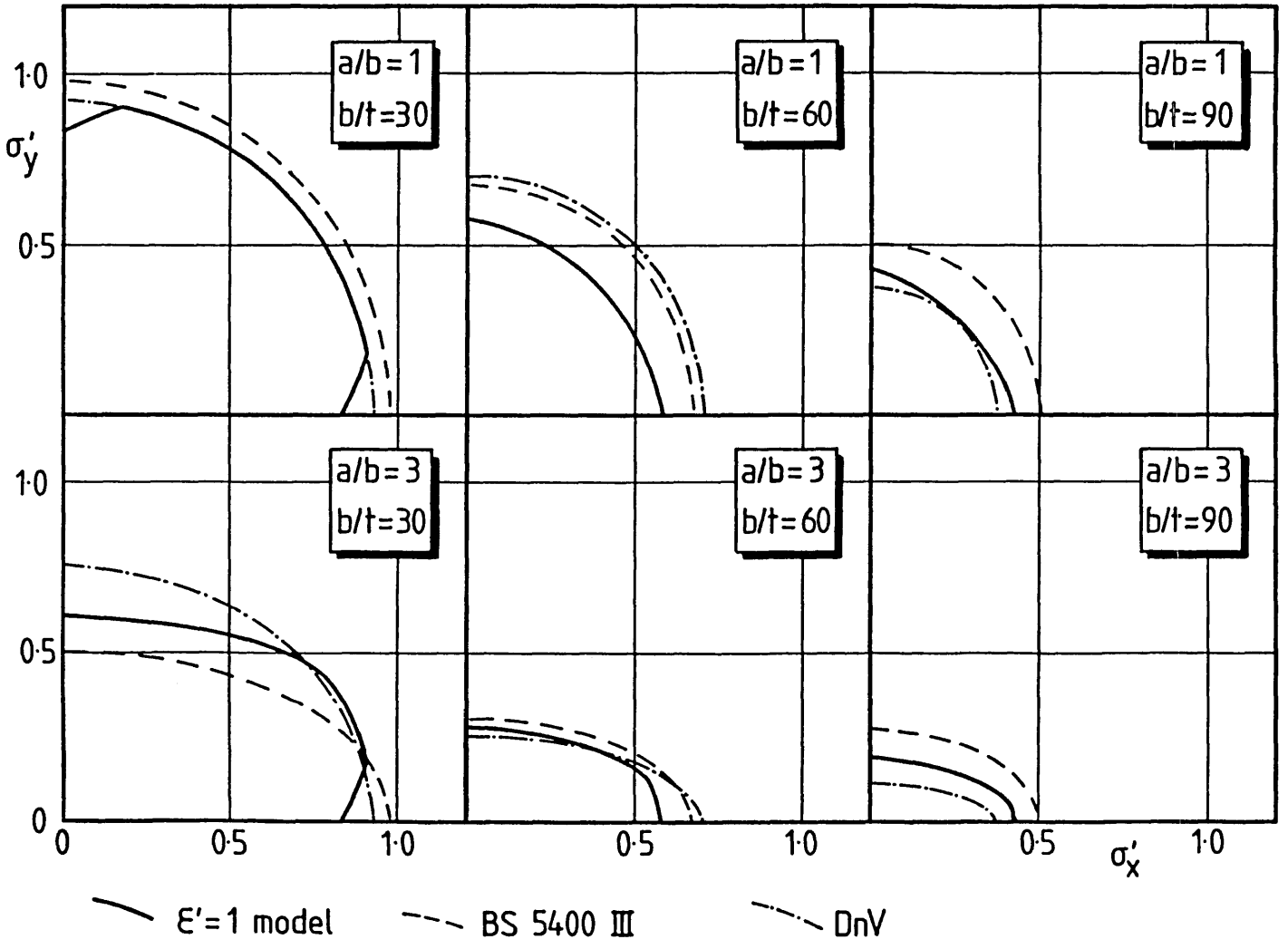

FIGURE 4.27 – Comparison between biaxial interactions produced by proposed yield strain model and interactions produced by (24) and (63)

CHAPTER 5 BIAXIAL COMPRESSION AND SHEAR

5.1 Critical Buckling

The purpose of this chapter is to present a simple design model for the interaction between biaxial compression and shear. The interaction model will be presented in the next section and will be validated by reference to further elasto-plastic numerical analyses using FINAS, but its development first requires a consideration of critical buckling, which will be the subject of this section.

The critical buckling Galerkin program of Appendix A, which calculates the first and second elastic buckling loads and modes for flat simply supported plates subjected to in-plane biaxial compression and shear, has already been referred to in Chapter 2. This program has been used to produce the buckling modes for 3:1 plates with various ratios of biaxial compression and shear, which are presented in figure 5.1.

Buckling modes for shear with or without biaxial compression are either symmetric or anti-symmetric about the mid-point of the plate. The Galerkin program which is listed in Appendix A will only produce the lowest buckling load, but if it is limited to operating only on symmetric or anti-symmetric Fourier terms then the lowest buckling loads for each type of mode will be found. An example of a symmetric Fourier term would be one with m=3 and n=1 (that is, 3 half waves in the long direction and 1 in the short direction), whereas an example of an anti-symmetric term would be m=2, n=1.

The critical buckling interactions, in terms of the buckling factor k, for a 3:1 plate under uniaxial or biaxial compression and shear, are shown on figure 5.2, with the points on the interactions which correspond to the modes of the previous figure indicated. The first three interaction curves are formed by the intersection of interaction curves for symmetric and anti-symmetric modes. Figure 5.3 shows the symmetric and anti-symmetric interactions for a square plate loaded by shear with uniaxial compression.

It was shown in (98), (99) and (56) that the interaction between shear and longitudinal compression in long rectangular plates of any aspect ratio could be accurately modelled by a parabola, having the form:

$$\left[\frac{k_X}{K_X}\right] + \left[\frac{k_\tau}{K_\tau}\right]^2 = 1 \qquad \ldots 5.1$$

where K_x and K_τ are the critical buckling factors in pure longitudinal compression and pure shear respectively, and k_x and k_τ are the compression and shear buckling factors when shear and compression act in combination. It was shown in (99), however, that this expression was conservative when applied to the interaction between transverse compression and shear in rectangular plates. The parabola given by equation 5.1 is drawn as broken lines to fit the interaction end-points in figures 5.2 and 5.3, confirming its accuracy for longitudinal compression and its conservatism for transverse compression.

It is also apparent that, whereas the interaction for a square plate is a single curve (for modes which, although they change continuously from one point on the interaction to another, still remain symmetric), for rectangular plates the net interaction is made up of the intersecting interactions for symmetric and anti-symmetric modes. Where the two interactions meet there is an abrupt change in buckling mode, and, for transverse compression, an abrupt change in the slope of the interaction. For longitudinal compression the change in slope at the intersection of the interactions is so slight that the continuous curve given by equation 5.1 is still a good fit.

To represent the interaction for biaxial compression and shear, figure 5.4 presents biaxial compression interactions for constant coexistent levels of shear, for square and 3:1 plates. In effect this figure plots contours of the three-dimensional interaction surface, where the height of the contour represents a particular level of shear stress.

It can be seen that the presence of coexistent shear does not change the straight line nature of the biaxial interaction (or, in the case of rectangular plates, the straight-line nature of the components of the biaxial interaction). Furthermore, the contours in the presence of shear are parallel to the equivalent contours at zero shear.

However, the amount by which the component straight lines of the 3:1 plate biaxial interaction in the absence of shear, are translated on this figure to form the equivalent interactions in the presence of shear, is not proportionally the same for each of the component interaction lines. This means that whereas the shape of the square plate biaxial interaction in the presence of shear is the same as the interaction in the absence of shear, this is not the case for the rectangular plate. In the latter case, the relative proportions of the component interaction lines vary with level of coexistent shear.

If a parabolic curve is applied to the interaction between biaxial compression and shear, then the contours (for the same levels of shear stress as the calculated contours), which result are shown as broken lines on figure 5.4. These are generally within the equivalent Galerkin contours, and are therefore a safe representation of them, except in the part of the interaction which corresponds to the m=2 line in the τ=0 case, when the broken lines are only slightly outside the Galerkin contours.

There is a rather complicated trend of behaviour seen in these critical interactions, but one which is shown to be conservatively or reasonably represented by a parabolic interaction function. Even though there will be qualitative parallels in the elasto-plastic maximum strength interactions (changes in mode types, intersecting interactions, and so on), the design model will not attempt to model these complexities of behaviour. This model will now be developed.

5.2 Design Model

The Von Mises interaction between biaxial compression and shear is given by:

$$\sigma_x^2 - \sigma_x \sigma_y + \sigma_y^2 + 3\tau^2 = \sigma_0^2 \qquad \ldots 5.2$$

The circular non-dimensionalised interaction between compression and shear that this produces, has been used for the design of offshore structures in (63), as

$$\left[\frac{\sigma_x}{\sigma_{xu}}\right]^2 + \left[\frac{\sigma_y}{\sigma_{yu}}\right]^2 + \left[\frac{\tau}{\tau_u}\right]^2 = 1 \qquad \ldots 5.3$$

If a plate is stocky enough for membrane yielding to be widespread over the area of the plate at maximum resistance, then the plate will be nearly fully effective (that is, its maximum strength will be near to the yield strength), and its interaction behaviour will be governed by the Von Mises interaction of equation 5.2. We might therefore expect the circular interaction of equation 5.3 to be reasonably appropriate for stocky plates (leaving aside the question, for the moment, of how stocky these plates would need to be).

A slender plate, on the other hand, is prone to buckling. The greater susceptibility to flexural deformation means that membrane yield at failure will be much more localized (whether it is distributed as zones of yield along the edges of compressed plates, or as diagonal tension fields in shear plates, for instance). Such a plate will be less than fully effective, and its interaction behaviour will be less governed by the (un-buckling) Von Mises interaction and more influenced by the flexural behaviour of the plate, which has given rise to the localization of yield in the first place. The

changing susceptibility to flexural deformation, as the load ratio is varied, is broadly indicated by the critical buckling interaction, which is based on the plate taking up a mode of flexural deformation which minimizes the bending energy in the plate.

Of course, critical buckling is only one indicator of a plate's susceptibility to flexural deformation. Post-buckling tangent modulus also changes with load ratio, and the buckling mode changes as non-uniformity develops in the membrane stress field, and both of these phenomena will influence the flexural deformations of the plate, and, thus, the degree to which membrane yield has localized at maximum resistance.

It was shown in Chapter 4 that biaxial strength interactions for square and 3:1 plates were more Von Mises-like at low slenderness than at high slenderness. At high slenderness, the square plate interactions tended towards the form of the critical buckling interaction (for the range of slendernesses studied), but this was not the case for the 3:1 plates. However, a modified critical buckling interaction, for 3:1 plates, was produced in figure 4.17, based on a buckling mode (illustrated in figure 3.9) which was more consistent with the buckling mode at maximum resistance, than with the theoretical critical buckling mode. This modified critical buckling interaction was much closer to the shape of the strength interactions.

None the less, despite the effect of post-buckling stiffness, and a buckling mode which is different, at maximum resistance, from the critical mode, there will be a broad trend in interaction shapes, from a Von Mises type of interaction at low slenderness, to a critical, or quasi-critical, interaction at high slenderness.

BS5400 (24) implicitly recognizes that the critical interaction will be reasonably appropriate at high slenderness, and safe at low slenderness, by adopting a parabolic interaction proposed in (34)(100), which has the same form as equation 5.1, as follows:

$$\left\{\left[\frac{\sigma_x}{\sigma_{xu}}\right]^2 + \left[\frac{\sigma_y}{\sigma_{yu}}\right]^2\right\}^{1/2} + \left[\frac{\tau}{\tau_u}\right]^2 = 1 \qquad \ldots 5.4$$

Equations 5.3 and 5.4 can then be seen to represent opposite ends of an anticipated trend in interaction shapes, the former being qualitatively more appropriate to the generally more stocky plates encountered in ship and offshore structures, the latter being more appropriate to the slender plates found in the webs of plate and box girder bridges. An important exception to this generalisation is, of course, the slender plates found in top-sides of offshore structures.

The design model, which is proposed below, recognizes the change in interaction

shape which is likely to occur with slenderness, and will encompass the shear interactions of (24) and (63) as limits. Such a model, for shear and longitudinal compression, for instance, will have the form:

$$\left[\frac{\sigma_x}{\sigma_{xu}}\right]^n + \left[\frac{\tau}{\tau_u}\right]^2 = 1 \qquad \ldots 5.6$$

where n will vary in an empirically defined way from 2, at low slenderness, to 1 at high slenderness. The interactions which are produced by varying n from 1 to 2, are illustrated in figure 5.5.

Numerical analyses have been carried out, using FINAS, of square and 3:1 plates, with b/t=40, 60, 80, 120 and 180, with CCCC boundary conditions subjected to combinations of shear with uniaxial longitudinal or transverse compression, or with biaxial compression. As with all the FINAS analyses carried out as part of the present work, residual stresses were not applied to the plate, but although this has little effect on the shear capacity of the plate, it can have a significant effect on the uniaxial and biaxial compression capacities. The purpose of the analyses, however, was to indicate the non-dimensionalised shape of the interaction, which would then be used with the previously defined shear and biaxial strength models, so quantitative interactions are not really required.

What is required is that interaction end-points should also be obtained with consistent assumptions to the intermediate points on the interactions. As a result, consistent analyses of plates subjected to shear only, uniaxial longitudinal and transverse compression only, and biaxial compression only, were also carried out to provide the end-points that would permit the interactions to be non-dimensionalised.

To economize on the number of analyses, it was decided only to analyse those stress combinations that would give a point close to the middle of the non-dimensionalized interaction; that is, where a 45 degree line from the origin of the non-dimensionalised stress axes would meet the interaction curve. This 45 degree line is shown as a broken line on figure 5.5. For the b/t=120 and 180 plates, additional points were obtained at intermediate points on the interactions, in one or two cases.

The question arises of what imperfection mode should be used in the analyses. It was argued in Chapter 3 that there was a possibility of affine imperfections developing during the life of a structure, and since the presence of non-affine (and, in terms of strength, beneficial) imperfections could not be guaranteed, it was simpler and safer to assume affine imperfections in producing a design model. It was,

therefore, decided to use the Galerkin program to obtain the Fourier terms that make up the preferred elastic critical buckling mode, and to use these to produce the plate imperfections for the elasto-plastic analyses. This required an eigen-analysis to be carried out prior to generating the input data for each of the FINAS runs used in this chapter.

The maximum amplitude of the imperfection modes was taken to be w_0=b/200 for consistency with the shear analyses of Chapter 2. Mesh sizes were 8x8 for square plates and 6x18 for 3:1 plates.

Figure 5.6 presents the shear and compression stress-strain curves which result from the analyses, for square plates of b/t=40, 80 and 180. It is clear from these that (just as was observed in Chapter 2 for CCCC plates in shear only) the shear strain in the plate can diminish as plate buckling proceeds. This will pose severe problems for stress-strain modelling, but this was not attempted as part of the present work.

The maximum stresses in the plate (which are generally achieved when the strains are in the region of 0.9 to 1.2 times the yield strain), are tabulated in Table 5.1.

Mesh correction factors have also to be applied. Meshes of the sizes used are sufficient for full convergence in compression (whether uniaxial or biaxial). They are also sufficient for full convergence in shear for b/t less than, or equal to 80. Correction factors need to be applied, however, for shear plates with b/t=120 and 180, as in Chapter 2. Furthermore, to the extent that combined load cases contain shear, but that the localized curvatures in the inclined buckling modes are ameliorated due to the uniaxial or biaxial compressions, there will be a need for a reduced mesh correction in these cases. Since the shear-compression ratios are approximately on the 45 degree line of the normalised interaction, it was assumed that half the mesh correction factor would be appropriate for the intermediate load cases in the b/t=120 and 180 cases. The mesh-corrected values are given in Table 5.2.

It can be seen from figure 5.5, that whatever value n has in the range 1 to 2, the interaction in the predominantly compression region is not greatly affected. The reason for this is that since coexistent shear loading will have the same effect on compression behaviour whether the shear is positive or negative, the interaction will always be symmetric about the compression axis, and will meet it at 90 degrees, however slender the plate is. The biggest change in interaction shape occurs in the predominantly shear part of the interaction. When n=2 the interaction is normal to both axes, but when n=1 the non-dimensionalised interaction meets the shear axis at an angle of 63 degrees. It seems intuitively reasonable therefore to look for a

variation in n which depends on the response of the plate to predominantly shear loading.

The intermediate interaction points from Table 5.2 have been used (with the end-points) to calculate what value n would need to have to predict an interaction curve which would fit the data. These values are plotted on figure 5.7 against λ. λ, which was introduced in the shear design model of Chapter 2, is the plate slenderness divided by the critical slenderness in shear. On the figure, 2 separate diagrams are plotted, these being for square plates and 3:1 plates. Each diagram plots the values of n derived from the data given in Table 5.2 for the five slendernesses. The values of n are listed in the Table.

A simple representation of the variation is to assume that n varies linearly from 2 at zero slenderness to 1 at the critical slenderness (for each particular aspect ratio), and remains at 1 for higher slendernesses. This bi-linear model is also shown on both diagrams of figure 5.7, and can be written:

$$n = \begin{cases} 2 - \lambda & ; \quad \lambda < 1 \\ 1 & ; \quad \lambda \geq 1 \end{cases} \qquad \ldots 5.7$$

Equation 5.7 is used to produce non-dimensionalised interactions for square and 3:1 plates with b/t=40, 80 and 180, which are compared with the relevant load combination data from Table 5.2 on figure 5.8. The data for shear combined with uniaxial longitudinal or transverse compression, or biaxial compression, are included on the same figure, since n varies only with the critical slenderness in shear. It can be seen that equation 5.7 gives a variation in interaction shapes which fits the data reasonably well.

Since the same shear interaction is being applied both to uniaxial and biaxial compression, then it is suggested that the uniaxial strength model of Chapter 3, and, if required, the biaxial interaction of Chapter 4, should be used to find the (biaxial) compressive strength in the absence of shear. This uniaxial or biaxial strength will then be reduced by multiplying it by a factor ζ (zeta), say, given by the solution to equation 5.6:

$$\zeta = \left\{ 1 - \left[\frac{\tau}{\tau_u} \right]^2 \right\}^{1/n} \qquad \ldots 5.8$$

This model, with the proposed models of Chapters 2 to 4, is compared in figure 5.9 with the design models of (24) and (63), for shear and uniaxial compression in square and 3:1 internal plates (although the design model of (63) makes no

distinction between boundary conditions). The Von Mises interaction is also shown, since this is occasionally needed to truncate the interactions produced by (24).

Having developed a model for the interaction between shear and uniaxial or biaxial compression, the next stage of design model development will be for biaxial compression and pressure.

a/b	b/t	β	λ	τ/τ_0	σ_x/σ_0	σ_y/σ_0
1	40	1.38	.363	.997 --- --- .720 .714	--- .904 .590 .613 .407	--- --- .590 --- .407
1	60	2.07	.545	.983 --- --- .697 .687	--- .753 .449 .475 .290	--- --- .449 --- .290
1	80	2.77	.726	.940 --- --- .648 .635	--- .646 .382 .396 .235	--- --- .382 --- .235
1	120	4.15	1.09	.835 --- .502	--- .555 .332	--- --- ---
1	180	6.22	1.64	.649 --- --- .385 .389	--- .406 .227 .259 .140	--- --- .227 --- .140

Note: (i) The values of τ/τ_0, etc., are the maximum resistances.
(ii) $\lambda = \beta/\beta_{cr}$

Compression and Shear FINAS data without Mesh Correction - a/b=1

Table 5.1(a)

a/b	b/t	β	λ	τ/τ_0	σ_x/σ_0	σ_y/σ_0
3	40	1.38	.44	.994	---	---
				---	---	.510
				---	.773	.384
				.695	.632	---
				.751	---	.385
				.811	.534	.266
3	60	2.07	.66	.950	---	---
				---	---	.354
				---	.530	.248
				.681	.443	---
				.781	---	.234
				.704	.332	.155
3	80	2.77	.88	.882	---	---
				---	---	.278
				---	.463	.176
				.554	.405	---
				.686	---	.179
				.639	.269	.102
3	120	4.15	1.32	.700	---	---
				---	---	.213
				---	.332	.127
				.421	.338	---
				.446	---	.136
				.442	.216	.083
3	180	6.22	1.98	.531	---	---
				---	---	.158
				---	.245	.096
				.329	.252	---
				.314	---	.093
				.328	.151	.059

Note: (i) The values of τ/τ_0, etc., are the maximum resistances.
(ii) $\lambda = \beta/\beta_{cr}$

Compression and Shear FINAS data without Mesh Correction - a/b=3

Table 5.1(b)

a/b	b/t	β	λ	τ/τ_0	σ_x/σ_0	σ_y/σ_0	n
1	40	1.38	.363	.997	---	---	
				---	.904	---	
				---	.590	.590	
				.720	.613	---	1.90
				.714	.407	.407	1.94
1	60	2.07	.545	.983	---	---	
				---	.753	---	
				---	.449	.449	
				.697	.475	---	1.52
				.687	.290	.290	1.53
1	80	2.77	.726	.940	---	---	
				---	.646	---	
				---	.382	.382	
				.648	.396	---	1.32
				.635	.235	.235	1.25
1	120	4.15	1.09	.825	---	---	
				---	.555	---	
				.499	.330	---	.876
1	180	6.22	1.64	.629	---	---	
				---	.406	---	
				---	.227	.227	
				.379	.255	---	0.97
				.383	.138	.138	0.93

Note: (i) The values of τ/τ_0, etc., are the maximum resistances.
(ii) $\lambda = \beta/\beta_{cr}$
(iii) n is used in equation 5.6 and is plotted on figure 5.7

Compression and Shear FINAS data corrected for Mesh Size - a/b=1

Table 5.2(a)

a/b	b/t	β	λ	τ/τ_0	σ_x/σ_0	σ_y/σ_0	n
3	40	1.38	.44	.994	---	---	
				---	---	.510	
				---	.773	.384	
				.695	.632	---	1.88
				.751	---	.385	3.01
				.811	.534	.266	2.96
3	60	2.07	.66	.950	---	---	
				---	---	.354	
				---	.530	.248	
				.681	.443	---	1.36
				.781	---	.234	2.72
				.704	.332	.155	1.70
3	80	2.77	.88	.882	---	---	
				---	---	.278	
				---	.463	.176	
				.554	.405	---	1.07
				.686	---	.179	2.11
				.639	.269	.102	1.37
3	120	4.15	1.32	.692	---	---	
				---	---	.213	
				---	.332	.127	
				.418	.336	---	.905
				.443	---	.135	1.16
				.440	.215	.083	1.19
3	180	6.22	1.98	.496	---	---	
				---	---	.158	
				---	.245	.096	
				.318	.244	---	1.04
				.303	---	.090	0.83
				.317	.146	.057	1.02

Note: (i) The values of τ/τ_0, etc., are the maximum resistances.
(ii) $\lambda = \beta/\beta_{cr}$
(iii) n is used in equation 5.6 and is plotted on figure 5.7

Compression and Shear FINAS data corrected for Mesh Size - a/b=3

Table 5.2(b)

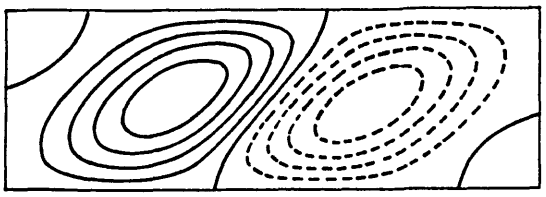

$$\sigma_{cr} = K \frac{\pi^2 E}{12(1-\nu^2)} \frac{t^2}{b^2}$$

(a) τ $K_{xy} = 5{\cdot}84$

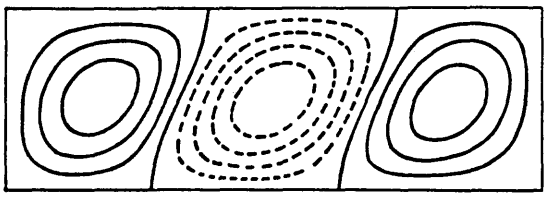

(b) $\tau = \sigma_x$ $K_{xy} = 3{\cdot}0$ $K_x = 3{\cdot}0$

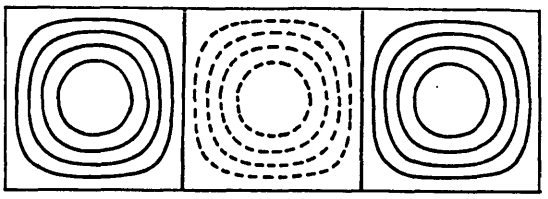

(c) σ_x $K_x = 4{\cdot}0$

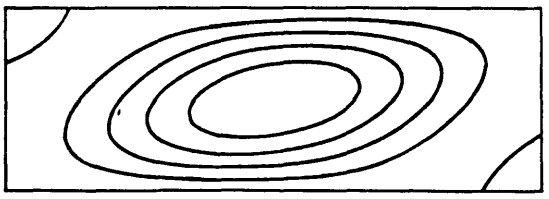

(d) $\tau = 4\sigma_y$ $K_{xy} = 3{\cdot}75$ $K_y = 0{\cdot}95$

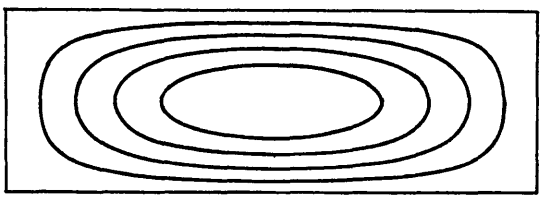

(e) σ_y $K_y = 1{\cdot}2$

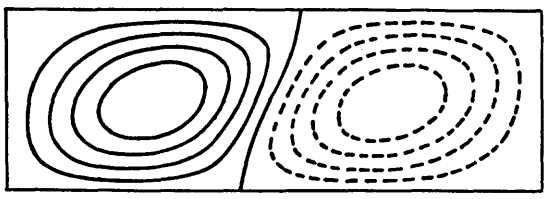

(f) $\tau = \sigma_x = 4\sigma_y$ $K_{xy} = K_x = 2{\cdot}46$

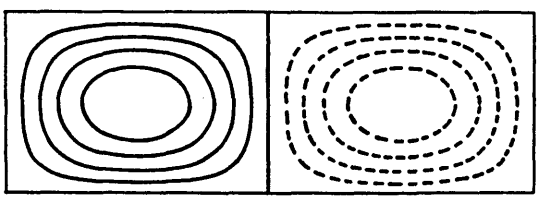

(g) $\sigma_x = 4\sigma_y$ $K_x = 3{\cdot}0$ $K_y = 0{\cdot}75$

FIGURE 5.1 - Shear and compression critical buckling modes - a/b=3

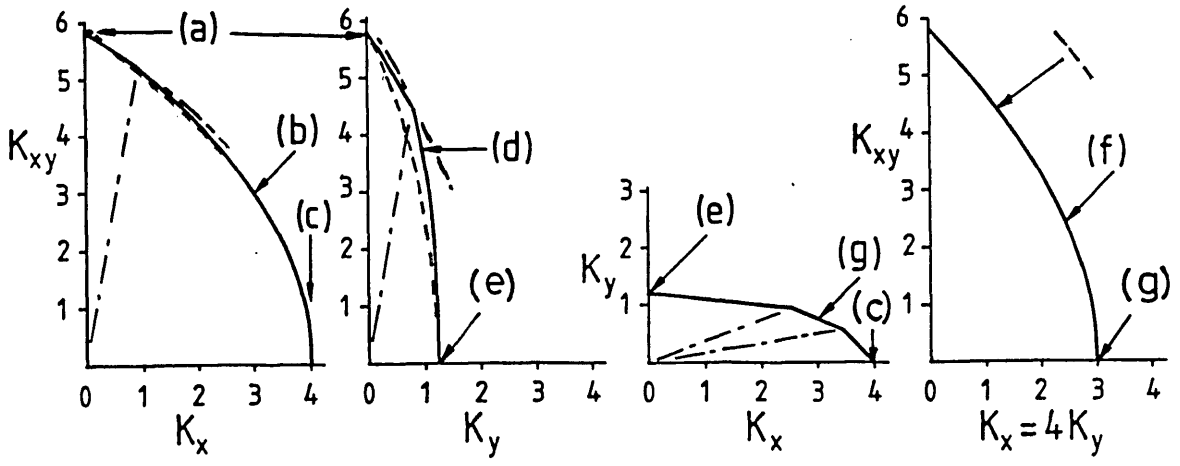

FIGURE 5.2 - Shear and compression critical interactions - a/b=3

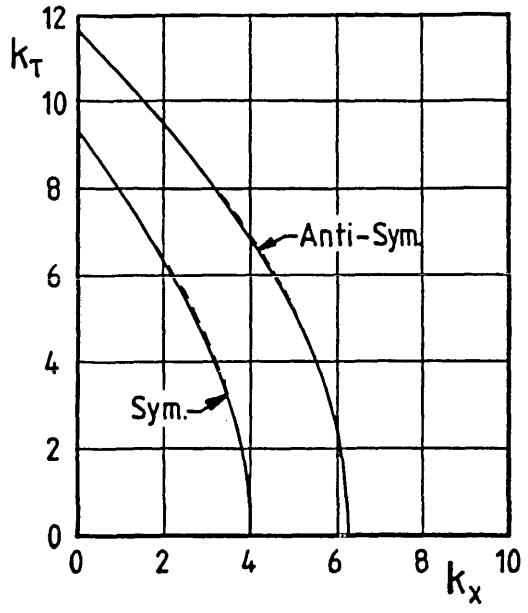

Shear & uniaxial compression critical interactions - a/b=1
FIGURE 5.3

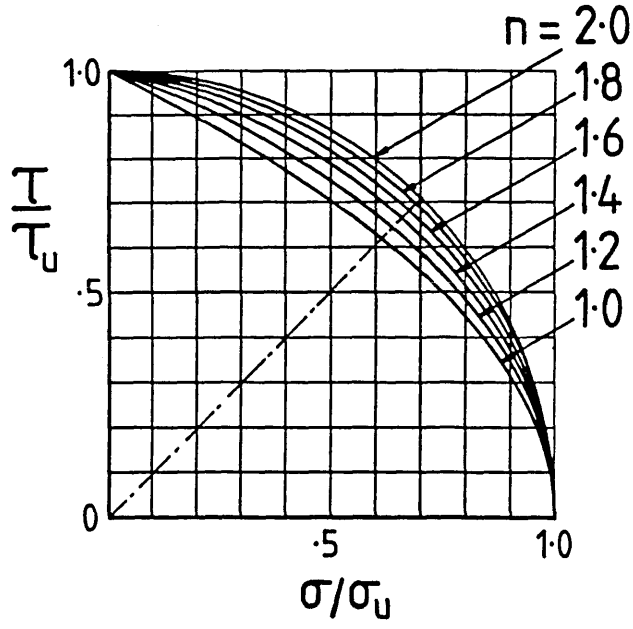

Curves produced by Eq.5.6 for n = 1 to 2
FIGURE 5.5

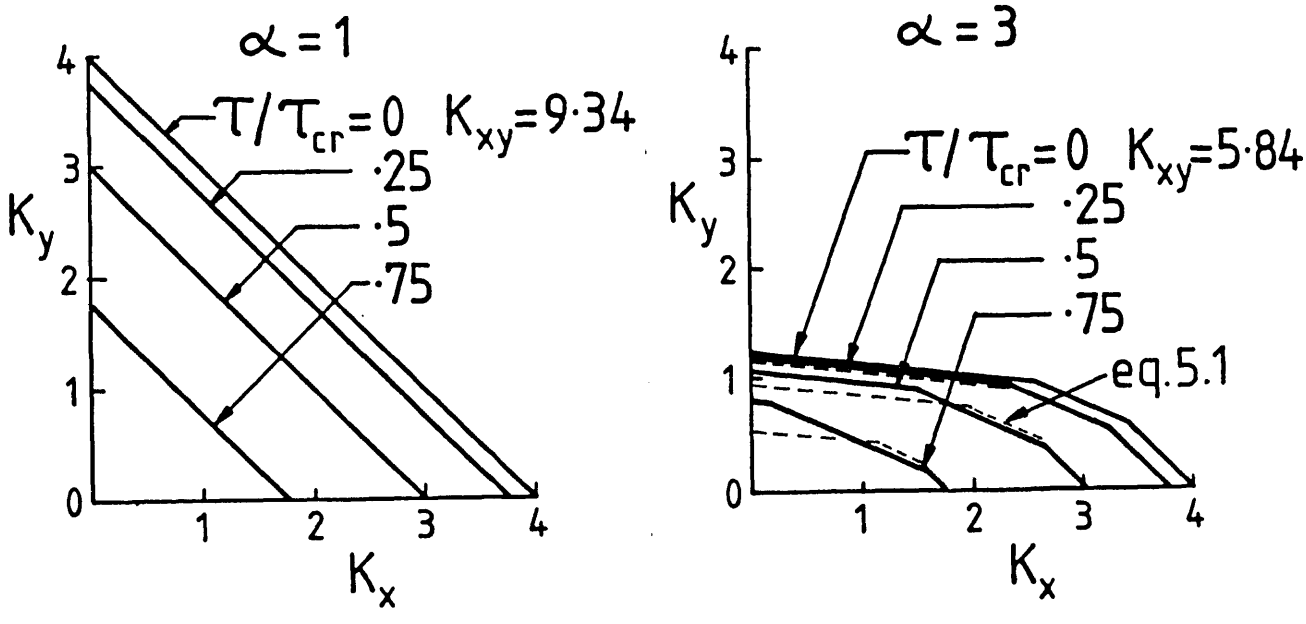

FIGURE 5.4 - Biaxial Interactions with coexistent shear - a/b=1, 3

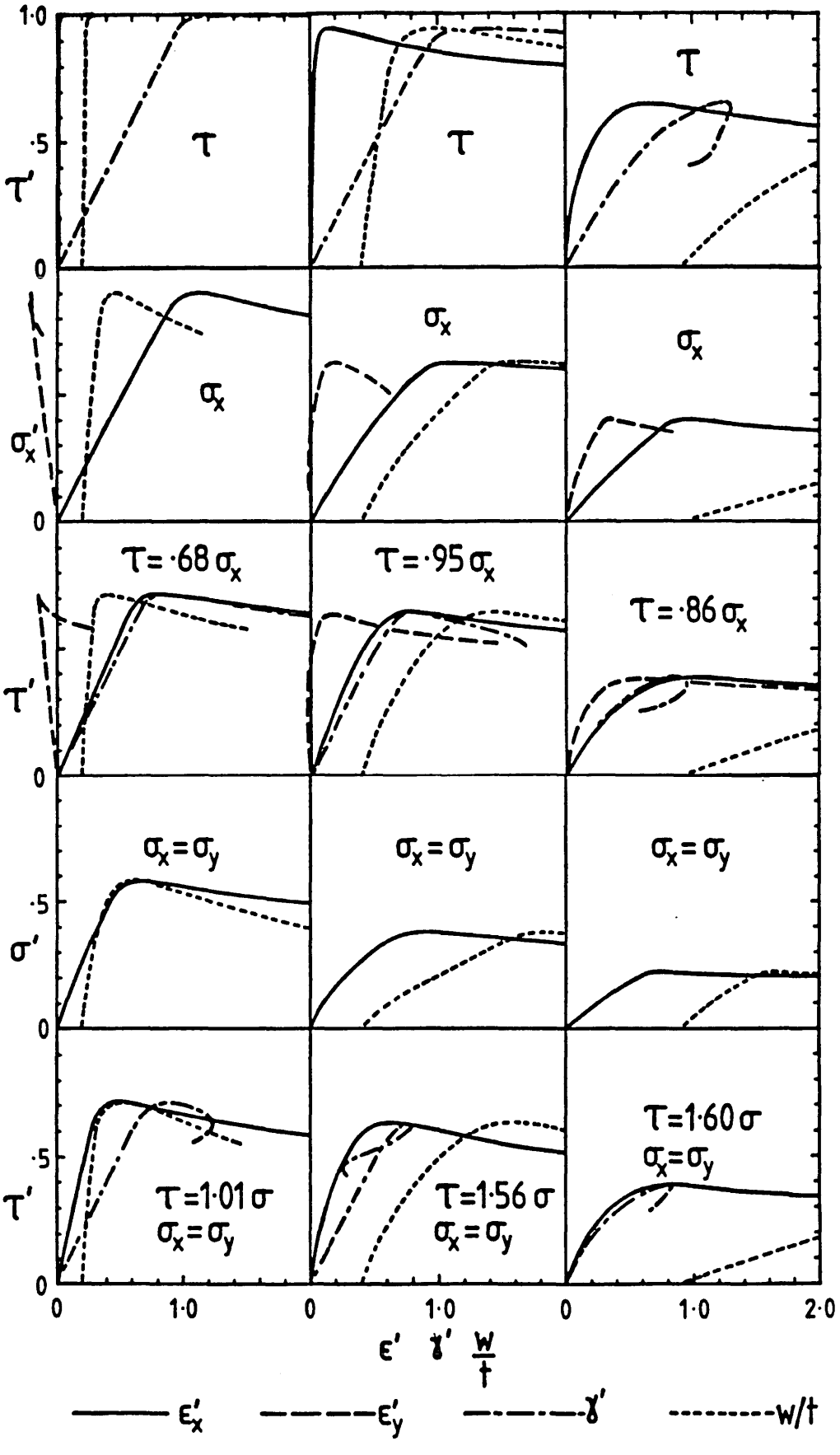

FIGURE 5.6 - Shear & compression stress-strain curves for a/b=1 b/t=40, 60 and 80

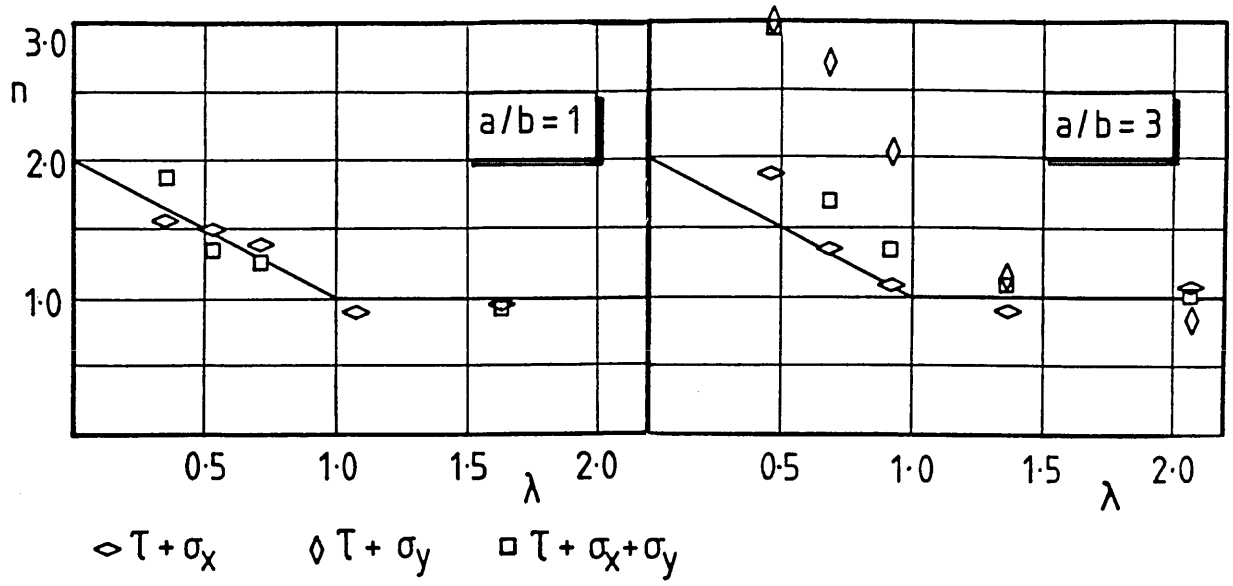

FIGURE 5.7 - Plot of n from Table 5.2 against λ (=β/β_{cr})

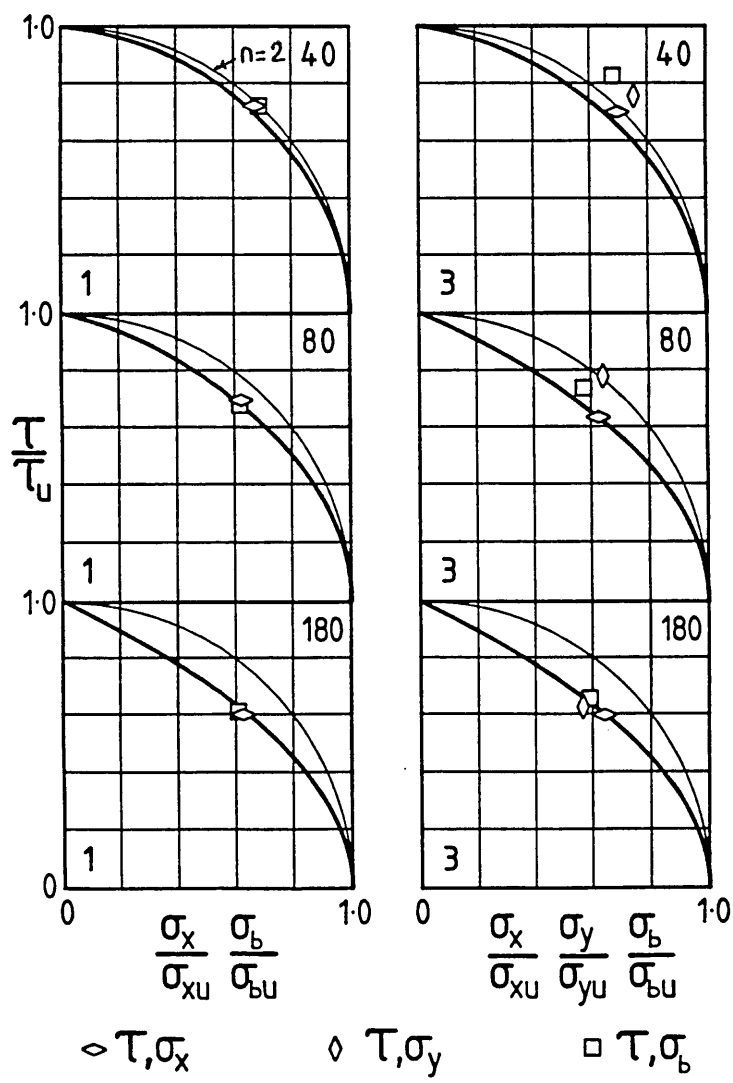

FIGURE 5.8 - Interactions produced by eq.5.6,7 for a/b=1 & 3 b/t=40, 80, 180 - $\tau+\sigma_x$, $\tau+\sigma_y$, $\tau+\sigma_x+\sigma_y$

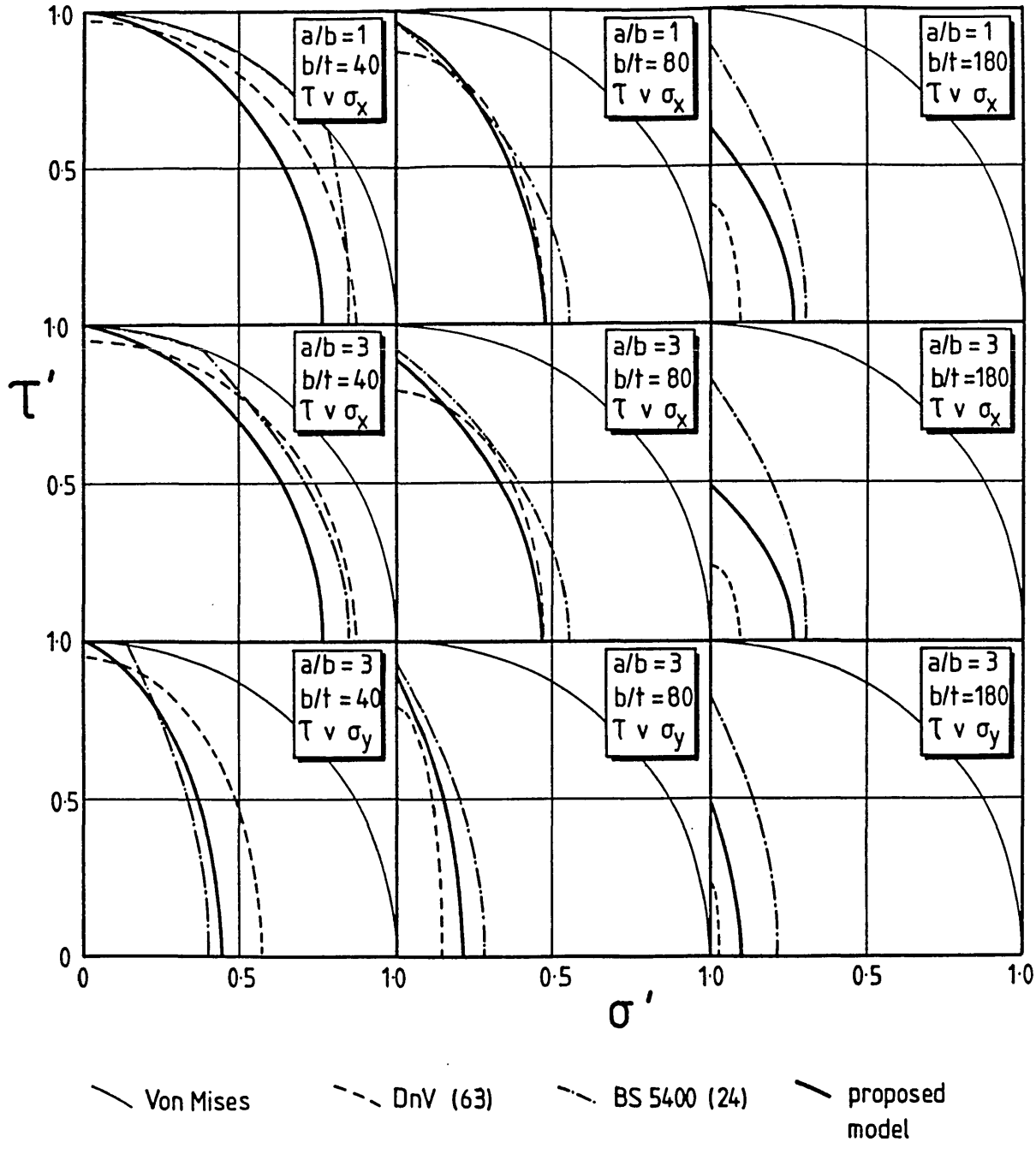

FIGURE 5.9 - Comparison between proposed method and BS5400 and DnV

CHAPTER 6 BIAXIAL COMPRESSION AND LATERAL PRESSURE

6.1 First Yield Model

Before developing a design model for constrained rectangular plates under biaxial compression, σ_x and σ_y, and uniform lateral pressure, Q, it will be useful to discuss some of the basic concepts using a simple elastic solution of the Marguerre equations for the same situation. The discussion of the basic concepts will be in two sections. The first will deal with plates subject to pressure alone, and the second will also include uni-axial and bi-axial compression. Certain qualitative aspects of the behaviour will be introduced by applying first yield criteria to the elastic model. Reference to numerical elastic and elasto-plastic analyses will be made in order to corroborate the elastic model, and to extend the discussion into aspects of behaviour which the model does not consider.

Appendix B presents a relatively simple solution of the non-linear differential equations of the elastic problem of a rectangular simply supported constrained plate subjected to biaxial compression with coexistent lateral pressure. The simplicity of the solution results from the following assumptions:

The first is that the mode of flexural deformation is made up of a single sinusoidal Fourier component for all magnitudes of loading and plate geometries.

The second is that, for rectangular plates which can buckle in a number of different modes depending on the relative ratios and magnitudes of the biaxial compressive stresses and the lateral pressure, the multi-half-wave modes are analysed as a plate panel of a reduced aspect ratio equal to the half wavelength of the buckling mode. This assumption is entirely appropriate for biaxial compression only, as discussed in Chapter 4, as no distinction between the adjacent half waves ensues from the fact that they are buckling in opposite directions. When lateral pressure is also acting, then the adjacent half waves are not equivalent. In the one case the plate will be buckling against the lateral pressure, and in the other case the plate will be buckling in the direction of the lateral pressure. The former regions of the plate will be stiffened against in-plane loading by the lateral pressure which will be trying to reduce the local buckling deformation, whereas the latter regions will be made less stiff due to the lateral pressure increasing the buckling deformation. Mode changes might then occur in which the part of the plate which the pressure is trying to flatten would suddenly snap through the plane of the panel so that the overall buckling mode would change to one with fewer half-waves. The actual modal

behaviour will depend, not only on the ratios of σ_x to σ_y to Q, and on their magnitudes, and on the plate geometry, but also on the order of loading, which in normal design applications cannot be predetermined. As a result, the phenomenon will be a very complex one.

The simplifying assumption made for the higher order modes, therefore, is to consider only that sub-panel with a single buckle which is deforming sympathetically with the lateral pressure, and to ignore the potentially stiffening and strengthening effect of the regions of the plate which deform against the lateral pressure. If, at the same time, all the lower order buckling modes are also considered then the snap through problem might be said to be conservatively allowed for.

Equation B.12 of Appendix B describes an elastic relationship between load and out-of-plane displacement for plates subjected to biaxial compression and lateral pressure. Three specific cases are then derived from the general result, these being uniaxial compression (equation B.14), equal biaxial compression (equation B.15), and lateral pressure only (equation B.17). The third case will be examined first.

6.1.1 Lateral Pressure

In the investigation of lateral pressure in this thesis, it is only the influence of pressure on biaxial compression which is considered. An investigation of the influence of lateral pressure on shear strength, for instance, has not been carried out, nor has pressure loading, as the main design condition, been fully considered.

As a consequence of this latter proviso, the implications of permanent set as a design limit state for plates subject primarily to lateral pressure, or of panel continuity over supporting stiffeners, have not been addressed.

Although an internal panel in a uniform grillage, subjected to uniform pressure, has clamped boundaries, some rotation will occur at the panel boundaries if either the pressure, or the grillage geometry is not uniform. Simply supported edges are a reasonable idealisation for panels subject to biaxial compression, and since it is the influence of pressure on biaxial compression behaviour which is being investigated with a view to producing a design model, it seems reasonable to limit the pressure only investigation to the same simply supported boundary conditions.

Figure 6.1 presents the results of Equation B.17 by plotting lateral pressure, Q, against out-of-plane displacement, w, for 5 imperfect square plates with b/t=40, 60,

80, 100, and 120. The magnitude of imperfection is given by $w_0/t=0.1\beta^2$, as in Chapters 3 and 4, from (47)-(49). The elastic analysis of figure 6.1 does not include residual stresses. As the plate deforms under load, membrane tensions develop in the central region of the plate, and these serve to stiffen the plate against out-of-plane deformation. The effect of this can be seen in figure 6.1. The initial influence of residual stresses on the response of the plate to lateral pressure is due primarily to the biaxial residual compressions which exist in the central area of the plate. Since these biaxial compressions exist in the part of the plate in which the biaxial membrane tension develops due to loading, then the magnitude of these membrane tensions will be reduced, giving rise to a reduction in the "large deflection" stiffening of the plate. As a result, a plate with residual stress will have a greater elastic deformation at a given pressure than will a plate free of residual stress.

The elastic model can be modified to incorporate an approximate allowance for residual stress, by applying to the plate a constant biaxial compression equal to the biaxial residual compressions. The residual tensions along the plate boundaries are being ignored in this approximation, but since they have a negligible influence on the elastic stiffness of the plate, only having a significant influence on the development of plasticity, they can be justifiably ignored. The significance of the residual tensions will be described later.

The general solution of equation B.12, for plates with lateral pressure and biaxial compression is used to provide a lateral pressure model incorporating residual stress. However, if the plate imperfection is set to the desired level of w_0, and the biaxial residual compressions are applied, the plate will deflect further due to the action of the residual stresses, and the out-of-plane displacement prior to the application of any lateral pressure will no longer be the specified w_0. It is, however, possible to find the smaller magnitude of imperfection, w_0', which will give rise to a total buckling displacement equal to w_0 when the biaxial residual compressions are applied. w_0' therefore represents the plate imperfection prior to welding.

To find w_0', the biaxial compression solution, equation B.15, is re-ordered to give a quadratic in the unknown pre-welding imperfection, w_0', as follows:

$$a_0 w_0'^2 + b_0 w_0' + c_0 = 0 \qquad \ldots 6.1$$

where $a_0 = \dfrac{1}{16\ b^2}$

$$b_0 = \frac{1}{6\ (1-\nu^2)} \left[\frac{t}{b}\right]^2 \frac{1}{w_0}$$

$$c_0 = \frac{\sigma_r}{\pi^2 E} - \frac{1}{6\ (1-\nu^2)} \left[\frac{t}{b}\right]^2 - \frac{w_0}{16\ b^2}$$

w_0 is the specified imperfection in the welded structure, and σ_r is the residual compressive stress, taken to be 0.2 σ_0, as in Chapter 3.

This process of applying the estimated biaxial residual compressions to a square plate with reduced imperfection is presented in figure 6.2. This figure plots σ_r/σ_{crb} against w/t, where σ_{crb} is the critical biaxial compressive stress (for equal biaxial stresses). Since the assumption of $\sigma_r=0.2\sigma_0$ and $w_0/t=0.1\beta^2$ results in definitions of σ_r/σ_{crb} and w_0/t which both vary with β^2, and which are therefore proportional to one another, this produces on the figure a straight line through the origin. Every point on that straight line denotes a combination of residual stress and imperfection for a particular slenderness. For b/t=40, 80, 120, 160 and 200, w_0' has been calculated from the solution to equation 6.1, and the buckling deformation incremented to the required level (when the total out-of-flatness is equal to w_0), at which point the biaxial stress is equal to the residual compressive stress. This process is analogous to the development of the compressive buckling which occurs in the plate as the weldments shrink, and follows the imperfect plate buckling curves shown on the figure, which begin at an initial imperfection of w_0', and end on the straight line, at which point the total buckling displacement is equal to $0.1\beta^2$, and the residual stress is 0.2 σ_0.

Also shown on this figure is the post-buckling curve for perfect plates, calculated using the elastic analysis, to illustrate certain aspects of assumed combinations of imperfections and residual stresses. The first point to note is that as a particular combination of w_0 and σ_r approaches the perfect plate buckling curve, as in the case of b/t=120, then the pre-welded plate imperfection, w_0', needs to approach zero, which gives rise to w_0'/t for the b/t=120 case being less than that for the b/t=80 case.

The main point to note is that if a combination of biaxial residual compressions and w_0 were chosen that, for some slenderness, produced a point on this figure which lay above the perfect plate post-buckling curve, then equation 6.1 would cease to have real roots. The implication of this is that such a combination could not occur in reality. Either the residual stresses would be lower than assumed at the specified imperfection level, or residual stress would have caused a greater out-of-plane deformation than the specified imperfection.

This is illustrated on figure 6.3 which plots the σ_r–w_0 lines for $w_0/t=0.05\beta^2$, $0.1\beta^2$, and $0.3\beta^2$, and also $w_0/t=0.145\beta$ (w_0=b/200 for mild steel). The three diagrams in

this figure are for three different levels of residual stress, 0.05 σ_0, 0.2 σ_0 and 0.4 σ_0. It can be seen that certain combinations of imperfections and residual stresses, by lying above the perfect plate post-buckling curve, are in fact incompatible, and the 0.145β specification, which keeps w_0/b constant (at 1/200 for mild steel) for all slendernesses, rather than allowing it to increase with increasing slenderness (as β^2 does) is particularly incompatible with the assumption that residual stress levels do not vary with slenderness.

Although the theoretical model of residual stress in (86) suggests that σ_r should diminish with increasing slenderness as one would expect, it was noted in (86) that ship surveys show residual stress levels typically of the order of a quarter of the yield stress. It may be that any slenderness-dependent variation is being masked by the wide variation in residual stress levels even for the same slenderness, which was reported in (95).

It is possible to use the solution to equation 6.1 to find the maximum level of residual stress that can be used in conjunction with a given imperfection level. This residual stress is given by setting the square root part of the quadratic solution to zero, leading to:

$$\sigma_{rmax} = \pi^2 E \left[\frac{1}{(1-\nu^2)} \left[\frac{t}{b}\right]^2 \left\{ \frac{1}{9(1-\nu^2)} \left[\frac{t}{w_0}\right]^2 + \frac{1}{6} \right\} + \frac{1}{16} \left[\frac{w_0}{b}\right]^2 \right] \quad \ldots 6.2$$

For the four imperfection specifications given above, this function is plotted against slenderness in figure 6.4. It can be seen that w_0=b/200 (w_0/t=0.145β) requires the maximum residual stress to reduce with slenderness, whereas $w_0/t=\beta^2$ allows σ_r to increase for large slendernesses.

It is of interest to note that the particular combination of imperfection and residual stress described as average in (47)-(49), and used in this chapter, falls within the limits of possible combinations of w_0 and σ_r as defined by this use of the elastic model, albeit coming very close to the limits of feasibility for some slendernesses (in the vicinity of b/t=120).

Of course, these purely elastic effects are only one constraint on the maximum possible residual stress. Equation 6.2 takes no account of assumed residual stress levels which exceed the elasto-plastic buckling capacity of the plate, so the increase in maximum σ_r for high slendernesses displayed on figure 6.4 should be regarded as illustrative only. If a symmetric biaxial residual stress equal to σ_r'=0.2 was assumed to exist in a square plate then this would exceed the maximum biaxial strength, given by equation 4.2, for b/t $\geq$ 180.

It may be noted that the contribution to the initial imperfection from angular shrinkage of the welds, the so-called "draw-down" effect, is not being taken into account in this analysis. If draw-down contributes to the initial imperfection, so that the magnitude of w_0 is not entirely due to residual compressive buckling (and to pre-welding lack of fairness), then the restrictions which have been described using the elastic model will be even more severe than has been demonstrated. That is, even smaller levels of residual compression stress will be consistent with a given imperfection level.

Having obtained the reduced imperfection level, w_0', needed for residual stresses to be included in the elastic analysis, equation B.12 can be used to produce pressure-lateral displacement curves with biaxial residual stresses, σ_r. These are shown on figure 6.5, together with the curves of figure 6.1 for square plates having b/t=40, 60 and 80. Also shown are the pressure displacement curves for perfect plates with no residual stresses, produced by using equation B.17 with very small imperfections.

In order to illustrate the effect of the residual tensions on the response of the plate to lateral pressure, an elasto-plastic analysis will need to be used. The elasto-plastic Dynamic Relaxation program of (47)-(49) has already been described in Chapters 3 and 4, in the context of uni- and bi-axial compression. In (47) and (48) it was used to study plates subjected to lateral pressure as well as biaxial compression. Additional pressure only analyses have been carried out using the same program, as part of the current investigation. The same three plates of figure 6.5 have been analysed with the same three variations in initial imperfections and residual stresses. These elasto-plastic analyses are shown on figure 6.5 (as broken lines), so that the elastic model can be compared with them. The load levels at which first surface and first mid-thickness yield occurs in the elasto-plastic analyses are indicated on the corresponding curves.

It can be seen that the elastic model, whether for perfect plates, or imperfect plates with or without residual stress, gives reasonably close agreement with the rigorous analyses, in the elastic regime of plate behaviour, but also, in some cases, for some way into the elasto-plastic regime.

As plasticity develops in the plate the Q-w curves for perfect and imperfect plates without residual stress merge at some level of pressure, after which the two curves are substantially coincident.

A tendency for the Q-w curves to merge can also be observed for imperfect plates with and without residual stress. In the early stages of loading, the curve with residual stress has larger out-of-plane displacements than the case with no residual stress, as was predicted by the elastic model. However, once sufficient plasticity has developed in the plate, the difference in these displacements diminishes. In fact, not only does the Q-w curve with σ_r approach the Q-w curve without σ_r, it can even cross it, leading to smaller displacements at a given level of pressure if residual stress is present than if it is not.

This is due to the second aspect of the influence of residual stresses on the response of a panel to lateral pressure. The first aspect, already remarked upon, was the reduction in the out-of-plane stiffness of the plate due to the residual compressions reducing the membrane tensions. These membrane tensions, which exist, to a varying extent, whether or not there are residual stresses, are reacted by compressions at the edges of the plate. When membrane yield develops in these edge zones of the plate, the average direct strain increases more rapidly than when the edge zones were still elastic. This gives rise to a reduction in the stiffness of the plate against out-of-plane displacements.

In the absence of residual stresses, this 'softening' of the plate will occur when the average strain is in the region of the yield strain, at which point the compressions which develop at the edge of the plate are at yield. A residual tensile yield stress existing at the edges of the plate, however, has the effect of pre-stressing the plate against these edge compressions, effectively delaying the attainment of compressive yield until the average strain in the plate is nearer to twice yield strain than to once yield strain.

Figures 6.6 show pressure plotted against compressive strain along an edge at its mid-point, and also against the average compressive strain in the plate, for the b/t=60 plate both with and without residual stresses. It can be seen that the strain at the mid-point begins to increase rapidly once it reaches the yield strain if there are no residual stresses, but when there are residual stresses this rapid increase in strain occurs nearer to twice yield strain, resulting in the two Q-ϵ curves crossing over. In terms of average strain this permits the Q-ϵ curves to cross over to a much smaller extent.

Having established, in this section, that there is good correspondence between the elastic model and elasto-plastic analyses for plates subjected to lateral pressure, and having used both analyses to bring out features of the behaviour of such plates, further aspects of this behaviour can be demonstrated by applying first yield criteria

to the elastic model as an approximate means of estimating comparative resistance. This will be included in the next section which will broaden the discussion to include externally applied biaxial compression.

6.1.2 Biaxial Compression and Lateral Pressure

Figure 6.7 presents the results of both equations B.14 and B.15, for uniaxial and biaxial compression, in square plates with different levels of initial imperfection. Identical curves are produced in terms of σ/σ_{cr} for both load cases. The format of the figure is taken from figure 4.19 of (73) which is derived using elastic finite difference analyses. These numerical analyses also produce identical curves to the simple elastic model, and are indistinguishable from the curves shown on figure 6.7. The particular equation for uniaxial compression that is produced by the more general solution of equation B.12 is not new and has been used in (94), for instance. It is also reassuring to see the excellent agreement that this component of the elastic model gives with elastic numerical analyses.

The elastic model will be used in this section to explore the effect of pressure on the biaxial compression interaction curve. For this purpose, the limiting compression has been taken as that which causes yield at a specified position. It is not intended to use the elastic model to quantify strength, but it is nonetheless desirable that the chosen position should be such that the limiting compression has a reasonably consistent relation to strength throughout the three dimensional interaction surface, for any plate aspect ratio and slenderness. It is unlikely that first yield on the surface of the plate will be a satisfactory indicator of plate failure as this will only give rise to a gradual loss of plate flexural stiffness. The increasing buckling deformations which will result from the loss of plate flexural stiffness, will be increasingly restrained by the plate membrane stiffness, and it is when the membrane stiffness has sufficiently deteriorated, due to excessive membrane yielding, that the plate buckling deformations and in-plane displacement will no longer be restrained and the plate will fail. As a result a membrane yield criterion is to be preferred.

It was shown in figure 3.19, that using the elastic model for uniaxial compression with an evaluation of membrane yield at the mid-length of the unloaded edge gave a reasonable representation of the variation in aspect ratio which gives minimum uniaxial compressive strength of constrained short plates. Membrane yield at that point should still be a reasonable criterion if lateral pressure is also included in the loading. The general result of equation B.12 (but without σ_y) can be used to plot an interaction between uniaxial compression and lateral pressure. This is done by

first setting the level of lateral pressure, and then incrementing the lateral deflection and calculating the uniaxial compression that would be needed to cause that amount of deflection. The stresses at the mid-length of the unloaded edge can then be found, and the equivalent stress compared to the yield stress. The result of this analysis is presented in figure 6.8, for square plates with b/t=40, 60 and 80, with imperfection magnitudes given by $w_0/t=0.1\beta^2$. Residual stresses are set to zero in the analysis. It is interesting to note that the interaction between uniaxial compression and lateral pressure is very nearly linear.

From the pressure-only Dynamic Relaxation elasto-plastic analyses of imperfect plates without residual stresses, referred to in the previous section, the pressure at which the average direct strain in the plate is equal to the yield strain is obtained, and plotted on the vertical axes of figure 6.8. There is a good correspondence between this yield strain pressure and the elastic model for b/t=40, but the elastic model is significantly conservative for b/t=80. Additional elasto-plastic analyses were carried out to find the uniaxial strength of a b/t=60 plate which is also subjected to 60 metres head of water. The plate is first loaded with the lateral pressure only, and the results of this analysis are used as the starting conditions for a number of proportional straining load-cases. The compressive strength is interpolated at $\epsilon_x'=1$ from the proportional strain analyses, and is shown on the middle diagram of figure 6.8. Also shown on the figure are the uniaxial compressive strengths (at $\epsilon'=1$) in the absence of lateral pressure, calculated using FINAS, from Chapter 4. These analyses also did not include residual stresses, but the imperfection magnitude was $w_0=b/200$, rather than $w_0/t=0.1\beta^2$. It has already been explained, in Chapter 3, why this difference in imperfection specifications will not have a significant effect on the uniaxial strength of square plates. From figure 6.8, it can be seen that the use of the mid-length membrane yield condition in the elastic model gives reasonable qualitative, and occasionally quantitative, agreement with the numerical elasto-plastic analyses.

Figure 6.9 shows the results of applying the mid-length membrane yield condition to the pressure-only elastic model to plot 'failure' pressure against slenderness for square plates with b/t less than 120. Also shown are the levels of pressure to cause $\epsilon_x'=1$ computed using the elasto-plastic analysis for b/t from 40 to 120. The b/t=40 to 80 results are the pressure-only points from the previous figure. Once again, it is evident that there is quite good agreement between the numerical analysis and the elastic model for stocky plates, but that the elastic model is significantly conservative for slender plates.

The previous two figures have used the evaluation of first membrane yield at a single

mid-side point in the plate as a failure criterion. However, membrane yield at a single point is unlikely to be a suitable relative indication of plate failure where there is a marked change in the failure mode as the loading vector moves around the interaction surface. Such a case would be, for instance, the interaction between shear and biaxial compression discussed in Chapter 5. Furthermore, even for the interaction between biaxial compression and pressure for which the mode of deformation does not vary markedly round the interaction surface (as for example in square plates) the position of the point of first equivalent membrane yield will vary with load condition.

In biaxially loaded plates (with or without lateral pressure) first membrane yield could occur on either of the adjacent edges, depending on the biaxial compression ratio. Used as the criterion for producing interaction curves this would give rise to bi-linear interactions even though there had not been a change in deformation mode. A single membrane yield criterion, which is not biased towards any pair of plate boundaries, but which incorporates membrane yielding on the boundaries, is therefore to be preferred for the present qualitative purpose. For this reason membrane yielding at the plate corners is used as an interaction criterion. It is accepted, however, that membrane yield at the plate corners, if it were to occur at all in reality, would generally be preceded by substantial mid-length edge yielding.

Figure 6.10 shows the effect of this corner yield criterion on the pressure-compression interaction for the same three plates (with the same w_0) as in figure 6.8, and it can be seen to produce an interaction which is once again very nearly linear, even though the interaction criteria used in the two figures are different.

Figure 6.11 shows the results of using the corner membrane yield criterion, to derive a set of biaxial interactions with pressure for the same square plates. The interaction curves are for 10 metres head of water increments of lateral pressure (pressure increments of 0.0981 N/mm^2). The even spacing of the interaction end-points for equal pressure increments, which is evident on the figure, is consistent with the almost linear interactions of figure 6.10.

On figure 6.12 the interactions of figure 6.11 are non-dimensionalised to end at unity on the axes. It is clear that the non-dimensionalised shape of the biaxial compression interaction not only becomes more straight with increasing slenderness (as was found in the biaxial compression data referred to in Chapter 4), but also with increasing pressure, and that this latter effect itself is also a function of slenderness. This interaction behaviour is quite complex to be modelled in a straightforward

enough manner for use in design. It is interesting to note from figure 6.11 that this straightening of the non-dimensionalised interactions, as pressure is applied, is approximately consistent with a translation of the zero pressure interaction in the 45 degree direction (ie down the line $\sigma_x=\sigma_y$). Lines, projected at 45 degrees, from the outer interaction to the end-point and mid-point of an interaction in the presence of pressure are shown on figure 6.11. That these projection lines are of approximately equal length for a particular slenderness indicates that the outer curve can be translated to form the inner curves.

Figure 6.13 shows the biaxial compression interactions, with no lateral pressure, for 3:1 plates with b/t=40, 60 and 80. It is worth noting that the intermediate 2 half wave mode, which was prevented from occurring by the analyses of (47)-(49), makes only a minor contribution to the net (ie the inner envelope) interaction in comparison to its contribution to the net elastic critical buckling interaction of figure 4.1. This point was also observed in the design model of chapter 4.

Figure 6.14 shows the interactions between lateral pressure and transverse uni-axial compressive strength in 3:1 plates, with 1, 2 or 3 half wave deformation modes, for b/t=40, 60 and 80. Because of the assumptions of the elastic analysis these can alternatively be regarded as the pressure-transverse compression interactions of 3:1, 1.5:1 and square plates, respectively, where the deformation mode in each case is the preferred single half wave. It can be seen that the elastic model predicts that the transverse strength of rectangular plates reduces in a linear fashion as lateral pressure is applied, and that this reduction is more severe for the longer wavelengths.

The interaction between lateral pressure and longitudinal strength in 3:1 plates for each of the 3 possible buckling modes is shown in figure 6.15. For ease of comparison the transverse compressive strength interaction with pressure for the m=1 buckling mode from the preceding figure is also shown (as a chain line). The figure shows that the interactions between longitudinal strength and pressure for the m=1 and m=2 modes are very convex, and that the intermediate, m=2, mode does not contribute to the net interaction.

Figure 6.16 presents biaxial compression interactions including lateral pressure, for the same 3:1 plates. These plates have again been allowed to deform in the 3 possible modes but, for the sake of clarity, only the inner envelope of the resulting interactions for each of the modes is shown. Even for the non-square buckling modes, the curves produced by the model suggest that the biaxial interaction in the absence of pressure, for a given mode, can be translated to produce the equivalent interaction in the presence of pressure. However, the direction of this translation

for the m=1 mode, for instance, is much nearer to the vertical than to the 45 degree line of the interaction for a square buckling mode.

The first yield model of Appendix B, with occasional reference to elasto-plastic analyses, has allowed the qualitative behaviour of square and rectangular plates subject to biaxial compression and lateral pressure to be introduced. Aspects of the behaviour that could be useful in devising a design model have been presented. Making further reference to elasto-plastic solutions, the design model will now be developed, beginning with a treatment of square plates.

6.2 Design Model for Square Plates

Maximum Resistance

Figure 6.17 shows the biaxial compression interaction curves from (48) for square plates of slendernesses b/t=40, 60 and 80. The interaction curves were produced as the envelope to σ_x-σ_y trajectories computed for proportional biaxial straining. In terms of proportional stressing, therefore, these interactions represent the maximum net stresses sustained by the panels. Lateral pressures equivalent to 0, 10 and 20 metres head of water were applied to the plates, prior to the application of the biaxial straining. The zero pressure case is part of the wider body of biaxial compression data that has already been referred to in Chapter 4. The residual stress and imperfection assumptions in (48) have already been described in Chapter 3. For square plates these amounted to a biaxial compressive residual stress equal to 0.2 σ_0, and a single sinusoidal half-wave of a magnitude given by $w_0/t=0.1\beta^2$.

From this figure we can see a qualitative similarity with the results of the simple first yield elastic model shown in figure 6.11. The end-points of the interactions for each of the three slendernesses considered in (48) reduce in a uniform fashion as lateral pressure is applied, as was found in figures 6.8 and 6.10. The values of these end-points are plotted against lateral pressure in figure 6.18, which confirms that the pressure-compression interaction is very nearly linear in the pressure range shown.

However, only for b/t=80 is the interaction in the presence of pressure a translation of the zero pressure interaction. The same projection lines, as on figure 6.11, are included on figure 6.17. It is clear that to translate the outer curve in the 45 degree direction would result in conservative predictions of biaxial compressive strength in the presence of pressure for b/t=40 and 60.

None the less, the degree of conservatism may not be great, and the notion of a 45 degree translation does offer a simple means of representing the change in the biaxial strength interaction due to pressure. To test this hypothesis, the biaxial interaction curves produced by the model of Chapter 4 should be translated down the 45 degree line until they cross the x and y axes at the values of compressive stress corresponding to linear reductions in uniaxial compressive strength caused by lateral pressure. If the maximum stress model of Chapter 4 is used, it will enable the effect of the 45 degree translation to be compared with the numerical results of (48).

A linear interaction between Q and σ_x requires the pressure end-point to be defined. For the three slendernesses analysed in (48) the compressive strengths on figure 6.18 can be extrapolated to obtain the value of pressure at which the compressive strength is zero. This extrapolation is shown as broken lines on figure 6.18, and arrives at pressure-only end-points of 160, 96.5 and 75 metres head of water, for b/t=40, 60 and 80 respectively. These pressures are assumed in this idealisation to be the levels of pressure at which the in-plane uni-axial compressive strength is zero. It would require a substantial amount of additional analysis in order to corroborate these end-points, however. Later in this chapter a definition of these end-points which may be more appropriate for design will be given, and this will be supported by numerical analysis. It will be found that linear extrapolations such as those on figure 6.18 are either appropriate or conservative, and indeed that linear extrapolation is more conservative for the stockiest plates. This is reassuring since the extent of the extrapolation is greatest for these stocky plates.

To permit the model to be developed in a way which allows direct comparison with the maximum resistance results of (48), it is necessary to define the pressure end-points in the above manner.

It is now necessary to produce a simple algebraic representation of these extrapolated pressure end-points. In order for this algebraic expression to have a rational parametric dependence, it can usefully be based on a simple yield line analysis, with an empirical adjustment to fit the data. If a yield line analysis, which ignores membrane effects, is applied to a square plate, then it will result in a failure mechanism composed of plastic hinge lines along the diagonals, and a level of pressure to cause this mechanism given by:

$$Q_{YL} = 6 \frac{\sigma_0}{E}^2 \frac{1}{\beta^2} \qquad \ldots 6.3$$

where β is the non-dimensional plate slenderness. A more sophisticated yield line analysis exists which includes the influence of membrane stress distributions (101), but

this has the disadvantage, for the present purpose, of being much more complicated to calculate. Equation 6.3 is plotted against slenderness on figure 6.19a, with the extrapolated pressure end-points also shown. Figure 6.19b shows the ratio between the extrapolated end-points and the yield line pressures.

The greater significance of membrane effects in slender plates than in stocky plates is apparent in figure 6.19(b). For instance, for the b/t=40 plate the extrapolated pressure end-point is 1.6 times the yield line pressure, but for the b/t=80 plate this value is 3.2, demonstrating the increase in conservatism, as slenderness increases, of yield line models which ignore membrane effects. A parabolic (or similar) curve could be fitted to these values, which would pass through unity at zero slenderness. Alternatively, a straight line can be plotted to fit the data which would conservatively reach unity at approximately b/t=20. This trend in the data tells us that simple yield line analyses become quantitatively reasonable models of the behaviour of plates under lateral loads for plate slendernesses less than b/t=20. (One may observe, in passing, that this is the range of slendernesses found in the elements of steelwork connections, such as an end-plate deformed by bolt forces, where the use of such yield line analyses in design is well established.)

A straight line drawn through the data which has a conveniently simple description, is given by:

$$Q_{xu}/Q_{YL} = (\beta+.3) \qquad \ldots 6.4$$

In the absence of further data it is prudent to limit the use of this expression to β less than 3 (b/t = 86). In addition, equation 6.4 is not used when β is less than 0.7, when Q_{xu}/Q_{YL} is set to unity instead. As a result we have:

$$Q_{xu} = \left\{ \begin{array}{ll} 6\,\frac{\sigma_0^{\,2}}{E}\,\frac{1}{\beta^2} & ;\ \beta < .7 \\ 6\,\frac{\sigma_0^{\,2}}{E}\left[\frac{1}{\beta}+\frac{.3}{\beta^2}\right] & ;\ .7 \leq \beta \leq 3 \end{array} \right\} \qquad \ldots 6.5$$

Equation 6.5 is included on figure 6.19.

Based on a linear interaction, the reduced uniaxial compressive strength in the presence of pressure, σ_{xq} is given by:

$$\sigma_{xq} = \left[1 - \frac{Q}{Q_{xu}}\right] \sigma_{xu} \qquad \ldots 6.6$$

The zero pressure interaction has previously been given, as equation 4.1, as follows:

$$\left[\frac{\sigma_x}{\sigma_{xu}}\right]^2 + \eta\left[\frac{\sigma_x}{\sigma_{xu}}\right]\left[\frac{\sigma_y}{\sigma_{yu}}\right] + \left[\frac{\sigma_y}{\sigma_{yu}}\right]^2 = 1 \quad \ldots 6.7$$

in which η, the measure of the convexity of the interaction, is obtained from the relationship between the empirically defined uniaxial and biaxial compressive strengths, the latter being for equal biaxial stresses. Due to symmetry, σ_{yu} is equal to σ_{xu}. If this interaction is to be translated in the 45 degree direction to such an extent that the end-points will reduce to some new value, σ_{xq} (where σ_{xq} is the uniaxial strength in the presence of pressure given by equation 6.6), then the new biaxial compressive strength on the 45 degree line, σ_{bq}, will be reduced from the zero pressure biaxial strength, σ_b (from equation 4.2), by an amount σ_{q0}, in accordance with the solution of a quadratic equation, giving:

$$\sigma_{bq} = \sigma_b - \sigma_{q0} \quad \ldots 6.8$$

$$\text{where } \sigma_{qo} = \sqrt{\frac{\sigma_{xq}^2}{4} + \left[\frac{\sigma_{xu}^2 - \sigma_{xq}^2}{2\eta}\right]} - \frac{\sigma_{xq}}{2}$$

An approximation, then, of the translated form of the zero pressure curve is to calculate a new value of η, say η_q, in exactly the same fashion as before, in equation 4.3, but now using σ_{xq} and σ_{bq} calculated as above, instead of σ_{xu} and σ_b. This gives:

$$\eta_q = \left[\frac{\sigma_{xq}}{\sigma_{bq}}\right]^2 - 2 \quad \ldots 6.9$$

This new cross-product coefficient, η_q, with the new values of the interaction end-points, σ_{xq} and $\sigma_{yq}(=\sigma_{xq})$, can then be used in:

$$\left[\frac{\sigma_x}{\sigma_{xq}}\right]^2 + \eta_q\left[\frac{\sigma_x}{\sigma_{xq}}\right]\left[\frac{\sigma_y}{\sigma_{yq}}\right] + \left[\frac{\sigma_y}{\sigma_{yq}}\right]^2 = 1 \quad \ldots 6.10$$

to produce the new biaxial compression interaction, in the presence of lateral pressure. This has been done, and the result compared with figure 6.17, in figure 6.20. The model gives predictions of biaxial strength in the presence of pressure for b/t=40 and 60, which are generally conservative by about 2% or 3%, with a maximum 7% conservatism in the case of equal biaxial compression with 20 metres of pressure in a b/t=40 plate. The discrepancy which exists at b/t=80 occurs at all pressure levels, and is as a result of a slight conservatism in the uniaxial strength model of equation 3.3 at b/t=80. The application of a linear interaction to the end-points of the biaxial interactions, using the modified yield line pressure model, corresponds well with the results of (48). This can now be used to produce maximum strength design curves for a range of slendernesses and pressures in figure 6.21.

Yield Strain Resistance

If, for design purposes, the panel strength given by the model is alternatively defined as being the resistance of the panel when opposite boundaries draw together by an amount equivalent to the yield strain, then a consistent definition of the pressure-only end-point, Q_{xu}, of the $Q-\sigma_x$ linear interaction, is that pressure which on its own causes the same amount of boundary displacement. That is, Q_{xu} is the pressure which causes the square plate boundaries to shorten with an average level of strain equal to the yield strain. Although this definition of Q_{xu} is required for a consistent model of the influence of pressure on the biaxial compression interactions, it is, in itself, a potentially useful design limit for panels subject primarily to pressure loading.

Pressure-only elasto-plastic analyses were attempted of square plates up to b/t=200 with $w_0/t=0.1\beta^2$ and $\sigma_r'=0.2$. However, the use of a residual stress level which does not reduce with slenderness gave rise to numerical convergence difficulties in the initial stages of the dynamic relaxation calculation, prior to the application of lateral pressure for the most slender plates. This initial stage of the calculation is necessary to bring the initial imperfection profile and the residual stress field into equilibrium, and is analogous to following the buckling curves on figure 6.2, from a stress-free state with a pre-welding imperfection, w_0', to a biaxially compressed state with a post-welding imperfection, w_0. The dynamic relaxation program brings the specified σ_r and w_0 into equilibrium by a process of iterative adjustments to the residual stress field and the imperfection profile, and this process is described in (47).

The main cause of the convergence breakdown is the tendency of residual compressions which are significant in relation to the biaxial critical buckling stress to cause large buckling displacements, and hence to give rise to significant departures from the assumed rectangular initial stress distributions and also from the initial sinusoidal imperfection profile. In the case of the b/t=200 plate there is an additional cause for convergence breakdown, in that $\sigma_r'=0.2$ is greater than the biaxial compressive strength of the plate. The maximum resistance design model is not valid for b/t>180 (in mild steel) but at this slenderness it predicts (albeit slightly conservatively) a biaxial strength equal to $0.2\ \sigma_0$. It is beyond the scope of the present work to make a proper re-examination of appropriate levels of residual stress, and one suspects that not enough survey data has been obtained to permit a statistically justified assumption about representative levels of residual stress that would describe the slenderness-dependency of σ_r.

As a result of the convergence difficulties, it was found to be necessary to reduce the

residual compressions to σ_r'=0.18, 0.15, 0.15 and 0.07 for b/t=100, 120, 140 and 200 respectively. If one assumes that a residual stress level of about 0.2 is an appropriate assumption for design, then these reductions in σ_r', with the exception of the b/t=200 case, can be expected not to have a significant effect on the utilization of the analytical results. The b/t=200 result, on the other hand, should clearly be regarded as an upper bound only, at least if $\sigma_r' \simeq 0.2$ is, in fact, appropriate for design at this slenderness. The yield strain pressures obtained from the analyses are plotted against slenderness in figure 6.22(a).

Although the intention had been to carry out this analysis for b/t=20, this case turned out to be time-consuming and labour-intensive using the dynamic relaxation method due to the extensive yielding which develops at this slenderness. Fortunately, for reasons discussed below, this result proved unnecessary.

The in-plane stress-strain curves presented in (48) for cases with coexistent lateral pressure are shown to begin at zero strain for zero stress. Therefore the strain due to the lateral pressure is not included in the given strain. If a strain criterion is to be used to define panel resistance, and since the application of lateral pressure forms part of the loading event, then the strain caused by the pressure must be included. These strains have therefore been taken at the 10 and 20 metre pressure levels from the analyses performed as part of the current investigation. By adding these pressure-only strains to the strains due to in-plane loading, and interpolating between proportional strain stress-strain curves at a total strain equal to yield, the uniaxial compression resistance (at ϵ_x'=1) in the presence of pressure can be found. Figure 6.23 demonstrates this for the b/t=60 plate. Although the interpolation need only be carried out at a total strain equal to the yield strain, this figure shows complete cross-plotted uniaxial compression stress-strain curves (ie σ_y=0) at 0, 10m and 20m pressure. The origins of the stress-strain curves in the 10 and 20 m cases have been offset along the strain axis by the amount of average strain in the plate after the pressure has been applied. Indicated at ϵ_x'=1 on the stress-strain curves are the reduced compressive strengths in the presence of pressure, which are then plotted against pressure on figure 6.24, together with the equivalent points for b/t=40 and 80. It should be noted that the residual strains are not included in this evaluation of strain limits.

The yield strain pressures from figure 6.22 for b/t=40, 60 and 80 are also shown on figure 6.24, and straight lines have been drawn from these pressure-only points to the compression-only points. It can be seen that the pressure-compression data lie below these straight lines for b/t=40 and 60, but are almost on the line for b/t=80.

There is a large gap in the data, however, for compressive strengths at pressures below the pressure-only end-point of the interaction, but above the 20 metre level. For the particular case of a b/t=60 plate without residual stresses, figure 6.8 presented three data values which lent additional support to a quasi-linear interaction, and these values are repeated here on figure 6.25. The b/t=60 points from figure 6.24 are also shown on this figure, and in both cases straight lines are drawn between the pressure and compression end-points.

Both with and without residual stresses the interactions between pressure and uniaxial compression fall below the straight line drawn between the interaction end-points, but the figure suggests that the case without residual stress is closer to the straight line than is the case with residual stress.

Analyses covering a wider range of slendernesses and pressure levels would be needed in order to define properly the shapes of these interactions and the extent to which they lie below straight lines. Such analyses are not needed, however, in order for a safe and simple design model to be proposed. The straight line interaction which was suggested by the elastic model has been shown to be a reasonable representation of the elasto-plastic behaviour of slender plates or plates with low or zero residual stress, but to be unsafe for use with stocky plates. As a result, for a linear interaction to be safe for stocky plates the pressure end-point would have to be obtained from an extrapolation to the pressure axis of the compressive strengths at 0, 10 and 20 metres of pressure, similar to that used in figure 6.18. The extrapolations are shown as broken lines on figure 6.24, and result in reduced pressure end-points of 120m, 61m and 44m, for b/t=40, 60 and 80, respectively. These extrapolated pressure end-points are plotted on figure 6.22(a). The corresponding computed pressure end-points are 151m, 75m and 47m. The better agreement between extrapolated and computed pressures, as the plate slenderness increases, again illustrates the point that the computed interactions are much more linear for slender plates, than for stocky plates. The trend of the comparison between computed and extrapolated end-points suggests that the interactions will become increasingly straight for slendernesses greater than b/t=80, or perhaps that they may even lie above a straight line. In either case, a straight line drawn to a computed pressure end-point will be reasonable or safe, and hence suitable for design. For plates more stocky than b/t=40, however, a computed pressure end-point could not be safely used with a linear interaction, which justifies abandoning the onerous b/t=20 analysis referred to above.

A similar process to that used in figure 6.19 is followed in figure 6.22 to arrive at an empirical adjustment to the basic yield line model. The yield line model of

equation 6.3 is drawn on figure 6.22(a), and the ratio between this model and the computed and extrapolated pressures are plotted on figure 6.22(b). A notable feature of this figure is that the computed points fall very closely on a straight line (shown as a broken line) with the exception of the b/t=200 point which had a significantly smaller residual stress, and lies above the straight line.

This line can be used to help to define the empirical adjustment factor to be applied to the yield line equation. A solid parallel line has been drawn which has a value of unity at β=0.5 (b/t=14.5). It is then curtailed for smaller values of β, implying that unadjusted yield line analyses may be used for b/t less than 14.5. In the absence of data for more slender plates, the other end of the line is curtailed at β=7.5 (b/t=217) where it reaches an ordinate of 3. This can be expressed as:

$$\frac{Q_{xu}}{Q_{YL}} = \left\{ \begin{array}{ll} 1 & ; \beta \leq 0.5 \\ \frac{6}{7} + \frac{2}{7}\beta & ; 0.5 < \beta \leq 7.5 \end{array} \right\} \quad \ldots 6.11$$

If equation 6.11 is used to modify the yield line equation then the following model results

$$Q_{xu} = \left\{ \begin{array}{ll} \frac{\sigma_0^2}{E}\frac{6}{\beta^2} & ; \beta \leq 0.5 \\ \frac{6}{7}\frac{\sigma_0^2}{E}\left[\frac{2}{\beta} + \frac{6}{\beta^2}\right] & ; 0.5 < \beta \leq 7.5 \end{array} \right\} \quad \ldots 6.12$$

Equation 6.12 is shown on figure 6.22(a).

The linearity of the relationship between the numerical data (which include membrane effects) and the yield line analysis (which ignores membrane effects) is sufficiently interesting to warrant additional examination. The elastic analysis of section 6.1, and figure 6.9, takes into account the membrane stresses which develop in the plate, but if the second term in the square brackets of equation B.18 is dropped (this term containing a cubic polynomial in the lateral displacement, $k=w/w_0$), then a linear relationship between pressure and displacement is given which ignores the development of membrane stresses (and which would be derived from small deflection theory). The original large deflection expression (equation B.18) and the small deflection sub-set of it have each been used to find the pressures at which surface yield first occurs at the corners of the plate due to large deflection and small deflection theory, and the ratio between these pressures has been plotted against slenderness (up to b/t=200) on figure 6.22(c). It is apparent from the figure, that the large deflection and small deflection elastic models (with a consistent yield criterion) are related in an approximately linear manner, of a similar qualitative nature to figure 6.22(b).

Equation 6.12 is used with the "average" curve of equations 3.15, and equations 6.6 and 6.8 to 6.10, to produce the range of design curves for square plates given in figure 6.26. The reduced radius Von Mises ellipse of equation 4.9 is used to truncate the design interaction curves.

In this section, a design model for square plates has been developed, which has been formulated using two alternative assumptions for resistance to biaxial compression and pressure. The first assumption was made to be directly comparable with published results, the second was considered to be more appropriate for design. It is now possible to use this treatment of square plates to develop a more general design model for rectangular plates.

6.3 Design Model for Rectangular Plates

In Chapters 3 and 4 it was pointed out that the imperfection mode assumed in (47)–(49) gave rise to overestimates of strength in wholly, or predominantly, longitudinally compressed rectangular plates with significant ripple imperfections. In Chapter 3 this overestimate was corrected by using the uniaxial strength of square plates to define the longitudinal strength of rectangular plates. In Chapter 4 the correction required the biaxial interaction curves for square plates to be used wherever they lay within the interaction curves for rectangular plates.

In Section 6.1, the point was made that the buckling mode taken up by rectangular plates under biaxial compression and lateral pressure depends on the ratio and magnitudes of the three load components, and on the order in which they are applied. Even with lateral pressure acting, a 3:1 plate can still deform in an m=3 buckling mode when the transverse compression is much less than the longitudinal compression. Whether the plate deforms in an m=3 or m=1 mode will depend, not only on the ratio of in-plane loads, but also on the coexistent lateral pressure, and the plate slenderness.

If, in the m=3 mode, the stiffening and strengthening effect of the half-wave which is deforming against the lateral pressure, is ignored, as in the elastic model, then this mode is conservatively allowed for by using that part of the square plate interaction curves in the presence of pressure, which lies within the corresponding rectangular plate curves, in an identical fashion to that employed in Chapter 4. Figure 6.27 shows the 3:1 plate interaction curves from (48) (based on a composite w_0), with the square plate curves indicated where these lie within the rectangular plate curves. It can be inferred from this figure that even at 20 metres pressure a b/t=40 plate under

in-plane loading which is mainly longitudinal will prefer to buckle in three half-waves, but that at that same pressure, a b/t=80 plate with the same ratio of σ_x to σ_y will buckle with only one half wave. This point is confirmed by the composite w_0 analyses which showed, in the former plate, a predominance of the m=3 buckling mode component, even though the magnitude of that component in the imperfection was only one third of the magnitude of the single half-wave component, and despite the lateral loading being applied prior to any in-plane loading, which might be expected to predispose the plate to deform in a single half-wave mode. In the b/t=80 plate the deformation was predominantly in the single half-wave mode since 20 metres pressure is a larger fraction of the maximum pressure that a b/t=80 plate can sustain than it is for a b/t=40 plate. These results indicate the complex modal behaviour which ensues from the variation in the response to lateral pressure and in-plane loads at different slendernesses.

The quasi-linear net interaction between pressure and uniaxial longitudinal or transverse compressive strength, which was exhibited by the elastic model for a given mode, and which was found to a lesser extent in the elasto-plastic square plate analyses, is also exhibited by the rectangular plates. Figure 6.28 shows the transverse compression end-points of figure 6.27 plotted against pressure. Straight dashed lines have also been drawn which closely fit the points.

As a means of describing the interaction between biaxial compression and pressure for rectangular plates, an extension is now proposed of the concept of Chapters 3 and 4, whereby the rectangular plate is partitioned into doubly curved end-regions which together behave like a plate of square or longer than square aspect ratio, and the remaining central region which deforms with single curvature.

If the pressure end-point of the Q-σ_y interaction, Q_{yu}, is known in addition to the σ_{yu} end-point (from equation 3.4), then at some lesser value of pressure, Q, the average σ_y stress that can be sustained by the panel in the absence of longitudinal compression can be defined in a similar way to equation 6.6, as:

$$\sigma_{yq} = \left[1 - \frac{Q}{Q_{yu}} \right] \sigma_{yu} \qquad \ldots 6.13$$

Equation 6.13 can be applied, not only to the plate as a whole, but also to the end regions of the plate (whose aspect ratio is given by equation 4.6) to calculate the local transverse compressions at the ends of the plate which are needed to cause failure there in the presence of the given level of lateral pressure. Consideration of equilibrium normal to the long edge of the plate will produce the lower level of transverse compression (or perhaps tension) which must exist in the central region of

the plate. This compression or tension is, in effect, the uniaxial capacity of the beam-strut or beam-tie which can be said to exist in the central part of the plate when pressure is acting on the plate. It should be noted, however, that the beam-strut capacity will degenerate to that of the strut, as the pressure is reduced to zero. This is because the beam-strut capacity is inferred from the transverse capacity in the presence of pressure of the panel as a whole, which (via equation 6.13) is calculated from the transverse capacity in the absence of pressure. This latter capacity is calculated from equation 3.4, and incorporates the strut models of equations 3.5 and 3.6, or 3.7. The beam-strut capacity is therefore given by:

$$\sigma_{cq} = \frac{\left[\sigma_{yq_1} - \frac{\alpha_b}{\alpha_p}\sigma_{yq}\right]}{\left[1 - \frac{\alpha_b}{\alpha_p}\right]} \quad \ldots 6.14$$

where σ_{yq} is from equation 6.13 for a plate of aspect ratio α_b, and σ_{yq_1} is from equation 6.13 for a plate of aspect ratio α_p. α_p is from equation 4.6, and α_b, the aspect ratio of a half-wavelength of buckle is in accordance with the treatment of biaxial compression buckling modes in Chapter 4.

If longitudinal (σ_x) compression is applied in addition, then, as before, the biaxial interaction for the end regions, but now modified due to the presence of pressure, can be applied to those parts of the plate. Furthermore, just as for in-plane loading only, it is still reasonable to say that σ_x does not affect the magnitude of transverse stress, σ_{cq}, that can be sustained by the beam-strut or beam-tie.

As a result of this reasoning, the biaxial compression interaction for rectangular plates in the presence of lateral pressure is produced by exactly the same procedure as was used for biaxial compression in Chapter 4, but with different end-points and shape of the interaction that is applied to the end-regions of the plate, and a different local transverse resistance for the central region of the plate. The new information that needs to be added to the model of Chapter 4 is the value of η_q from the square plate model of Section 6.2, and the reduced interaction end-points and strut capacity due to lateral pressure. The biaxial interaction that is applied to the plate becomes:

$$\left[\frac{\sigma_x}{\sigma_{xq_1}}\right]^2 + \eta_q \left[\frac{\sigma_x}{\sigma_{xq_1}}\right]\left[\frac{\sigma_{y_1}}{\sigma_{yq_1}}\right] + \left[\frac{\sigma_{y_1}}{\sigma_{yq_1}}\right]^2 \leq 1.0 \quad \ldots 6.15$$

where $\sigma_{xq_1} = \left[1 - \frac{Q}{Q_{xu}}\right]\sigma_{xu_1}$

$$\sigma_{y_1} = \frac{\alpha_b}{\alpha_p}\sigma_y + \left[1 - \frac{\alpha_b}{\alpha_p}\right]\sigma_{cq}$$

σ_{xu_1} is from equation 4.7, Q_{xu} is from equation 6.5 or 6.12, η_q is from equation

6.9, and σ_{yq_1} is as required by equation 6.14 which defines σ_{cq}.

In order to obtain the values of σ_{yq}, σ_{yq_1}, and σ_{cq}, a definition of Q_{yu} is needed which can be used with the linear $Q-\sigma_y$ interaction model of equation 6.13 (and hence with equation 6.14). The approach of the previous section where a simple yield line analysis of a square panel was empirically adjusted will now be applied to the more general case of rectangular panels. The yield line analysis of equation 6.3, when extended to rectangular panels leads to:

$$Q_{YL} = 6 \frac{\sigma_o^2}{E \beta^2} \frac{(1 + 1/\alpha)}{(3 - 1/\alpha)} \quad \ldots 6.16$$

This is plotted against aspect ratio for slendernesses in the range b/t=30 to 120 in figure 6.29. The end-points on the right hand side of the figure are for square plates, and the left hand end points are for infinitely long plates (ie $1/\alpha=0$). Equation 6.4 gave an empirical upwards adjustment of the yield line pressure for square plates. As aspect ratio increases, the local transverse compressions in the end regions can resist a diminishing amount of transverse tensile stress in the remainder of the length of the plate, so that for an infinitely long plate there is no transverse tension stress (although there is still a finite tensile force). For the infinitely long plate, therefore, the absence of membrane forces in the yield line calculation is appropriate, and the plastic collapse of a simply supported beam, which is what the yield line model becomes in that limit, is appropriate for design. Therefore the values of Q_{YL} for infinitely long plates, in figure 6.29, do not require adjustment. The adjustment which is applied for plates of finite length will depend on whether maximum resistance or yield strain resistance is being modelled. As before, maximum resistance is considered first.

Maximum Resistance

It is desirable to retain the form of equation 6.16, but to adjust it to agree with the previously modified yield line model for square plates (in equation 6.5), while still giving the unadjusted yield line pressures for infinitely long plates. Such a modification to equation 6.16 leads to:

$$Q_{yu} = 6 \frac{\sigma_o^2}{E \beta^2} \frac{(K + 10/\alpha)}{(3K - 1/\alpha)} \quad \ldots 6.17$$

$$\text{where } K = \begin{cases} 1 & ; \beta \leq 0.7 \\ \dfrac{(10.3 + \beta)}{(3\beta - 0.1)} & ; 0.7 < \beta \leq 3 \end{cases}$$

This is shown in figure 6.30. The term $10/\alpha$ in the numerator rather than $1/\alpha$ is to give a better agreement with the extrapolated pressure end-points of figures 6.18 and

6.28. These extrapolated end-points for both square and 3:1 plates are also shown on figure 6.30. The values of pressure for 3:1 plates, obtained from figure 6.28, are Q_{yu} = 68.2, 41.5 and 28.1 metres, for b/t=40, 60 and 80 respectively.

Equations 6.13 and 6.17 can now be used with equations 6.5 to 6.10, in the design approach described above, to produce biaxial compression interaction curves in the presence of lateral pressure for 3:1 plates to compare with the numerically derived curves for maximum resistance. This comparison is made in figure 6.31.

It can be seen that the modification to the biaxial compression model due to lateral pressure which is being proposed for rectangular plates fits the numerical curves very well. In particular, the model accurately describes what is otherwise a difficult phenomenon to model, namely the change in preferred buckling mode for a given biaxial compression ratio, as increasing magnitudes of pressure are included. It has already been mentioned that this aspect of behaviour depends greatly on slenderness, and it can be seen that the model gives an accurate prediction of the behaviour for all three slendernesses.

Furthermore, the changing shape of interaction, as pressure is applied, is also accurately represented by the model. There is a slight non-conservatism for the b/t=40 plate, but this is actually introduced by the transverse strength model of Chapter 3, which although it gives very good agreement with numerically derived transverse strengths over a whole range of plate geometries (in figure 3.12), is slightly non-conservative for a 3:1 b/t=40 plate. Maximum strength interaction curves over a wider range of slendernesses and pressures are shown in figure 6.32.

Yield Strain Resistance

In section 6.2 the use of a strain limit consistent with Chapters 3 and 4 has already been developed for pressure on square plates. What remains to be defined, then, is a model of Q_{yu} for the same strain limit.

As with square plates, the average strains due to pressure alone are added to the strains due to in-plane loading. The transverse uni-axial stress sustained by the plate when the total transverse strain is equal to the yield strain is then interpolated from the stress-strain curves. These uni-axial stresses are plotted against pressure in figure 6.33, and straight lines extrapolated to the pressure axis are shown.

Additional analyses were carried out for 3:1 plates under pressure only to obtain the levels of lateral pressure to cause ϵ_y'=1. Residual stress and imperfection levels were

the same as in (48), and are described in Chapter 3. The computed levels of pressure for b/t=40, 60 and 80 are shown on figure 6.33. It is apparent that the linear interaction model between pressure and transverse compression is a much better fit to the numerical data for all 3 slendernesses, than it was for the square plates. Figure 6.34 shows the extrapolated end-points from figure 6.33, as well as the computed pressure levels to cause $\epsilon_y'=1$ for b/t=40 to 200, plotted against slenderness. Just as for square plates the residual stresses had to be reduced for the most slender plates, as $\sigma_r'=0.2$ gave rise to convergence problems in the Dynamic Relaxation program. For the b/t=160 plate, the longitudinal residual stress was reduced to 0.165 σ_o, and for the b/t=200 plate, it was reduced to 0.12 σ_o. The fact that these reductions in the residual stresses are less than the reductions required for the square plate analyses is a reflection of the residual stresses in rectangular plates being principally applied in the longitudinal direction, with the residual stresses in the transverse direction being an order of magnitude less (nominally the longitudinal residual stress is 0.2 σ_0 whereas the transverse residual stress is 0.0286 σ_0). The transverse residual stress magnitude was derived in (48) on the basis of the tensile yield blocks along the short edges being half the width of those on the long edges.

From section 6.2 the empirical adjustment to the square plate yield line resistance for $\beta>0.5$ was to multiply it by (6/7 + 2β/7) up to β=7.5. Using the rectangular plate form of the yield line equation, but adjusting it to fit the square plate model, as well as the 3:1 plate data, leads to

$$Q_{yu} = 6 \frac{\sigma_0^2}{E \beta^2} \frac{(K + 1/\alpha)}{(3K - 1/\alpha)} \qquad \ldots 6.18$$

$$\text{where } K = \begin{cases} 1 & ; \beta \leq 0.5 \\ \dfrac{(13 + 2\beta)}{(11 + 6\beta)} & ; 0.5 < \beta \leq 7.5 \end{cases}$$

This is compared with the data in figure 6.34. Figure 6.35 plots equation 6.18 against aspect ratio for various slendernesses, and includes the numerical data for comparison. These numerical data values are those pressure end-points which are required to make a linear interaction safe, and are extrapolated values where computed values would make such an interaction unsafe. The strain limit yield interaction of equation 4.9 is incorporated on the figure.

This single expression for pressure now gives Q_{yu} and Q_{xu} (by putting α=1). Design curves based on the yield strain models of equations 6.18, 3.15b and 4.7 are shown as figure 6.36.

It is interesting to compare equation 6.18 with an alternative model for Q_{yu} which

more fully expresses the beam-tie idealisation of the central region. Whereas previously the beam-tie capacity of the central region in the absence of biaxial compression could be deduced from Q_{yu} based on a modified yield line analysis, an alternative would be to define the beam-tie capacity first, and to use it to derive a consistent value of Q_{yu}.

This is done by explicitly idealising the central region of the plate as a plastic beam with coexistent axial tension which holds the geometric shortening of the beam to be equivalent to $\epsilon_y'=1$. The total axial tension must balance the end compressions since there are no applied in-plane loads, and to do so in the presence of a pressure on the beam equal to the pressure on the end regions. These end regions have the same Q_{xu}-σ_{xu} model at $\epsilon'=1$ as previously. These requirements necessitate the solution of a quadratic equation for the level of pressure to cause this:

$$\bar{a}\left[\frac{Q_{yu}}{Q_{xu}}\right]^2 + \bar{b}\left[\frac{Q_{yu}}{Q_{xu}}\right] + \bar{c} = 0 \qquad \ldots 6.19$$

where:

$$\bar{a} = -2\left[\frac{\sigma_{xu}}{\alpha - 1}\frac{t}{b}\right]^2$$

$$\bar{b} = 4\left[\frac{\sigma_{xu}}{\alpha - 1}\frac{t}{b}\right]^2 - 4\left[\frac{\sigma_{xu}}{\alpha - 1}\frac{t}{b}\right]\sqrt{1 - (1 - \epsilon_0)^2} - \frac{Q_{xu}}{\sigma_0}$$

$$\bar{c} = -2\left[\frac{\sigma_{xu}}{\alpha - 1}\frac{t}{b}\right]^2 + 4\left[\frac{\sigma_{xu}}{\alpha - 1}\frac{t}{b}\right]\sqrt{1 - (1 - \epsilon_0)^2} + 2\left[\frac{t}{b}\right]^2$$

Q_{xu} is from equation 6.12, σ_{xu} is the uniaxial strength model of equation 3.3, and ϵ_0 is the yield strain. α is > 1.

This model for Q_{yu} is shown against the results of eqn 6.18 in figure 6.37. This shows that this model agrees quite well with the modified yield line analysis although it is much more complicated to calculate. However, it does break down for some aspect ratios and slendernesses, for which the various requirements of equal pressures on beam and plate regions, and of net beam tension balancing net plate compression, such that the geometric shortening is equal to $\epsilon_y'=1$ cannot be satisfied (mathematically the roots of the quadratic equation become complex). The locus of the points for which it breaks down are shown in figure 6.38.

Various rational adjustments to the model, to attempt to correct this, have been tried but they all resulted in making a model, which was already more complicated than the modified yield line model, even more so, and were not considered to be worth using. Even with this alternative approach, an empirically modified yield line analysis still has to be applied to the end regions of the plate, so there was not a great deal of theoretical benefit to be gained by this more involved analysis.

Having developed the design model for biaxial compression and lateral pressure it remains to compare this with the design rules of (63) for this situation. (63) specifies a minimum plate thickness which is required when certain levels of biaxial compression and lateral pressure are acting in combination, but a relationship between lateral pressure and biaxial compression can be inferred from this. It was pointed out in (66) that the rules of (63) permit no reduction in the in-plane capacity of the plate until quite substantial levels of pressure are applied, and this can be seen on figure 6.39, which presents biaxial interactions produced by the method in (63), for square and 3:1 plates with b/t=40, 60 and 80, for 4 metre increments of pressure. The figure also shows the interactions between uniaxial longitudinal or transverse compression with lateral pressure. Figure 6.40 presents the equivalent plot to figure 6.39, produced by the proposed yield strain design model. It can be seen, for instance, that whereas the proposed model predicts a uniaxial compression resistance at yield strain of about $0.4\sigma_0$, in the presence of 60 metres of pressure, for an a/b=1, b/t=40 plate (this being reduced from $0.75\sigma_0$ at zero pressure), the rules of (63) predict that the same plate can sustain a uniaxial compression of $0.88\sigma_0$ in the presence of pressures up to 60 metres head. Since even the maximum resistance design model of figure 6.21, gives a maximum uniaxial compression resistance in the presence of 60 metres of pressure, of about $0.5\sigma_0$ (reduced from $0.84\sigma_0$ at zero pressure), for this plate, then it can be seen that the rules of (63) can be very non-conservative.

This concludes the development of a design model in this thesis. The next chapter will draw the various components of the design model in the previous chapters into a single design summary.

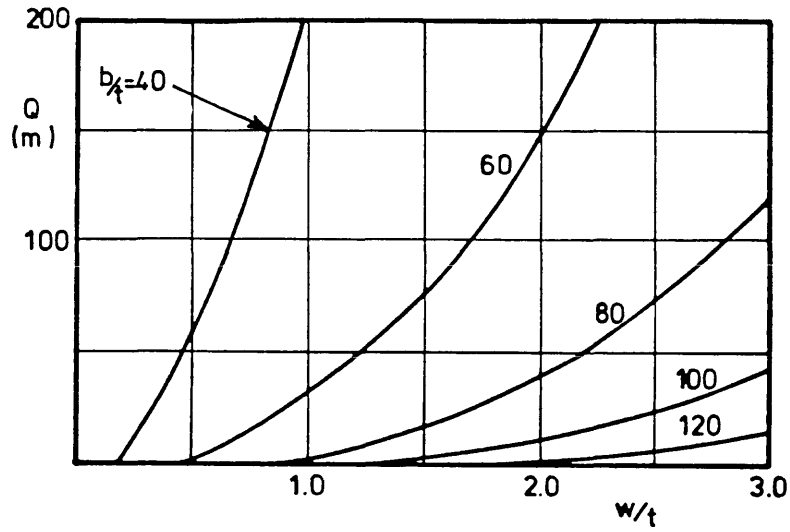

FIGURE 6.1 – Pressure versus out-of-plane displacement from elastic model

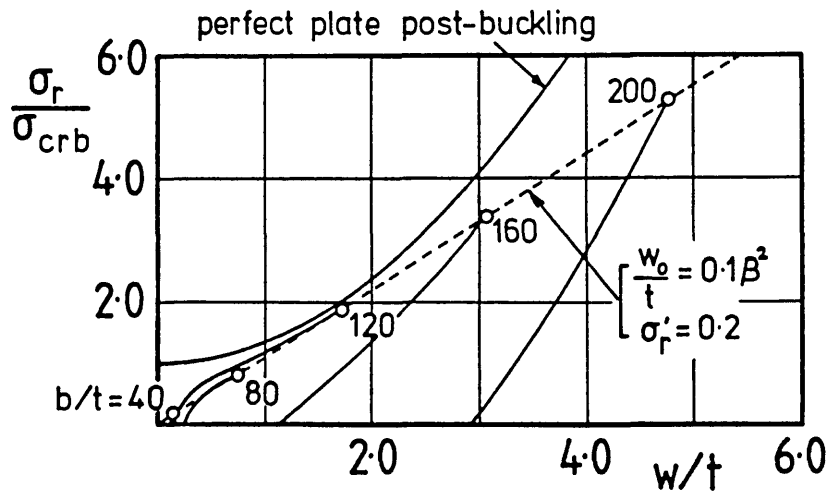

FIGURE 6.2 – Plate buckling due to residual compressions, giving rise to initial imperfections, w_0

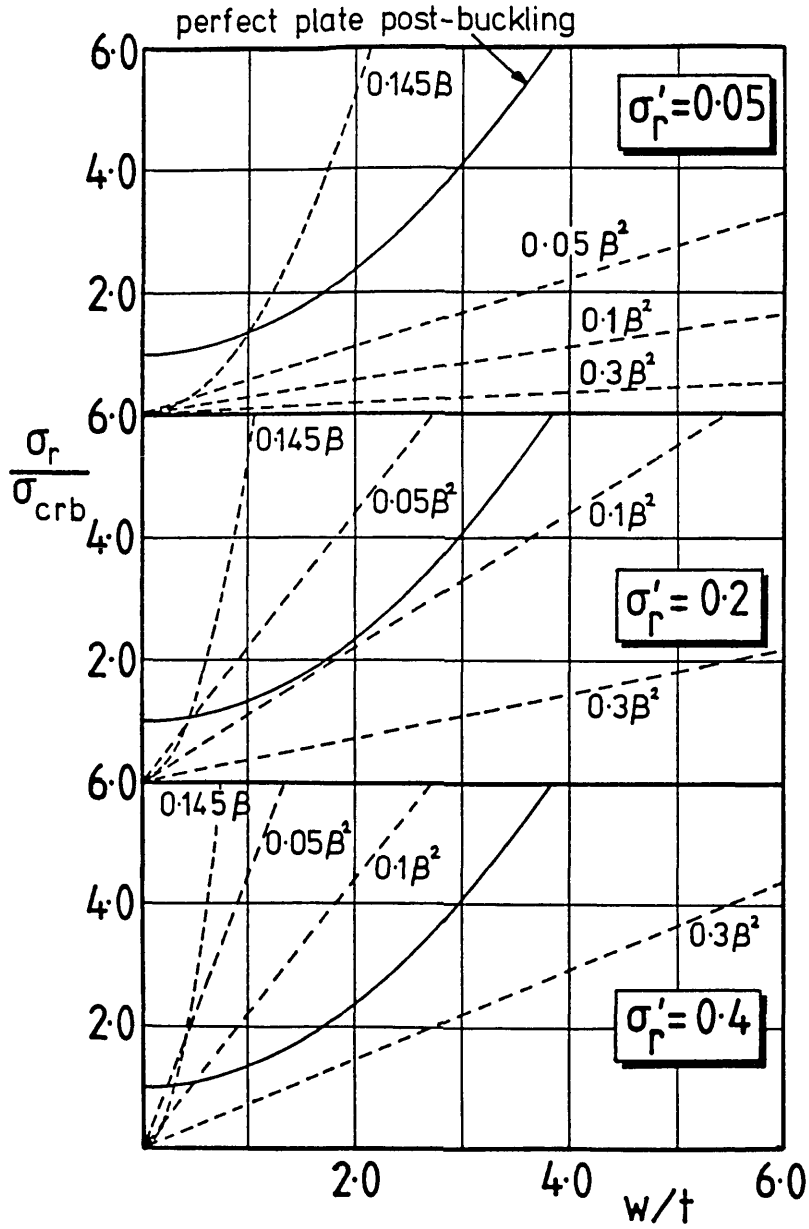

FIGURE 6.3 – Viable combinations of σ_r and w_0 – viable if below perfect-plate post-buckling curve shown on each figure

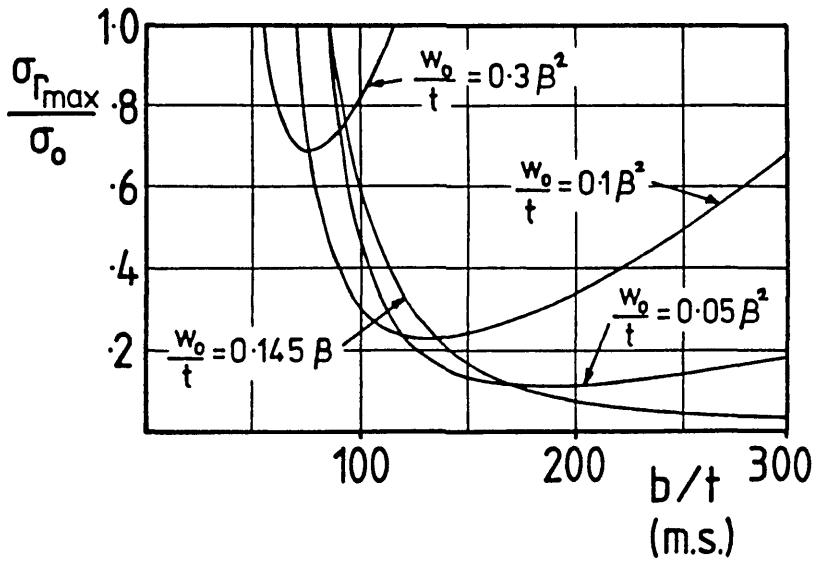

FIGURE 6.4 – Maximum possible residual stress consistent with w_0/t assumptions from elastic model

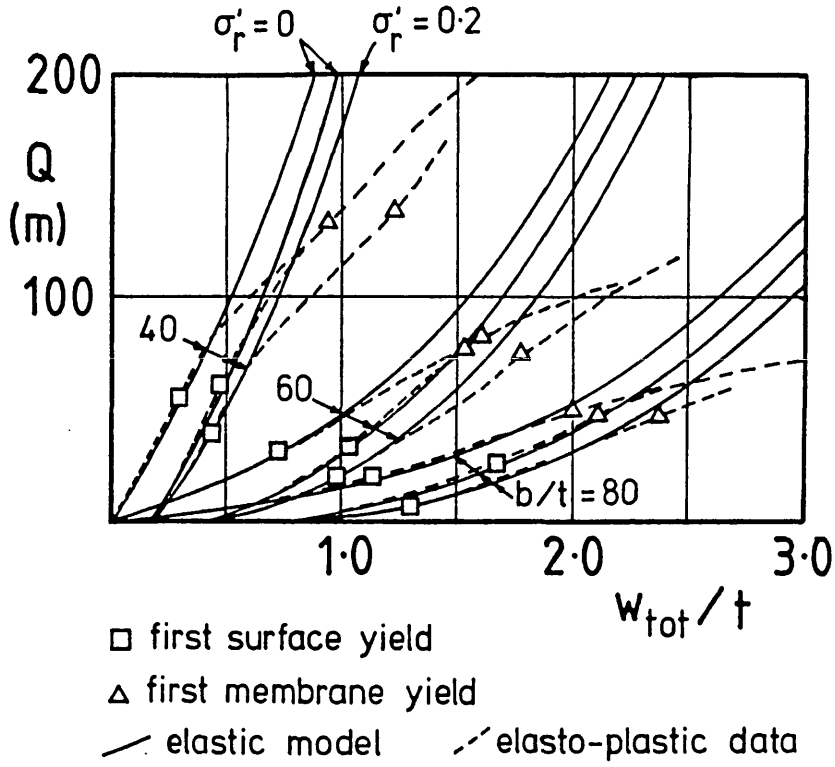

FIGURE 6.5 – Pressure – displacement curves for perfect plates, for imperfect plates without σ_r, and for imperfect plates with σ_r'=0.2, from elastic model and from elasto–plastic analyses

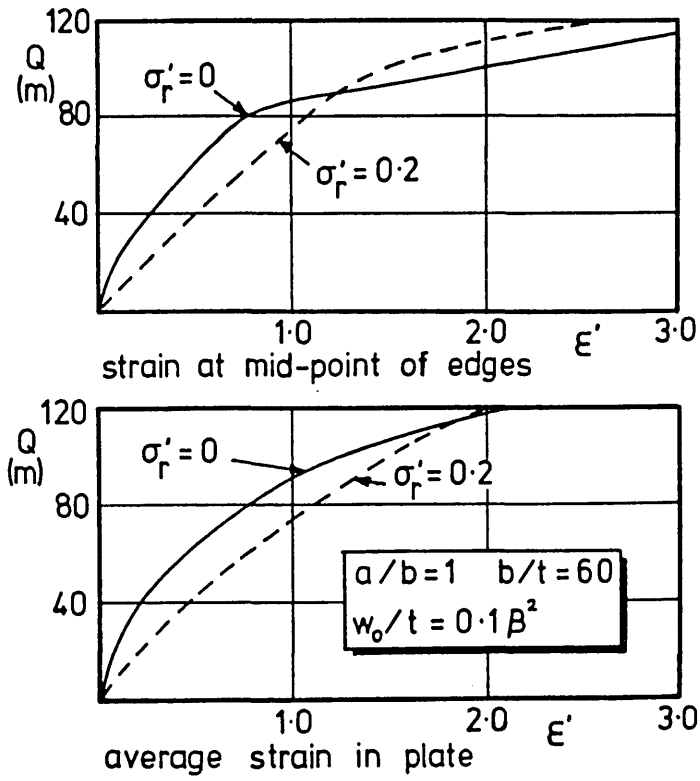

FIGURE 6.6 – Pressure–strain, for σ_r=0 and σ_r'=0.2

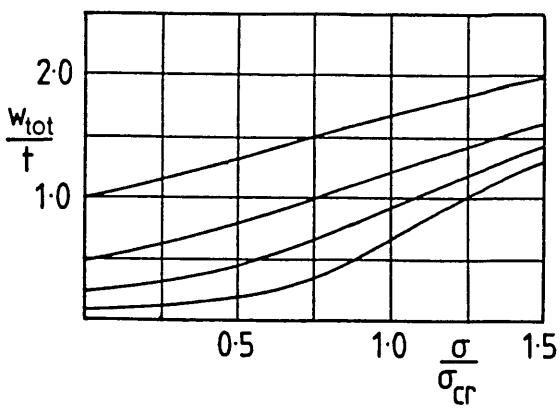

Elastic model for uni- and bi-axial compression, producing identical curves to finite difference analyses

FIGURE 6.7

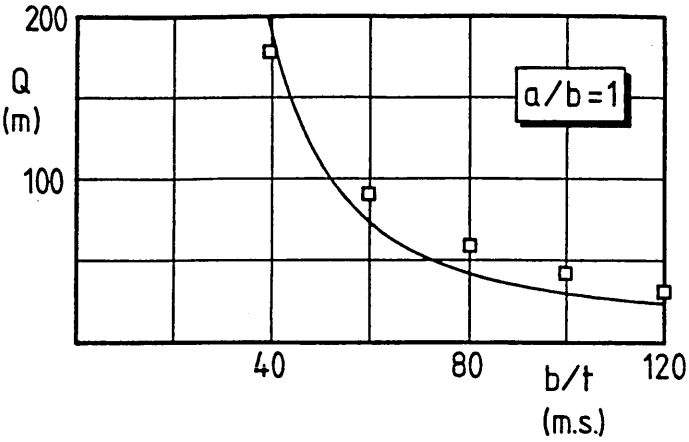

"Failure" pressure from elastic model with mid-length edge yield compared to yield strain results from elasto-plastic analyses

FIGURE 6.9

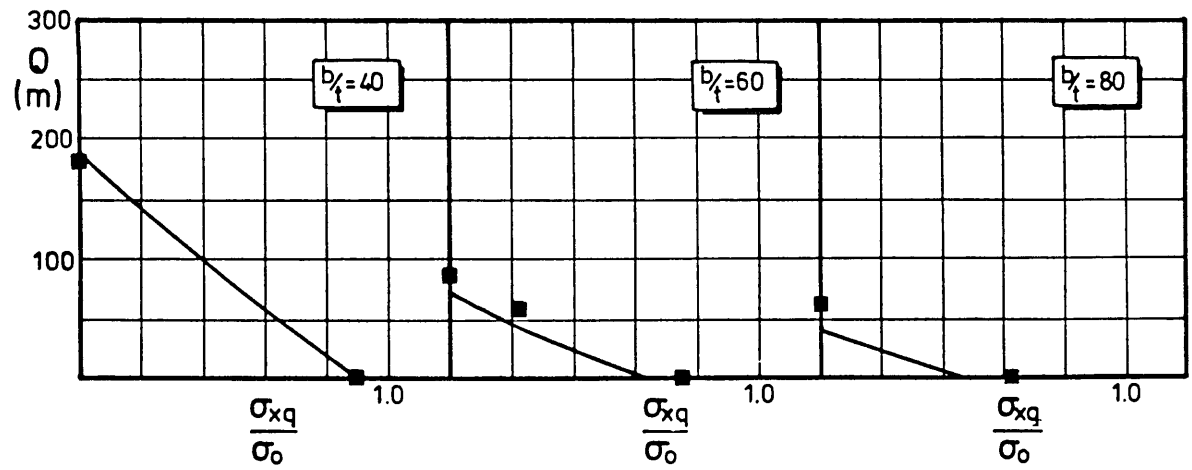

FIGURE 6.8 – Interaction between pressure and uniaxial compression in square plates from elastic analysis with mid-length edge membrane yield criterion, with elasto-plastic data at yield strain

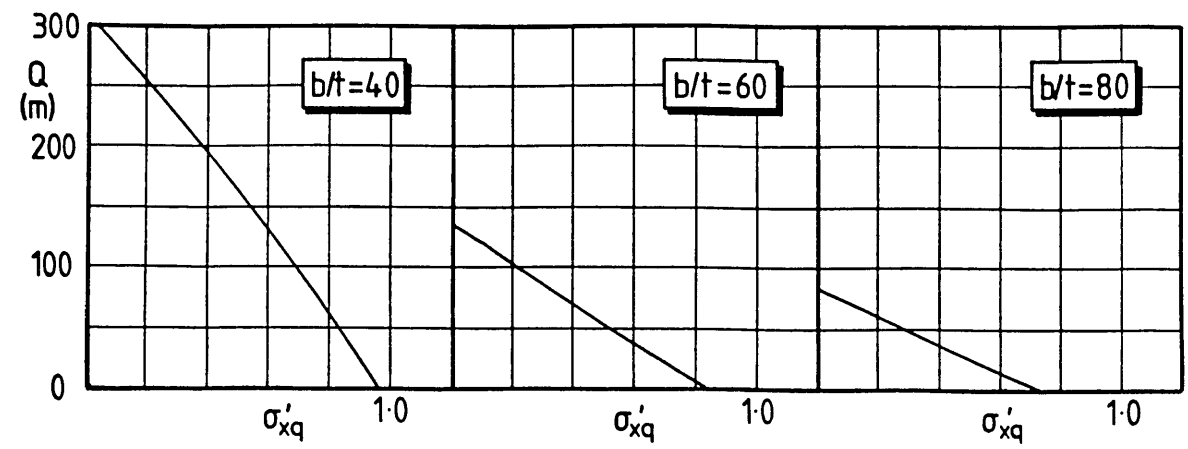

FIGURE 6.10 – Interaction between pressure and uniaxial compression in square plates from elastic analysis with corner membrane yield criterion,

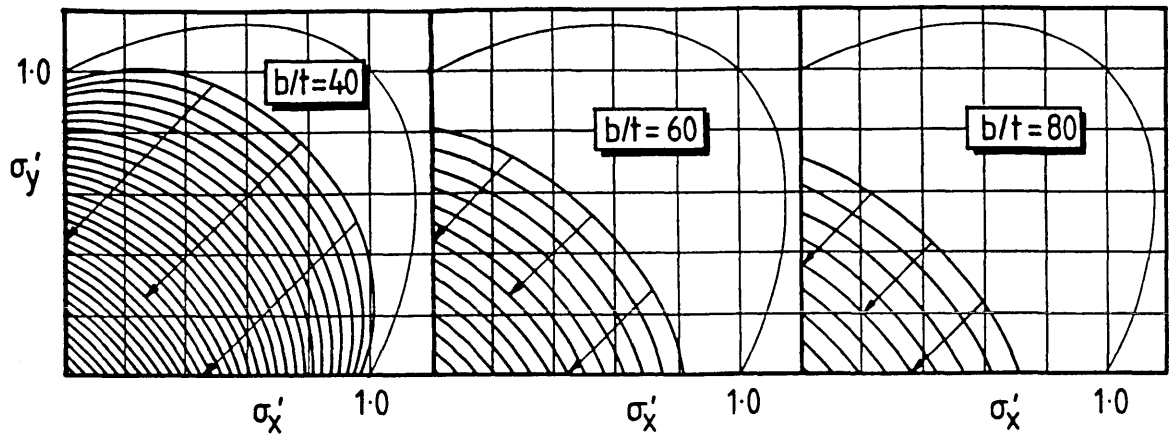

FIGURE 6.11 – Biaxial compression interactions in the presence of pressure (10m increments of pressure), from elastic analysis with corner membrane yield criterion – a/b=1

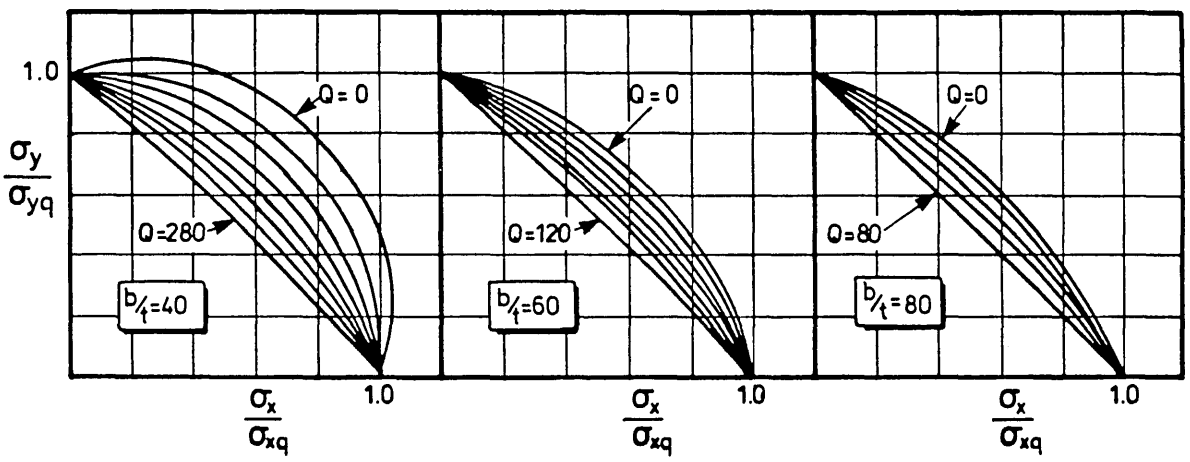

FIGURE 6.12 – Interactions of figure 6.11 normalised

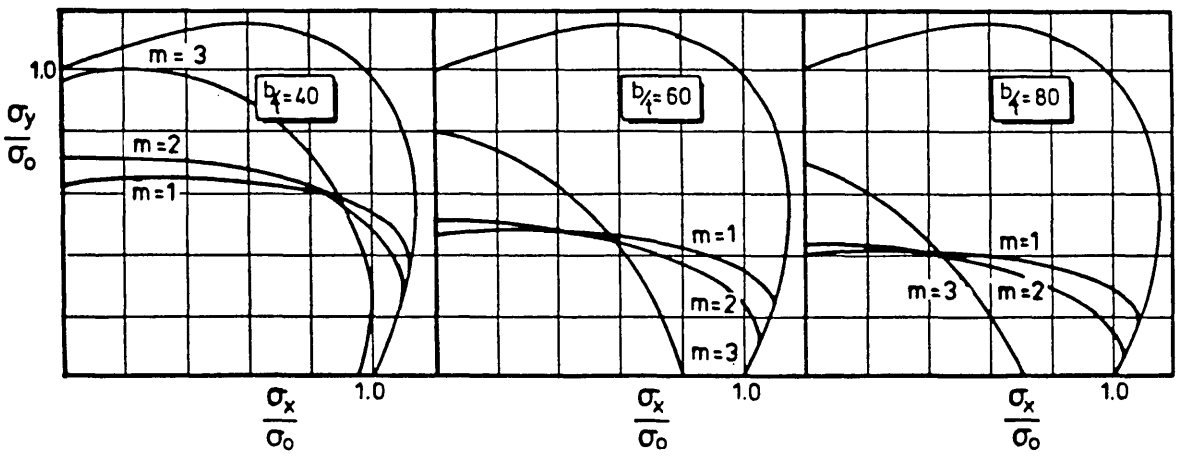

FIGURE 6.13 – Biaxial interactions for 3:1 plates for zero pressure for m=1, m=2 and m=3 modes

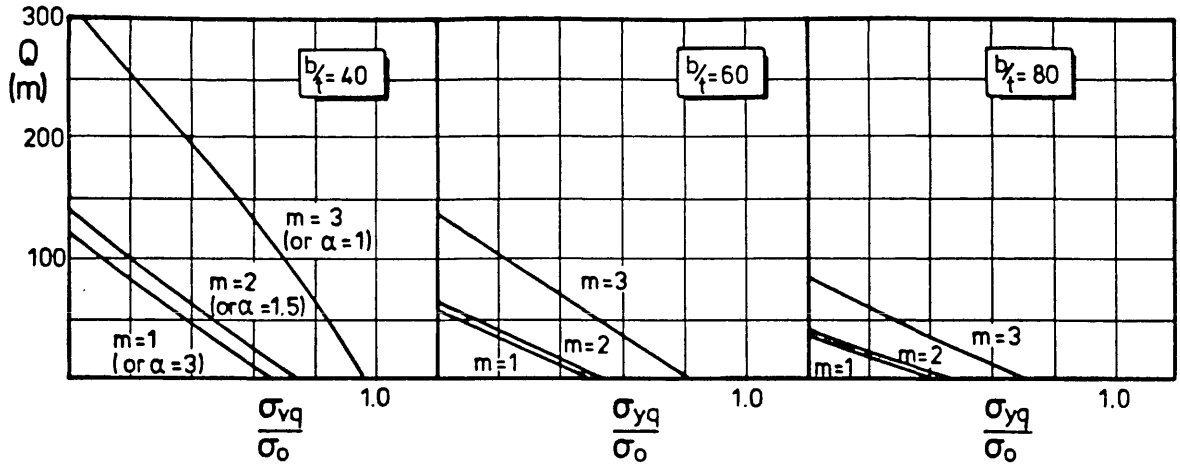

FIGURE 6.14 – Interaction between pressure and transverse uniaxial compression in 3:1 plates, deforming in m=1, m=2 and m=3 modes

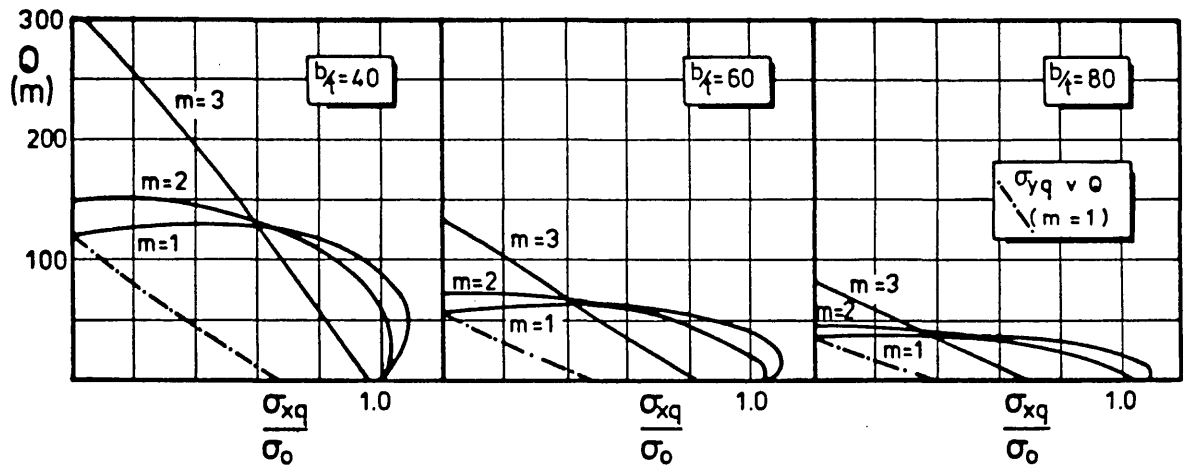

FIGURE 6.15 – Interaction between pressure and longitudinal uniaxial compression in 3:1 plates, deforming in m=1, m=2 and m=3 modes

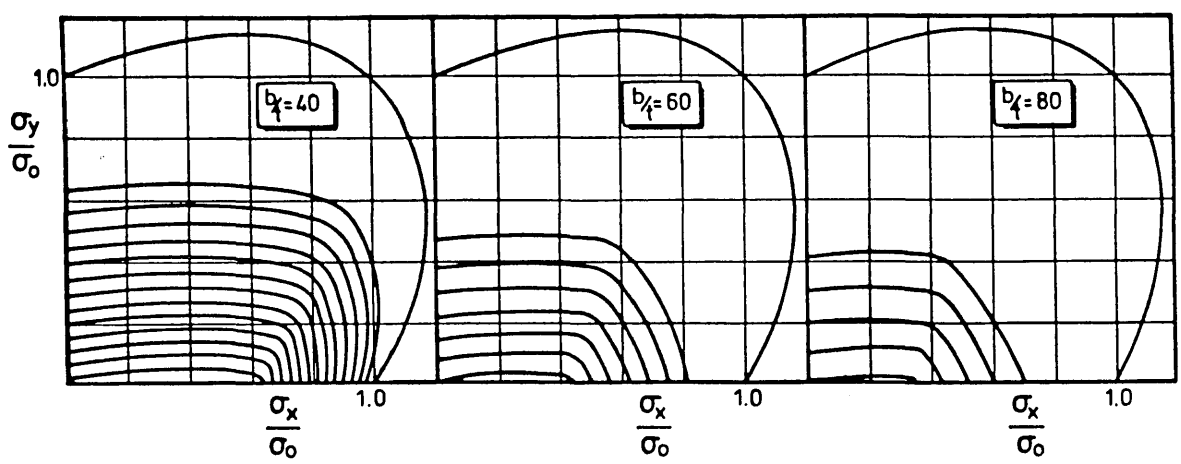

FIGURE 6.16 – Biaxial compression interactions in the presence of pressure (10m increments of pressure), from elastic analysis with corner membrane yield criterion – a/b=3

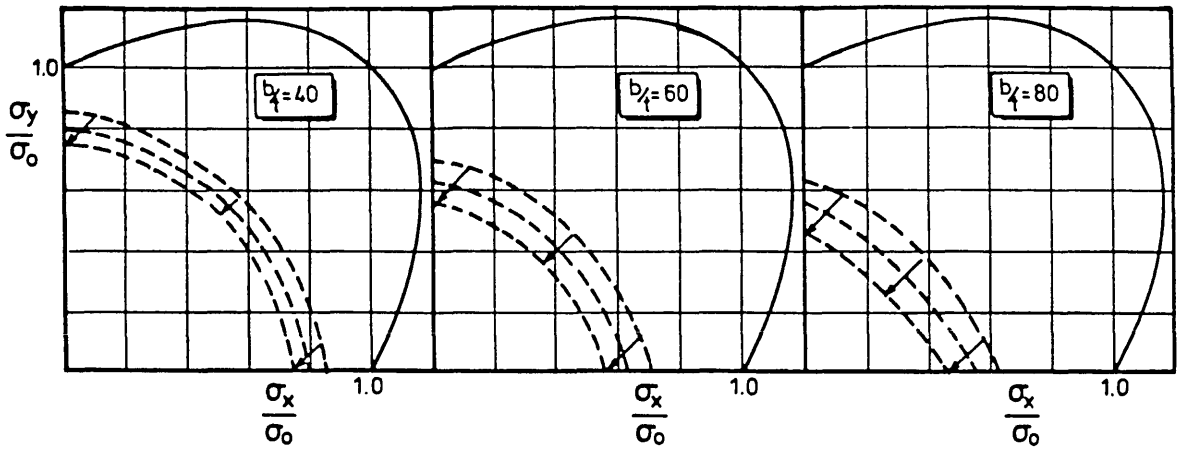

FIGURE 6.17 – Biaxial compression interactions in the presence of pressure (10m increments of pressure), from elasto–plastic analyses of (48) for square plates, b/t=40, 60 & 80

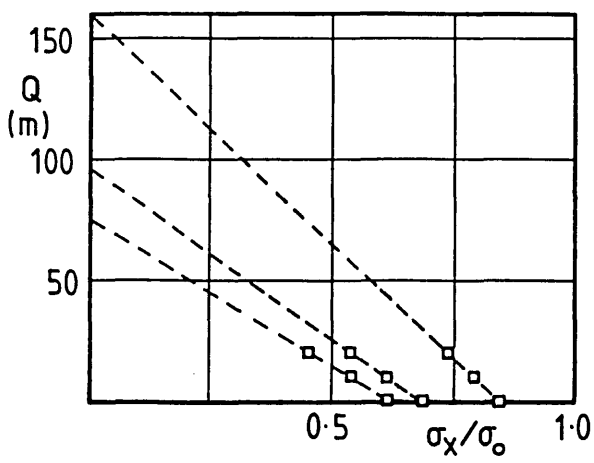

End–points of interactions in figure 6.17 plotted against pressure

FIGURE 6.18

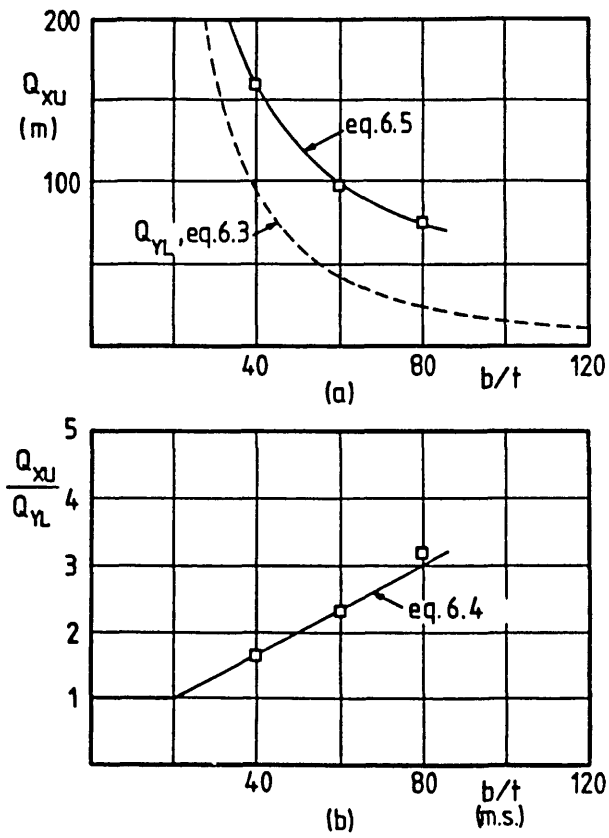

Empirical modification to yield line analysis to fit pressures obtained from extrapolation on figure 6.18

FIGURE 6.19

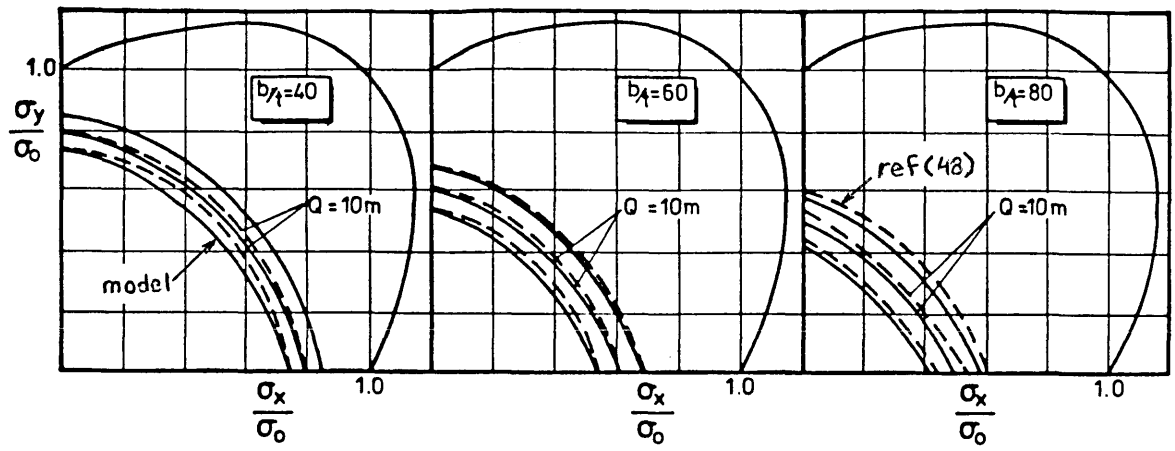

FIGURE 6.20 – Design model for square plates compared to interactions from (48)

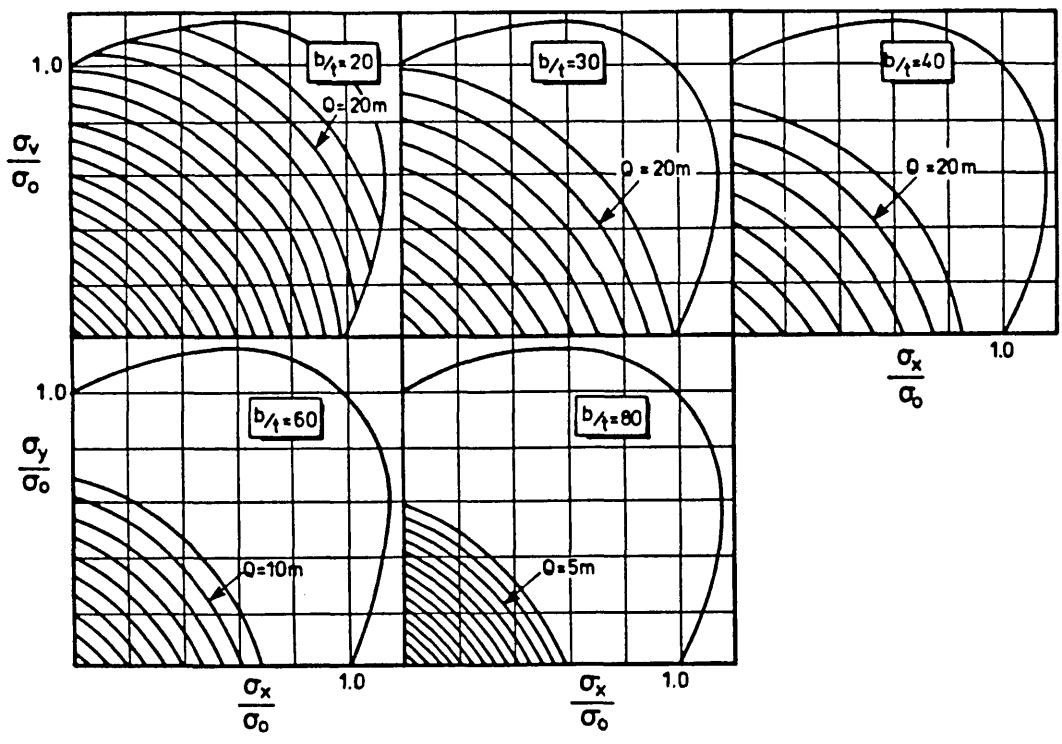

FIGURE 6.21 – Maximum resistance design curves from proposed model, for a/b=1

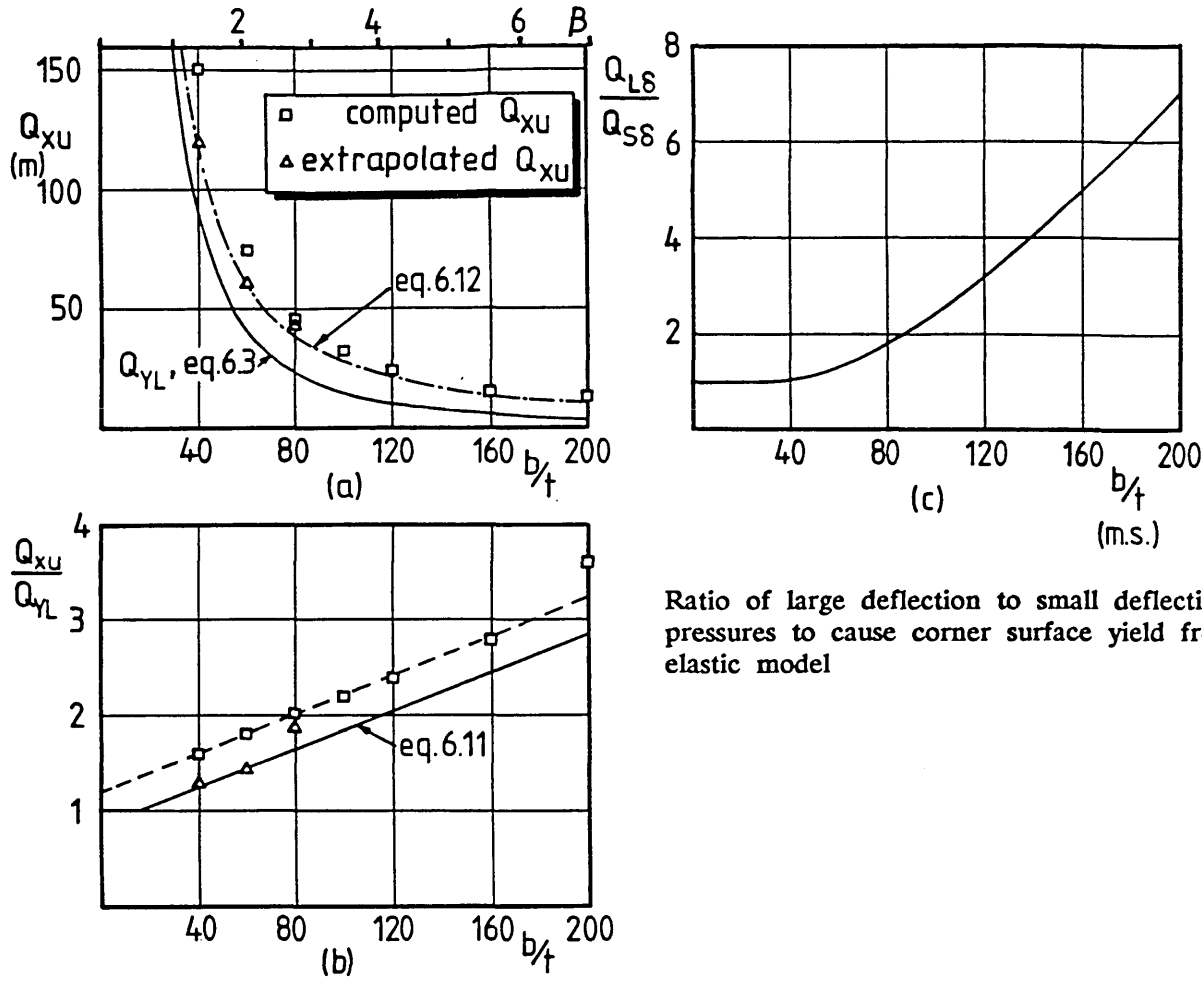

Ratio of large deflection to small deflection pressures to cause corner surface yield from elastic model

FIGURE 6.22 – Empirical modification to yield line analysis to fit yield strain pressures, obtained from elasto–plastic analysis or extrapolation (on figure 6.24).

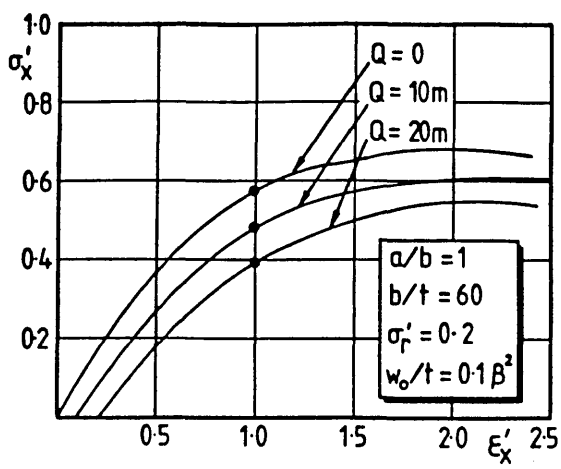

FIGURE 6.23 – Stress–strain curves in the presence of pressure, showing strains caused by the initial pressure–only loading

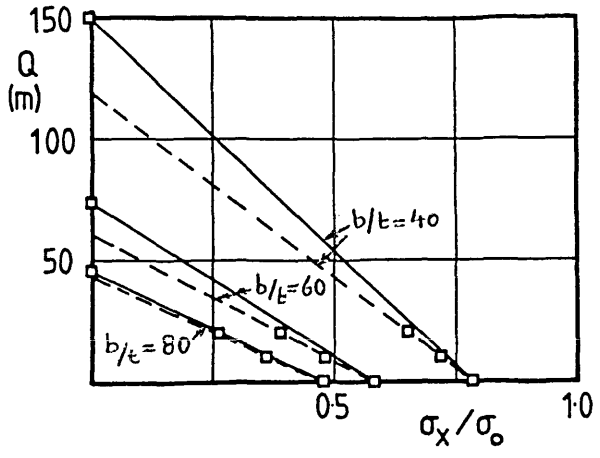

Reduced compressive strengths in the presence of pressure at $\epsilon_x'=1$ and pressure–only results at $\epsilon_x'=1$ (a/b=1)

FIGURE 6.24

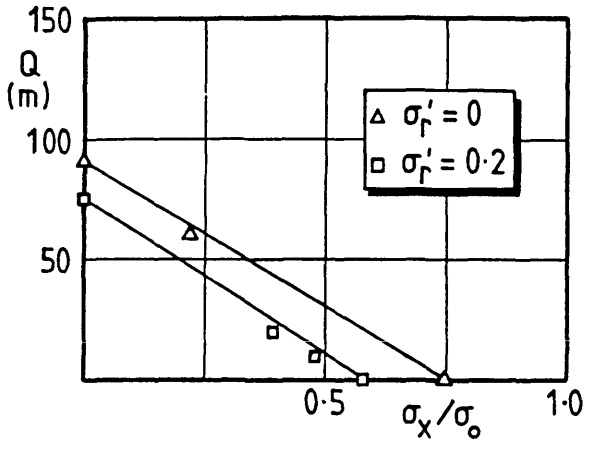

Reduced compressive strengths in the presence of pressure at $\epsilon_x'=1$ and pressure–only results, for a/b=1, b/t=60 with and without residual stresses

FIGURE 6.25

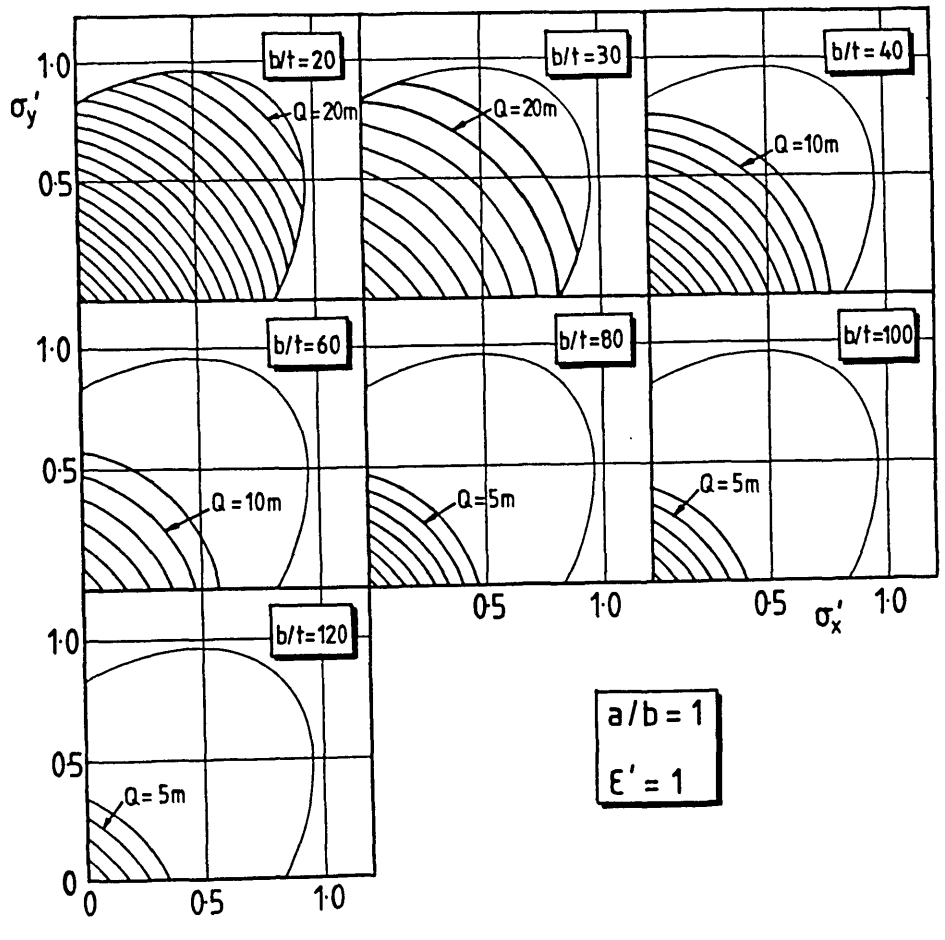

FIGURE 6.26 – Design curves for resistance at yield strain from proposed model, a/b=1

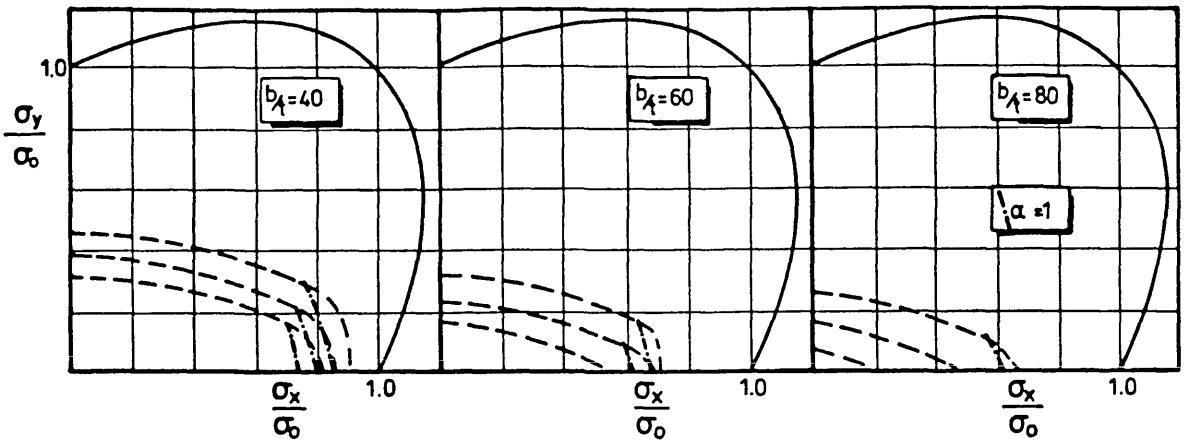

FIGURE 6.27 – Biaxial interactions in the presence of pressure from (48) for 3:1 plates (with square plate interactions shown when within 3:1 plate interactions)

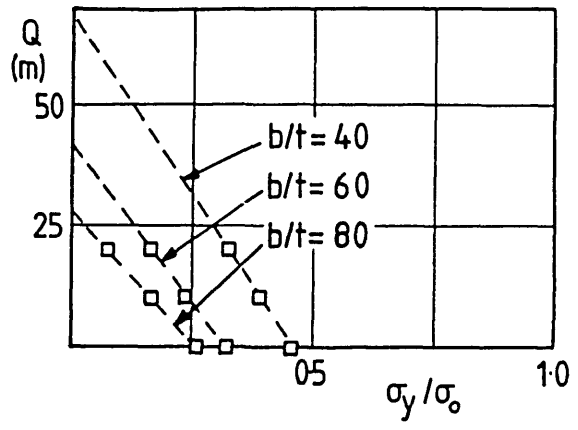

Transverse compression interaction end–points in the presence of pressure plotted against pressure

FIGURE 6.28

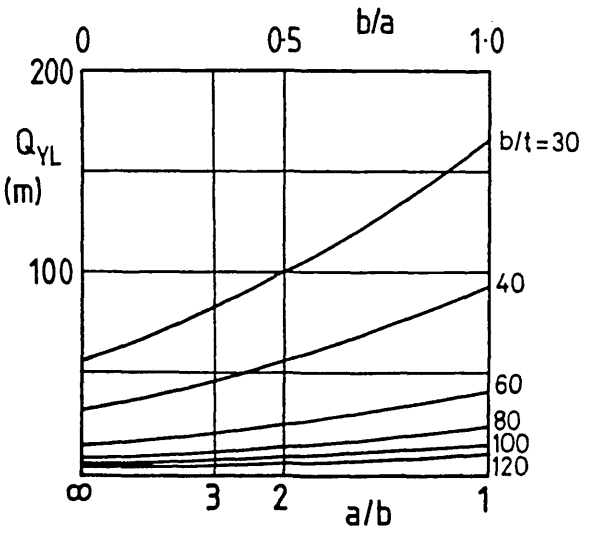

Yield line pressures for rectangular plates, b/t=30 to 120

FIGURE 6.29

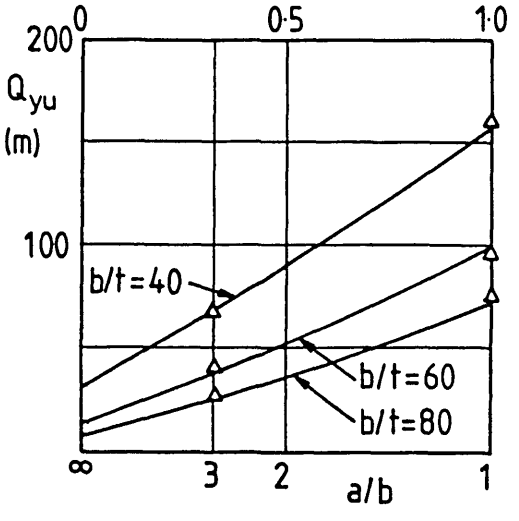

FIGURE 6.30 – Empirically modified yield line pressure (extrapolated pressures shown)

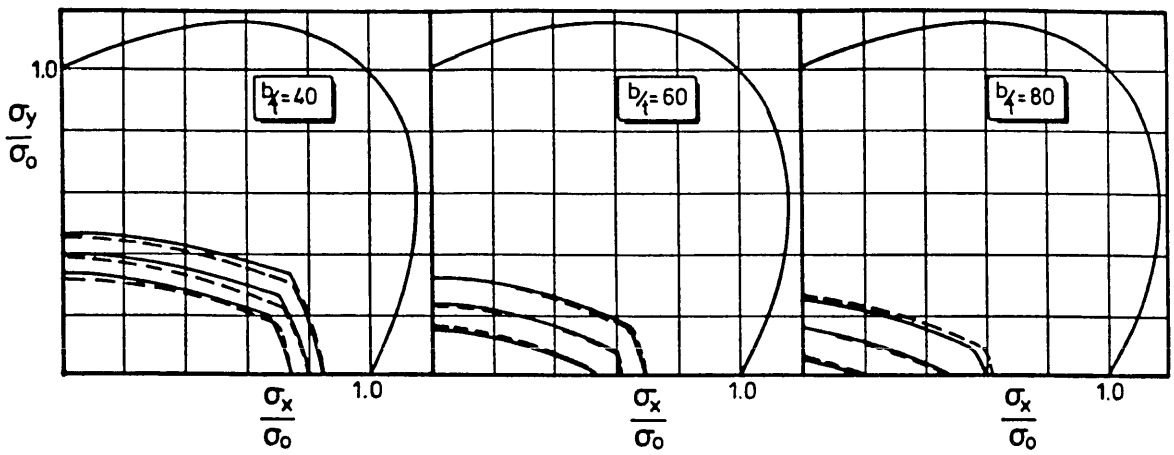

FIGURE 6.31 – Biaxial compression interactions in the presence of pressure from proposed maximum resistance model, compared to figure 6.27

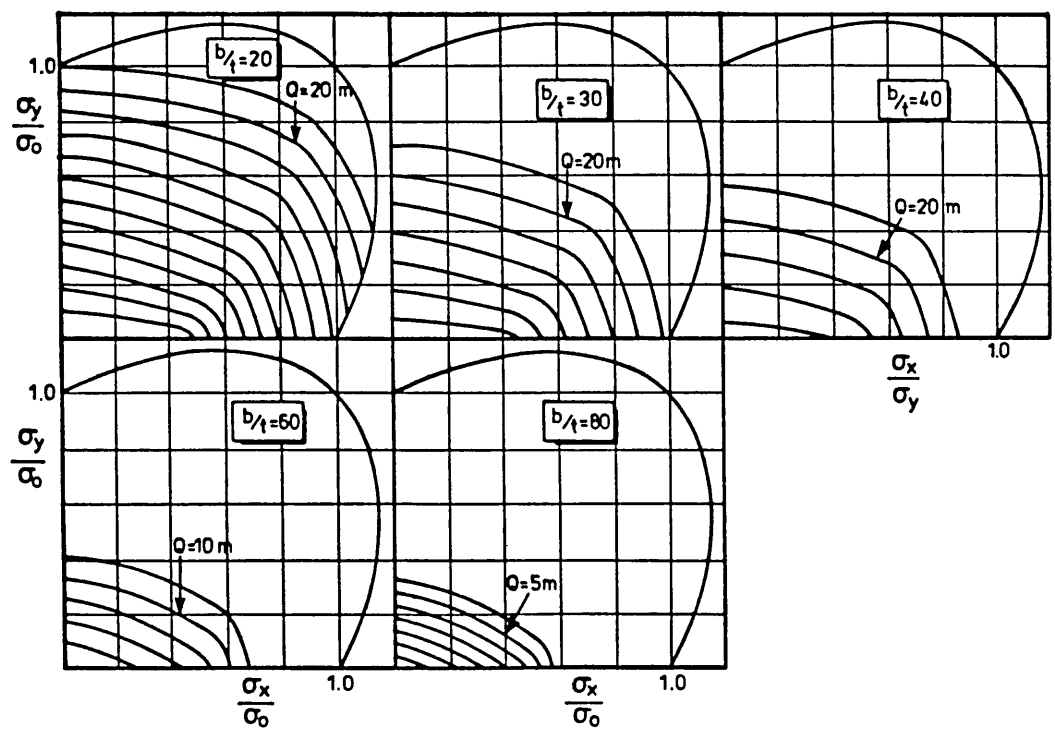

FIGURE 6.32(a) – Design curves for biaxial compression with coexistent pressure from maximum resistance design model – a/b=2

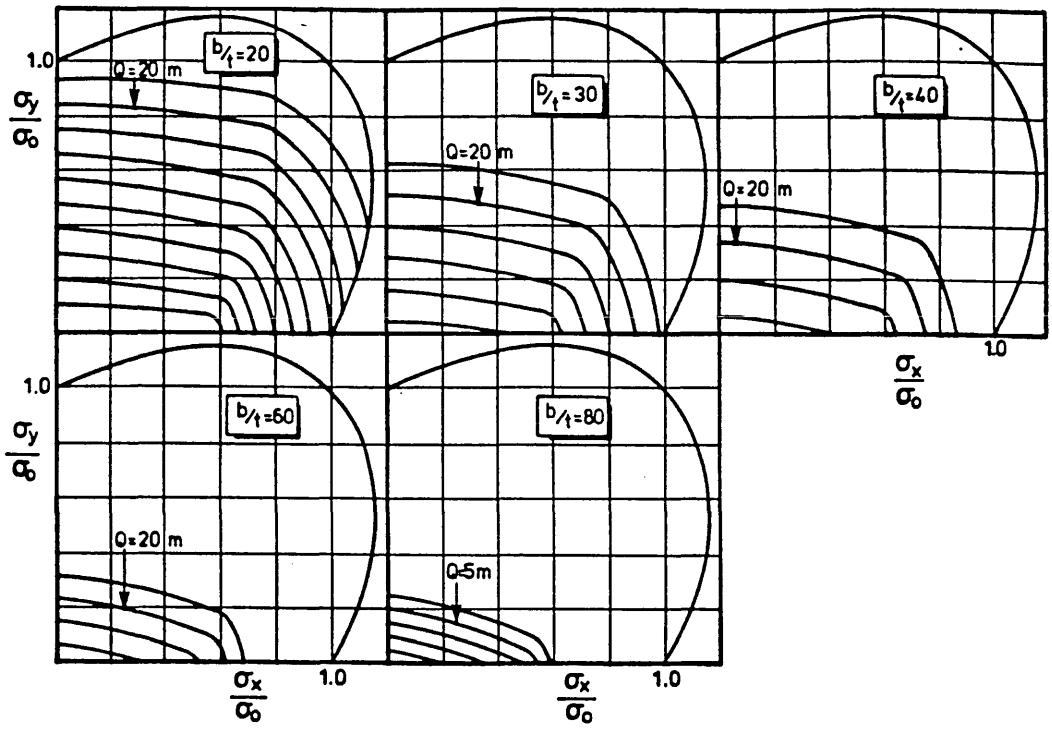

FIGURE 6.32(b) – Design curves for biaxial compression with coexistent pressure from maximum resistance design model – a/b=3

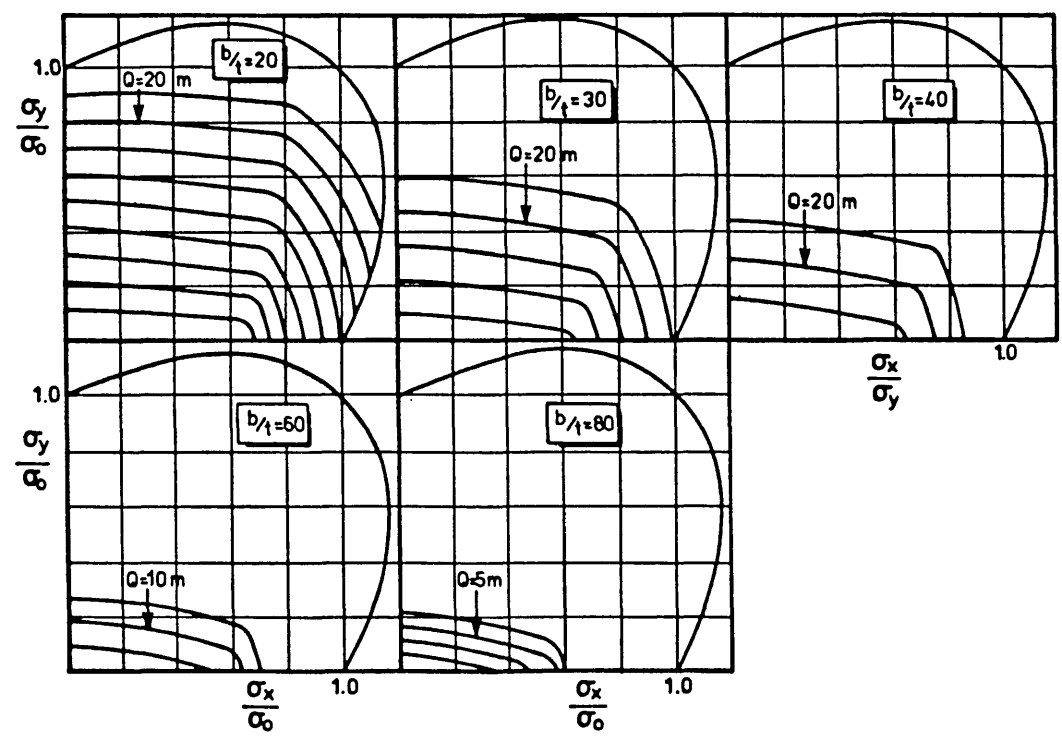

FIGURE 6.32(c) – Design curves for biaxial compression with coexistent pressure from maximum resistance design model – a/b=4

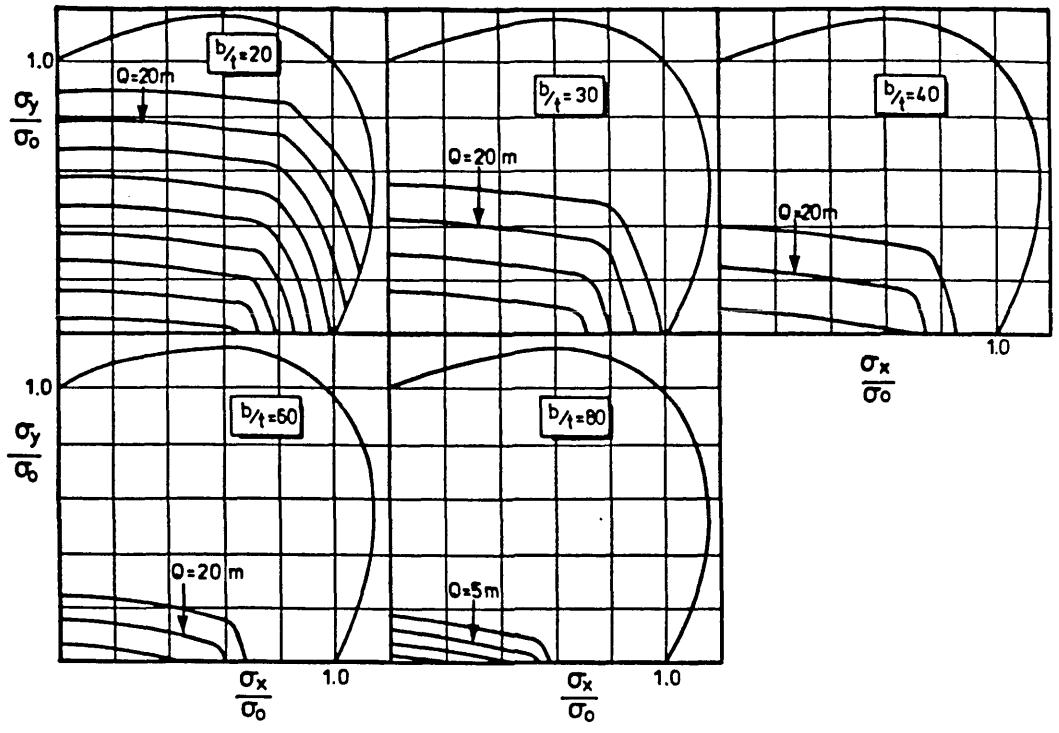

FIGURE 6.32(d) – Design curves for biaxial compression with coexistent pressure from maximum resistance design model – a/b=5

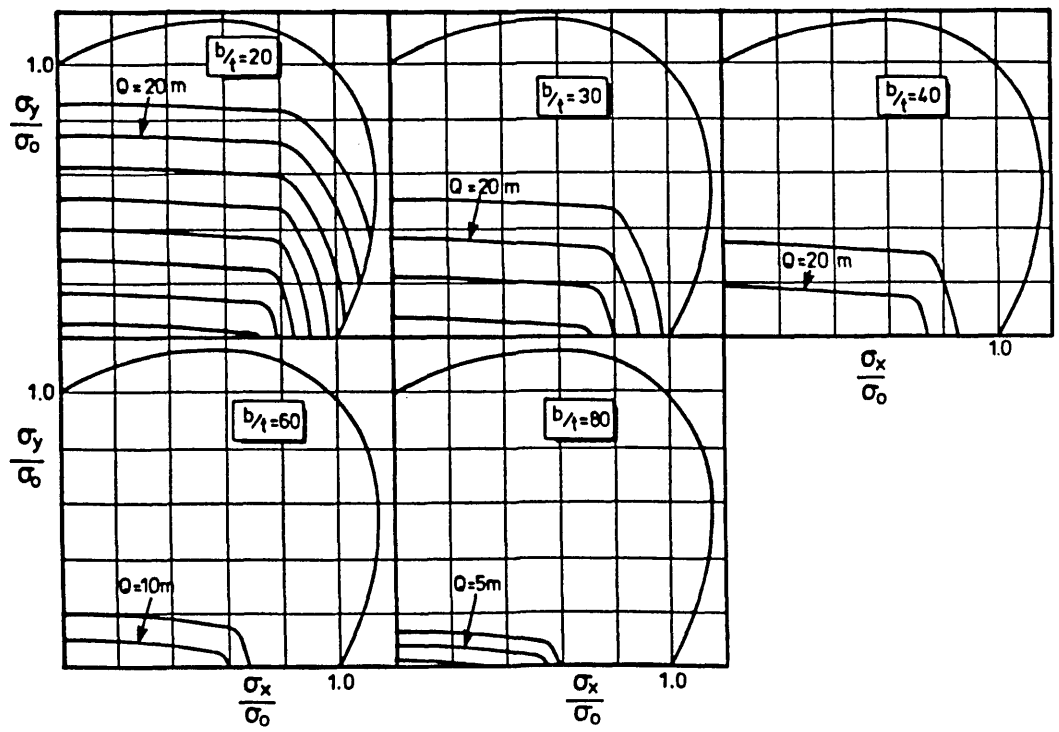

FIGURE 6.32(e) – Design curves for biaxial compression with coexistent pressure from maximum resistance design model – a/b=10

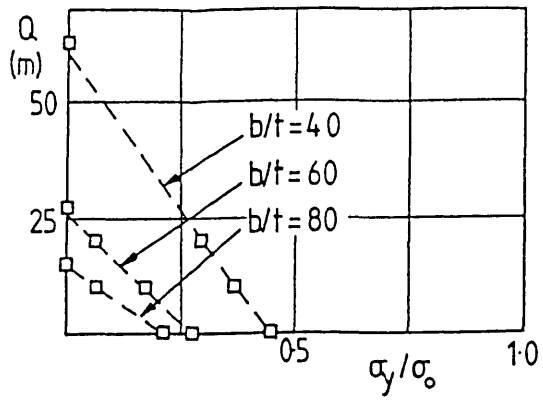

FIGURE 6.33 – Transverse compression resistance at yield strain, of 3:1 plates, with coexistent pressure

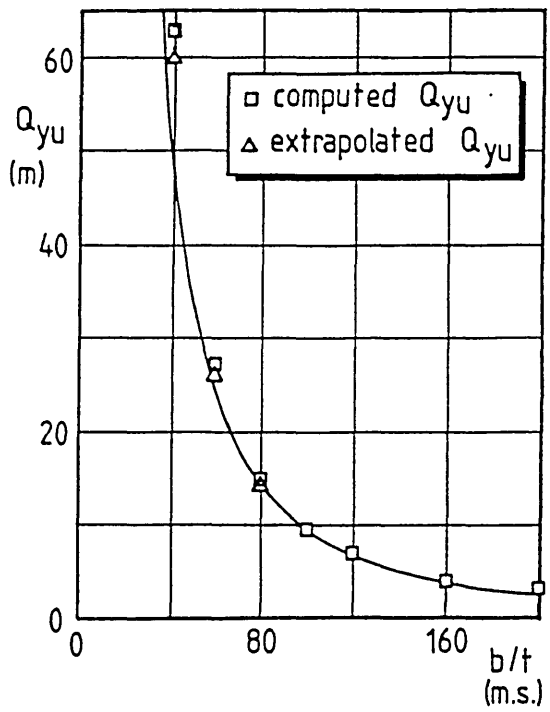

FIGURE 6.34 – Yield strain pressure model of eq.6.18, for 3:1 plates, compared to computed yield strain pressures and extrapolations from fig.6.33

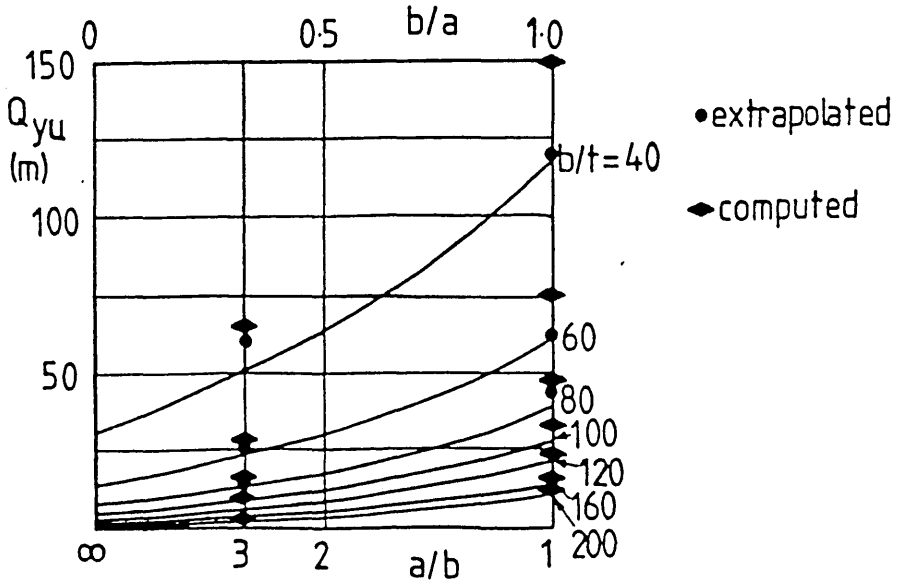

FIGURE 6.35 – Yield strain pressure model of eq.6.18, plotted against aspect ratio, compared to computed and extrapolated pressures

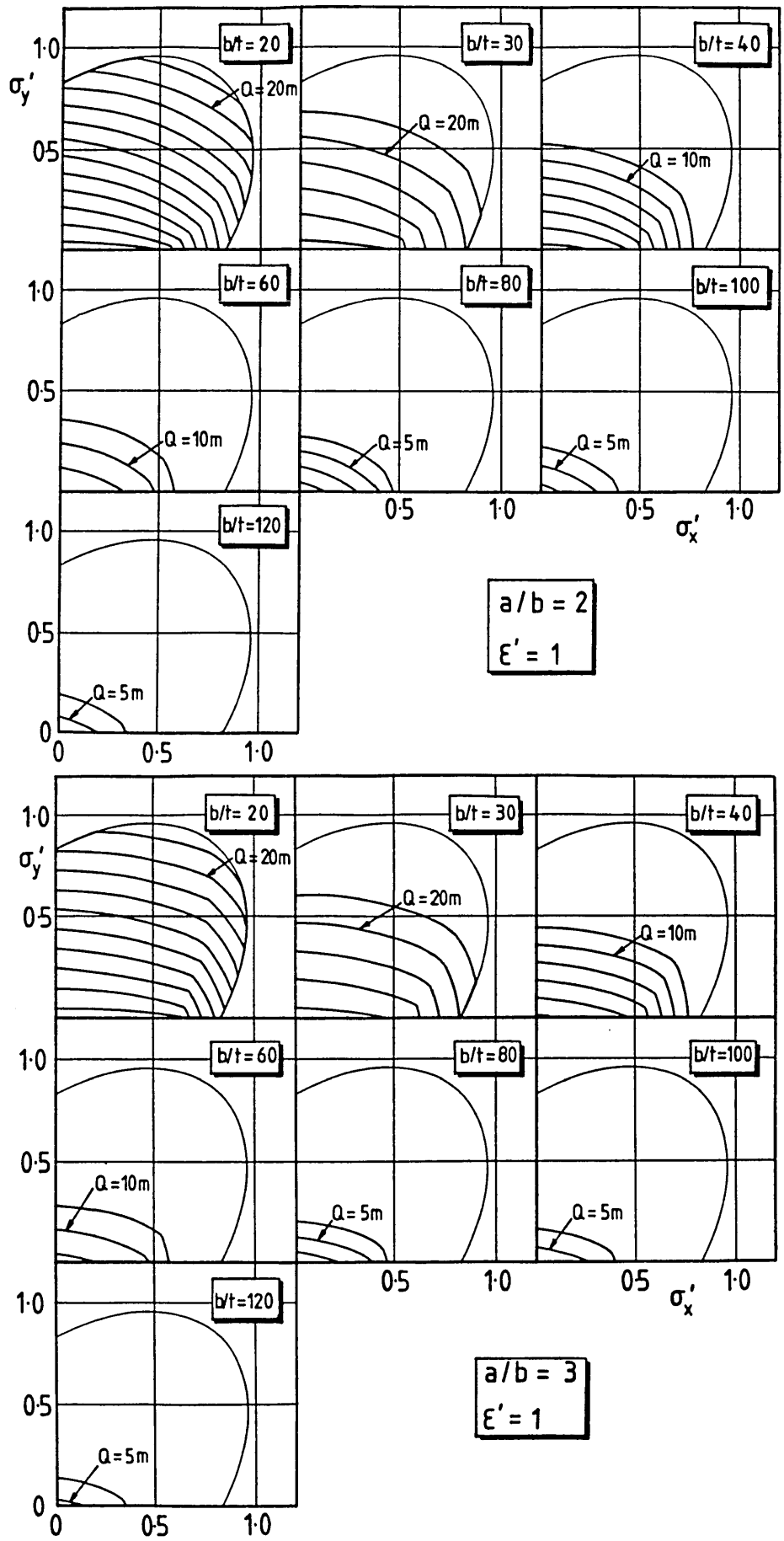

FIGURE 6.36(a) – Yield strain design curves for biaxial compression with coexistent pressure – a/b=2 & 3

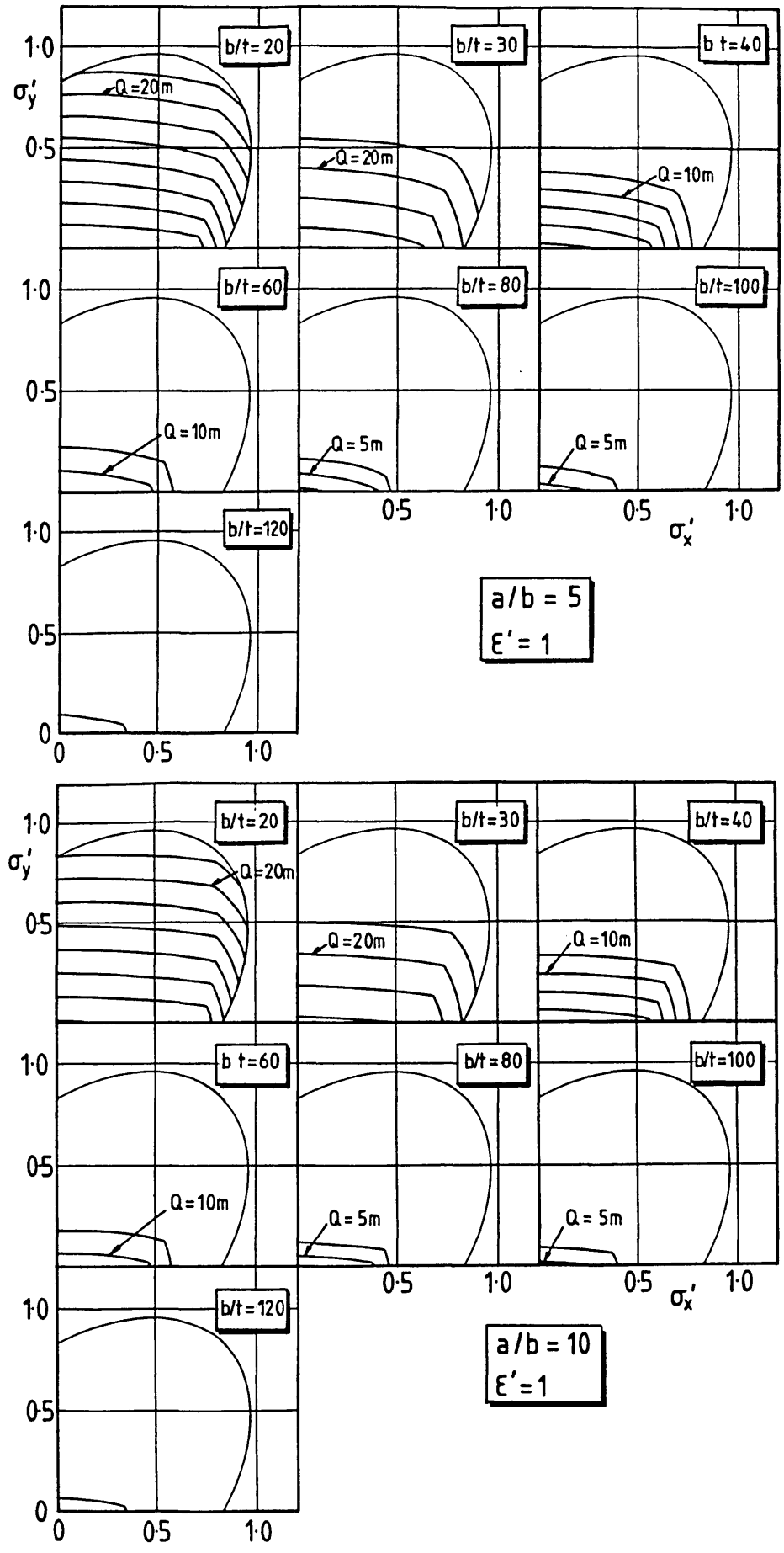

FIGURE 6.36(b) – Yield strain design curves for biaxial compression with coexistent pressure – a/b=5 & 10

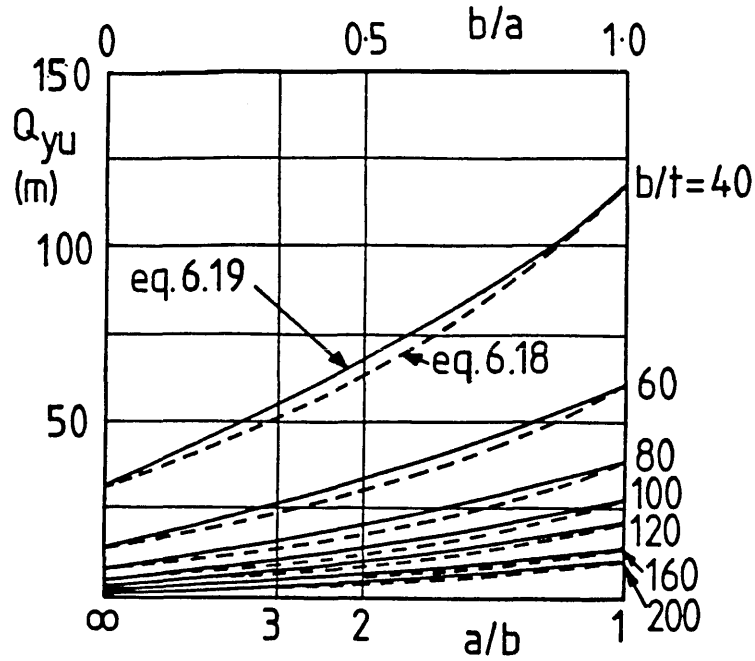

FIGURE 6.37 – Comparison between pressure models of equations 6.18 and 6.19

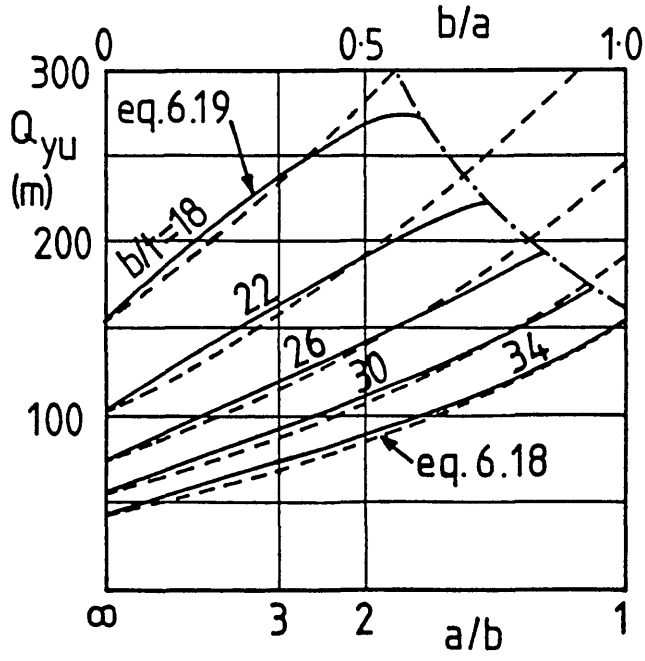

FIGURE 6.38 – Locus of points at which pressure model of eq.6.19 breaks down

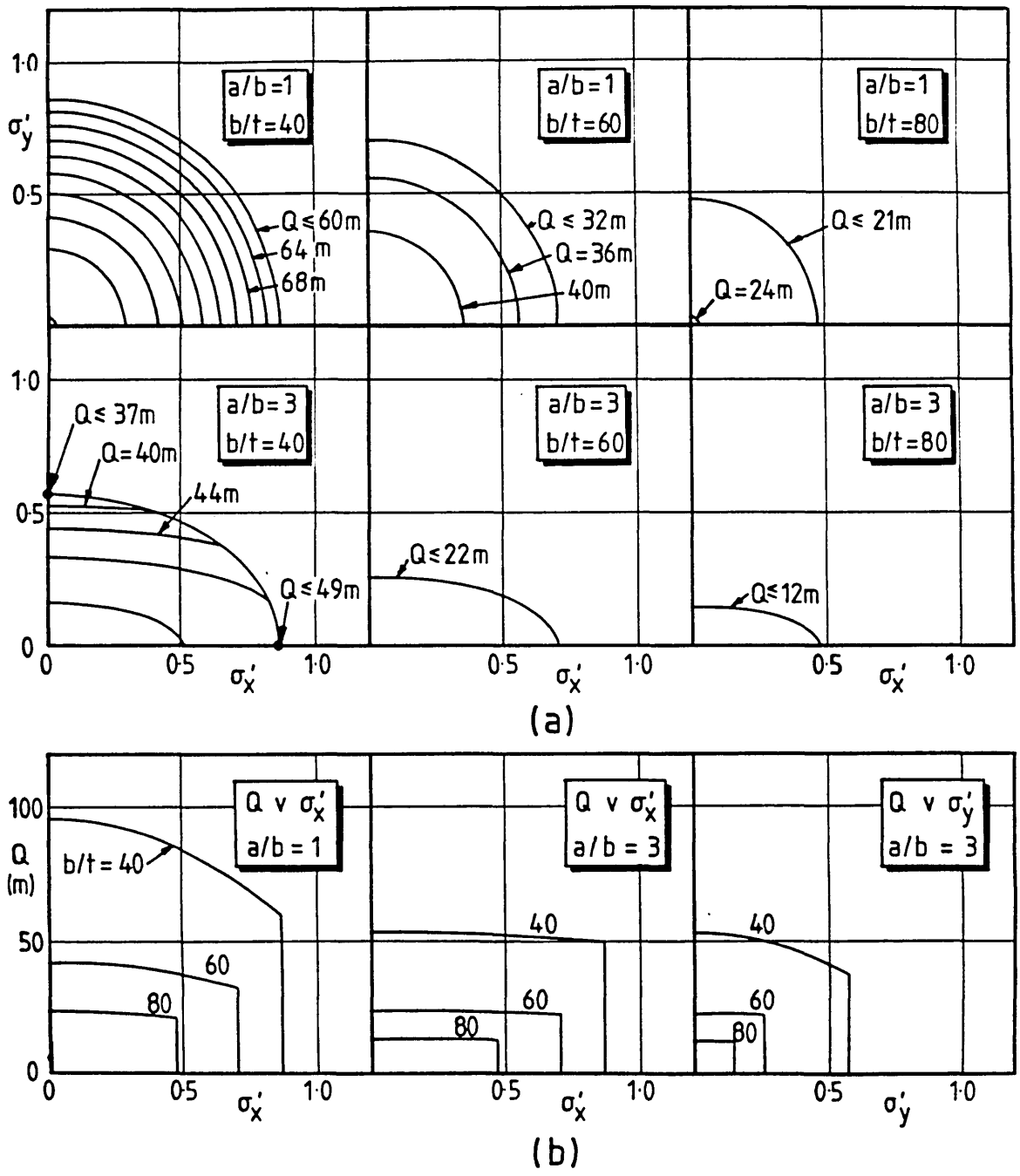

FIGURE 6.39 – Biaxial interactions in the presence of pressure, and interactions between pressure and uniaxial compression from (63) – 4 metre increments of water pressure

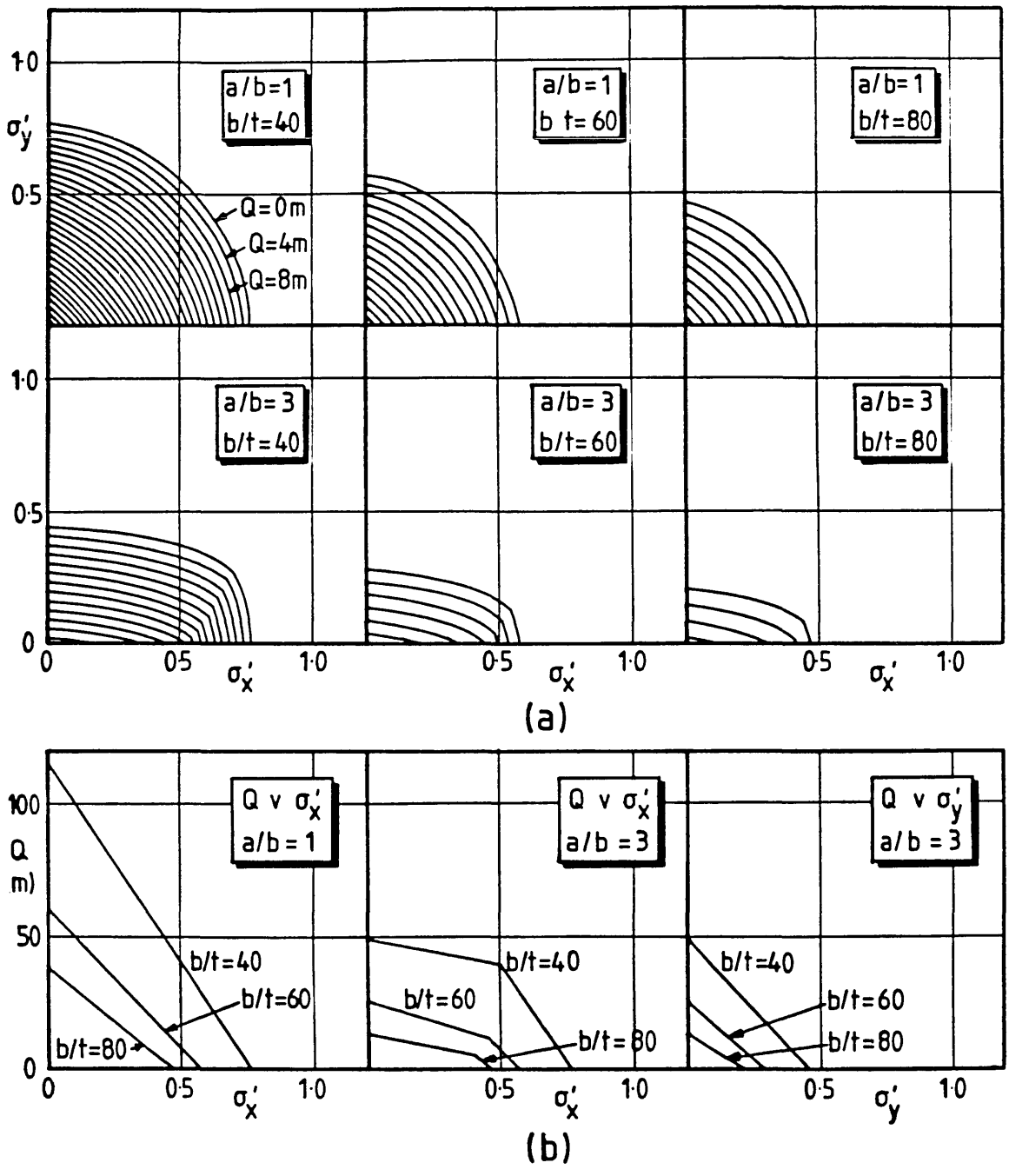

FIGURE 6.40 – Biaxial interactions in the presence of pressure, and interactions between pressure and uniaxial compression from proposed yield strain model – equivalent to figure 6.39

CHAPTER 7 DESIGN MODEL SUMMARY

7.1 Introduction

This Chapter presents a summary of all the design models presented in the preceding Chapters, which are relevant to the design resistance at yield strain, of rectangular panels with initial imperfections no greater than $w_0/t=0.1\beta^2$, and residual stresses no greater than $0.2\ \sigma_0$. For design models for the maximum resistance of panels, or for the resistance at other imperfection levels, or for guidance on how to use the models to calculate the loss of compressive strength in dented panels, the reader is referred to the preceding Chapters.

It should be noted that, although the interaction between biaxial compression and lateral pressure is treated separately from the interaction between biaxial compression and shear, it is the intention that a single unified treatement will in due course be given. It is because this has not yet been validated, that the shear and pressure interaction effects have been separated.

Ideally, the design method which is summarized in this chapter should be presented together with a background document and commentary, which would explain the basis of the equations contained in the method, and of the overall approach. For the present purposes, however, the preceding chapters can be regarded as the required background document. To this end, the numbers of the sub-sections in this chapter correspond to the chapter number in which the relevant modelling is developed (for instance, chapter 3 provides the background to sections 7.3, 7.3.1, 7.3.2 and 7.3.3).

In addition, the equation numbers from the preceding chapters are also referred to in the following summary.

7.1.1 Notation

The notation used in this design summary is given at the beginning of the thesis. Attention is drawn, however, to the use of a non-dimensional parameter, β, to denote slenderness, where β is defined as

$$\beta = b/t\ \sqrt{(\sigma_0/E)}$$

7.2 Shear

The shear which is applied to a panel should be less than the design shear resistance which is given by 7.2.1 to 7.2.3.

The design shear resistance differentiates between the different constraint conditions which will exist at a boundary of a panel by virtue of the presence or absence of an adjacent panel (in the same plane) at the boundary. If an adjacent panel exists at a panel boundary, then that boundary is described as "constrained", whereas if no such panel exists, then the boundary is described as "un-constrained".

7.2.1 Constrained Panels

A constrained panel is one which has all of its edges constrained. The design shear resistance of such a panel, τ_{cc}, is given by

$$\tau_{cc} = \tau_u$$

where τ_u is given in 7.2.4, with $c_1 = 1.3 - 0.05\,\alpha$; for $\alpha \leq 5$ (2.7)

$c_1 = 1.05$; for $\alpha > 5$

$c_2 = 0.85 - c_1$; for all α

7.2.2 Unconstrained Panels

An unconstrained panel is a panel which has two unconstrained edges meeting at a corner, whatever the boundary conditions which exist on the remaining two edges. The design shear resistance of such a panel, τ_{uu}, is given by

$$\tau_{uu} = \tau_u$$

where τ_u is given in 7.2.4, with $c_1 = 1.12 - 0.15\,\alpha$; for $\alpha < 3$ (2.8)

$c_1 = 0.67$; for $\alpha \geqslant 3$

$c_2 = 0.14\,\alpha - .3$; for $\alpha < 3$

$c_2 = 0.12$; for $\alpha \geqslant 3$

7.2.3 Panels neither Constrained nor Unconstrained

Panels which satisfy neither of the boundary condition combinations of 7.2.1 and 7.2.2 have their design shear resistance defined by interpolation between τ_{cc} and τ_{uu} as defined in 7.2.1 and 7.2.2.

The interpolation is based on the aspect ratio of the panel and on whether the unconstrained edge is longer or shorter than the adjacent constrained edges.

7.2.3.1 Unconstrained edge longer than Constrained

When the unconstrained edge is longer than (or equal in length to) the adjacent constrained edges, then the design shear resistance, τ_{cu}, is given by

$$\tau_{cu} = \frac{\tau_{cc} - \tau_{uu}}{1 + \alpha^3} + \tau_{uu} \qquad \ldots (2.11,12)$$

where τ_{cc} is given in 7.2.1, and τ_{uu} is given in 7.2.2.

7.2.3.2 Unconstrained edge shorter than Constrained

When the unconstrained edge is shorter than the adjacent constrained edges, then the design shear resistance, τ_{cu}, is given by

$$\tau_{cu} = \frac{\tau_{cc} - \tau_{uu}}{1 + 1/\alpha} + \tau_{uu} \qquad \ldots (2.11,12)$$

where τ_{cc} is given in 7.2.1, and τ_{uu} is given in 7.2.2.

7.2.4 Shear Resistance Design Curve

The shear resistance design curve which is used for constrained and unconstrained panels is given by

$$\tau_u = \begin{cases} \tau_0 \left\{ \frac{c_1}{\lambda} + \frac{c_2}{\lambda^2} \right\} & ; \quad \text{for } \lambda \geq 1 \qquad \ldots (2.6) \\ \tau_0 \left\{ c_3 + c_4\lambda + c_5\lambda^2 + c_6\lambda^3 \right\} & ; \quad \text{for } 0.5 \leq \lambda < 1 \qquad (2.9) \\ \tau_0 & ; \quad \text{for } \lambda < 0.5 \end{cases}$$

where c_1 and c_2 are from 7.2.1 or 7.2.2, and c_3 to c_6 are given by

$$\begin{aligned} c_3 &= -4 + 6\,c_1 + 7\,c_2 \\ c_4 &= 24 - 29\,c_1 - 34\,c_2 \\ c_5 &= -36 + 44\,c_1 + 52\,c_2 \\ c_6 &= 16 - 20\,c_1 - 24\,c_2 \end{aligned} \qquad \ldots (2.10)$$

and $\lambda = \frac{0.8}{\sqrt{k}}\,\beta$

The buckling factor, k, is given by $k = 5.34 + 4/\alpha^2$

7.3 Uniaxial Compression

Uniaxial compressions which act along the length of a rectangular panel are described as longitudinal, whereas compressions which act across its width are described as transverse.

The uniaxial compression resistances of panels which are not constrained as defined in 7.2.1 are not covered by these recommendations. A simple modification factor is given in (24) which can be applied to the compression resistance of constrained panels in order to obtain the uniaxial strengths of unconstrained panels, but this has not been verified as part of the current model.

The magnitude of the applied longitudinal or transverse compressions should be less than the Buckling Resistance from 7.3.2 or 7.3.4, as appropriate, and less than the Yield Limit of 7.3.1. The Buckling Resistance is the design resistance of a panel which is prone to buckling. The Yield Limit is the design resistance of a panel which is sufficiently stocky for the panel to be fully effective in resisting the applied loads. It is necessary to check that both limits are satisfied.

If a shear stress is also applied to the uniaxially compressed plate, then the compression design resistance should be reduced, by using a multiplier, ζ, given in 7.5.

7.3.1 Uniaxial Compression Yield Limit

Due to the effect of residual stresses (equal to 20% of the yield stress) on the average stress which will exist in an unbuckling panel at yield strain, the longitudinal or transverse uniaxial compression stresses should not exceed $0.83\sigma_0$.

7.3.2 Longitudinal Compression Buckling Resistance

The longitudinal compression design resistance, σ_{xu}, is given by

$$\sigma_{xu} = \left[0.08 + \frac{1.21}{\beta} - \frac{0.40}{\beta^2} + \frac{0.05}{\beta^3} \right] \sigma_0 \qquad \ldots (3.15)$$

7.3.3 Transverse Compression Buckling Resistance

The transverse compression design resistance, σ_{yu}, is given by

$$\sigma_{yu} = \sigma_c + \frac{(\sigma_{xu} - \sigma_c)}{\alpha} \qquad \ldots (3.4)$$

where σ_{xu} is from 7.3.1, and σ_c is given by

$$\sigma_c = \left\{ \frac{0.025}{\beta} + \frac{0.641}{\beta^2} - \frac{0.188}{\beta^3} \right\} \sigma_0 \quad \ldots (3.7)$$

7.4 Biaxial Compression and Shear

If a constrained panel (as defined in 7.2.1) is subjected to both longitudinal compression, σ_x, and transverse compression, σ_y, then the magnitudes of these stresses should be less than the yield limits of 7.4.1 and the buckling resistance of 7.4.2 for square panels, and 7.4.3 for rectangular panels.

If a shear stress is also applied to the panel then the biaxial resistance of the panel is reduced. In the following clauses this is taken into account by incorporating a factor, ζ, which is given in 7.5, into the calculation of the biaxial resistance. If no shear stress is applied to the panel then ζ is set to 1.0.

7.4.1 Yield Limit

Due to the effect of residual stresses on the average stress in an unbuckling panel at yield strain, the biaxial compressions, σ_x, and σ_y, should satisfy the following limit:

$$\sigma_x^2 - \sigma_x \sigma_y + \sigma_y^2 \leq 0.7 \sigma_0^2 \zeta^2$$

The 0.7 on the right hand side is for consistency with the $0.83\sigma_0$ limit of 7.3.1 (ie $0.7 \sigma_0^2 = (0.83 \sigma_0)^2$).

7.4.2 Buckling Limit for Square Plates

The applied longitudinal and transverse compressive stresses should satisfy the following limit

$$\sigma_x^2 + \eta \sigma_x \sigma_y + \sigma_y^2 \leq \sigma_{xu}^2 \zeta^2 \quad \ldots (4.1)$$

where σ_{xu} is from 7.3.2, and η is given by

$$\eta = \left[\frac{\sigma_{xu}}{\sigma_{bu}} \right]^2 - 2 \quad \ldots (4.3)$$

and $$\sigma_{bu} = \frac{0.937}{\beta} - \frac{0.32}{\beta^2} + \frac{0.053}{\beta^3} \quad ; \quad \text{but } \sigma_{bu} \leq \frac{\sigma_{xu}}{2} \quad \ldots (4.8)$$

7.4.3 Buckling Limit for Rectangular Plates

If a rectangular panel is subject to biaxial compression stresses, σ_x, and σ_y, then these stresses must satisfy the buckling stress limits given in 7.4.3.1, for each of the possible modes of buckling for the panel. These modes are obtained by dividing the length of the panel into an integer number of buckling mode half-waves. The length of each half-wave divided by the panel width, b, is denoted by the buckle aspect ratio, α_b.

The longest mode (which will be for predominantly transverse loading) is such that $\alpha_b = \alpha$, whereas α_b in the shortest mode (which will be for predominantly longitudinal compression) will depend on the longitudinal compression critical buckling mode of the panel, and will be equal to 1 for integer values of α. For non-integer values of α, the number of half-waves in the shortest wavelength mode should be an integer which does not lie outside the range $\alpha \pm 0.5$, unless reference is made to critical buckling theory for more accurate guidance on the buckling modes appropriate to longitudinally compressed rectangular panels of non-integer aspect ratios.

7.4.3.1 Rectangular Plate Buckling Interaction

The following limit must be satisfied

$$\left[\frac{\sigma_x}{\sigma_{xu1}}\right]^2 + \eta\left[\frac{\sigma_x}{\sigma_{xu1}}\right]\left[\frac{\sigma_{y1}}{\sigma_{yu1}}\right] + \left[\frac{\sigma_{y1}}{\sigma_{yu1}}\right]^2 \leq \zeta^2 \qquad \ldots (4.7)$$

where

$$\sigma_{y1} = \frac{\alpha_b}{\alpha_p}\sigma_y + \left(1 - \frac{\alpha_b}{\alpha_p}\right)\sigma_c \zeta$$

$$\alpha_p = 2.5/\beta \quad ; \quad \text{but} \quad \alpha_p \not< 1.0 \quad \text{unless} \quad \alpha_b < 1.0 \qquad (4.6)$$
$$\alpha_p \not> \alpha_b$$

$$\sigma_{xu1} = \sigma_{cp} + \alpha_p\left(\sigma_{xup} - \sigma_{cp}\right)$$

$$\sigma_{yu1} = \sigma_c + \left(\sigma_{xu} - \sigma_c\right)/\alpha_p \qquad \ldots (3.4)$$

$$\sigma_{xup} = \sigma_0\left\{0.08 + \frac{1.21}{\beta_p} - \frac{0.40}{\beta_p^2} + \frac{0.05}{\beta_p^3}\right\} \qquad \ldots (3.15)$$

$$\sigma_{cp} = \sigma_0\left\{\frac{0.025}{\beta_p} - \frac{0.641}{\beta_p^2} + \frac{0.188}{\beta_p^3}\right\} \qquad \ldots (3.7)$$

$$\beta_p = \alpha_p \beta$$

σ_{xu} is given by σ_{xu} from 7.3.2, σ_c is given in 7.3.3, and η is from 7.4.2.

7.5 Shear Reduction factor on Compression Resistance

When a shear stress, τ, is acting in conjunction with biaxial compression, then the biaxial compression interactions of 7.4 are modified by a factor, ζ, which is less than unity and is a function of the magnitude of shear stress being applied to the panel,

and of the panel slenderness.

$$\zeta = \left\{ 1 - \left[\frac{\tau}{\tau_r} \right]^2 \right\}^{1/n} \quad \ldots (5.8)$$

$$\text{where} \quad n = \begin{cases} 2 - \lambda & ; \text{ for } \lambda < 1 \\ 1 & ; \text{ for } \lambda \geq 1 \end{cases} \quad \ldots (5.7)$$

where λ is defined in 7.2.4, and τ_r is the design shear resistance given by τ_{cc}, τ_{uu} or τ_{cu} from 7.2.1, 7.2.2 or 7.2.3 as appropriate (but note that, in their current form, 7.3 and 7.4 are for constrained plates only).

7.6 Biaxial Compression and Uniform Lateral Pressure

If a constrained panel (as defined in 7.2.1) is subjected to biaxial compression and uniform lateral pressure, Q, then the magnitudes of the biaxial stresses, σ_x and σ_y, should be less than the buckling resistance of 7.6.2 for square panels, and 7.6.3 for rectangular panels.

The biaxial stresses should also comply with the yield limit of 7.6.1.

7.6.1 Yield Limit

Due to the effect of residual stresses on the average stresses in an unbuckling panel at yield strain, the biaxial compressions, σ_x, and σ_y, should satisfy the following limit

$$\sigma_x^2 - \sigma_x \sigma_y + \sigma_y^2 \leq 0.7 \sigma_0^2$$

7.6.2 Buckling Limit for Square Plates

The applied longitudinal and transverse compressive stresses should satisfy the following limit

$$\sigma_x^2 + \eta_q \sigma_x \sigma_y + \sigma_y^2 \leq \sigma_{xq}^2 \quad \ldots (6.10)$$

where η_q is given by

$$\eta_q = \left[\frac{\sigma_{xq}}{\sigma_{bq}} \right]^2 - 2 \quad \ldots (6.9)$$

$$\text{and} \quad \sigma_{xq} = \left[1 - \frac{Q}{Q_{xu}} \right] \sigma_{xu} \quad \ldots (6.6)$$

$$\sigma_{bq} = \sigma_{bu} + \frac{\sigma_{xq}}{2} - \sqrt{\frac{\sigma_{xq}^2}{4} + \left\{ \frac{\sigma_{xu}^2 - \sigma_{xq}^2}{2\eta} \right\}} \quad \ldots (6.8)$$

$$Q_{xu} = \begin{cases} 6\,\dfrac{\sigma_0^{\,2}}{E\beta^2} & ;\ \beta \leq 0.5 \\ \dfrac{6}{7}\,\dfrac{\sigma_0^{\,2}}{E}\left\{\dfrac{2}{\beta} + \dfrac{6}{\beta^2}\right\} & ;\ 0.5 \leq \beta < 7.5 \end{cases} \quad \ldots (6.12)$$

σ_{xu} is from 7.3.2, and σ_{bu} and η are from 7.4.2.

7.6.3 Buckling Limit for Rectangular Plates

If a rectangular panel is subject to biaxial compression and uniform lateral pressure, Q, then the biaxial stresses, σ_x and σ_y, must satisfy the buckling stress limits given in 7.6.3.1, for each of the possible modes of buckling for the panel. These modes are obtained by dividing the length of the panel into an integer number of buckling mode half-waves. The length of each half-wave divided by the panel width, b, is denoted by the buckle aspect ratio, α_b.

The longest mode to be considered is when the panel deforms in a single buckle, and is such that $\alpha_b = \alpha$, whereas the shortest mode will depend on the critical buckling mode of the panel in longitudinal compression only, and will be equal to 1 for integer values of α. For non-integer aspect ratios, the number of half-waves in the shortest wavelength mode should not lie outside the range $\alpha \pm 0.5$, unless reference is made to critical buckling theory for more detailed guidance on the buckling modes appropriate to longitudinally compressed rectangular panels of non-integer aspect ratios.

7.6.3.1 Rectangular Plate Buckling Interaction

The following limit must be satisfied

$$\left[\frac{\sigma_x}{\sigma_{xq_1}}\right]^2 + \eta_q\left[\frac{\sigma_x}{\sigma_{xq_1}}\right]\left[\frac{\sigma_{y_1}}{\sigma_{yq_1}}\right] + \left[\frac{\sigma_{y_1}}{\sigma_{yq_1}}\right]^2 \leq 1.0 \quad \ldots (6.15)$$

where

$$\sigma_{y_1} = \frac{\alpha_b}{\alpha_p}\sigma_y + \left(1 - \frac{\alpha_b}{\alpha_p}\right)\sigma_{cq}$$

$$\alpha_p = 2.5/\beta \quad ; \quad \text{but} \quad \alpha_p \leq 1.0 \text{ unless } \alpha_b < 1 \quad \ldots (4.6)$$
$$\alpha_p \geq \alpha_b$$

$$\sigma_{xq_1} = \left[1 - \frac{Q}{Q_{xu}}\right]\sigma_{xu_1}$$

$$\sigma_{yq_1} = \left[1 - \frac{Q}{Q_{yu}}\right]\sigma_{yu_1} \quad \ldots (6.13)$$

$$\sigma_{xu_1} = \sigma_{cp} + \alpha_p\left(\sigma_{xup} - \sigma_{cp}\right)$$

$$\sigma_{yu_1} = \sigma_c + \left(\sigma_{xu} - \sigma_c\right)/\alpha_p$$

$$\sigma_{xup} = \sigma_0 \left\{ 0.08 + \frac{1.21}{\beta_p} - \frac{0.40}{\beta_p^2} + \frac{0.05}{\beta_p^3} \right\} \quad \ldots (3.15)$$

$$\sigma_{cp} = \sigma_0 \left\{ \frac{0.025}{\beta_p} - \frac{0.641}{\beta_p^2} + \frac{0.188}{\beta_p^3} \right\} \quad \ldots (3.7)$$

$$\beta_p = \alpha_p \beta$$

$$\sigma_{cq} = \begin{cases} 0 & ; \text{ if } \alpha_b = \alpha_p \\ \dfrac{(\sigma_{yq} \alpha_b - \sigma_{yq_1} \alpha_p)}{\alpha_b - \alpha_p} & ; \text{ if } \alpha_b \neq \alpha_p \end{cases} \quad \ldots (6.14)$$

$$Q_{yu} = 6 \frac{\sigma_0^2}{E\beta^2} \frac{(K + 1/\alpha_b)}{(3K - 1/\alpha_b)} \quad \ldots (6.18)$$

$$Q_{yu_1} = 6 \frac{\sigma_0^2}{E\beta^2} \frac{(K + 1/\alpha_p)}{(3K - 1/\alpha_p)} \quad \ldots (6.18)$$

$$K = \begin{cases} 1 & ; \beta < 0.5 \\ \dfrac{(13 + 2\beta)}{(11 + 6\beta)} & ; 0.5 < \beta \leq 7.5 \end{cases}$$

σ_{xu} is given by σ_{xu} from 7.3.2, σ_c is given in 7.3.3, and Q_{xu} and η_q are from 7.6.2.

CHAPTER 8 CONCLUSIONS

(1) Existing design models of panel shear strength rely on the existence of axial forces in the stiffeners (and flanges) at the panel boundaries, in order to develop the shear capacity of the web. However, in current applications of these design models, not all of these axial forces are accounted for, and this is considered to be non-conservative.

(2) A shear strength design model is proposed which defines the shear capacity of panels with a variety of different configurations of internal and external boundaries. Moreover, the panel shear resistance defined by this model does not rely on the surrounding stiffeners and flanges being able to supply tangential restraint forces to the panel. It seems reasonable therefore to neglect these axial force effects in the design of the stiffeners and flanges.

(3) Principal stress diagrams, derived from the numerical analyses, clearly show the presence of diagonal tension fields. In addition, the stress field in the off-diagonal regions is reasonably represented by the uniform critical shear stress which is predicted by tension field models, but with the inclusion of tangential compressions along the panel boundaries. These edge compressions, which replace the flange and stiffener compressions required by tension field models, equilibrate the diagonal tension field which in all cases is much closer to the angle of the diagonal than to half the angle of the diagonal which is the basis of Basler's tension field model. Even when all four edges of a square panel are unconstrained, tension fields can be seen, balanced by edge compressions along all four edges.

(4) It is suggested that the designer of full-depth webs can usefully be offered the option of using either the design model for CUCU plates, or the tension field models which are already in use. The former option will generally give a heavier web (especially so for tall panels), but lighter stiffening (and a simpler design process for the stiffeners), whereas the latter option will produce a lighter web, but with heavier stiffening. This kind of flexibility gives the designer the freedom to make the most economic and/or convenient choice for the particular circumstance.

(5) Design models for the strength of constrained rectangular panels subjected to uniaxial longitudinal or transverse compression are also proposed. The transverse strength model partitions the plate into doubly-curved end regions which together make up a square plate, with the remaining central portion of the plate forming a transverse strut. The models have been shown to give good agreement with the

numerical data.

(6) It has been shown that the uniaxial compression model can also be used to find the reduced longitudinal strength of rectangular panels which have suffered local indentation damage, or which have been otherwise predisposed to buckle with a half-wavelength of less than the width.

(7) The implications of using strength functions which define the maximum panel resistance without regard to the average strain in the panel at maximum resistance have been pointed out. In particular, the maximum strength of a multi-panel assemblage cannot simply be taken to be the aggregate of the maximum resistances of the component panels, since some may be un-loading while others have not yet attained their maximum resistance. In addition, a maximum resistance which is attained at several times the yield strain requires the surrounding stiffeners to maintain their stability and flexural stiffness in the presence of significant axial plastic straining. This has onerous implications for stiffener compactness criteria. A design resistance which is defined as being the resistance of the panel when the average strain is equal to the yield strain provides a more satisfactory basis for design. This also provides a consistent failure criterion for lateral pressure acting in combination with in-plane biaxial compression.

(8) A simple elastic analysis is used to estimate how the numerical results would differ if the residual stress and initial imperfection assumptions were to be changed, and this is shown to agree well with numerical data for slight and severe levels of both σ_r and w_0. It has also been used to estimate the resistance at yield strain, given the maximum resistance from the numerical data. Where the original stress-strain curves are available it has been possible to show that the elastic model also gives a good prediction of these yield strain resistances. This has provided a basis for generalizing the numerical data in order to define design functions at yield strain, and for other levels of σ_r and w_0. It also indicates how compressive stress-strain curves, consistent with the strength functions, can be derived.

(9) The simple elastic analysis mentioned in the previous paragraph is a subset of the wider analysis which is derived for plates subjected to biaxial compression, with coexistent uniform lateral pressure. This analysis is shown to give good qualitative, and occasionally quantitative, agreement with rigorous analyses. In particular, when the elastic analysis is used with a suitable yield criterion, it predicts an effect of pressure on uniaxial strength, and on the biaxial compression interactions, which suggests a suitable basis for generalizing the numerical data.

(10) The elastic analysis is also shown to predict accurately the influence of residual stresses and initial imperfections on the response of simply supported constrained plates to lateral pressure.

(11) The elastic model has also been used to demonstrate that there are limits on the combinations of residual stress and initial imperfection which may be assumed to exist in a plate. It has been shown that certain combinations of σ_r and w_0 are inconsistent at certain slendernesses. Particular difficulties arise from assuming that w_0/t does not increase, and that σ_r does not decrease, with increasing slenderness.

(12) The pressure to cause average strains in the plate equal to the yield strain, obtained from elasto-plastic analyses, is shown to be related to the pressure obtained from simple flexure-only yield line analyses by a multiplier which varies linearly with slenderness. An approximately linear relation is also indicated between large and small deflection elastic analyses with a consistent yield criterion.

(13) There is some evidence to suggest that the maximum uniaxial compressive resistance reduces in an approximately linear fashion as the lateral pressure is increased. The evidence suggests that linear extrapolations from these reduced compressive strengths, in order to find the pressure at which the compression resistance will have reduced to zero, will provide a safe basis for design at maximum resistance. The suitability of the linear interaction between lateral pressure and uniaxial compression has been clearly demonstrated, where a yield strain criterion is adopted as the limit state.

(14) A design model for biaxial compression, with or without coexistent lateral pressure has been formulated, which is based on identifying the different types of behaviour which occur in the doubly-curved end regions of a single buckle half-wave, and in the singly curved central region, in the presence of biaxial compression and lateral pressure. This results in a relatively simple, but rational, design model which takes explicit account of the different buckling modes of the plate and gives good agreement with the numerical data, for all aspect ratios, slendernesses, and coexistent lateral pressures for which there are data.

(15) A simple empirical design model for the interaction between shear and biaxial compression is suggested. This gives reasonable agreement with the numerical data.

(16) The shapes of $\tau-\gamma$ curves for τ alone vary greatly, according to panel geometry and boundary conditions. In particular, it is found that for slender panels

constrained on all four edges, a reduction in the average shear strain may occur after the peak stress has been attained. This reduction is accompanied by increasing buckling displacements, w, and increasing direct compressive strains, ϵ.

(17) The shapes of stress–strain curves for combined biaxial compression and shear also vary widely, according to the ratios of the applied stresses, and the panel geometry.

(18) In previous research into panels subjected to combined in–plane loads, using the Dynamic Relaxation method, loads were applied as proportional strains, giving rise to applied stresses which varied in their proportion to one another as the strain was increased. It has been shown that a stress–strain curve for proportional stresses can be inferred from the proportional strain stress–strain curves, by interpolating between them. The interpolated stress–strain curves agree very well with the stress–strain curves produced by finite element analyses with truly proportional stressing. This has been shown to be the case both for shear applied to restrained and unrestrained plates, and for biaxial compression applied to constrained plates.

(19) Design models have been presented which are simple to use, yet which are demonstrated to give good agreement with numerical data, and are an advance on the methods given in design codes.

REFERENCES

1. Komatsu, S., & Kitada, T.: "Statistical Study on Compression Butt-Welded Plate", *Jl.Struct.Eng.*, ASCE, Vol.109, No.2, 1983, pp.386-403.

2. Komatsu, S., & Nara, S.: "Statistical Study on Steel Plate Members", *Jl.Struct.Eng.*, ASCE, Vol.109, No.4, 1983, pp.977-992.

3. Antoniou, A.C.: "On the Maximum Deflection of Plating in Newly Built Ships", *Jl. Ship Research*, Vol.24, March 1980, pp.31-39.

4. Antoniou, A.C., Lavidas, M., & Karvounis, G.: "On the Shape of Post-Welding Deformations of Plate Panels in Newly Built Ships", *Jl. Ship Research*, Vol.28, No.1, March 1984, pp. 1-10.

5. Carlsen, C.A., & Czujko, J.: "The Specification of Post-Welding Distortion Tolerances for Stiffened Plates in Compression", *The Structural Engineer*, Vol.65A, No 5, May 1978 pp.133-141.

6. Galambos, T.V., & Ravindra, M.K.: "Properties of Steel for use in LRFD", *Jl.Struct.Div.*, ASCE, Vol.104, ST9, 1978.

7. Guedes Soares, C.: "Design Equation for the Compressive Strength of Unstiffened Plate Elements with Initial Imperfections", *Jl.Constr.Steel Res.*, Vol.9, 1988, pp.287-310.

8. Pham, L., & Bradford, M.A.: "Safety Index Analysis of the Design Rules for Webs of Steel Members under Shear", *UNICIV Report No.R-244*, Univ. of New South Wales, 1987.

9. "Uncertainty and Structural Reliability", *Volume 2*, Proc. 10th Intl. Ship & Offshore Structures Congress, Lyngby, 1988.

10. Planeix, J.M.: "Recent Progress in Probabilistic Structure Design", *Paper No.31*, Conf. on Advances in Marine Structures, ARE, Dunfermline, 1986.

11. Smith, C.S.: "Influence of Local Compressive Failure on Ultimate Longitudinal Strength of Ship's Hull", *Proc. Intl. Symp. on Practical Design in Shipbuilding (PRADS 77)*, Tokyo, 1977.

12. Ueda, Y., Rashed, S.M.H., & Paik, J.K.: "Plate and Stiffened Plate Units of the Idealized Structural Unit Method (1st Report) - Under In-plane loading", *Jl.Soc.Nav.Arch. of Japan*, Vol.156, 1984, pp.366-377 (in Japanese).

13. Ueda, Y., Rashed, S.M.H., Paik, J.K., & Masaoka, K.: "The Idealized Structural Unit Method Including Global Non-linearities - Idealized Rectangular Plate and Stiffened Plate Elements", *Jl.Soc.Nav.Arch. of Japan*, Vol.159, 1986, pp.271-281 (in Japanese).

14. Ueda, Y., Rashed, S.M.H., & Paik, J.K.: "Plate and Stiffened Plate Units of the Idealized Structural Unit Method (2nd Report) - Under In-plane and Lateral Loading Considering Initial Deflection and Residual Stress", *Jl.Soc.Nav.Arch. of Japan*, Vol.160, 1986, pp.318-336 (in Japanese).

15. Viner, A.C.: "Development of Ship Strength Formulations", *Paper No.8*, Conf. on Advances in Marine Structures, ARE, Dunfermline, 1986.

16. Volume 1, Proc. 10th Intl. Ship & Offshore Structures Congress, Lyngby, 1988, pp.365-367.

17. Caldwell, J.B.: "Structural Optimization - What is wrong with it?", *Paper No.26*, Conf. on Advances in Marine Structures, ARE, Dunfermline, 1986.

18. Wagner, H.: "Ebene Blechwandträger mit sehr dünnem Stegblech", *Zeitscrift für Flugtechnik und Motorluftschiffart*, Vol.20, 1929, pp.200, 227, 256, 279, and 306.

19. Basler, K.: "Strength of Plate Girders in Shear", *Jl.Struct.Div.*, ASCE, Proc. No. 2967, ST7, October 1961, pp.151-180.

20. Fujii, T.: "On an Improved Theory for Dr. Basler's Theory", *Proc. 8th Congress*, IABSE, New York, September 1968, pp.477-487.

21. Rockey, K.C., & Skaloud, M.: "The Ultimate Load Behaviour of Plate Girders Loaded in Shear", *The Structural Engineer*, Vol.50, No.1, 1972.

22. Porter, D.M., Rockey, K.C., & Evans, H.R.: "The Collapse Behaviour of Plate Girders Loaded in Shear", *The Structural Engineer*, Vol.53, No.8, August 1975.

23. Evans, H.R., & Tang, K.H.: "A Report on Five Tests carried out on a Large-Scale Transversely Stiffened Plate Girder - TRV3", *Report No. DT/SC/8*, Univ.Coll. Cardiff, 1981.

24. BS 5400 part 3: "Steel, Concrete and Composite Bridges - Code of Practice for the Design of Steel Bridges", British Standards Institution, 1982.

25. BS 5950 part 1: "Structural Use of Steelwork in Buildings - Code of Practice for Design in Simple and Continuous Construction: Hot Rolled Sections", British Standards Institution, 1985.

26. Eurocode 3 part 1: "Design of Steel Structures - General Rules and Rules for Buildings", Final Draft, December 1988.

27. Von Mises, R.: "Mechanik der Festen Korper in Plastisch Deformablen Zustand", *Gottinger Nachr. Math. Phys. Kl.*, 1913, p.582

28. Tresca, H.: "Mémoire sur l'écoulement des Corps Solides Soumis à des Fortes Pressions", *Comptes Rendus Acad. Sci.*, Paris, Vol.59, 1864, p.754.

29. "Stability of Steel Structures", 2nd Intl. Colloquium on Stability, *Introductory Report,* Liege, ECCS, 1977.

30. Dubas, P.: "Zür Erschöpfungslast schubbeanspruchter Stehbleche", Professor Steinhardt Festschrift, Karlsruhe, 1974. See also page 201 of reference (29).

31. Marsh, C.: "Theoretical Model for Collapse of Shear Webs", *Jl.Eng.Mech.Div.* ASCE, Vol.108, EM5, pp.819-832.

32. Marsh, C.: "Photoelastic Study of Post-buckled Shear Webs", *Canadian Jl. of Civ.Eng.*, Volume 12, No.2, 1985, pp.415-417.

33. Rockey, K.C.: "An Ultimate Load Method of Design for Plate Girders", *Developments in Bridge Design and Construction*, Rockey, K.C., Bannister, J.L., & Evans, H.R., (editors), Crosby Lockwood, 1971, pp.487-504.

34. Harding, J.E. & Dowling, P.J.: "The Basis of the Proposed New Design Rules for the Strength of Web Plates and Other Panels Subject to Complex Edge Loading", *Stability Problems in Engineering Structures and Components*, Richards, T.H. & Stanley, P. (editors), Appl.Sci.Publ., 1979, pp.355-376.

35. Harding, J.E., Hobbs, R.E., Neal, B.G., & Slatford, J.: "Parametric Study on Plates under Combined Direct and Shear In-plane Loading", *CESLIC Report BG44*, Imperial College, 1976.

36. Harding, J.E., Hobbs, R.E., & Neal, B.G. : "Ultimate Load Behaviour of plates under combined direct and shear in-plane loading", *Steel Plated Structures*, Dowling, P.J., Harding, J.E., Frieze, P.A. (editors). London, Crosby Lockwood Staples, 1977, pp.369-403

37. Ilyushin, A.A., Plasticité, Editions Eyrolles, Paris, 1956.

38. Otter, J.R.H., Cassell, A.C., & Hobbs, R.E.: "Dynamic Relaxation", *Proc.I.C.E.*, Vol.35, December 1966, pp.633-656.

39. Rockey, K.C., Evans, H.R., & Porter, D.M.: "Tests on Longitudinally Reinforced Plate Girders Subjected to Shear", Stability of Steel Structures, 2nd Intl. Colloquium on Stability, *Preliminary Report,* Liege, ECCS, 1977, pp.295-304.

40. Evans, H.R.: "Longitudinally and Transversely Reinforced Plate Girders", *Plated Structures - Stability & Strength*, Narayanan, R. (editor), Appl.Sci.Publ., 1983, pp.1-37.

41. "Review of experimental work on stiffened plates", *Contractor Report No.17*, TRRL, 1986.

42. Evans, H.R.: "An Appraisal, by Full-Scale Testing, of New Design Procedures for Steel Girders Subjected to Shear and Bending", *Report No. P8972*, Univ. Coll. Cardiff, 1985.

43. Maeda, Y., Okura, I., & Hirano, H.: "Formulation of Finite Out-of-Plane Deformation of Rectangular Plate in Shear", *Tech. Reports of Osaka Univ.*, Vol.35, No.1793, March 1985, pp.91-100.

44. Marguerre, K.: "Zur theorie der Gekrümmter Platte grosser Formänderung", *Proc. 5th Intl. Congress for Applied Mechanics*, Cambridge, 1938, pp.93-101.

45. Libai, A., Weller, T., Kollet, M., & Singer, J.: "Stiffened Shear Panels Subjected to Repeated Bucklings - Durability Studies", *Sci. Report No.4, TAE No.545*, Technion Israel Inst. Tech., Haifa, July 1984.

46. Valsgaard, S.: "Ultimate Capacity of Plates in Biaxial In-Plane Compression", *Report 78-678*, Det Norske Veritas, Feb. 1978.

47. Dier, A.F.: "Collapse of Metal Plates", *PhD Thesis*, London, Imperial College, 1981.

48. Dier, A.F. & Dowling, P.J.: "Strength of Ships Plating - Plates under Combined Lateral Loading and Biaxial Compression", *CESLIC Report SP8*, Imperial College, London, 1980.

49. Dier, A.F. & Dowling, P.J.: "The Strength of Plates Subjected to Biaxial Forces", *Proc. Conf. on Behaviour of Thin-Walled Structures*, University of Strathclyde, Glasgow, 1983.

50. Czujko, J.:"Strength of Plates with Large Initial Deflections Subjected to Biaxial Compression and Lateral Pressure", *Project Rep. No.2 DnV Report No. 83-0290*, 1983.

51. Soreide, T.H., & Czujko, J.: "Load-carrying Capacity of Plates under Combined Lateral Load and Axial/Biaxial Compression", *Proc. 2nd Intl. Symp. on Practical Design in Shipbuilding (PRADS 83)*, Tokyo, 1983.

52. Steen, E., & Valsgaard, S.: "Simplified Buckling Strength Criteria for Plates Subjected to Biaxial Compression and Lateral Pressure", *Ship Structures Symp.*, Soc. Nav. Arch. & Marine Eng., Arlington, 1984.

53. Stein, M.: "Postbuckling of Long Orthotropic Plates in Combined Shear and Compression", *A.I.A.A Journal*, Vol.23, No.5, 1985, pp.788-794.

54. Stein, M.: "Postbuckling of Long Orthotropic Plates under Combined Loading", *A.I.A.A. Journal*, Vol.23, No.8, 1985, pp.1267-1271.

55. Stein, M., & Neff, J.: "Buckling Stresses of Simply Supported Rectangular Flat Plates in Shear", *NACA Tech. Note No.1222*, 1947.

56. Batdorf, S.B., & Stein, M.: "Critical Combinations of Shear and Direct Stress for Simply Supported Rectangular Flat Plates", *NACA Tech. Note No.1223*, 1947.

57. Ueda, Y., Rashed, S.M.H., & Paik, J.K.: "Buckling and Ultimate Strength Interactions of Plates and Stiffened Plates under Combined Loads (1st report) - In-plane Biaxial and Shearing Forces", *Jl.Soc.Nav.Arch. of Japan*, Vol.156, 1984, pp.355-365.

58. Ueda, Y., Rashed, S.M.H., & Paik, J.K.: "Elastic Buckling Interaction Equation of Simply Supported Rectangular Plates Subjected to Five load Components", *Jl.Soc.Nav.Arch. of Japan*, Vol.157, 1985, pp.425-438.

59. Ueda, Y., Rashed, S.M.H., & Paik, J.K.: "Effective Width of Rectangular Plates Subjected to Combined Loads", *Jl.Soc.Nav.Arch. of Japan*, Vol.159, 1986, pp.258-270.

60. Ohtsuba, H., & Yoshida, J.: "Ultimate Strength of Rectangular Plates under Combinations of Loads (part 1) - Biaxial Compression", *Jl.Soc.Nav.Arch. of Japan*, Vol.156, 1984, pp.323-329. (in Japanese)

61. Ohtsuba, H., & Yoshida, J.: "Ultimate Strength of Rectangular Plates under Combinations of Loads (part 2) - interaction of Compressive and Shear Stresses", *Jl.Soc.Nav.Arch. of Japan*, Vol.158, 1985, pp.368-375. (in Japanese).

62. Ohtsuba, H.: "Interframe Collapse of Stiffened Plate Due to Combined Loading", *OMAE 86*, Tokyo, 1986, pp.403-410.

63. DNV : "Rules for the Design, Construction and Inspection of Offshore Structures", Det Norske Veritas, 1977.

64. Rules and Regulations for the Classification of Ships, *Lloyds Register of Shipping*, London, 1981.

65. American Bureau of Shipping (Annual) Rules for Building and Classing Steel Vessels, *ABS*, New York.

66. "Buckling of Offshore Structures", J.P.Kenny & Partners Ltd., Granada, 1975.

67. ASASNL User Manual, Version 6, KINS Development Ltd, Epsom, UK, August 1982.

68. Trueb, U. : "Stability Problems of Elasto-plastic Plates and Shells by Finite Elements", *PhD Thesis,* London, Imperial College, 1983.

69. Chapman, J.C., & Davidson, P.C.: "Behaviour and Design of Full-Depth Web Panels under Shear", *The Structural Engineer*, Vol.65B, No.4, December 1987.

70. Maquoi, R.J.H.: "Longitudinally Stiffened Plate Girders", *ECCS/BCSA Intl. Symp. on Steel Bridges*, London, 1987.

71. Stanway, G.: "The Behaviour and Design of Transversely Stiffened Plates subject to In-Plane Shear Forces", *PhD Thesis*, London, Imperial College, to be presented.

72. Bates, D.N.: "The Mechanics of Thin-Walled Structures with Special Reference to Finite Rotations", *PhD Thesis*, London, Imperial College, 1987.

73. Williams, D.G. & Aalami, B.: "Thin Plate Design for In-plane Loading", *Constrado Monographs*, Granada, 1979.

74. Ho, D.: "The Buckling of Perforated Web-plates", *PhD Thesis*, London, Imperial College, 1964.

75. Dowling, P.J., Frieze, P.A. & Harding, J.E.: "Imperfection Sensitivity of Steel Plates under Complex Edge Loading", Stability of Steel Structures, 2nd Intl. Colloquium on Stability, *Preliminary Report,* Liege, ECCS, 1977, pp.305-314.

76. BS 2573, part 1 : "Specification for Classification, Stress Calculation and Design Criteria for Structures", (British Standard for Cranes), British Standards Institution, 1983.

77. SIA 161, Swiss Standard for Steel Strutctures, Swiss Society of Engineers and Architects, Zürich, 1979.

78. Standard Specifications for Highway Bridges, American Association of State Highway & Transportation Officials, 1983.

79. Dow, R.S., & Smith, C.S.: "Effects of Localized Imperfections on Compressive Strength of Long Rectangular Plates", *Jl. Constr. Steel Res.*, Vol.4, No.1, 1984.

80. Kaminski, M.: "The Behaviour of Imperfect Plates Subjected to Cyclic Compression Loads", *ECCS Coll. on Stability of Plate and Shell Structures*, Ghent, April 1987, pp.201-208.

81. Merrison Committee: "Inquiry into Basis of Design and Method of Erection of Steel Girder Bridges", *Report of the Committee*, HMSO, London, 1973.

82. Frieze, P.A., Dowling, P.J., & Hobbs, R.E.: "Steel Box Girders - Parametric Study on Plates in Compression", *CESLIC Report BG39*, Imperial College, London, 1975.

83. Rhodes, J.: "On the Approximate Prediction of Elasto-plastic Plate Behaviour", *Proc. I.C.E.*, Part 2, March 1981, pp.165-183.

84. von Kármán, T.: Die Mittragende Breite , Springer, Berlin, 1924.

85. Faulkner, D.: "Compression Strength and Chance", *Defence Fellowship Thesis*, M.I.T., 1970-71.

86. Faulkner, D.: "A Review of Effective Plating for Use in the Analysis of

Stiffened Plating in Bending and Compression", *Jl. Ship Research*, Vol.19, No.1, March 1975, pp.1–17.

87. Winter, G.: "Stress Distribution in and Equivalent Width of Flanges of Wide, Thin–Wall Steel Beams", NACA Technical Note 784.

88. Smith, C.S., Davidson, P.C., Chapman, J.C., & Dowling, P.J.: "Strength and Stiffness of Ship's Plating under In–plane Compression and Tension", *Trans. Royal Inst. Naval Arch.*, Vol.130, 1988 pp.277–296.

89. Fukomoto, Y., & Itoh, Y.: "Basic Compressive Strength of Steel Plates From Test Data", *Proc. of Japanese Soc.Civ.Eng.*, No.344/I–1, April 1984, pp.129–139.

90. Chapman, J.C., & Dowling, P.J.: "A New Design Code for Steel Bridges", *Second Intl. Conf. on Short and Medium Span Bridges*, Ottawa, Vol.2, August 1986.

91. Ayrton, W.E., & Perry, J.: "On Struts", *The Engineer*, London, 1886.

92. Frieze, P.A., Dowling, P.J. & Hobbs, R.E.: "Ultimate Load Behaviour of Plates in Compression", *Steel Plated Structures*, Dowling, P.J., Harding, J.E., Frieze, P.A. (editors). London, Crosby Lockwood Staples, 1977, pp.24–50.

93. Little, G.H.: "The Collapse of Rectangular Steel Plates under Uniaxial Compression", *The Structural Engineer*, Vol.58B, No.3, September 1980, pp.45–61.

94. Dubas, P.: "Some Remarks on the Post–critical Behaviour of Plated Structures", *Steel Structures – Recent Research Advances and their Applications to Design*, Pavlović, M.N. (editor), Elsevier Science, 1987 pp.247–263.

95. Somerville, W.L., Swan, J.W., & Clarke, J.D.: "Measurement of Residual Stresses and Distortions in Stiffened Panels", *Jl. Strain Analysis*, Vol.12 No.2, 1977, pp.107–116.

96. Dowling, P.J.: "Residual Stresses in Welded Steel Box Girder Flanges", *Paper No.14*, Residual Stresses in Welded Construction and Their Effects, Welding Institute, London, 1977.

97. Frieze, P.A.: "Ultimate Load Behaviour of Steel Box Girders and Their Components", *Phd Thesis*, London, Imperial College, 1975.

98. Dowling, P.J., Frieze, P.A., Slatford, J.E., & Dier, A.F.: "Strength of Ships Plating – Plates in Biaxial Compression", *CESLIC Report SP3*, Imperial College, June 1978.

99. Stowell, E.Z., & Schwartz, E.B.: "Critical Stress for an Infinitely Long Flat Plate with Elastically Restrained Edges under Combined Shear and Direct Stress", *NACA ARR No. 3K13*, 1943.

100. Hopkins, H.G., and Rhao, B.V.S.C.: "The Initial Buckling of Flat Rectangular Panels under Combined Shear and Compression", *R.&M. No. 1965*, British A.R.C., 1943.

101. Dean, J.A.: "The Collapse Behaviour of Steel Plating Subject to Complex Loading", *PhD Thesis*, London, Imperial College, 1975.

102. Galerkin, B.G.: "Series–Solutions of Some Cases of Equilibrium of Elastic Beams and Plates", *Vestnik. Inshenernov.*, Vol.1, 1915, pp.879–903 (in

Russian).

103. Brush, D.O., & Almroth, B.O.: "Buckling of Bars, Plates and Shells", McGraw Hill, 1975, p.272.

104. von Kármán, T.: "Festigkeitsprobleme in Maschinenbau", *Encycklopaedie der Mathematischen Wissenschaften*, IV, 1910, pp.348–351.

105. Young, T.: "A Course of Lectures on Natural Philosophy and the Mechanical Arts", London, 1807, pp.320–324.

APPENDIX A CRITICAL BUCKLING - BIAXIAL COMPRESSION AND SHEAR

The purpose of this Appendix is to present the derivation of the critical buckling analysis of flat, simply-supported rectangular plates subjected to biaxial compression and shear. The Galerkin method (102),(103) will be used to derive a set of simultaneous equations in the unkown Fourier coefficients of the buckling mode, and these will be solved by Matrix Iteration. The listing of a micro-computer program is included at the end of this Appendix, which carries out this analysis.

The current analysis extends the analysis in (56), of plates subjected to shear with uniaxial longitudinal or transverse compression, to include biaxial compression. In (56), a Rayleigh-Ritz analysis was performed, using 10 Fourier terms to define the bucklng modes, and Matrix Iteration to solve the equations. The current analysis has been carried out on a desk-top micro-computer, which allowed 32 Fourier terms to be evaluated, and a listing is included at the end of this Appendix.

Whereas the Rayleigh-Ritz analysis of (56) is based on consideration of strain energy and work done, the present Galerkin solution is based on the equilibrium equation for the plate (104), which is (for compressive stresses positive):

$$\nabla^4 w = \frac{t}{D}\left\{ -\sigma_x \frac{\partial^2 w}{\partial x^2} - \sigma_y \frac{\partial^2 w}{\partial y^2} + 2\tau \frac{\partial^2 w}{\partial x \partial y} \right\} \quad \ldots \text{A.1}$$

For the simply supported boundary conditions which are assumed in this analysis, a general description of the shape of the buckling mode, w, is given by:

$$w = \sum_{m=1}^{\infty} \sum_{n=1}^{\infty} a_{mn} \sin \frac{m\pi x}{a} \sin \frac{n\pi y}{b} \quad \ldots \text{A.2}$$

Equation A.2 can be differentiated and incorporated into equation A.1, to give:

$$\sum_m \sum_n \left\{ \frac{m^4}{a^4} + \frac{2m^4n^4}{a^2b^2} + \frac{n^4}{b^4} \right\} \pi^4 a_{mn} \sin \frac{m\pi x}{a} \sin \frac{n\pi y}{b}$$
$$+ \frac{t}{D}\left\{ -\sigma_x \sum_m \sum_n \frac{\pi^2 m^2}{a^2} a_{mn} \sin \frac{m\pi x}{a} \sin \frac{n\pi y}{b} - \sigma_y \sum_m \sum_n \frac{\pi^2 n^2}{b^2} a_{mn} \right.$$
$$\left. \sin \frac{m\pi x}{a} \sin \frac{n\pi y}{b} - 2\tau \sum_m \sum_n \frac{\pi^2 mn}{ab} a_{mn} \cos \frac{m\pi x}{a} \cos \frac{n\pi y}{b} \right\} = 0 \quad \ldots \text{A.3}$$

The Galerkin method (102), (103) of solving a differential equation, given by the general notation:

$$L(\psi) = 0 \qquad \ldots A.4$$

requires ψ to be defined as:

$$\psi = \sum \Psi_i \psi_i \qquad \ldots A.5$$

where Ψ_i are coefficients and ψ_i are functions which satisfy the boundary conditions. If equation A.4 is multiplied by each of the ψ_i in turn, and the resultant expression integrated over the domain and set to zero, then a system of simultaneous equations will result, whose solution will supply the unkown coefficients, Ψ_i. That is, the i'th equation in the system of equations is given by:

$$\oint L(\psi) \cdot \psi_i = 0 \qquad \ldots A.6$$

Applying this process to equation A.3 leads to:

$$\sum_m \sum_n \left[\left\{ \frac{m^2}{a^2} + \frac{n^2}{b^2} \right\}^2 \pi^2 - \frac{t}{D} \left\{ \sigma_x \left[\frac{m}{a}\right]^2 + \sigma_y \left[\frac{n}{b}\right]^2 \right\} \right] a_{mn} \int_0^a \int_0^b \sin \frac{m\pi x}{a} \sin \frac{n\pi y}{b}$$

$$\sin \frac{p\pi x}{a} \sin \frac{q\pi y}{b} \, dx \, dy - 2 \frac{\tau t}{ab D} \sum_m \sum_n m \, n \, a_{mn} \int_0^a \int_0^b \cos \frac{m\pi x}{a} \cos \frac{n\pi y}{b}$$

$$\sin \frac{p\pi x}{a} \sin \frac{q\pi y}{b} \, dx \, dy = 0 \qquad \ldots A.7$$

Making use of the following identities:

$$\int_0^a \cos \frac{m\pi x}{a} \sin \frac{p\pi x}{a} \, dx = \begin{cases} 0 & ; \text{ if } p \pm m \text{ is even} \\ \frac{2a}{\pi} \frac{p}{p^2 - m^2} & ; \text{ if } p \pm m \text{ is odd} \end{cases}$$

$$\int_0^a \sin \frac{m\pi x}{a} \sin \frac{p\pi x}{a} \, dx = \begin{cases} 0 & ; \text{ if } p \neq m \\ \frac{a}{2} & ; \text{ if } m = p \end{cases} \qquad \ldots A.8$$

equation A.7 becomes:

$$a_{pq} \left\{ \left[\left[\frac{p}{a}\right]^2 + \left[\frac{q}{b}\right]^2 \right]^2 \pi^2 - \frac{t}{D} \left[\sigma_x \left[\frac{p}{a}\right]^2 + \sigma_y \left[\frac{q}{b}\right]^2 \right] \right\}$$

$$- \frac{32\tau t}{\pi^2 abD} \sum_m \sum_n a_{mn} \frac{m \, n \, p \, q}{(p^2 - m^2)(q^2 - n^2)} = 0 \qquad \ldots A.9$$

where the τ term is set to zero if $p \pm m$ and $q \pm n$ are not both odd. If:

$$\sigma_x = k_x \frac{\pi^2 D}{b^2 t} \quad ; \quad \sigma_y = k_y \frac{\pi^2 D}{b^2 t} \quad ; \quad \tau = k_s \frac{\pi^2 D}{b^2 t} \qquad \ldots A.10$$

then equation A.9 becomes:

$$a_{pq}\left\{\left[\,p^2 + q^2\,\alpha^2\,\right]^2 - k_x\,p^2\,\alpha^2 - k_y\,q^2\,\alpha^4\right\} - \frac{32\,k_s\,\alpha^3}{\pi^2}\sum_m\sum_n a_{mn}\,\frac{m\,n\,p\,q}{(p^2-m^2)(q^2-n^2)} = 0 \qquad \ldots\ A.11$$

where α = a/b.

Buckling modes due to shear and biaxial compression must be either symmetric or anti-symmetric about the middle of the plate. A symmetric mode is one in which all the Fourier components have m and n coefficients which add up to an even number (ie m+n is even for each a_{mn}) and an anti-symmetric mode has coefficients which add up to an odd number (ie m+n is odd). As an example of evaluating equation A.11, the first equation for symmetric modes is obtained by setting p=1 and q=1, and leads to:

$$a_{11}\left\{\left[\,1+\alpha^2\,\right]^2 - k_x\alpha^2 - k_y\alpha^4\right\}\frac{\pi^2}{32\,k_s\,\alpha^3} + 0.a_{13} - \frac{4}{9}\,a_{22} - \frac{8}{45}\,a_{24}\ldots. \qquad \ldots\ A.12$$

The listing, which begins on the following page, calculates all the coefficients of the determinant which is given by these simultaneous equations, and proceeds to solve the determinant iteratively. The program is written in BBC BASIC.

```
  10 REM **********************
  20 REM *                     *
  30 REM *  Shear  Buckling   *
  40 REM *  Fourier Series    *
  50 REM *                     *
  60 REM *  Eigen Solution    *
  70 REM * Matrix Iteration   *
  80 REM *      Method         *
  90 REM *                     *
 100 REM **********************
 110 :
 120 REM error = convergence criterion
 130 REM Tlimit = Time limit (secs*100)
 140 REM N = number of fourier coefficients
 150 REM Xi() = previous Iteration
 160 REM Xj() = next Iteration
 170 REM Xm() = diagonal elements in Determinant
 180 REM M(),N() = suffices in fourier term, Amn
 190 REM B(,) = Determinant, less its diagonal terms
 200 REM Kx = Amount of longitudinal stress
 210 :
 220 error=.0001
 230 Tlimit=6000000
 240 @%=&20309
 250 :
 260 INPUT "aspect ratio ? "alpha
 270 INPUT "Kx ? "Kx'"Ky ? "Ky
 280 PRINT'"Do you want symmetric, anti-symmetric   bucklin
g or both (S/A/B) ?";:REPEAT:J=INSTR("sSaAbB",GET$):UNTIL J>
0
 290 IF J<3 THEN RESTORE 1450:PRINT"SYMMETRIC"
 300 IF J>2 AND J<5 THEN RESTORE 1460:PRINT"ANTI-SYMMETRIC
"
 310 IF J>4 THEN RESTORE 1450:N=62:PRINT"BOTH"
 320 IF J<5 THEN REPEAT:PRINT'"How many Fourier terms (<=3
1) ";:INPUTN:UNTIL N<=31
 330 :
 340 REM Set up Arrays before beginning calculation
 350 :
 360 DIM B(N,N), Xi(N), Xj(N), Xm(N), M(N), N(N)
 370 FOR I%=1 TO N:READ M(I%),N(I%):NEXT
 380 A=32*alpha^3/PI/PI
 390 FOR I%=1 TO N:Xm(I%)=SQR((M(I%)^2+N(I%)^2*alpha*alpha)
^2-Kx*M(I%)^2*alpha^2-Ky*N(I%)^2*alpha^4):NEXT
 400 :
 410 REM Perform Matrix Iteration Calculation
 420 :
 430 PROCsolve
 440 :
 450 REM Output Results
 460 :
 470 PRINTalpha,N,Kcrit,Kx,Ky
 480 FOR I=1 TO N:PRINTM(I),N(I),Xj(I):NEXT
 490 END
 500 :
```

```
  510 DEF PROCsolve
  520 T%=TIME
  530 PROCsetup_B
  540 PROCinitialize_Xj
  550 REPEAT
  560   PROCset_Xi_to_Xj
  570   PROCmultiply_B_Xi
  580   PROCdivide_Xj_Xm
  590   PROCnormalize_Xj
  600   Kcrit=1/T:PRINTKcrit
  610   PROCaverage_Xi_Xj
  620   PROCnormalize_Xj
  630   Xjmax=0
  640   FOR I%=1 TO N
  650     IF ABS(Xj(I%))>ABS(Xjmax) THEN Xjmax=Xj(I%)
  660     NEXT
  670   UNTIL FNconverged OR TIME-T%>Tlimit:IF TIME-T%>Tlimi
t THEN VDU7:PRINT'"TIMEOUT"
  680 FOR I%=1 TO N
  690   Xj(I%)=Xj(I%)/Xjmax
  700   NEXT
  710 ENDPROC
  720 :
  730 DEFPROCsetup_B
  740 FOR I=1 TO N
  750   i=M(I)
  760   j=N(I)
  770   FOR J=1 TO N
  780     p=M(J)
  790     q=N(J)
  800     IF (i+p) MOD2=0 OR (j+q) MOD 2=0 THEN B(I,J)=0 ELS
E B(I,J)=-i*j*p*q/(i*i-p*p)/(q*q-j*j)*A/SQR((i*i+j*j*alpha*a
lpha)^2-Kx*i*i*alpha*alpha-Ky*j*j*alpha^4)
  810     NEXT
  820   NEXT
  830 ENDPROC
  840 :
  850 DEF FNW(x,y):LOCALPax,Pby,w,I%:Pax=PI*x/alpha:Pby=PI*y
:w=0
  860 FORI%=1 TO N:m%=M(I%):n%=N(I%)
  870   w=w+Xj(I%)*SIN(m%*Pax)*SIN(n%*Pby)
  880   NEXT:=w
  890 :
  900 :
  910 DEF PROCmultiply_B_Xi
  920 LOCAL S
  930 FOR I%=1 TO N
  940   S=0
  950   FOR J%=1 TO N
  960     S=S+B(I%,J%)*Xi(J%)
  970     NEXT
  980   Xj(I%)=S
  990   NEXT
 1000 ENDPROC
 1010 :
 1020 DEF PROCaverage_Xi_Xj
```

```
 1030 FOR I%=1 TO N
 1040   IF SGN(Xj(I%))<>SGN(Xi(I%)) THEN Xj(I%)=(Xj(I%)+Xi(I
%))/2 ELSE Xj(I%)=SQR(Xj(I%)*Xi(I%))*SGN(Xj(I%))
 1050   NEXT
 1060 ENDPROC
 1070 :
 1080 DEF PROCnormalize_Xj
 1090 T=0
 1100 FOR I%=1 TO N:T=T+Xj(I%)^2:NEXT
 1110 T=SQR(T):IF T=0 THEN CRASH!!!!
 1120 FORI%=1TO N:Xj(I%)=Xj(I%)/T:NEXT
 1130 ENDPROC
 1140 :
 1150 DEF FNconverged:LOCAL C:C=TRUE
 1160 FOR I%=1 TO N
 1170   IF ABS(Xj(I%)-Xi(I%))>ABS(Xjmax)*error THEN C=FALSE
 1180   NEXT
 1190 =C
 1200 :
 1210 DEF PROCinitialize_Xj
 1220 T=0:FOR I%=1 TO N:T=T+I%*I%/N/N:NEXT:T=SQR(T)
 1230 FOR I%=1 TO N:Xj(I%)=(N-I%)/N/T:NEXT
 1240 ENDPROC
 1250 :
 1260 DEF PROCdivide_Xj_Xm
 1270 FORI%=1 TO N:Xj(I%)=Xj(I%)/Xm(I%):NEXT
 1280 ENDPROC
 1290 :
 1300 DEF PROCset_Xi_to_Xj
 1310 FOR I%=1 TO N:Xi(I%)=Xj(I%):NEXT
 1320 ENDPROC
 1330 :
 1340 DEF PROCshow_Xj
 1350 PRINT
 1360 T%=@%:@%=&A0A
 1370 FOR I%=1 TO N
 1380   PRINTTAB((I%-1)*8+1);"a";M(I%);N(I%);
 1390   NEXT
 1400 @%=T%
 1410 FOR I%=1 TO N:IF Xj(I%)<0 THEN PRINTTAB((I%-1)*8);:ELS
E PRINTTAB((I%-1)*8+1);
 1420   PRINT;INT(Xj(I%)*1000+.5)/1000;:NEXT
 1430 ENDPROC
 1440 :
 1450 DATA1,1,2,2,1,3,3,1,3,3,2,4,4,2,5,1,4,4,3,5,5,3,2,6,6,
2,7,1,5,5,4,6,6,4,3,7,7,3,8,2,9,1,5,7,7,5,8,4,9,3,10,2,11,1,
10,2,11,3,12,2,13,1
 1460 DATA1,2,2,1,2,3,3,2,1,4,4,1,3,4,4,3,2,5,5,2,1,6,6,1,4,
5,5,4,3,6,6,3,2,7,7,2,8,1,5,6,6,5,4,7,7,4,8,3,9,2,10,1,8,5,9
,4,10,3,11,2,12,1
>
```

APPENDIX B ELASTIC MODEL - BIAXIAL COMPRESSION AND LATERAL PRESSURE

This Appendix will present the derivation of a simple elastic analysis of simply supported constrained plates subjected to biaxial compression and lateral pressure. This analysis is used in Chapter 6 with various first yield criteria to investigate the influence of coexistent lateral pressure on the uniaxial and biaxial strengths of square and rectangular plates. Details of the application of the elastic analysis are given in Chapter 6, and will not be repeated here.

The differential equation of equilibrium of imperfect plates subjected to lateral and in-plane loads (44) is:

$$\nabla^4 w = \frac{Q}{D} + \frac{t}{D}\left\{ \sigma_x \frac{\partial^2(w+w_0)}{\partial x^2} + 2\tau \frac{\partial^2(w+w_0)}{\partial x \partial y} + \sigma_y \frac{\partial^2(w+w_0)}{\partial y^2} \right\} \quad . . \text{ B.1}$$

where tensile stresses are assumed positive. A simple solution of this equation results from assuming that both the initial out-of-plane imperfection, w_0, and the out-of-plane displacements due to the application of load, w, take the form of a single half sine-wave in both the longitudinal and transverse directions, as follows:

$$\left.\begin{aligned} w_0 &= \bar{w}_0 \sin\frac{\pi x}{a} \sin\frac{\pi y}{b} \\ w &= k\, w_0 \end{aligned}\right\} \quad . . . \text{ B.2}$$

where $\bar{w}_0$ is the amplitude of the initial imperfection. If the plate boundaries are assumed to be constrained such that they are free to draw together, but have to remain straight, while the shear stresses on the boundaries are uniform (or uniformly zero), then the distribution of direct stresses in the plate, as the plate deforms, can be derived from the mid-thickness straining which will result from these deformations. These direct stresses are given by:

$$\left.\begin{aligned} \sigma_x &= -\bar{\sigma}_x - \frac{\pi^2 E}{8a^2}\left(k^2 + 2k\right)\bar{w}_0^2 \cos\frac{2\pi y}{b} \\ \sigma_y &= -\bar{\sigma}_y - \frac{\pi^2 E}{8b^2}\left(k^2 + 2k\right)\bar{w}_0^2 \cos\frac{2\pi x}{a} \end{aligned}\right\} \quad . . . \text{ B.3}$$

Since $\partial\sigma_x/\partial y$ and $\partial\sigma_y/\partial x$ are both zero, it follows from equilibrium that the shear stress is uniform everywhere in the plate, and since the deformation mode is inappropriate for plates with applied shear, the shear stress is found to be zero throughout the plate.

Incorporating equations B.3 and the appropriate derivatives of equations B.2 into equation B.1 gives:

$$\left[\frac{1}{a^2} + \frac{1}{b^2}\right]^2 k\,\bar{w}_0\,\pi^4 \sin\frac{\pi x}{a} \sin\frac{\pi y}{b} - \frac{Q}{D} + \frac{t}{D}\left\{\left[\bar{\sigma}_x + \frac{\pi^2 E}{8a^2}\left[k^2 + 2k\right]\right.\right.$$
$$\left.\bar{w}_o{}^2 \cos\frac{2\pi y}{b}\right].\left[-\bar{w}_0\,(1+k)\,\frac{\pi^2}{a^2}\sin\frac{\pi x}{a}\sin\frac{\pi y}{b}\right]$$
$$\left.+\left[\bar{\sigma}_y + \frac{\pi^2 E}{8b^2}\left[k^2 + 2k\right]\bar{w}_0{}^2 \cos\frac{2\pi x}{a}\right].\left[-\bar{w}_0\,(1+k)\,\frac{\pi^2}{b^2}\sin\frac{\pi x}{a}\sin\frac{\pi y}{b}\right]\right\}$$
$$= 0 \qquad \ldots \text{B.4}$$

The Galerkin Method (102),(103) of solving differential equations, which is described in Appendix A, states that an approximate solution of the equation:

$$L(\psi) = 0 \qquad \ldots \text{B.5}$$

can be found, having the form:

$$\psi = \sum \Psi_i\,\psi_i \qquad \ldots \text{B.6}$$

if the system of equations formed by:

$$\oint L(\psi)\,.\,\psi_i = 0 \qquad \ldots \text{B.7}$$

is solved simultaneously. In the present case the solution being sought contains only one unkown, k, resulting in a particularily straightforward and direct solution.

The procedure requires equation B.4 to be mutliplied by $\sin(\pi x/a)\,\sin(\pi y/b)$ and the resulting equation to be integrated over the whole plate area and this integral set to zero. The multiplication and integration will be applied to the various terms of equation B.4 separately. The first term of B.4 becomes:

$$\left[\frac{1}{a^2} + \frac{1}{b^2}\right]^2 k\,\bar{w}_0\,\pi^2 \int_0^a \int_0^b \sin^2\frac{\pi x}{a}\sin^2\frac{\pi y}{b}\,dx\,dy = \left[\frac{1}{a^2} + \frac{1}{b^2}\right]^2 k\,\bar{w}_0\,\frac{\pi^2 ab}{4} \qquad \ldots \text{B.8}$$

The second term becomes:

$$\frac{Q}{D}\int_0^a \int_0^b \sin\frac{\pi x}{a}\sin\frac{\pi y}{b}\,dx\,dy = \frac{48\,\alpha\,Q\,(1-\nu^2)}{\pi^2\,Et}\left[\frac{b}{t}\right]^2 \qquad \ldots \text{B.9}$$

The terms involving the applied biaxial compressions can be lumped together and become:

$$- \frac{t}{D} \left[\frac{\bar{\sigma}_x}{a^2} + \frac{\bar{\sigma}_y}{b^2} \right] \bar{w}_0 \, (1 + k) \, \pi^2 \int_0^a \int_0^b \sin^2 \frac{\pi x}{a} \sin^2 \frac{\pi y}{b} \, dx \, dy =$$

$$= - \frac{12 \, (1 - \nu^2)}{E t^2} \left[\frac{\bar{\sigma}_x}{a^2} + \frac{\bar{\sigma}_y}{b^2} \right] \bar{w}_0 \, (1 + k) \, \frac{\pi^2 ab}{4} \qquad \ldots \text{ B.10}$$

The remaining terms involve the in-plane stress variations, and become:

$$- \frac{t}{D} \frac{\pi^2 E}{8a^2} (k^2 + 2k) \, \bar{w}_0^3 \, (1 + k) \, \frac{\pi^2}{a^2} \int_0^a \int_0^b \cos \frac{2\pi y}{b} \sin^2 \frac{\pi x}{a} \sin^2 \frac{\pi y}{b} \, dx \, dy =$$

$$= - \frac{3 \, \pi^4}{16} (1 - \nu^2) \, (k^2 + 2k) \, (1 + k) \left[\frac{\bar{w}_0}{a} \right]^3 \left[\frac{b}{t} \right] \qquad \ldots \text{ B.11}$$

$$- \frac{t}{D} \frac{\pi^2 E}{8b^2} (k^2 + 2k) \, \bar{w}_0^3 \, (1 + k) \, \frac{\pi^2}{b^2} \int_0^a \int_0^b \cos \frac{2\pi x}{a} \sin^2 \frac{\pi x}{a} \sin^2 \frac{\pi y}{b} \, dx \, dy =$$

$$= - \frac{3 \, \pi^4}{16} (1 - \nu^2) \, (k^2 + 2k) \, (1 + k) \left[\frac{\bar{w}_0}{b} \right]^3 \left[\frac{a}{t} \right]$$

Equations B.8 to B.11 can then be gathered and re-ordered, and using α to denote the aspect ratio, a/b, this gives:

$$\frac{\bar{\sigma}_x}{\alpha^2} + \bar{\sigma}_y = \frac{k}{1 + k} \left[1 + \frac{1}{\alpha^2} \right]^2 \frac{\pi^2 E}{12 \, (1 - \nu^2)} \left[\frac{t}{b} \right]^2 - \frac{16 \, Q}{\pi^4 \, (1 + k)} \left[\frac{t}{\bar{w}_0} \right] \left[\frac{b}{t} \right]^2$$

$$+ \left[1 + \frac{1}{\alpha^4} \right] \frac{\pi^4 E}{16} (k^2 + 2k) \left[\frac{\bar{w}_0}{b} \right]^2 \qquad \ldots \text{ B.12}$$

If μ denotes the ratio of the applied in-plane stresses, $\bar{\sigma}_x / \bar{\sigma}_y$, then the left hand side can be written:

$$\bar{\sigma}_x \left[\mu + \frac{1}{\alpha^2} \right] \qquad \ldots \text{ B.13}$$

The case of uniaxial compression only, in square plates, can be obtained from equation B.12, as follows:

$$\bar{\sigma}_x = \frac{4 \, \pi^2 E}{12 \, (1 - \nu^2)} \left[\frac{t}{b} \right]^2 \frac{k}{1 + k} + \frac{\pi^2 E}{8} (k^2 + 2k) \left[\frac{\bar{w}_0}{b} \right]^2 \qquad \ldots \text{ B.14}$$

This result is referred to in Chapter 3. If, alternatively, equal biaxial compressions are applied, then equation B.12 gives:

$$\bar{\sigma}_x = \bar{\sigma}_y = \frac{2 \, \pi^2 E}{12 \, (1 - \nu^2)} \left[\frac{t}{b} \right]^2 \frac{k}{1 + k} + \frac{\pi^2 E}{16} (k^2 + 2k) \left[\frac{\bar{w}_0}{b} \right]^2 \qquad \ldots \text{ B.15}$$

It should be noted that the first term on the right hand side of equations B.14 and B.15 incorporates the critical buckling load for each load case, and that these first terms on their own give a solution equivalent to the buckling solution of imperfect

struts, originally due to (105):

$$w_{tot} = \frac{w_0}{1 - P/P_{cr}} \quad \ldots \text{B.16}$$

where w_{tot} is the total out-of-plane displacement, ie $w_{tot} = w_0 + w$. If, on the other hand, there are no in-plane stresses applied to the plate then Equation B.12 becomes:

$$\frac{16\,Q}{\pi^4\,(1+k)}\left[\frac{t}{\bar{w}_0}\right]\left[\frac{b}{t}\right]^2 = \frac{k}{1+k}\left[1+\frac{1}{\alpha^2}\right]^2\frac{\pi^2 E}{12\,(1-\nu^2)}\left[\frac{t}{b}\right]^2 + \left[1+\frac{1}{\alpha^4}\right]\frac{\pi^2 E}{16}\,(k^2+2k)\left[\frac{\bar{w}_0}{b}\right]^2 \quad \ldots \text{B.17}$$

which can be re-ordered, to give:

$$Q = \frac{\pi^6 E}{64}\left[\frac{\bar{w}_0}{b}\right]\left[\frac{t}{b}\right]\left[\left[1+\frac{1}{\alpha^2}\right]^2\frac{k}{3\,(1-\nu^2)}\left[\frac{t}{b}\right]^2 + \left[1+\frac{1}{\alpha^4}\right]\frac{(1+k)(k^2+2k)}{4}\left[\frac{\bar{w}_0}{b}\right]^2\right] \quad \ldots \text{B.18}$$

The first term in the square brackets gives the linear relationship between lateral load and out-of-plane displacement, which would result if the effect of membrane stresses was ignored.

The behaviour which is described by these equations is illustrated in section 6.1 of Chapter 6, where it will be shown to give reasonable correspondence with rigorous numerical analyses. Nonetheless, this analysis is not primarily used, in this thesis, as a design tool, but is rather used as a discussion tool, to explore, by a simple and economical means, aspects of behaviour which would otherwise require an undue amount of mainframe computer time.

A subset of this analysis is used, however, to develop the design model for uniaxial compression for different residual stress and imperfection levels in Chapter 3.